SYNTHESIS OF SOLAR AND VISIBLE-LIGHT-ACTIVE HIGHLY ORDERED TITANIA NANOTUBE ARRAYS (TNTS) FOR PHOTOCATALYTIC APPLICATIONS

SIM LAN CHING

THESIS SUBMITTED IN FULFILMENT OF THE
REQUIREMENTS FOR THE DEGREE OF DOCTOR OF
PHILOSOPHY

FACULTY OF ENGINEERING
UNIVERSITY OF MALAYA
KUALA LUMPUR

2015

ABSTRACT

The present contribution work focused on the development of solar-light and visible light responsive binary and ternary TiO_2 nanotube arrays (TNTs) based composite photocatalysts. The developed photocatalysts were implemented for the competent removal of dye and phenolic derivative from the liquid waste. The implication was also extended for the photocatalytic conversion of CO_2 and H_2O to light hydrocarbon. The binary composite was achieved by mashing-up the semiconductor oxides namely nickel oxide (NiO) and tin oxide (SnO_2) with TNTs through impregnation route. The morphological analysis revealed that both of the binary composite are bunches free, self organized and highly ordered with better geometry. The inclusion of semiconductor oxides onto TNTs significantly promoted the shift towards the visible light spectrum than that of the unmodified TNTs. The same was reflected in the solar-light-driven photocatalytic degradation of prominent cationic dye solution, methylene blue (MB) which was adopted as model pollutant for the binary composite with varied loading. However, the increasing loading of both NiO and SnO_2 did not exert significant effect on the degradation efficiency of MB. The visible light development was approached further by including the noble metals and conducting carbon materials. This led to the formation of ternary composite, bound the localized surface plasmon resonance (LSPR) and efficient electron transport endorsed by Ag and GO, respectively. The light source was truncated to artificial visible light to eliminate the unsteady illumination conditions as seen in solar spectrum. Implicit microscopic and spectroscopic techniques substantiated the significance of the presence of Ag as nanoparticles (NPs) and the role of GO in the ternary composite. The ternary exhibited a more appreciable red shift towards the visible range and plunged the recombination of the electron-hole pair compared to that of the binary. The photocatalytic investigation was carried out by degrading MB and additionally chlorinated compound, 2-chlorophenol (2-CP) comprehensively along with their uniqueness in the degradation mechanism. The reusability studies showed a deprived performance for MB degradation than that of 2-CP, due to the chemisorption of MB. The successful results from our continuous work motivated us to further explore the possibility of combining graphene (RGO) and platinum (Pt) for a complicated gas phase conversion of carbon dioxide (CO_2) to light hydrocarbon under visible light irradiation. This ternary composite was synthesized by depositing rapid thermally reduced GO over the surface of TNTs which was predeposited with Pt. The resulting composite demonstrated a stunning visible light absorption over the others. The prepared composite exhibited its accomplishment by energetically photoreacting CO_2 with H_2O for the production of methane. This synergetic CH_4 production rate was attributed predominantly to the coexistence of RGO and Pt which efficiently prolonged the lifetime of the photoinduced electrons and extended the visible light response. Thus the present thesis enlightened and overcame with much promising composite photocatalysts that upbeat the limitations experienced by most of the conventional photocatalysts. It also provided a demanding sustainable and greener solution for environmental cleanup and greenhouse gas reduction through alternative fuel generation.

ABSTRAK

Kertas kerja ini memfokuskan kepada penggunaan nanotiub TiO_2 tersusun (TNTs) sebagai bahan asas komposit fotokatalis secara perduaan dan pertigaan yang bertindak balas dengan cahaya solar dan cahaya nampak. Fotokatalis yang dihasilkan ini akan digunakan untuk menyingkirkan perwarna dan fenolik komplek daripada air yang tercemar. Kegunaannya turut diperluaskan dan digunakan sebagai pengurai fotokatalitik bagi CO_2 dan H_2O yang akan ditukarkan menjadi hidrokarbon ringkas. Komposit perduaan dihasilkan dengan menggabungkan oksida semikonduktor iaitu oksida nikel (NiO) dan oksida timah (SnO_2) dengan TNTs melalui kaedah peresapan. Analisis morfologi membuktikan bahawa kedua-dua komposit perduaan adalah teratur dan bebas dari serpihan TiO_2 dengan keadaan geometri yang lebih baik. Kehadiran oksida semikonduktor dalam TNTs mengalihkan spektrum ke arah cahaya nampak berbanding dengan semasa penggunaan TNTs sahaja. Pemerhatian yang sama dapat dilihat dalam penguraian fotokatalitik di bawah cahaya solar terhadap pewarna kationik, metilena biru (MB) yang dipilih sebagai model bahan tercemar untuk komposit perduaan yang diuji dalam jumlah penggunaan yang berbeza. Walau bagaimanapun, penambahan jumlah kedua-dua NiO dan SnO_2 tidak memberi kesan ketara ke atas keberkesanan penguraian MB. Perkembangan cahaya nampak diubah dengan menggunakan logam mulia dan bahan karbon. Ini membawa kepada pembentukan komposit pertigaan, terikat resonans setempat plasmon permukaan (LSPR) dan pengangkutan elektron efisien yang masing-masing disebabkan oleh Ag dan GO. Sumber cahaya itu digantikan dengan cahaya nampak untuk menghilangkan keadaan pencahayaan yang tidak stabil seperti yang dilihat dalam spektrum matahari. Mikroskopik tersirat dan teknik spektroskopik membuktikan kehadiran Ag sebagai nanopartikel (NP) dan peranan GO dalam komposit pertigaan. Komposit pertigaan menunjukkan pergeseran merah yang lebih ketara ke arah cahaya nampak dan mengurangkan penggabungan semula pasangan elektron dibandingkan dengan kaedah perduaan. Penyelidikan fotokatalitik dilakukan dengan menguraikan MB dan penambahan sebatian berklorin, 2-klorofenol (2-CP) secara komprehensif melalui mekanisme penguraian yang unik. Kajian menunjukkan prestasi MB yang menurun berbanding dengan 2-CP adalah disebabkan oleh penyerapan kimia MB. Kejayaan yang cemerlang daripada kerja yang berterusan ini mendorong kami untuk terus mencuba kaedah lain dengan menggabungkan graphene (RGO) dan platinum (Pt) untuk penguraian fasa gas yang komplek iaitu karbon dioksida (CO_2) kepada hidrokarbon ringkas di bawah pengaruh sinaran cahaya nampak. Komposit pertigaan ini disintesis dengan melekatkan RGO yang diturunkan oleh tenaga haba yang sangat cepat pada permukaan TNTs yang mana terlebih dahulu dilekatkan dengan Pt. Keputusan yang dihasilkan oleh komposit menunjukkan penyerapan cahaya nampak berbanding dengan yang lain. Komposit yang dihasilkan menunjukkan kejayaan yang cemerlang dalam tindakbalas CO_2 dengan H_2O untuk penghasilan metana. Kadar penghasilan CH_4 adalah bergantung kepada kewujudan RGO dan Pt yang berkesan dalam memanjangkan jangka hayat elektron dan melanjutkan tindak balas kepada cahaya nampak. Oleh itu secara keseluruhannya tesis ini mengetengahkan mengenai komposit fotokatalisis yang berpotensi dalam mengatasi keterbatasan yang dialami dengan penggunaan fotokatalis konvensional. Ia juga menyediakan permintaan yang berterusan dan persekitaran hijau dengan mengurangkan kesan gas rumah hijau melalui penggunaan bahan api alternatif.

ACKNOWLEDGEMENTS

The first person I would like to express my deepest gratitude is my supervisor, Dr. Saravanan Pichiah. He is a great mentor who gave me lots of freedom to work on the study in my way and fully committed whenever I need his guidance and supports on paper writing and experimental works. I appreciate your positive problem solving skills, clear minded and open minded for giving me many chances to attend international conference in overseas. I wish him all the best and may him blossom in where he is planted. Next, I would like to thank my co-supervisor, Prof. Shaliza for her continuous support and encouragements. I am thankful to Prof. Dr. Wan Jefrey Basirun for allowing me to use the equipments in his laboratory during the initial stage of my study.

I also thank my friend Azrina for introducing me to my supervisor and willing to share her knowledge throughout my study; Leong Kah Hon for teaching me UPLC and valuable discussion on our research works and paper writting. Special thanks are given to all of my labmates and friends: Wong Shiao Dhing, Kang Yee Li, Anis, Ranjinni, Sharmini, Atiqah, Illiah, Haslina, Shan, Wong Kien Tek, Mossem, Paryam and Azie who make my life enjoyable in laboratory. Special acknowledgements go to Madam Kalai, Madam Rozita and Alliah for their kind technical and administrative supports; Afzalina and Mulan from NANOCAT for continuous supports in XRD analysis; Siew Siew for her excellent contribution in FESEM and TEM analysis.

Lastly, I would like to convey the most important gratitude to my family. Mom and dad, you are the strongest supports to me. Your unconditional love and cares gave me strength to continue this journey. Sincerest thanks to my aunt, Sim Chye Hong for providing me accommodation and countless support throughout my stay in Kuala Lumpur.

TABLE OF CONTENTS

CHAPTER 1: INTRODUCTION

CHAPTER 2: LITERATURE REVIEW

CHAPTER 3: METHODOLOGY

CHAPTER 4: RESULTS AND DISCUSSION

CHAPTER 5: CONCLUSIONS AND RECOMMENDATIONS

LIST OF FIGURES

LIST OF TABLES

LIST OF SYMBOLS AND ABBREVIATIONS

Symbols/Abbreviations	**Meanings**
GHG	greenhouse gases
CO_2	carbon dioxide
UV	ultraviolet
$^{\bullet}OH$	hydroxyl radicals
$^{\bullet}O_2^{-}$	superoxide radical anion
TiO_2	titanium dioxide
TNTs	titanium dioxide nanotube arrays
GO	graphene oxide
RGO	reduced graphene oxide
NiO	nickel oxide
ZnO	zinc oxide
SnO_2	tin oxide
E_{CB}	energy of conduction band edge
Ag	silver
Pt	platinum
LSPR	localized surface plasmon resonance
MB	methylene blue
2-CP	2-chlorophenol
CdSe	cadmium selenide
CdS	cadmium sulfide
$ZnFe_2O_4$	zinc iron oxide
Fe_2O_3	iron (III) oxide
Cu_2O	copper oxide
E_g	band gap energy
e^-	electron
VB	valence band
CB	conduction band
h^+	holes
$h\nu$	photon energy

E_{NHE}	potential versus normal hydrogen electrode
HCl	hydrochloric acid
Bu_4N^+	tetrabutylammonium ion
$AgNO_3$	silver nitrate
$KMnO_4$	potassium permanganate
MO	methyl orange
ARS	Alizarin Red S
AO7	Acid Orange 7 azo-dye
Ni_2O_3	nickel (III) oxide
Hg	mercury
Xe	xenon
E_f	Fermi energy
λ	wavelength
$Ni(NO_3)_2 \cdot 6H_2O$	nickel nitrate hexahydrate
$SnCl_4 \cdot 5H_2O$	tin (IV) chloride pentahydrate
H_2PtCl_6	chloroplatinic acid
I_D	intensity of D band
I_G	intensity of G band
k^b	reaction rate
r_{ion}	ionic radii

CHAPTER 1

INTRODUCTION

1.1 Generalities

The rapid growth of industry has created a series of problems related to energy and environment. Water pollution has become the global risk and continues to threaten the entire ecosystem irrespective of developed and developing nations. This is due to the complexity and variety of new pollutants discharged into the aquatic system by numerous industries. It becomes a challenge to identify an ideal treatment process that can meet stringent environmental regulations. The formal treatment methods such as flocculation, adsorption, reverse osmosis and etc tend to generate secondary pollutants which will inevitably create additional cost for secondary pollutants removal. Further, some of the discharged organic pollutants including commercial dyes, endocrine disrupting compounds (EDCs) and persistent organic pollutants (POPs) are not handled well by these methods.

On the other hand, the planet is also experiencing the depletion of conventional energy sources especially fossil fuel and the increasing levels of greenhouse gases (GHG) in the atmosphere. Carbon dioxide (CO_2) is the primary greenhouse gas emitted through the combustion of fossil fuel. The rising of atmospheric CO_2 levels resulted in global warming and climate change. Asia being a consortium of developing nations, the emission of CO_2 reached an average annual growth rate of 5.3 percent within 25 years from 1980 (2136 million ton) to 2005 (7692 million ton) (Timilsina and Shrestha, 2009). The drastic consumption of fossil fuels owing to the energy demand will lead to its shortage sooner or later. Recently, many efforts have been devoted to reduce CO_2 emissions such as pre and post-combustion capture of CO_2 followed by compression and geological sequestration. However, these processes are energy intensive and expensive. Hence, both the environmental pollution and energy crisis have inspired the research into green and sustainable solutions.

1.2 Photocatalysis

Photocatalysis, a classification of advanced oxidation process (AOPs) has undergone a significant development since the breakthrough discovery of photocatalytic splitting of water with titanium dioxide (TiO_2) electrodes by Fujishima and Honda (Fujishima and Honda, 1972). This photocatalysis is categorized as homogeneous and heterogeneous photocatalysis according to the different phases of reactants and photocatalysts employed. In heterogeneous photocatalysis, semiconductors are commonly used as photocatalysts and are excited by photon energy obtained from different light source (UV, visible light and solar energy). When these semiconductor photocatalysts are illuminated by photon energy (hv) higher than its band-gap energy (E_g), oxidation-reduction reactions are triggered at the surface of semiconductors due to the generation of positive holes (h^+) and electrons (e^-). In the oxidation reactions, the holes react with water (H_2O) to form hydroxyl radicals ($^\bullet OH$). On the other hand, oxygen is reduced by electrons to produce superoxide radical anion ($^\bullet O_2^-$). The organic pollutants are oxidized by $^\bullet OH$ and $^\bullet O_2^-$ to form CO_2, water and non hazardous substances in the complete photocatalytic reaction.

The advantages of heterogeneous photocatalysis over the conventional water treatment process are: (i) the degradation products (CO_2, water and mineral products) are harmless to environment, (ii) atmospheric oxygen is used as oxidant instead of other strong oxidants such as hydrogen peroxide (H_2O_2) and ozone (O_3), (iii) low energy input to drive photocatalysis, and (iv) less secondary pollutants are generated. Concurrently, the heterogeneous photocatalysis also provides a feasible way to convert the predominant GHG (CO_2) into valuable hydrocarbon fuels. In a simple statement, it is referred as “a mimic of photosynthesis process”. As like photosynthesis, this process also reduces CO_2 through the photoexcited electrons (e^-) in the presence of water (H_2O) to yield energy-bearing products such as methane (CH_4), methanol (CH_3OH), formaldehyde (HCHO), formic acid (HCOOH) and etc (Li et al., 2010). This ground breaking process provides a new insight to handle the excessive atmospheric CO_2 through a sustainable pathway with simultaneous production of renewable energy resource.

1.3 Titania (TiO_2) Photocatalyst

Titania (TiO_2) is one of the most common types of semiconductor photocatalyst used in heterogeneous photocatalysis to mediate the photoreaction between the adsorbed species and charge transfer. Table 1.1 indicates a wide range of potential semiconductors (TiO_2, ZnO, ZnS, CdSe, CdS, WO_3 and SnO_2) for the use of heterogeneous photocatalysis. Among these semiconductors, TiO_2 blossom as the best candidate due to its non-toxicity, biologically and chemically inertness, long-term photostability, low cost, easy availability and high photoactivity (Mor et al., 2007; Chen and Mao, 2007; Seger and Kamat, 2009).

Table 1.1: Semiconductors used in photocatalysis process (Daghrir et al., 2013)

Semiconductor	Band gap (eV)	Wavelength (nm)	Light absorption	Valence band (V vs NHE)	Conduction band (V vs NHE)
TiO_2	3.2	387	UV	3.1	-0.1
SnO_2	3.8	318	UV	4.1	0.3
ZnO	3.2	387	UV	3	-0.2
ZnS	3.7	335	UV	1.4	-2.3
WO_3	2.8	443	visible	3	0.4
CdS	2.5	496	visible	2.1	-0.4
CdSe	2.5	729	visible	1.6	-0.1

In most cases, TiO_2 is employed in particles form but the random electron transport pathway and structural disorder at the contact between two crystalline leads to recombination due to the trapping/detrapping of photoinduced electron-hole pairs and an enhanced scattering of free electrons, thus hindering electron mobility (De Jongh and Vanmaekelbergh, 1996; Kudo and Miseki, 2009; Mohamed and Rohani, 2011). These limitations are succeeded through a modified structure of titania particles to one dimensional (1D) architectures such as nanotubes, nanorods, nanowires and etc. Off them, self-organized and vertically oriented TiO_2 nanotube arrays (TNTs) is known for its excellence in surface-to-volume ratios, surface area, charge transport properties and chemical stability (Xie et al., 2010). Many studies have demonstrated TNTs with improved properties compared to other forms of TiO_2 for various applications including photocatalytic degradation of dyes and organic compounds, water splitting, photoreduction of CO_2 to hydrocarbon fuel and dye-sensitized solar cells (Mohapatra et al., 2008; Varghese et al., 2009; Wang and Lin, 2010; Sun et al., 2011).

1.4 Problem Statements

Regardless the nanostructure of TiO_2 in particle or nanotube form, their photocatalytic efficiency highly depends on its band gap energy (E_g). The band gap energy of TiO_2 varies with respect to their crystallographic phase i.e., 3.2 eV for anatase and 3.0 eV for rutile. This wider band gap restricts its excitation to ultraviolet (UV) spectrum only ($\lambda \leq 390$ nm) that slumps to ~5% by the ozone layer while the visible light contributes as a majority (~43%). Therefore, the photoresponse of TiO_2 or TNTs need to be extended to visible light spectrum for the purpose of sustainable and renewable energy harvesting.

The recombination between electrons in conduction band (CB) and holes in valence band (VB) could occur through the defect in TiO_2 surface states accompanied by the indirect recombination via oxygen vacancy and surface recombination via Ti-OH (Liu et al., 2006). The high recombination rate of electron-hole pairs lead to a low photoactivity in both nanoparticle and nanotube form of titania photocatalyst. The above limitations also raise a concern associated with the photocatalytic conversion of CO_2 to hydrocarbon fuel. The prime setback in CO_2 photoreduction is the high energy barrier due to the stable chemistry of CO_2 molecule. Further, a competence will rise between H_2O and CO_2 to react with electrons in CB. This could support water reduction and results in hydrogen generation rather than the light hydrocarbon. This specific reaction is not favourable for the CO_2 photoreduction. Thus, it is essential to design and develop a photocatalyst that minimize the electron loss and suppress the unfavourable reactions.

Significant efforts have been devoted to overcome these aforementioned limitations through metal(s) (Tseng et al., 2004; Kočí et al., 2010; Yui et al., 2011), non metal(s) (Ihara et al., 2003; Wang et al., 2011a) doping, mash-up with semiconductors (Hou et al., 2007; Chen et al., 2008) and composite with conducting carbon materials (Gao et al., 2012; Shah et al., 2013). However, most of the reported modification works focused on the nanoparticle form rather than nanotube form of titania. It is indeed a tough task to revive the physicochemical properties of TNTs compared to that of nanoparticles due to its closely packed tubular morphology. Thus, it stimulated to find modified titania composite that could be tailored through prospective synthesis route.

While evaluating the photocatalytic performance of environmental pollutants, dye compound is the one that was mostly studied by the researchers (Liu et al., 2009; Ma et al., 2010; Wu et al., 2012; Chang et al., 2011). However, its special role as electron donor was either neglected or not studied in most of the investigations. Besides, there is also a vacuum to compare the behaviour of the same photocatalyst using different genera of pollutants. Numerous information have been provided on visible-light-driven photocatalytic degradation of dye pollutants (Mohapatra et al., 2008; Shah et al., 2013; Song et al., 2012; Xu et al., 2010), but there is a wide lag on employing readily available solar light as an alternative source.

The evolution in the photocatalysis finally peaked into “artificial photosynthesis”, converting inorganic to organic compound as processed by the autotrophs. This could be a feasible solution for recycling GHG as feedstock for energy products. Though this process spells easily but it is one of the complicated and challenging reactions that demand more comprehensive and detailed considerations. Despite of few researches have been carried out, majority of them utilized UV light that is harmful and not readily available (Wu et al., 2005; Kočí et al., 2010; Krejčíková et al., 2012; Wang et al., 2012b). Thus necessitates the development of photocatalysts that utilize harmless light source sustainably. Collectively all the aforementioned problems provoke the utilization of solar or artificial visible light for both environmental remediation and energy conversion, thereby urging the researchers for their extensive contribution in this specific discipline.

1.5 Objective and Scope of Research

The major objective of the present study is to develop and tailor modified TNTs for impressive visible and solar-light-driven photocatalysis. Thus obtained photocatalysts were successfully applied for the removal of methylene blue (MB) and 2-chlorophenol (2-CP) from aqueous solution as environmental remediation. The photocatalyst was also successfully applied for the gas phase conversion of CO_2 and H_2O to hydrocarbon fuel. This research significantly contributed to a new development of composite photocatalysts that endorsed the sustainability in both environmental and energy applications.

The specific objectives are as follows:

(1) Synthesis of backbone materials – “TNTs”.

(2) Construct solar and visible-light-responsive photocatalysts through:
  - Semiconductor mashing-up
  - Localized surface plasmon resonance (LSPR)
  - Conducting carbon materials

(3) Dissection of materials chemistry of synthesized photocatalysts.

(4) Study the interaction between photocatalysts and reactants (photocatalysis mechanism).

(5) Evaluate the photocatalytic performance for environmental and energy remediation.

To achieve the said objective, following investigations were performed.

- **Semiconductor Mashing-up:** Different types of semiconductor composite photocatalysts were successfully developed by mashing-up TNTs with nickel oxide (NiO) and tin oxide (SnO_2).
- **Localized Surface Plasmon Resonance (LSPR):** The LSPR phenomenon was

incorporated into the TNTs through noble metals namely silver (Ag) and platinum (Pt) loading.

- **Conducting Carbon Materials:** Alternately, graphene oxide (GO) and reduced graphene oxide (RGO) were engulfed to further enhance electron transport efficiency.
- **Material Science:** As synthesized photocatalysts were exclusively characterized for its major materials insight through crystalline phase analysis, morphology, lattice fringes, chemical composition with chemical and electronic state, Raman scattering, optical, photoluminescence properties and etc with appropriate techniques.
- **Environmental Remediation:** The photocatalytic performance was investigated by degrading different classes of organic compounds namely methylene blue (MB), a good photosensitizing compound and 2-chlorophenol (2-CP), a poor photosensitizing compound.
- **Energy Conversion:** The successful implication of the developed photocatalysts extended the thesis scope towards the gas phase photocatalytic conversion of CO_2 to light hydrocarbon.

1.6 Thesis Overview

Chapter 1 starts with the introduction on environmental and energy issues which is the major subject of discussion of present thesis. This is followed by an introductory note on photocatalysis, TiO_2 and TNTs photocatalysts. Then the major limitations of these specific studies were signified and the specific research hypotheses were sculptured. This was succeeded through major scope and precise objectives with explicit steps.

Chapter 2 furnishes the literature survey relevant to the thesis. In a prima facie, the chapter elaborates the background of semiconductor photocatalysis, development of electrochemical anodization, various reports on modification approach and finally the photocatalytic performance for degradation of aqueous phase organic pollutants and gas phase conversion of CO_2 to hydrocarbon fuels.

Chapter 3 outlines the detailed synthesis route for TNTs, followed by modification methods using semiconductors (SnO_2, NiO), noble metals (Ag, Pt) and conducting carbon materials (GO, RGO). The synthesis is followed by the characterization techniques that were involved in understanding the physicochemical nature of the prepared samples. The last section of this chapter elaborates the experimental setup and conditions adopted for the degradation of aqueous phase organic pollutants and gas phase conversion of CO_2 to hydrocarbon fuels.

Chapter 4 presents the outcome of the thesis findings with comprehensive discussions. This chapter necessitates the insights, importance and influence of the chosen composites along with its significance of materials chemistry. The photocatalytic performance of organic pollutant degradation and its mechanism is categorized as NiO/TNTs, SnO_2/TNTs and GO/Ag-TNTs and presented, while the performance of RGO/Pt-TNTs was presented under gas conversion section. The conclusions and recommendations are included in **Chapter 5**.

CHAPTER 2

LITERATURE REVIEW

2.1 Heterogeneous Photocatalysis

Photocatalysis is defined as the “acceleration of a photoreaction by the presence of a catalyst” (Mills and Le Hunte, 1997). They can occur either homogeneously or heterogeneously. The heterogeneous photocatalysis is based on the photo-excitation of a semiconductor due to the absorption of electromagnetic radiation mostly in the near UV spectrum. Over the last few decades, the application of heterogeneous photocatalysis has expanded rapidly over the homogeneous. They have gained substantial interest in the areas of organic pollutants degradation, water splitting (hydrogen generation) and CO_2 reduction either by using natural or artificial light. Despite the differences in character and utilization, all these applications have the same basis.

A photocatalyst is characterized by its capability to mediate the reduction and oxidation by the use of light through an efficient absorption ($h\nu \geq E_g$). Semiconductors have a small band gap (1 ~ 4 eV) that allows the excitation of electrons between VB to CB. Fig. 2.1 indicates the band gap energy of several semiconductor catalysts (TiO_2, ZnO, NiO, CuO, SnO_2 and etc) along with the standard potential of redox couples. The charge transfer rates between photogenerated carriers in semiconductors and the solution species depend on the correlation of energy levels between the semiconductor and the redox agents in the solution. The photoexcited electrons in the more negative CB of semiconductor have the greater ability to reduce the adsorbed couples, and able to oxidize them which have more negative redox potentials than the VB (Rajeshwar, 1994).

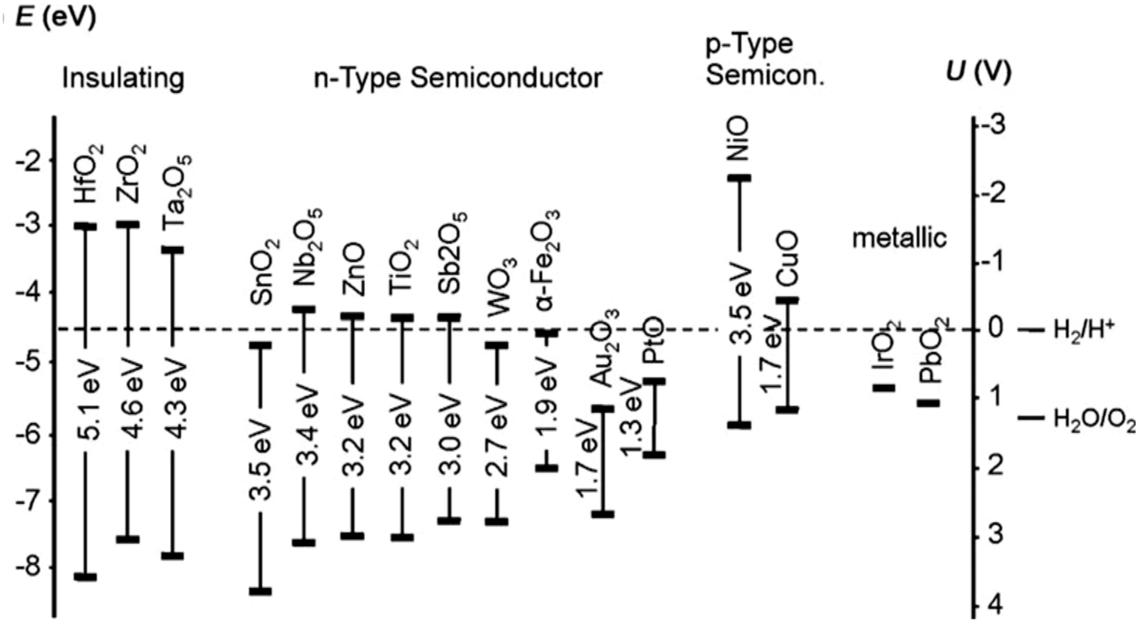

Figure 2.1: Electronic band structure of different metal oxides and relative band-edge position to electrochemical scale (Nah et al., 2010)

As shown in Fig. 2.2, when semiconductor catalysts (SC) such as TiO_2, ZnO, CdS, ZnS, Fe_2O_3, WO_3 and Cu_2O are excited by photons with higher energy than the band gap (E_g), electron (e^-) is promoted from the VB to the CB. This leads to the formation of free electron (e^-) in the CB and a hole (h^+) in the VB. The separated electron and holes will diffuse to the surface of SC (pathway C and D). The electrons are captured by the surface hydroxyls of SC to form surface-trapped CB electrons which will react with electron acceptor (i.e. oxidant). Meanwhile, the surface-trapped holes will oxidize electron donor species (i.e. reductant). However, recombination of electron-hole pairs (pathway A and B) can occur by releasing the absorbed light energy as heat, with no chemical reaction taking place. This recombination process should be prevented for higher photocatalytic performance.

$$\mathrm{SC} + h\nu\ (\geq E_g) \rightarrow e^- + h^+ \tag{2.1}$$

$$e^- + \mathrm{Ox} \rightarrow \mathrm{Ox}^{\bullet} \tag{2.2}$$

$$h^+ + \mathrm{red} \rightarrow \mathrm{red}^{\bullet +} \tag{2.3}$$

where red is “reductant” (electron donor), and Ox is “oxidant” (electron acceptor) (Hoffmann et al., 1995).

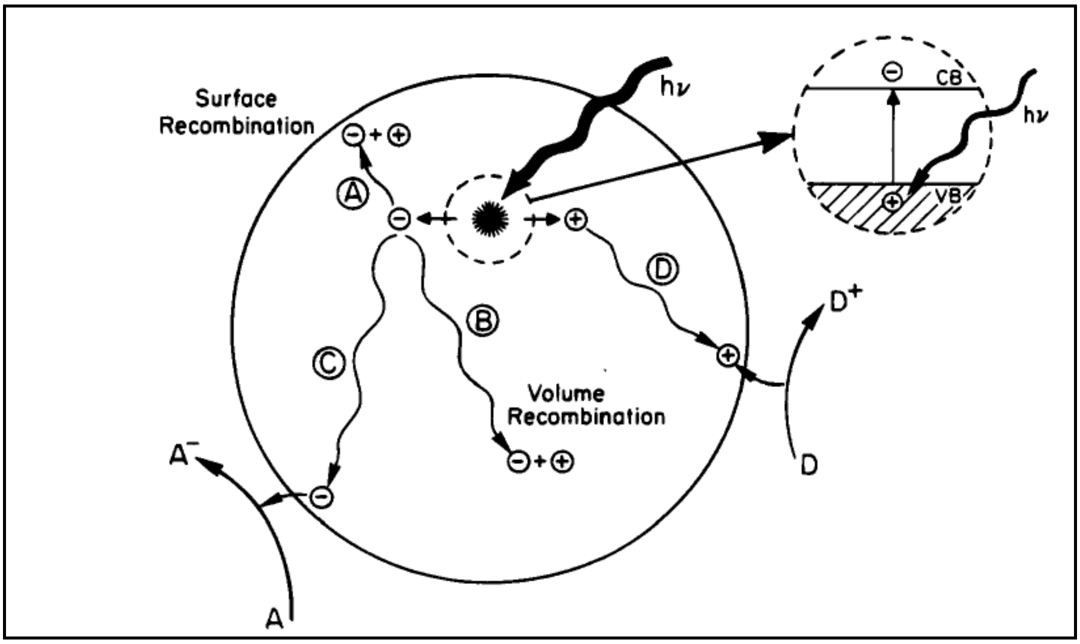

Figure 2.2: Illustration of semiconductor photocatalysis mechanism (Linsebigler et al., 1995)

2.2 Titania (TiO_2) Photocatalyst

Among all available semiconductor photocatalysts, TiO_2 shine as competent versatile candidate, owing to its unique character that allows simultaneous oxidation of water (E_{NHE} (O_2/H_2O) = 1.23 eV) and reduction of protons (E_{NHE} (H^+/H_2) = 0.0 eV) (Fig. 2.1). Since the discovery of photocatalytic splitting of water aided by TiO_2 electrodes (Fujishima and Honda, 1972), TiO_2 nanomaterials have attracted much attention for widespread environmental applications due to its following characteristic: non-toxicity, long-term stability, low cost, chemical inertness, easy availability and high photoactivity (Mor et al., 2007; Chen and Mao, 2007; Seger and Kamat, 2009).

TiO_2 is further sub-classified as n-type semiconductor due to the presence of a small amount of oxygen vacancies which are compensated by the presence of Ti^{3+} (Hernández-Alonso et al., 2009). The VB in TiO_2 is mainly formed by the overlapping of the oxygen 2p orbitals, while the lower part of the CB is formed by the 3d orbitals of Ti^{4+} (Daghrir et al., 2013). Anatase, rutile, and brookite are the three phases in which TiO_2 usually exists in nature. Among them, anatase and rutile are commonly utilized as photocatalysts. Anatase could be transformed to the equilibrium rutile phase at temperature between 550 and about 1000 ℃. They are mainly used as UV light-driven photocatalyst, while rutile TiO_2 is mainly used as white pigment in paint. Rutile phase of TiO_2 exhibits lower photocatalytic activity due to its higher recombination rate of electron-hole pairs compared to that of anatase (Choi et al., 1994). The last phase, brookite possess orthorhombic crystalline structure which is seldom considered because it leads to the formation of secondary minority phase with the support of rutile and anatase (Addamo et al., 2006).

2.3 TiO_2 Nanotube Arrays (TNTs)

Nanoparticulated forms of TiO_2 are widely used for various applications owing to its maximized specific surface area and to achieve a maximum overall efficiency. However, one dimensional (1D) TiO_2 materials such as nanorods, nanotubes and nanowires have received a greater attention recently due to its ordered and strongly interconnected nanoscale architecture which could improve electron transport leading to higher photoefficiency (Yang et al., 2008).

Among these 1D materials, self-organized and vertically oriented TiO_2 nanotube arrays (TNTs) are of great interest because of its larger surface area, vectorial charge transfer, long term stability to photo and chemical corrosion (He et al., 2011; Mun et al., 2010). TNTs offers a large internal surface area with its lengths sufficient to capture incident illumination and provide facile separation of photogenerated charge. TNTs are also widely applied for various applications including degradation of organic compounds, water splitting, carbon dioxide (CO_2) conversion to methane, and dye-sensitized solar cells (Lai et al., 2010a; Mohapatra et al., 2008; Varghese et al., 2009; Wang and Lin, 2010; Sun et al., 2011; Liu et al., 2011).

2.4 Electrochemical Anodization Approach

In 1999, Zwilling and co-workers successfully synthesized ordered nanoporous TiO_2 by anodizing Ti in F^- containing electrolytes (Zwilling et al., 1999). Since then, electrochemical anodization has attracted more attention due to its ability to produce vertically oriented highly ordered nanotube arrays with controllable dimensions. It is economical and versatile approach that is not limited to titanium (Ti) but can be applied to other metal surfaces to form closely packed and well aligned nanotubes.

Mor and co-workers (Mor et al., 2006) illustrated the anodization of TNTs as shown in Fig. 2.3. The interaction of metal with O^{2-} or OH^- ions creates the oxide layer (Fig. 2.3a) on the surface of the metal substrate. After the development of initial oxide layer, these anions move through the oxide layer towards the metal/oxide interface. The localized dissolution of the oxide (Fig. 2.3b) causes the formation of small pits in this oxide layer. The electric field intensity across the remaining barrier layer increases owing to the thin barrier layer at the bottom of the pits, resulting in further pore growth (Fig. 2.3c). The electric field in these protruded metallic regions increases as the pores deepen. The field-assisted oxide growth and oxide dissolution are enhanced, and hence well-defined inter-pore voids are formed (Fig. 2.3d).

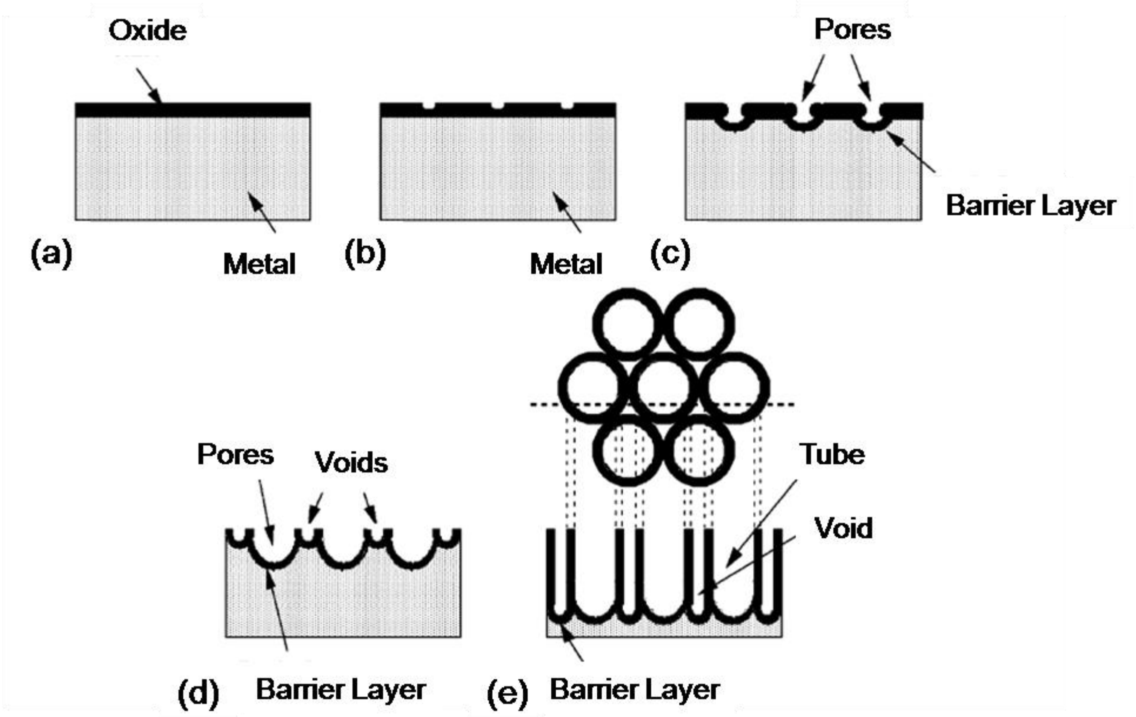

Figure 2.3: Illustrative diagram of the electrochemical anodization of TNTs: (a) oxide layer formation, (b) pit formation on the oxide layer, (c) growth of the pit into scallop pores, (d) metallic part between the pores undergoes oxidation and field assisted dissolution, and (e) fully developed TNTs with a corresponding top view (Mor et al., 2006)

They also suggested the overall reactions for the anodization process of titanium (Ti) in fluoride based electrolytes as:

$H_2O \rightarrow O_2 + 4e^{-} + 4H^{+}$ (2.4)

$Ti + O_2 \rightarrow TiO_2$ (2.5)

$TiO_2 + 6F^{-} + 4H^{+} \rightarrow TiF_6^{2-} + 2H_2O$ (2.6)

2.4.1 Electrochemical Anodization Using Different Generations of Electrolyte

TNTs synthesis via electrochemical anodization approach started with first generation HF based electrolytes, followed by second generation buffered electrolysis, third generation polar organic electrolytes (such as formamide (FA), ethylene glycol (EG), dimethyl sulfoxide (DMSO) and diethylene glycol (DEG)), and fourth generation non-fluoride based electrolytes (Grimes and Mor, 2009).

Almost ideal longer TNTs can be obtained using EG because the low water content in the polar organic electrolytes decreases the chemical dissolution of oxide at TNTs mouth. In comparison with growth rates observed by using other polar organic or aqueous based electrolytes, the growth rate in EG based electrolytes is progressive i.e., 750−6000% higher than the rest (Paulose et al., 2006; Cai et al., 2005; Shankar et al., 2007). The increase in H_2O concentration can compensate the anodic dissolution due to the increased weight percentage (wt%) of ammonium fluoride (NH_4F), and resulted in the formation of longer nanotubes with higher growth rates. TNTs synthesized using EG electrolyte exhibited close packing, better morphology and higher growth rate than that of FA and DMSO based electrolyte (Prakasam et al., 2007). The evolution of different generations of electrolytes is summarized in Table 2.1.

Table 2.1: The evolution of different generations of electrolytes used to synthesize TNTs via electrochemical anodization

Generation	Research Highlights	Reference
First generation: HF based electrolytes	TNTs up to 500 nm length was achieved by the anodization in 0.5 wt% HF solution at 20 V for 20 min. Nanotube structure collapsed when voltage exceeded 40 V. TNTs length was limited to less than a micron.	Gong et al., 2001
	Straight tubes with inner diameter of 22 nm and tube length of 200 nm was synthesized by decreasing the anodization voltage from 23 to 10 V followed by a constant 10 V for 40 min.	Mor et al., 2003
	The effect of anodization temperature on the wall thickness and tube length was reported. The tube length changed by an approximate factor of two and the wall thickness by an approximate factor of four at different temperatures.	Mor et al., 2005
Second generation: Buffered electrolytes	Dissolution rate of TiO_2 was adjusted by localizing acidification at the pore bottom to achieve high-aspect-ratio growth of TNTs.	Macak et al., 2005a
	TNTs length over 6 μm was achieved by adjusting pH of both KF and NaF aqueous electrolytes. Higher pH solution resulted in longer nanotubes formation. The nanotube length was independent of the anodization time in highly acidic electrolytes (pH < 1). pH 3−5 was the best for the formation of longer nanotubes, while lower pH was for formation of shorter nanotubes.	Cai et al., 2005
	Nanotubes with pore diameter ranging between 90 and 110 nm and thickness ~2.5 μm was formed in electrolyte containing 0.5 wt% NH_4F with a sweep rate 0.1 Vs^{-1}.	Taveira et al., 2005
	Synthesis of nanotubes at 1 mA/cm^2 to form 950 nm thick tubular layer, with a tube diameter ranging between 60 and 90 nm using the same electrolyte as previous work.	Taveira et al., 2006

Table 2.1, continued

Generation	Research Highlights	Reference
Third generation: Polar organic electrolyte (glycerol based)	Synthesis of TNTs in electrolyte consisting of 0.5 wt% NH_4F in glycerol with $(NH_4)_2SO_4$ at 20 V for 13 h. Smooth wall TNTs with 6−7 µm long with inner diameter of 40−50 nm was obtained.	Macak and Schmuki, 2006; Macak et al., 2005b
	Effect of pH of 75% glycerol + 25% water + 0.5 wt% NH_4F was studied by adding H_2SO_4. When pH was 5.6, TNTs of 950 nm long was achieved. With further addition of 0.1 M sodium acetate at pH 5.6, it drastically ascended the tube length to 4.16 µm.	Yin et al., 2007
Dimethyl sulfoxide (DMSO) based	Synthesis of TNTs under fluorinated DMSO and ethanol electrolyte environment, at 20 V for 70 h resulted in tube length of 2.3 µm with diameter of 60 nm.	Ruan et al., 2005
	Pre-anodized Ti foil in 0.5% HF in water at 20 V followed by anodizing with the support of DMSO electrolyte containing 2% HF at 40 V for 69 h. Thus the adopted fabrication conditions yielded TNTs with 120 nm of diameter and 45 µm of length. Further increasing the anodization voltage to 60 V under identical electrolyte condition resulted tube with 150 nm diameter and 93 µm of length.	Paulose et al., 2006; Grimes and Mor, 2009
Formamide (FA) based	FA-H_2O mixtures containing F^- ions were used to study the effect of different cationic species on TNTs formation. Under similar condition, different cationic species yielded TNT_S of different tube length. The cation Bu_4N^+ derived from tetrabutylammonium fluoride endorsed the fabrication of TNTs with the longest tube length (94 µm). In contrast, shortest nanotubes were produced in the electrolyte containing only H^+ ions.	Shankar et al., 2007
	TNTs with 101 and 93 µm long was achieved by anodizing at 60 V, 70 h and 35 V, 48 h, respectively in FA electrolyte.	Yoriya et al., 2007

Table 2.1, continued

Generation	Research Highlights	Reference
Ethylene glycol (EG) based	Anodization at 12 V for 3 h in EG electrolyte containing 0.5 wt% NH_4F and 0.4 wt% water resulted in descended tube length and diameter with unwanted debris on the tube mouth.	Macak and Schmuki, 2006
	Synthesis with varied electrolytes conditions EG + NH_4F (0.25−0.5 wt%) + H_2O (1−3 wt%) at 60 V for 17 h delivered TNTs with promising geometry (length = 134 µm and diameter =160 nm).	Paulose et al., 2006
	First attempt to synthesize lengthiest (720 µm) TNTs through anodization in EG electrolyte containing 0.3 wt% NH_4F and 2 vol% of water at 60 V for 96 h. The variation in anodizing time highly influenced the tailoring of tube length.	Prakasam et al., 2007
	TNTs was further elongated to ~2000 µm with each side consisted a layer of 1000 µm long in EG electrolyte containing 0.6 wt% NH_4F and 3.5% distilled water at 60 V with prolonged anodization time, 216 h.	Paulose et al., 2007
Diethylene glycol (DEG) based	Synthesis of TNTs using DEG electrolyte containing HF, NH_4F or tetrabutylammonium fluoride trihydrate, Bu_4NF. Higher anodization voltage contributed for greater tube separation with marginal increase in pore diameter. Bu_4N^+ well supported the longer tube formation compared to NH_4^+, with a closer tube alignment.	Yoriya et al., 2008
Fourth generation: Non-fluoride based electrolyte	Perchlorate electrolyte was used to form TiO_2 nanotubes bundles with diameter ranging from 20 to 40 nm.	Hahn et al., 2007
	Electrolyte solutions containing 0.05−0.3 M of HCl was used to form TNTs with diameter ~80, 10 and 30 nm in 0.06 M, 0.15 M and 0.3 M of HCl, respectively.	Chen et al., 2007
	H_2O_2 was added with concentrations ranging between 0.1 and 0.5 M to 0.5 M HCl electrolyte with voltage ranging 5−25 V to establish a wider processing window after obtaining a limited outcome in their preliminary investigations.	Allam et al., 2008

2.5 Modification of TNTs

TiO_2 photocatalyst, regardless of its structure and morphology, can only be excited by UV light ($\lambda < 390$ nm) because of their large band gap. Thus limits its extensive usage owing to the shortage of natural UV spectrum. In contrast, harmless visible light spectrum is abundantly available (43%) than that of harmful UV spectrum (< 5%) from the nature. Thus necessitates the tuning of TiO_2 band gap by various means for the utilization of either natural or artificial visible light. Besides, their photocatalytic performance is also highly restricted by fast recombination of photogenerated electron-hole pairs.

Thus, three main strategies have been developed to overcome these limitations employing: (1) semiconductor composites, to promote heterojunction formation that facilitates charge separation and introduction of secondary species into the lattice for sensitizing TNTs to visible light, (2) noble metal nanoparticles (NPs), to promote localized surface plasmon resonance (LSPR) effect for visible light harvesting and enhanced electron transport, and (3) high conductive materials that promote increased electron mobility.

2.5.1 Semiconductor Mashing-up

The semiconductor composites can be categorized into metal oxide/TNTs (M_xO_y/TNTs) and sensitizers (M_xS_y/TNTs). Sensitizers such as CdS, Bi_2S_3 and CdSe are used to allow visible light absorption and to generate electron-hole pairs. However, their photostability due to photocorrosion and volatility under applied voltage are questionable (Lin et al., 2010). For photostability concern, metal oxide (M_xO_y) such as NiO, Cu_2O, Fe_2O_3, SnO_2, ZnO, $ZnFe_2O_4$ and etc are widely used to form composites. Fig. 2.4 shows the two different cases for semiconductor composites: (1) one of the semiconductors is active while the other is passive (Fig. 2.4a), or (2) both are active (Fig. 2.4b). The summary on the findings of semiconductor composites are tabulated in Table 2.2.

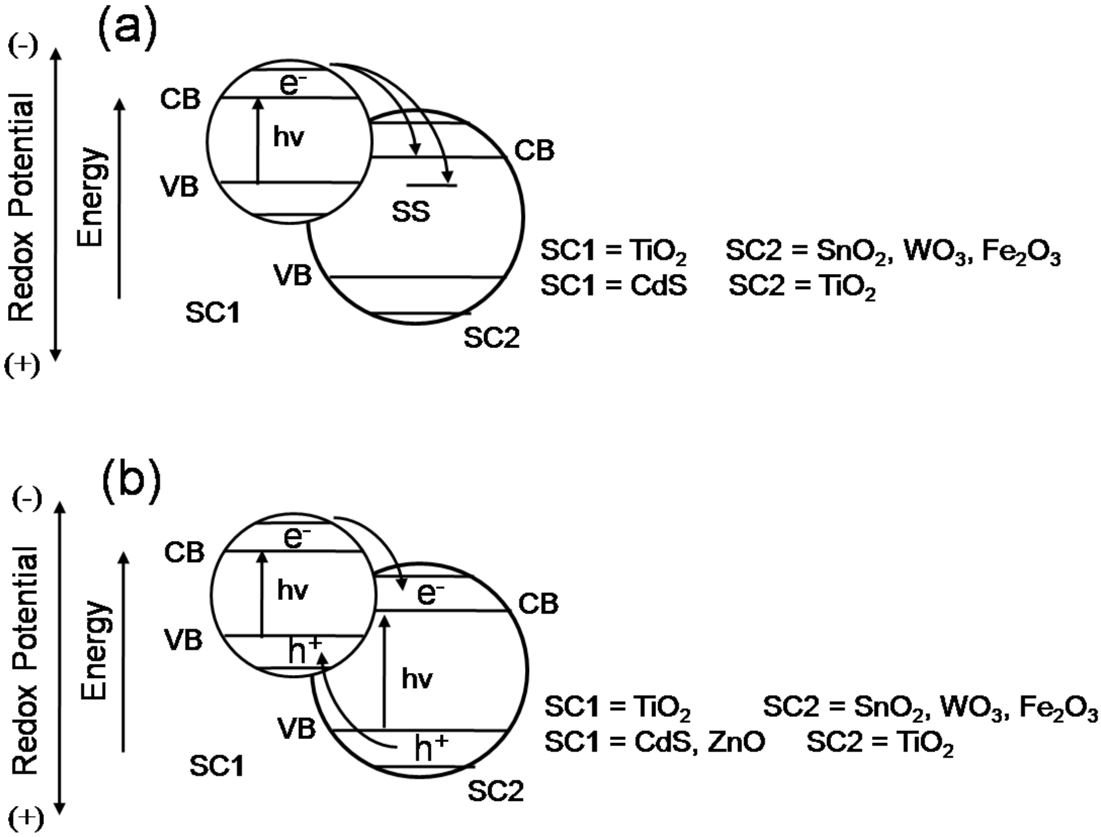

Figure 2.4: Energy diagram illustrating the coupling of various semiconductors. SS stands for solid solution. (a) vectorial electron transfer from the active SC to the passive SC, (b) both SCs are active with vectorial displacement of electrons and holes (Serpone et al., 1995)

Table 2.2: Compilation of selected literature reports on semiconductor composites

Semiconductors	Functions of Semiconductor	Preparation Method & Finding Remarks	Reference
NiO	(i) Higher p-type concentration, holes mobility and cost effectiveness (Zhang et al., 2010b). (ii) Promotes the separation of electron-hole pairs through the electric junction field and favours the interfacial charge transfer (Chen et al., 2008; Ku et al., 2011; Chen et al., 2005b). (iii) Stable in neutral and alkaline solution.	TNTs was coated with a layer of NiO particles (20−40 nm) using electroless plating and annealing. Under AM 1.5 G (100 mWcm^{-2}), a photocurrent of 3.05 mAcm^{-2} at 0.65 V and overall conversion efficiency of 1.41% were successfully obtained.	Guo et al., 2010
		NiO/TNTs was synthesized via simple chemical bath precipitation technique that immersed as anodized TNTs in ethanol containing nickel chloride solution. Compared to the N-doped TNTs, NiO loaded TNTs showed a significant higher photocatalytic activity in the visible light range.	Shrestha et al., 2010
Cu_2O	(i) p-type semiconductor with band gap 2.17 eV and more negative CB than that of TNTs. (ii) Act as sensitizer and facilitates electron transfer to the CB of TNTs (Wang et al., 2013a).	Synthesis of Cu_2O/TNTs was achieved through photoreduction method. The obtained binary semiconductor possessed enhanced photo-harvesting and reduced the recombination of electron-hole pairs by injecting electrons to the CB of TNTs.	Hou et al., 2009
		Electrodeposition was performed to couple Cu_2O with TNTs by employing $CuSO_4$ as precursor. Large area of {111} facets of octahedral Cu_2O improved the adsorption and photoactivity of TNTs.	Li et al., 2010

Table 2.2, continued

Semiconductors	Functions of Semiconductor	Preparation Method & Finding Remarks	Reference
SnO_2	(i) Overcome SnO_2 limitations of large band gap (3.8 eV) and instability to reduce oxygen. (ii) Act as electron trapper to promote improved charge separation.	Macroporous SnO_2 was assembled on TNTs by a liquid crystal soft template method. The band gap was narrowed to 2.93 eV. The resistance and impedance between SnO_2/TNTs and electrolyte was highly reduced.	Li et al., 2012
ZnO	(i) Almost same band gap as TNTs (3.2 eV). (ii) Nanorod structure facilitates holes transfer and encourages charge separation. (iii) ZnO acts as holes acceptor, while TNTs serves as electron trapper.	ZnO nanorods were grafted into TNTs providing a favourable platform for Ag deposition and contributed for increased surface area. ZnO nanorods were nucleated along the (0 0 2) direction following the structural correlation ZnO (1 0 0)∥TNTs (1 0 3).	Huang et al., 2011
CdS CdSe	(i) Both have small band gap (CdS, 2.4 eV; CdSe, 1.8 eV). (ii) CdS has more negative CB than that of TNTs to promote efficient charge separation.	CdS nanoparticles were coated with ionic layer adsorption and reaction process. A thin layer of CdSe was then deposited onto TNTs through chemical bath deposition. The CdS/CdSe showed higher power conversion efficiency of 2.40% under simulated solar condition.	Lai et al., 2012

Table 2.2, continued

Semiconductors	Functions of Semiconductor	Preparation Method & Finding Remarks	Reference
CdS ZnO	(i) Formation of a cascade of electronic energy structures within the composites that facilitates interfacial charge separation and inhibits charge carriers recombination.	Both binary and ternary hybrid was fabricated by sequential deposition of ZnO and CdS layer onto the surface of TNTs. The ternary hybrid exhibited excellent performance over the binary composites.	Lin et al., 2013
Fe_2O_3	(i) More stable than Cu_2O in neutral and alkaline solution. (ii) Band gap of 2.2 eV. (iii) Suitable to capture a significant portion of the solar spectrum with a maximum theoretical photoconversion efficiency (Murphy et al., 2006).	α-Fe_2O_3 was deposited on TNTs by electrochemical deposition route. The prepared photocatalyst possessed a higher stability in alkaline condition rather than acid condition.	Cong et al., 2012
$ZnFe_2O_4$	(i) Good stability and enhanced visible light absorption. (ii) Photocorrosion resistance.	$ZnFe_2O_4$ was deposited into TNTs by cathodic electrodeposition that hindered the aggregation reaction at tube entrances. It showed strong photoresponse and higher photocurrent density towards visible region.	Hou et al., 2010

2.5.2 Noble Metals

Noble metals including palladium (Pd), osmium (Os), ruthenium (Ru), rhodium (Rh), silver (Ag), iridium (Ir), gold (Au) and platinum (Pt) are highly resistant to corrosion and oxidation (Teh and Mohamed, 2011). They also serve as “charge-carrier traps” to inhibit recombination of photogenerated electron-hole pairs. In recent years, many works have focused on the combination of noble metal nanoparticles (NPs) and TNTs that unveil the inherent plasmonic phenomenon that ascends the photocatalytic performance. Among the noble metals, Au and Ag are known for its inclusive ability to absorb visible light promoted by localized surface plasmon resonance (LSPR) phenomenon. The lower cost of Ag makes it more suitable for broad applications compared to that of Au. Hence, the behaviour of Ag was widely studied by several researchers (Seery et al., 2007; Tomás et al., 2009; Binitha et al., 2009). The Ag NPs have an ability to surpass the energy barrier arises at the interface of Ag/TiO_2. This is acknowledged by the LSPR excitation that inject electrons from Ag NPs to CB of TiO_2 under visible light irradiation (Fan et al., 2014; Eom et al., 2014; Chen et al., 2014; Nolan et al., 2010).

This LSPR phenomenon is highly influenced by the morphology, interparticle interactions and local dielectric environment of noble metals (Palmisano et al., 2010; Galian and Pérez-Prieto, 2010; Mohapatra et al., 2008; Haruta, 2005). For example, Pd NPs of about 6 nm were restricted only to the UV spectrum (Ho and Chi, 2004). Instead, the same Pd with modified morphology i.e., larger particles and clusters broke the restriction by well absorbing the visible light (Xiong et al., 2005). The reports pertaining to LSPR properties achieved through Pt or Pd are scant compared to that of the Ag and Au.

Xiong and Chen groups (Xiong et al., 2005; Chen et al., 2005a) have reported LSPR phenomenon triggered by Pd as nanocubes and Pd-Ag and Pt-Ag as nanoboxes, respectively. Langhammer and co-workers (Langhammer et al., 2006) found that Pt and Pd nanodisks promoted LSPR with a higher sensitivity of the plasmon to the disk aspect ratio than that of Ag. The finding of significant tunable LSPR in Pt and Pd together with the prediction from the reliable spheroid model elevated them as promising alternatives for plasmonic mediated chemistry. Gao and co-workers (Gao et al., 2007) reported that the LSPR peak locations of the bimetallic particles can be tuned across UV and visible region by varying the Pt concentration.

Most commonly, Pt is recognized for the following plausible functions: (i) as electron trap to suppress the recombination of electron-hole pairs (Vijayan et al., 2010; Huang et al., 2007; Neppolian et al., 2012), (ii) creates a defect energy level (Li and Li, 2002), (iii) shift the Fermi level of TiO_2 by controlling its size (Wang et al., 2012b), and (iv) creates Schottky barrier for better charge carriers separation (An et al., 2009). Hence, it necessitates the investigation on LSPR phenomenon contributed by the noble metals. The major findings of noble metal and TNTs combinations are detailed in Table 2.3.

Table 2.3: Compilation of selected literature reports on noble metals

Type of Noble Metals	Preparation Method & Finding Remarks	Reference
Ag	Uniform sized Ag NPs were decorated onto the outer and inner surface of TNTs through a wetting-thermal decomposition route. Ag NPs resulted in the formation of interfacial barrier between Ag and TNTs electrode, which increased the diffusion of OH^- or H^+ across the barrier.	He et al., 2011
	A simple pulse current electrodeposition method was developed to fabricate uniformly distributed regular sized Ag NPs on TNTs surface. The rapid growth of Ag particles was suppressed by this method and uniform deposition of small Ag particles onto TNTs was promoted, minimizing deposition and clogging at tube entrances. The enhanced photocurrent and higher incident photon-to-charge carrier efficiency (IPCE) of Ag/TNTs suggested that electron-hole pair recombination was effectively suppressed.	Lai et al., 2010b
	Ag NPs were loaded onto TNTs via ultrasound-aided photochemical route by varying $AgNO_3$ concentration. Ag/TNTs showed enhanced visible light absorption in range between 400 and 650 nm.	Sun et al., 2009
	The surface of TNTs was decorated with Ag NPs through thermal decomposition reaction. The presence of Ag NPs improved the electronic conductivity, charge-discharge capacity, and cycle stability of TNTs.	Fang et al., 2008
Au	Au/TNTs electrocatalysts were formed by loading a low content (1.9 at.%) of Au NPs on TNTs matrix through immersion and hydrolysis. The strong synergistic interaction between TiO_2 and Au NPs with smaller size significantly improved the activity and anti-poisoning capability for ethanol electrooxidation.	Xu et al., 2011

Table 2.3, continued

Type of Noble Metals	Preparation Method & Finding Remarks	Reference
	Pulse electrodeposition (PED) was used to disperse Au NPs on TNTs electrodes. The small bias potential and strong interaction between Au NPs and TNTs facilitated the Au plasmon-induced charge separation and transfer, leading to highly efficient and stable visible-light PEC activity towards methyl orange (MO) degradation.	Wu et al., 2015
Ag, N	N-doped TNTs were fabricated first then Ag NPs (~5nm) were electrodeposited on TNTs. The carrier density of Ag/N-doped TNTs is higher 2 orders of magnitude enhancement of TiO_2 and its photocurrent responds rapidly with illumination owing to fast photoelectron transport.	Jiao et al., 2015
Au, Ag	Ag NPs were loaded onto the TNTs by immersing them in $AgNO_3$ solution and followed by photodecomposition by UV-light illumination. Au NPs were sputtered onto TNTs by using Au sputtering system. It was then annealed to improve adhesion of NPs on the tube. Both Au and Ag NPs were found to significantly enhance the photocatalytic activity of TNTs.	Paramasivam et al., 2008
Pt	Synthesized Pt/TNTs from H_2PtCl_6 through cathodic reduction method. A decline in anatase phase led to the reduction of available reactive sites and thus resulted in deprived photocatalytic activity.	Su and Deng, 2011
	Pt NPs were electrodeposited on the surface of TNTs at a constant current of 2.5 mA/cm^2 for 5 min in H_2PtCl_6 electrolyte. As synthesized Pt/TNTs was used as efficient photoanode catalyst for photoelectrocatalytic reduction of CO_2 into valuable chemicals.	Cheng et al., 2014
	In situ deposition of ultrafine Pt NPs within TNTs through rapid microwave-assisted solvothermal approach. NPs size was controlled by adjusting the concentration of the precursor.	Feng et al., 2011

Table 2.3, continued

Type of Noble Metals	**Preparation Method & Finding Remarks**	**Reference**
Pt, Ag, Au	Self-assembled construction of highly ordered metal-TNTs heterostructures (M/TNTs, M = Au, Ag, Pt) with tunable catalytic activities was synthesized through layer-by-layer self-assembly route. Ag/TNTs composite emerged as the best candidate over Pt/TNTs and Au/TNTs with excellent photocatalytic performance towards the degradation of organic dye pollutant.	Xiao, 2012a
Pd	An incipient wetness method was adopted for homogeneous dispersion of Pd NPs on TNTs. The bulky and large sized NPs were well responsive to visible region. An appreciable photocatalytic performance was experienced for a sample with dopant concentration of 1.25 wt%, whereby exceeding this concentration a deprived trend was observed. This descent was attributed to the reduction of active sites by higher dominance of Pd NPs.	Mohapatra et al., 2008
Pd, SnO_2	SnO_2-Pd/TNTs heterostructure was fabricated by sensitization and activation method. It was observed that the lattice orientations of the SnO_2-Pd NPs were dominated by the crystallinity of TNTs.	Chang et al., 2011

2.5.3 Conducting Carbon Materials

Graphene oxide (GO) is a main derivative of graphene (RGO) and can be directly synthesized from graphite oxide. In 1958, Hummers (Hummers and Offeman, 1958) reported the most common method to synthesize GO, namely Hummer's method. As shown in Fig. 2.5, GO contains oxygenated functional groups such as hydroxyl, epoxy, carbonyl and carboxyl in sp^3 carbons (Loh et al., 2010; Barron and Hamilton, 2009). These oxygenated functional groups provide hydrophilic nature to the GO layers that ease their deposition onto the surface of metal/metal oxides (Mkhoyan et al., 2009). The transformation of carbon atoms from graphite to reduced graphene oxide is displayed in Fig. 2.6. This figure clearly illustrates the expansion of inter-layer spacing (d-spacing, d_{002}) when graphite was oxidized into graphite oxide.

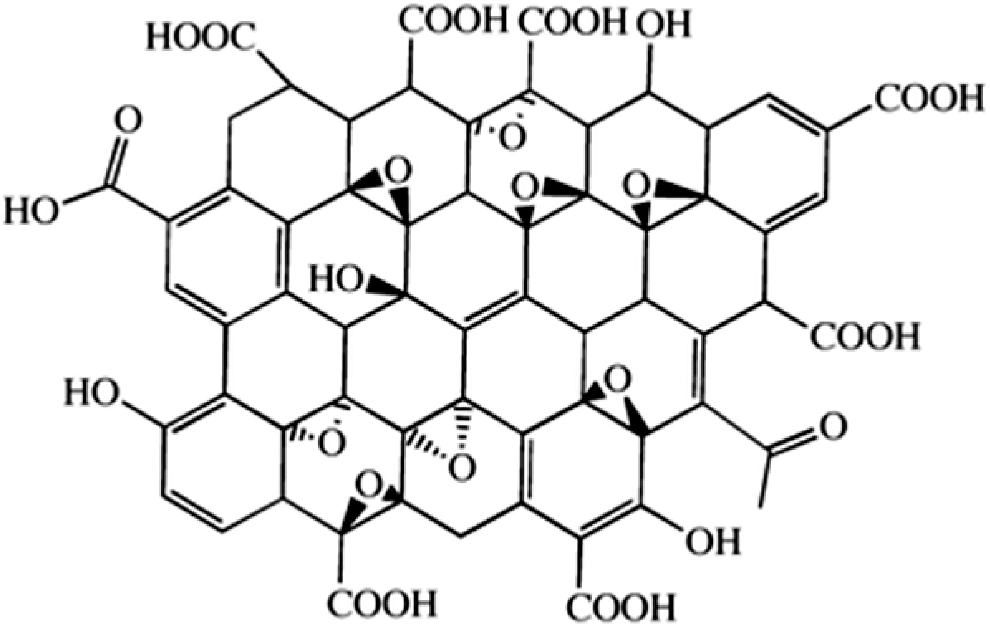

Figure 2.5: Graphene oxide structure representation (Barron and Hamilton, 2009)

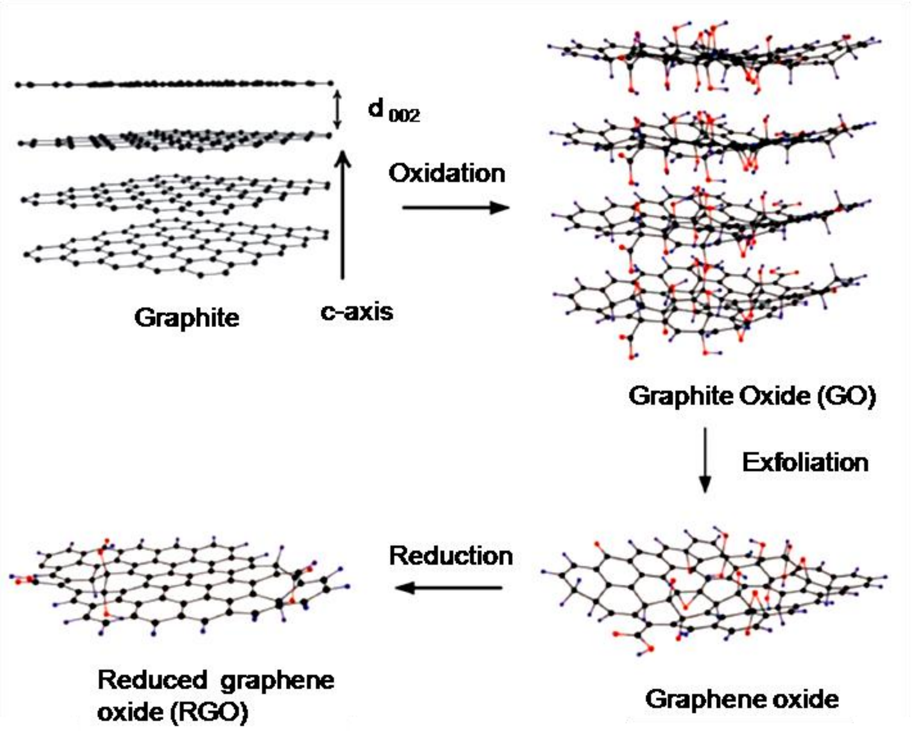

Figure 2.6: Illustrates the transformation of graphite to reduced graphene oxide (RGO) (Bai et al., 2011)

Graphene (RGO) is a two-dimensional sp^2-hybridized carbon nanosheet which possesses high specific surface area with a large interface, high electron mobility and tunable band gap (Liu et al., 2008). The interaction between different graphene layers is controlled by the out-of plane π bonds, allowing delocalized π electrons to be easily conducted throughout the basal plane (normal to the c-axis of graphite as shown in Fig. 2.6). Thus, graphene is considered as zero-band gap semiconductor with higher electron mobility (Nair et al., 2008). The oxygen functional groups in GO can be reduced to graphene with partial restoration of the sp^2 hybridization by various means including hydrothermal (Zhang et al., 2009), thermal (Schniepp et al., 2006), chemical (Gao et al., 2010), electrochemical (Ramesha and Sampath, 2009), photothermal (Abdelsayed et al., 2010), photocatalytic (Williams et al., 2008), sonochemical (Vinodgopal et al., 2010) and solvothermal (Cao et al., 2009) methods.

The unique nanostructure of these conducting carbon materials makes them suitable for enhancing the photocatalytic properties of TNTs due to its high surface area, adsorption capacity, and strong electron transfer ability in hybrid materials. In this regard, GO and RGO were examined by various researchers in combination with TNTs as consolidated in Table 2.4.

Table 2.4: Summary of the literature reports on conducting carbon materials

Conducting Carbon Materials		**Synthesis & Finding Remarks**	**Reference**
Types	**Preparation Method**		
GO	Modified Hummers method	GO was assembled on the surface of TNTs through a simple impregnation method. The presence of GO significantly improved the photoelectrochemical response of TNTs, showing approximate 15 times enhanced maximum photoconversion efficiency.	Song et al., 2012
GQD	Thermal reduction of GO, followed by concentrated acid oxidation, hydrothermal treatment and dialysis isolation to obtain GQD.	A controllable electrophoresis deposition was used to synthesize graphene-quantum-dot (GQD) sensitized TNTs. This photocatalyst showed excellent photoelectrocatalytic activity under visible light excitation and remained stable over many cycles (400 min/4 cycles). However, visible light sensitization of TNTs was still limited by wide band gap of GQDs (2.90 eV).	Pan et al., 2013
RGO	Cyclic voltammetric electrochemical reduction was performed in GO dispersion to deposit RGO on the surface of TNTs	To obtain Ag/RGO-TNTs, as prepared RGO/TNTs was photodeposited with Ag NPs. The size and density of Ag NPs were modulated using different concentrations of $AgNO_3$ solutions. This material exhibited excellent photoelectrochemical property, adsorptivity, stability with additional easy recovery properties.	Tang et al., 2012

Table 2.4, continued

Conducting Carbon Materials		Synthesis & Finding Remarks	Reference
Types	**Preparation Method**		
		One step electrodeposition was performed in GO dispersion containing $Na_3[Ag(S_2O_3)_2]$ to fabricate RGO/Ag-TNTs. Ag NPs were deposited between RGO and surface of TNTs. The resulting material effectively improved the transfer of charge carriers.	Wang et al., 2013e
		As prepared RGO/TNTs was further photoreduced by simulated solar light to achieve the maximum restoration of π-conjugation in the RGO planes. Prolonged electrodeposition with 26-cycle resulted RGO/TNTs with largest interfacial area between them. They outpoured with the highest photocatalytic performance. Further surge in RGO loading hindered the light transmittance to TNTs.	Liu et al., 2011

2.6 Application of Modified TiO_2 Nanotube Arrays (TNTs)

2.6.1 Photocatalytic Degradation of Organic Pollutants

TiO_2 nanoparticles have limitations on the post treatment separation or recovery from the slurry system after reaction. This could be defeated by TNTs which also have wider range of applications in energy and environmental realm. In recent years, TNTs are widely used for the photocatalytic degradation of organic pollutants. The basic principles involved in the photocatalytic mechanism are shown in Fig. 2.7. Under UV light irradiation, the photoexcited electrons will react with oxygen (O_2) to form superoxide radical anions ($^\bullet O_2^-$) ($O_2 + e^- \rightarrow {}^\bullet O_2^-$), while holes will react with water (H_2O) or hydroxyl ion (OH^-) to form hydroxyl radicals ($^\bullet OH$) ($H_2O + h^+ \rightarrow {}^\bullet OH$). The strong oxidizing activity of $^{\bullet}OH$ and $^{\bullet}O_2^-$ radicals mineralizes the organic pollutants to its non-toxic derivatives, CO_2 and H_2O. The complete mechanism is illustrated in Fig. 2.7.

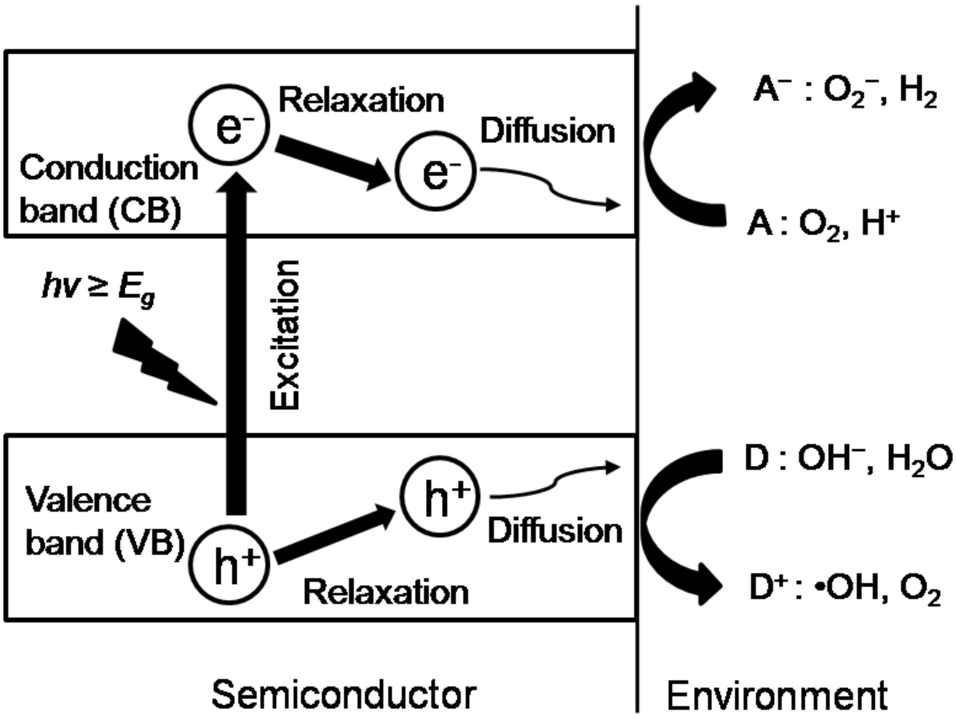

Figure 2.7: Scheme of photoinduced processes at the interface between TiO_2 and organic pollutants. Light (hν) excites VB electron to CB. Electrons and holes react with environment acceptor (A) and/or donor (D) (Huang et al., 2013)

The modifications of TNTs with semiconductors, noble metals and conducting carbon materials well contributed for the photocatalytic removal of lethal organic pollutants. The studies pertaining to it is reviewed and summarized in Table 2.5.

Table 2.5: Compilation of literature reports on photodegradation of organic pollutants

Photocatalyst	Loading	Preparation Method	Organic Pollutant	Initial Pollutant Concentration (mg/L)	Radiation Period (min)	Light Source	Degrade Efficiency, %	Reference
TNTs	-	impregnating-precipitation-photoreduction	Methyl Orange (MO)	1×10^{-5} M	60	300 W xenon lamp (λ ≤ 400 nm)	0	Yu et al., 2009
Ag/AgCl/TNTs (amorphous)	-						55	
Ag/AgCl/TNTs (anatase)	-						75	
TNTs-$_x$N$_x$ (anatase)	-						100	
TNTs	-	incipient wetness method	Methyle Red (MR)	2.33×10^{-5} M	60	UV (λ=330 ± 70 nm)	36.5	Mohapatra et al., 2008
Pd/TNTs	1.25 wt% Pd						55.6	
TNTs	-					visible (λ=520 ± 46 nm)	8.7	
Pd/TNTs	1.25 wt% Pd						32	
Ag/TNTs	1.23 at% Ag	wetting-thermal decomposition	MB,	30	360	tubular UV lamp	54	He et al., 2011
			Pentachloro-Phenol (PCP)	13.33	240		12	

Table 2.5, continued

Photocatalyst	Loading	Preparation Method	Organic Pollutant	Initial Pollutant Concentration (mg/L)	Radiation Period (min)	Light Source	Degrade Efficiency, %	Reference
TNTs	-	sensitization and activation	MB	1×10^{-5} M	180	Xe lamp (AM 1.5)	60	Chang et al., 2011
Pd-SnO_2 TNTs (5A)	0.34 at% Pd, 0.93 at% Sn						88	
Pd-SnO_2 TNTs (10A)	0.18 at% Pd, 1.02 at% Sn						84	
Pd-SnO_2 TNTs (15A)	0.14 at% Pd, 1.10 at% Sn						90	
Pd-SnO_2 TNTs (5B)	0.19 at% Pd, 0.80 at% Sn						83	
Pd-SnO_2 TNTs (10B)	0.23 at% Pd, 0.90 at% Sn						83	
Pd-SnO_2 TNTs (15B)	0.51 at% Pd, 1.37 at% Sn						70	
** Remarks: 5/10/15A: sensitization and activation period (min), after annealing TNTs* *5/10/15B: sensitization and activation period (min), before annealing TNTs*								
N,F co doped TNTs	-	dip coating	MB	2	120	metal halogen desk lamp	77	Li and Shang, 2010
N,F co doped PdO/TNTs	-						86	

Table 2.5, continued

Photocatalyst	**Loading**	**Preparation Method**	**Organic Pollutant**	**Initial Pollutant Concentration (mg/L)**	**Radiation Period (min)**	**Light Source**	**Degrade Efficiency, %**	**Reference**
TNTs	-	self assembly	4-nitrophenol (4-NP)	10	60	300 W Xe lamp (λ>420 nm)	32	Xiao et al., 2013
Nanoporous-TNTs	-						32	
CdS/TNTs	1:11 (Cd:S)						48	
CdS/Nanoporous-TNTs	1:11 (Cd:S)						90	
TNTs	-	layer-by-layer deposition (ZnO), sequential chemical bath deposition (CdS)	Alizarin Red S (ARS)	40	180	300 W UV lamp (λ=385 nm)	39.2	Lin et al., 2013
TNTs/ZnO	10.5% ZnO						47.8	
TNTs/CdS	31.9% CdS						57.9	
TNTs/ZnO/CdS	-						75	
CdS/TNTs (water content in electrolyte)		sequential chemical bath deposition	Methyl Orange (MO)	10	180	250 W metal halogen lamp (λ>400 nm)		Liu et al., 2013
CdS/TNTs (5 vol%)	-						74	
CdS/TNTs (8 vol%)	-						85	
CdS/TNTs (10 vol%)	-						93	
CdS/TNTs (12 vol%)	-						96.7	

Table 2.5, continued

Photocatalyst	Loading	Preparation Method	Organic Pollutant	Initial Pollutant Concentration (mg/L)	Radiation Period (min)	Light Source	Degrade Efficiency, %	Reference
TNTs	-	chemical bath precipitation	Acid Orange 7 (AO7)	15×10^{-6} M	240	10 mW Diode Blue Laser (λ=405 nm)	2	Shrestha et al., 2010
NiO/TNTs (annealing temp.)								
NiO/TNTs (450)	29.2 at% Ni						10	
NiO/TNTs (550)							16	
NiO/TNTs (630)							14	
N-TNTs	-						1	
TNTs	-	seed growth (ZnO), sputtering (Ag)	MB	1×10^{-5} M	105	400 W Hg lamp (λ=365 nm)	60	Huang et al., 2011
ZnO/TNTs (ZnO growth time)								
ZnO/TNTs (2 h)	-						75	
ZnO/TNTs (4 h)	-						75	
ZnO/TNTs (4 h)/Ag	-						78	
TNTs	-		MO	5×10^{-5} M	270		20	
ZnO/TNTs (2 h)	-						20	
ZnO/TNTs (4 h)	-						25	
ZnO/TNTs (4 h)/Ag	-						70	
TNTs	-	impregnation	MB	5	150	500 W Xe lamp (λ>420 nm)	16	Song et al., 2012
GO/TNTs	-						20	

Table 2.5, continued

Photocatalyst	Loading	Preparation Method	Organic Pollutant	Initial Pollutant Concentration (mg/L)	Radiation Period (min)	Light Source	Degrade Efficiency, %	Reference
ZnO/TNTs (wt% ZnO)		impregnation	Rhodamine B (RhB)	5	150	300 W Xe arc lamp (λ=365 nm)		Xiao, 2012b
ZnO/TNTs (5%)	5 wt% ZnO						75	
ZnO/TNTs (10%)	10 wt% ZnO						76	
ZnO/TNTs (15%)	15 wt% ZnO						73	
ZnO/TNTs (20%)	20 wt% ZnO						70	
TNTs	-	photodeposition (Ag), electrodeposition (RGO)	2,4-dichlorophenoxyacetic acid	10	160	500 W Xe arc lamp	24	Tang et al., 2012
Ag/TNTs	-						49	
RGO/TNTs	-						58.8	
Ag/RGO/TNTs	-						100	

From the studied literature findings, it is well evident that the presence of composites either as binary or ternary will result in varied photocatalytic mechanism and relevant literatures are summarized in Table 2.6.

Table 2.6: Compiled reaction mechanism of binary or ternary hybrid based on TNTs

Photocatalyst	Proposed Reaction Mechanism	Reference
ZnO/CdS/TNTs	The presence of both ZnO and CdS created a cascade of electronic energy structures within the ternary hybrid that assisted interfacial charge separation and inhibited recombination behaviour.	Lin et al., 2013
Pd-SnO_2 TNTs	The combination of two electron-hole transfer mechanisms was involved in TNTs/SnO_2-Pd heterostructure. First, electrons were injected from CB of TNTs to SnO_2 and reverse hole transfer in the VB from SnO_2 to TNTs to prevent the recombination of electron-hole pairs. Second, Pd NPs on TNTs or SnO_2 acted as an electron reservoir to trap more electrons from CB of TNTs that prevent the recombination effect.	Chang et al., 2011
Ag/AgCl/TNTs	LSPR phenomenon contributed by Ag NPs induced the excitation of electron-hole pairs under visible-light irradiation. Electrons were injected from Ag NPs to the CB of TNTs while, the holes transferred to negatively charged AgCl NPs, causing the oxidation of Cl^- ions to Cl^0 atoms. Dye pollutant was easily oxidized by the highly reactive zero valence atoms.	Yu et al., 2009
Ag/TNTs	The energy level of CB edge of TNTs was higher than the new Fermi energy level of the TNTs-Ag heterostructure, the electrons transferred from TNTs to Ag NPs until a Fermi level equilibrium was attained. In addition, Schottky barriers formed at Ag-TNTs junction captured the photogenerated electrons to prevent the recombination.	He et al., 2011

Table 2.6, continued

Photocatalyst	Proposed Reaction Mechanism	Reference
Ag/RGO/TNTs	Ag NPs overhauled the limited contact between the TNTs and RGO to promote an efficient electron transfer in this catalyst system.	Tang et al., 2012
CdS/TNTs	Electrons were photoexcited from VB to CB of CdS under visible light irradiation. The electrons were subsequently injected from the CB of CdS to the CB of TNTs, led to a better electron-hole pairs separation.	Xiao et al., 2013
ZnO/TNTs	The photoexcited electrons in the CB of ZnO were injected to the CB of TNTs when ZnO was irradiated by photon energy. The heterojunction was formed between TNTs and ZnO, where TNTs and ZnO served as an electron and hole acceptor, respectively. Thus, their recombination was inhibited and efficient separation of photoexcited electron-hole pairs was promoted.	Xiao, 2012b

2.6.2 Photocatalytic Conversion of CO_2 to Hydrocarbon Fuels

Photocatalytic conversion of CO_2 using photon energy is a feasible alternative to derive fuels in sustainable and eco-friendly manner. This artificial photosynthesis process has been emerging as one of the most promising solution because it generates alternative energy resource by using abundant atmospheric CO_2 as feedstock. This photocatalytic conversion was achieved through CO_2-saturated aqueous solution containing suspended TiO_2 (Sasirekha et al., 2006; Li et al., 2010), high pressure CO_2 system with TiO_2 powders suspended in isopropyl alcohol (Kaneco et al., 1998), and gas phase CO_2 and water (H_2O) (Varghese et al., 2009; Nishimura et al., 2009; Wang et al., 2010). Among these, the gas phase conversion overwhelms the rest owing to its strong workability i.e., zero recovery of catalyst from aqueous phase and overcome the low solubility of CO_2.

The reaction pathway from inorganic precursor to organic energy products is shown below (Indrakanti et al., 2009).

Photoreduction Reactions	**E°_{redox}/V vs. NHE**	
CO_2 radical formation:		
$CO_2 + e^- \rightarrow {}^{\bullet}CO_2^-$	= -1.90	(2.7)
Formic acid formation:		
$CO_2 + H^+ + 2e^- \rightarrow HCO_2^-$	= -0.49	(2.8)
Carbon monoxide formation:		
$CO_2 + 2H^+ + 2e^- \rightarrow CO + H_2O$	= -0.53	(2.9)
Formaldehyde formation:		
$CO_2 + 4H^+ + 4e^- \rightarrow HCHO + H_2O$	= -0.48	(2.10)
Hydrogen formation:		
$2H^+ + 2e^- \rightarrow H_2$	= -0.41	(2.11)
Methanol formation:		
$CO_2 + 6H^+ + 6e^- \rightarrow CH_3OH + H_2O$	= -0.38	(2.12)
Methane formation:		
$CO_2 + 8H^+ + 8e^- \rightarrow CH_4 + 2H_2O$	= -0.24	(2.13)
Oxygen formation:		
$H_2O \rightarrow 1/2O_2 + 2H^+ + 2e^-$	= 0.82	(2.14)

It is apparent that photoreduction of CO_2 involves multiple reaction pathways. CO_2 activation is proposed to involve the formation of a negatively charged ${}^{\bullet}CO_2^-$ species, but the single electron transfer to CO_2 occurs at potential as negative as –1.9 V (Eq. 2.7), which is highly endothermic because of the negative adiabatic electron affinity of CO_2 (Indrakanti et al., 2009). Thus, this precludes the likelihood of a single electron transport mechanism for the reduction of CO_2. Some researchers (Varghese et al., 2009; Roy et al., 2010) proposed that methane (CH_4) could be formed through reaction (2.13) or the following reactions as well

$$CO + 6H^+ + 6e^- \rightarrow CH_4 + H_2O \tag{2.15}$$

$$CH_3OH + 2H^+ + 2e^- \rightarrow CH_4 + H_2O \tag{2.16}$$

In addition to these desired redox reactions, some reversible reactions are also possible, making the CO_2 photoreduction system more complex. For example, the strong oxidation power of the photoexcited holes, protons, OH radicals, or O_2 could oxidize the intermediates and products to form CO_2. Moreover, the competition between H_2O and CO_2 for the reduction process will cause electron quenching and thus reducing the yield of hydrocarbon products. Numerous reports in the literature describing the yield from CO_2 photoreduction is summarized in Table 2.7. The overall conclusion of the summarized literature findings is that the researchers are still very far from having the scientific and technological capability to optimize this process.

Although extensive works have been carried out in this field, several insights are yet to be explored to fill the gaps of previous research. This includes synthesizing enhanced visible and solar promoted composite photocatalysts and unveiling the interactions of the photocatalysts with the categorized pollutants with good and poor photosensitizing characteristic. The limitation of adapting photocatalysts for successful “Artificial Photosynthesis” in sustainable spectrum is also considered.

Table 2.7: Compilation of literature reports on photocatalytic CO_2 reduction

Catalysts	**Loading**	**Products**	**Methane Yield**	**Reactants**	**Light Source**	**Reactor/Sample Cell**	**Reference**
Pt/TNTs	Pt^{4+} = 0.15 mM	CH_4	4 ($ppm/cm^2/h$)	Argon, H_2O	sunlight (AM 1.5)	stainless steel reaction chamber with quartz window	Feng et al., 2011
TNTs			3 ($ppm/cm^2/h$)	CO_2, H_2O			
Pt/TNTs			25 ($ppm/cm^2/h$)	CO_2, H_2O			
TNTs-anneal temp.		CH_4		CO_2, H_2O	Hg lamp (λ = 365 nm)	teflon reaction chamber with quartz window	Schulte et al., 2010
TNTs-480	-		3.4 ($\mu mol/m^2/h$)				
TNTs-550	-		2.0 ($\mu mol/m^2/h$)				
TNTs-580	-		2.5 ($\mu mol/m^2/h$)				
TNTs-620	-		1.4 ($\mu mol/m^2/h$)				
TNTs-680	-		3.7 ($\mu mol/m^2/h$)				
TNTs-550	-		0.25 ($\mu mol/m^2/h$)		Xe arc (λ = 380 nm)		
TNTs-580	-		0.44 ($\mu mol/m^2/h$)				
TNTs-620	-		0.71 ($\mu mol/m^2/h$)				
TNTs-680	-		0.80 ($\mu mol/m^2/h$)				
TNTs-550	-		0.29 ($\mu mol/m^2/h$)		Xe arc (λ = 400 nm)		
TNTs-580	-		0.33 ($\mu mol/m^2/h$)				
TNTs-620	-		0.72 ($\mu mol/m^2/h$)				
TNTs-680	-		0.65 ($\mu mol/m^2/h$)				

Table 2.7, continued

Catalysts	**Loading**	**Products**	**Methane Yield**	**Reactants**	**Light Source**	**Reactor/ Sample Cell**	**Reference**
N doped Pt/TNTs-anneal temp.		H_2, CO, CH_4, alkanes, olefin, branched paraffin		CO_2, H_2O	sunlight (AM 1.5)	stainless steel chamber	Varghese et al., 2009
N doped Pt/TNTs-460	0.75 at%N		1.19 (µmol/g-cat/h)				
N doped Pt/TNTs-600	0.4 at%N		2.86 (µmol/g-cat/h)				
N doped Cu/TNTs-600	0.4 at%N		3.09 (µmol/g-cat/h)				
N doped Cu/TNTs-600	0.4 at%N		0.09 (µmol/g-cat/h)		sunlight (> 400 nm)		
Pt/CdS-TNTs	-	CH_4	0.44 µmol/min	CO_2, H_2O	visible light	-	Yuan et al., 2011
			130 µmol/min		UV-vis light		
Cu-Pt/PMTNTs (periodically modulated double-walled TNTs)	33%-Cu 67%-Pt	CH_4, C_2H_4, C_2H_6	2.60 $mLg^{-1}h^{-1}$	CO_2 (99.9%), H_2O	sunlight (AM 1.5)	high-pressure reaction chamber	Zhang et al., 2012
Cu-Pt/PMTNTs			3.55 $mLg^{-1}h^{-1}$	CO_2 (0.998%), H_2O			
Cu-Pt/TNTs	33%-Cu 67%-Pt		0.49 $mLg^{-1}h^{-1}$	CO_2 (99.9%), H_2O			
Cu-Pt/TNTs			0.26 $mLg^{-1}h^{-1}$	CO_2 (0.998%), H_2O			

CHAPTER 3

METHODOLOGY

The chapter furnishes the detailed insights of materials adopted in the study for the preparation of various combinations of photocatalysts. It also features the step by step procedure followed in tailoring the photocatalysts along with comprehensive information on the analytical techniques adopted for unveiling its materials chemistry. The procedure practised for carrying out the photocatalytic experiments for environmental and energy applications with analytical protocol for the quantification of the studied pollutants are deliberated in the culmination of the chapter.

3.1 Preparation of TiO_2 Nanotube Arrays (TNTs)

All the chemical reagents were of analytical purity and purchased from Sigma-Aldrich Chemical Co. The Ti foil (99.7%, Sigma-Aldrich) was employed as substrate to electrochemically grow self-organized TNTs layers through electrochemical mediated anodic oxidation. The anodization was carried out by using ethylene glycol (anhydrous, 99.8%) electrolyte containing 0.3 M ammonium fluoride (NH_4F, 98%) and 2 vol% water (H_2O). The electrochemical reaction was triggered with graphite rod as the counter electrode under 50 V for duration of 3 h. The photograph of experimental setup is shown in Fig. 3.1(a)-(b).

The detailed anodization procedures are as follows: The Ti substrate (20 × 30 × 0.25 mm) was ultrasonically cleaned with acetone and ethanol prior to anodization. The anodized samples were rinsed thoroughly with deionized (DI) water and then annealed at 450 ℃ for 1 h. The annealed samples were sonicated with ethanol for 30 min to remove the bundled impurities on pore mouths of the nanotubes. After sonication step, as synthesized debris free TNTs was used as base material for subsequent modification works with semiconductors (NiO, SnO_2), noble metals (Ag, Pt) and conducting carbon materials (GO, RGO).

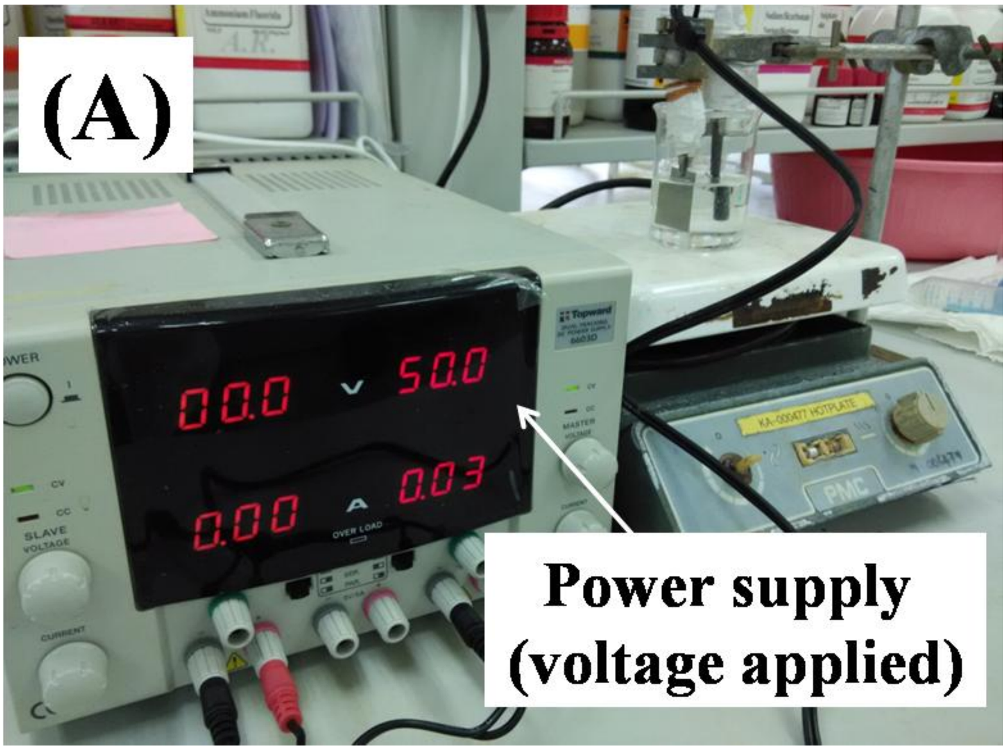

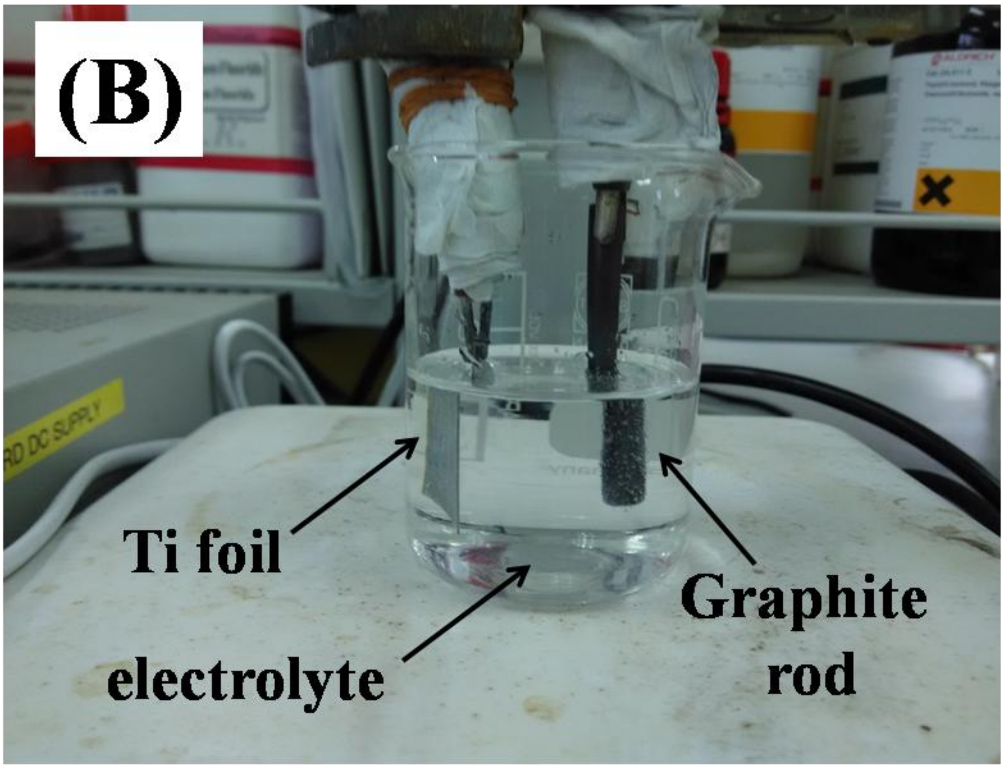

Figure 3.1: (a)-(b) Photograph of anodization experimental set-up

3.2 Modification of TNTs

3.2.1 Semiconductor Mashing-up

(a) Preparation of NiO/TNTs and SnO_2/TNTs

Wet impregnation method was adopted for the preparation of both NiO/TNTs and SnO_2/TNTs. The procedures are as follows: TNTs samples were immersed overnight in $Ni(NO_3)_2 \cdot 6H_2O$ and $SnCl_4 \cdot 5H_2O$ aqueous solution to synthesize NiO/TNTs and SnO_2/TNTs, respectively. The molar concentrations of both precursor aqueous solutions were varied in a range between 0.5 and 2.5 M. This resulted in different concentrations of NiO/TNTs and SnO_2/TNTs, named accordingly in Table 3.1. As-prepared samples were annealed at 450 ℃ for 2 h with a heating rate of 10 ℃ min^{-1}. The photograph of the fabricated materials is shown in Fig. 3.2.

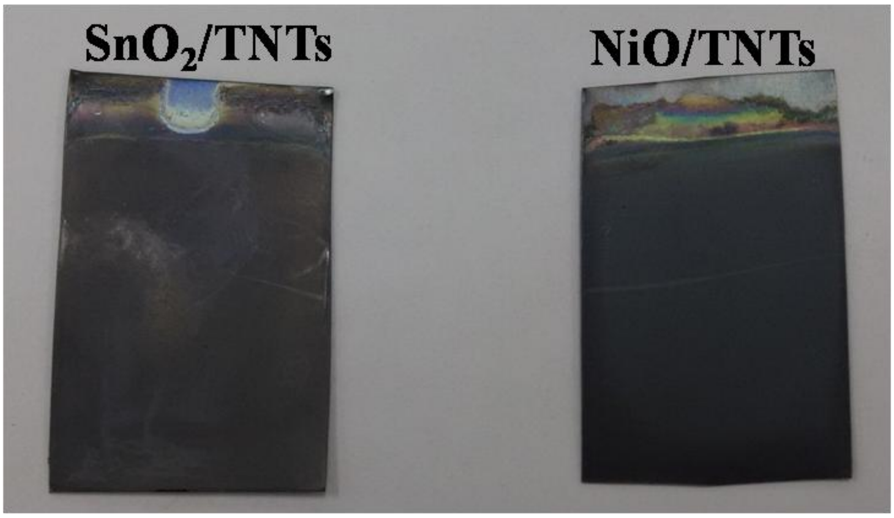

Figure 3.2: Image of synthesized NiO/TNTs and SnO_2/TNTs on Ti substrate

Table 3.1: Prepared samples for different concentrations of NiO/TNTs and SnO_2/TNTs

Precursor Concentration (M)	Prepared Samples	
	NiO/TNTs	SnO_2/TNTs
0	TNTs	TNTs
0.5	NiO/TNTs (0.5 M)	1.59 Sn
1.5	NiO/TNTs (1.5 M)	2.25 Sn
2.5	NiO/TNTs (2.5 M)	2.84 Sn

3.2.2 Engulfing Noble Metals

(a) Preparation of Ag-TNTs and Pt-TNTs

Both of Ag-TNTs and Pt-TNTs samples (Fig. 3.3) were prepared via photodeposition method. Photodeposition of Ag and Pt NPs on TNTs was carried out by dipping TNTs in an equal volume ratio of methanol-water mixture containing 1 mM of $AgNO_3$ and H_2PtCl_6, respectively. The surface of the TNTs under nitrogen atmosphere was irradiated with high pressure Hg lamp (400 W) for 1 h with sonication for Ag-TNTs and 2 h without sonication for Pt-TNTs. The sonication was exclusively adopted for Ag NPs photodeposition that prevented the agglomeration of Ag NPs. The resulting product was designated as Ag-TNTs and Pt-TNTs, respectively. As synthesized Ag-TNTs and Pt-TNTs were used for the combination with conducting carbon materials (GO and RGO) to produce ternary composites as described in next section.

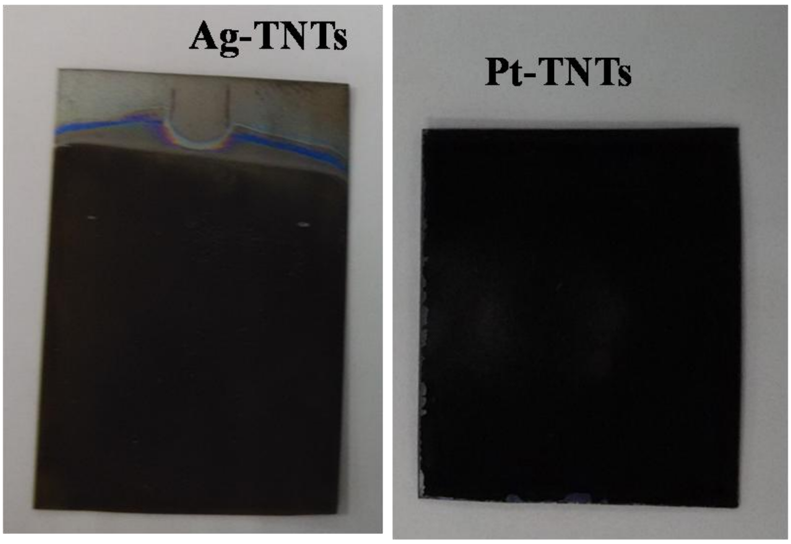

Figure 3.3: Photograph of synthesized Ag-TNTs and Pt-TNTs on Ti substrate

3.2.3 Engulfing Conducting Carbon Materials

(a) Preparation of GO and RGO

Graphite oxide was obtained through simplified Hummers method (Hummers and Offeman, 1958), 3 g of nature graphite powder (99.99%, Sigma-Aldrich) were oxidized by a mixture of 400 mL of H_2SO_4 and 18 g of $KMnO_4$. The mixture was stirred for three days to ensure complete oxidation of the graphite. Then, H_2O_2 solution was added to terminate the oxidation process. The graphite oxide was repeatedly washed with 1 M of HCl and DI water until pH 4−5 was achieved. This washing process led to the exfoliation of graphite oxide to form a GO gel. It was then dried at 60 ℃ under vacuum for 24 h to obtain brownish GO solid. In order to obtain blackish

RGO, the brownish GO was reduced rapid thermally at 300 °C for 5 min in furnace. The images of both brownish GO and blackish RGO suspension are depicted in Fig. 3.4.

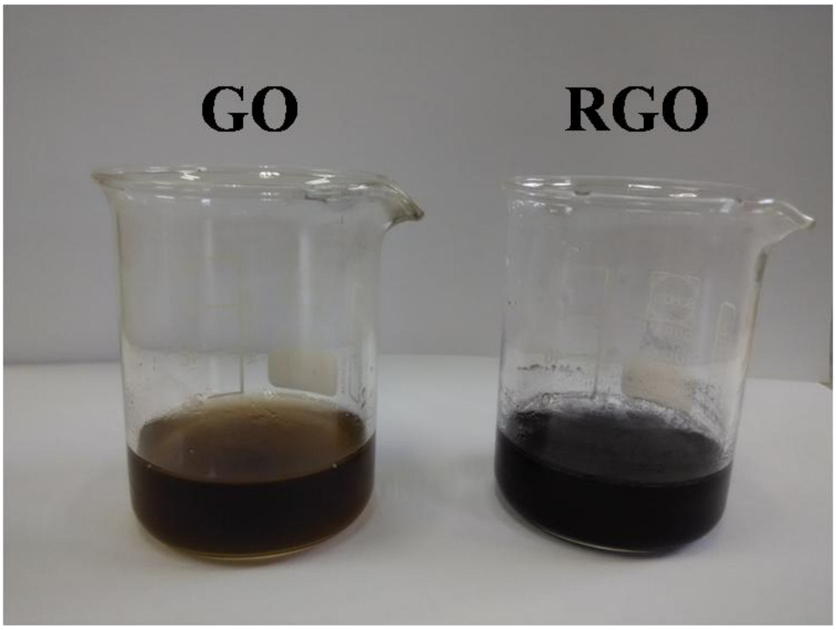

Figure 3.4: Image of brownish GO and blackish RGO suspension obtained during synthesis

(b) Preparation of GO/Ag-TNTs and RGO/Pt-TNTs

The preparation procedure of RGO/Pt-TNTs was analogous to the GO/Ag-TNTs. Both of Ag-TNTs and Pt-TNTs were immersed in a 0.5 mg mL^{-1} GO and RGO suspension for 5 h, respectively. The samples for comparison like GO/TNTs and RGO-TNTs were also prepared using the above method by immersing TNTs in these solutions. The obtained materials were vacuum dried for 3 h. Thus fabricated composites were denoted as GO/Ag-TNTs and RGO/Pt-TNTs, respectively (Fig. 3.5).

The illustrative procedure for the preparation of GO/Ag-TNTs is metaphorized in Fig. 3.6.

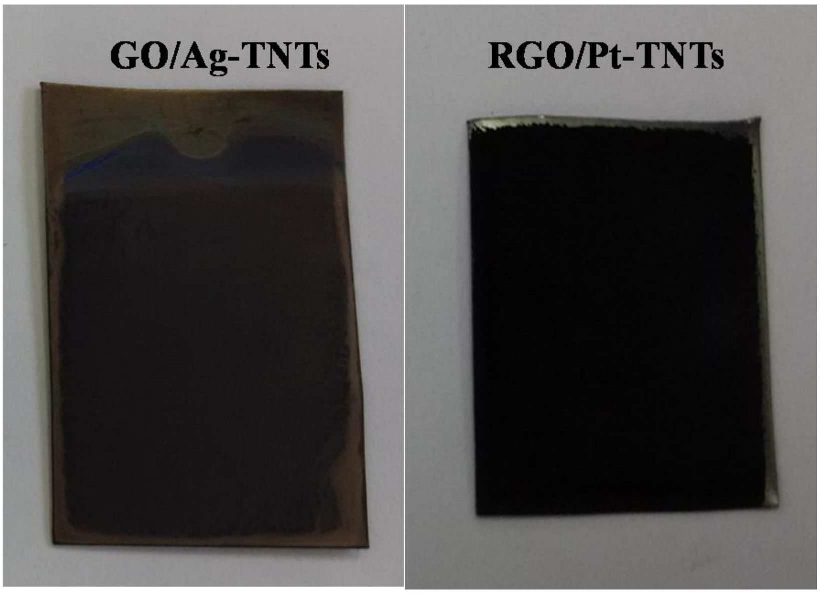

Figure 3.5: Image of GO/Ag-TNTs and RGO/Pt-TNTs on Ti substrate

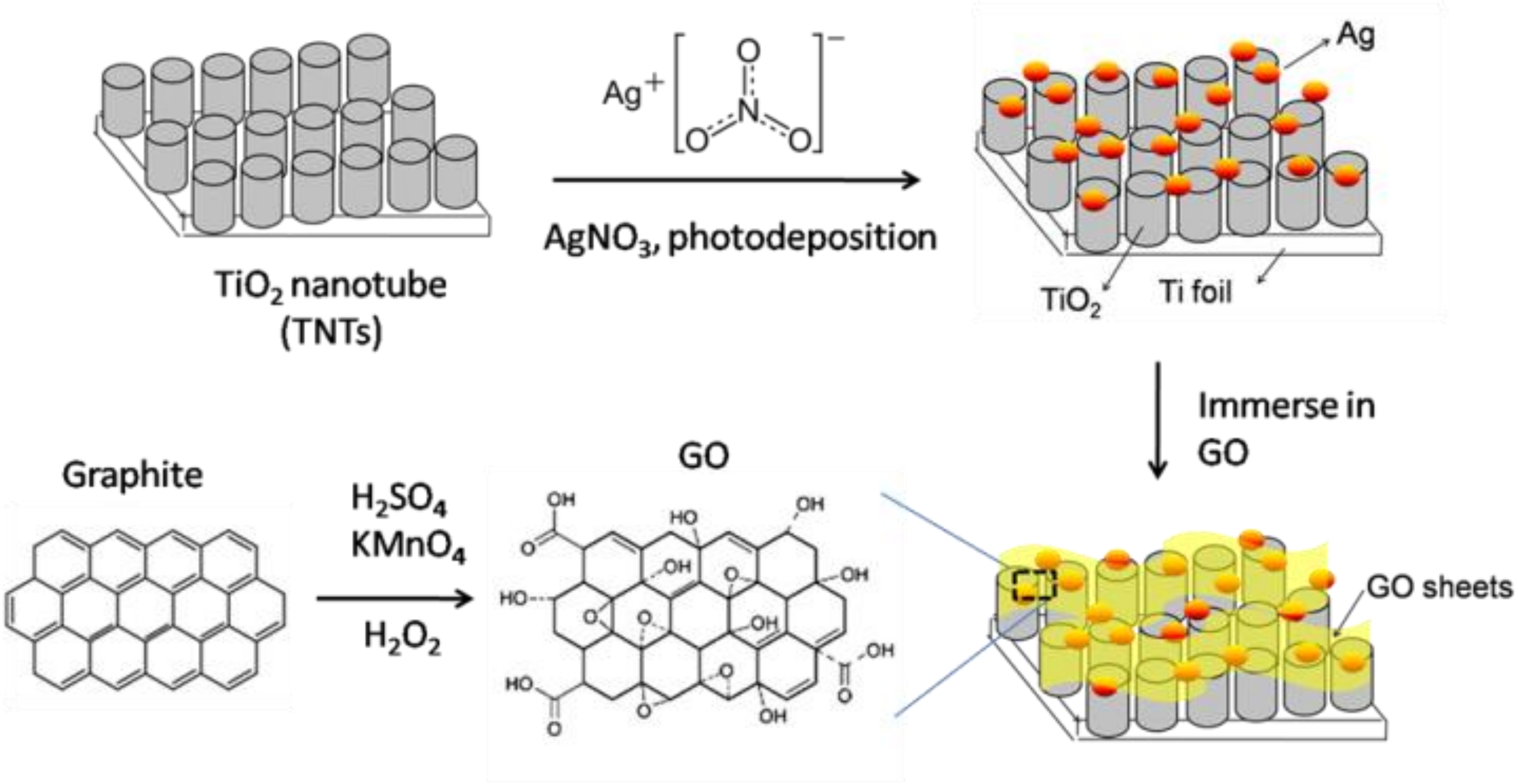

Figure 3.6: Illustrative procedure for the preparation of GO/Ag-TNTs

3.3 Characterization

3.3.1 NiO/TNTs and SnO_2/TNTs

The morphology and composition of the samples were observed using a field emission scanning electron microscope (FESEM, Auriga, Zeiss) equipped with an energy dispersive X-ray spectroscopy (EDS). The images were obtained at an accelerating voltage of 20 kV. A scanning transmission electron microscope (STEM, SU8000, Hitachi) was carried out at 30 kV to determine the crystal distribution of NiO/TNTs samples. High resolution transmission electron microscope (HRTEM, Tecnai 20, Philips) images were obtained at 200 kV. The crystalline phase was identified using an X-ray diffractometer (XRD, D8 Advance, Bruker). The target used in the diffractometer is copper (Cu Kα radiation, λ = 1.54 Å). The surface chemical composition of samples was analyzed by X-ray photoelectron spectroscopy (XPS, Axis Ultra DLD, Kratos) with Al Kα radiation source. Peak fitting to the spectra was applied using Gaussian-Lorentzian peak shape after subtraction of Shirley background. The binding energy of C 1s peak at 284.6 eV was used as internal charge correction. Diffuse reflectance ultraviolet and visible spectra (UV-vis DRS) were performed using UV-vis-NIR spectrophotometer (Lambda 750, Perkin Elmer) with a wavelength range of 200–800 nm. Raman shift was recorded with a Raman spectroscopy (RamanMicro 200, Perkin Elmer) ranging in wavelengths from 100 to 700 cm^{-1}. Necessary characterization works were also applied for those materials used for experimental comparison.

3.3.2 GO/Ag-TNTs and RGO/Pt-TNTs

The phase composition of the synthesized photocatalysts were obtained using X-ray diffractometer (XRD, D8 Advance, Bruker) operated in the reflection mode with Cu Kα radiation (λ = 1.54 Å). For the photocatalysts applied in RGO/Pt-TNTs work, such analysis was carried out using X-ray diffraction (XRD, PANalytical-Empyrean). The morphologies of samples were examined by a field emission scanning electron microscope (FESEM, SU8000, Hitachi) equipped with an EDS (energy dispersive X-ray spectroscopy) detector. The images were taken at an accelerating voltage of 20 kV. High resolution transmission electron microscope (HRTEM, JEM-2100F, Jeol) images were obtained at 200 kV. A Micro-PL/Raman spectroscope (Renishaw, inVia Raman Microscope) was used to acquire the Raman and photoluminescence (PL) spectra with the excitation wavelength at 514 nm and 325 nm, respectively. Fourier transform infrared (FTIR) spectra were obtained on a Perkin Elmer Spectrum 400 spectrophotometer with scan range of 4000−450 cm^{-1}. UV-vis diffuse reflectance spectra (UV-DRS) were measured using UV-vis spectrophotometer (UV-2600, Shimadzu) equipped with an integrating sphere attachment. The spectra were collected with $BaSO_4$ as a reference. The surface chemical composition of the samples was analyzed by X-ray photoelectron spectroscopy (XPS, Omicron, Germany) with Al Kα radiation source. All XPS spectra were referenced to the C1s peak at 284.6 eV from the adventitious hydrocarbon contamination. Necessary characterization works were also applied for those materials used for experimental comparison.

3.4 Photocatalytic Experiment

3.4.1 Photocatalytic Degradation of Organic Pollutants

(a) NiO/TNTs and SnO_2/TNTs

The solar energy induced photocatalytic activity of both NiO/TNTs and SnO_2/TNTs was evaluated by adopting methylene blue (MB) as model pollutant under solar light irradiation. For comparison, NiO/TNTs and SnO_2/TNTs with varying concentration, pure TNTs and control sample were also studied. The control experiment was performed without a photocatalyst under identical conditions. The schematic of the experimental setup is illustrated in Fig. 3.7.

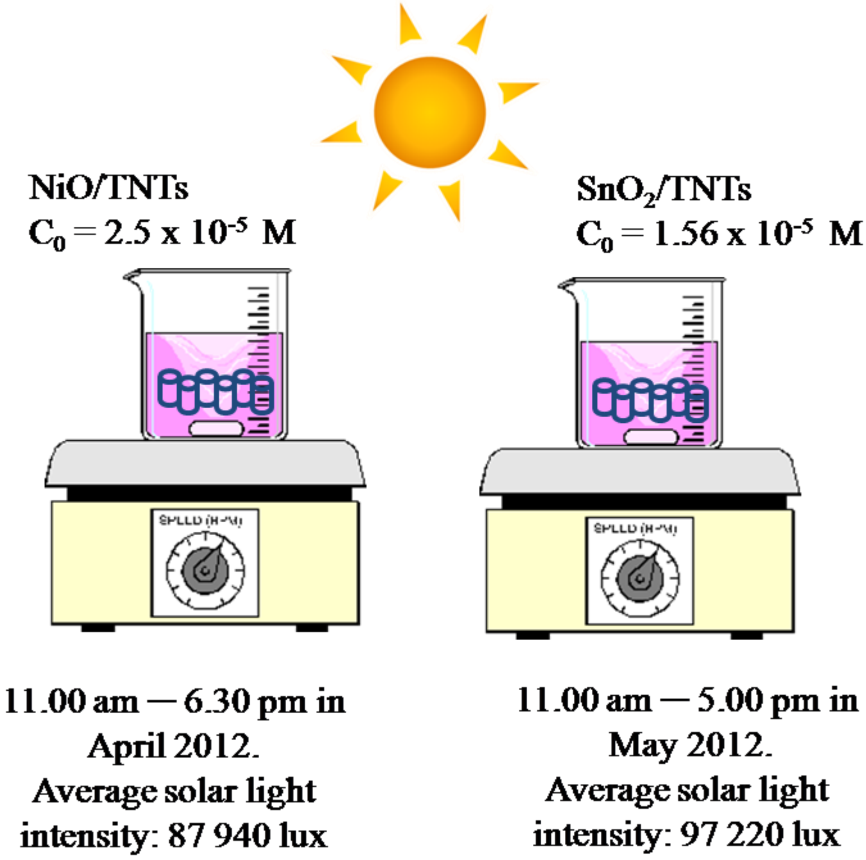

Figure 3.7: Schematic of experimental setup for the solar light-driven photocatalytic degradation of MB for both NiO/TNTs and SnO_2/TNTs

The degradation of MB was carried out in a 1000 mL beaker with the working volume of 200 mL MB solution (2.5×10^{-5} M) and (1.56×10^{-5} M) for NiO/TNTs and SnO_2/TNTs, respectively. The prepared samples were loaded in MB solution with only one side faced to solar light irradiation. Prior to the photocatalytic experiment, the dark reaction was carried out for 30 min in order to achieve the adsorption equilibrium. The samples were collected at regular time interval and analyzed for residual MB concentration with visible spectrometer (Spectroquant® Pharo 100, Merck) at $\lambda_{max} = 664$

nm. The calibration curve generated for the quantification of MB concentration is shown in Fig. 3.8. The drawn samples were dispensed back into the beaker after the measurement to allow further degradation.

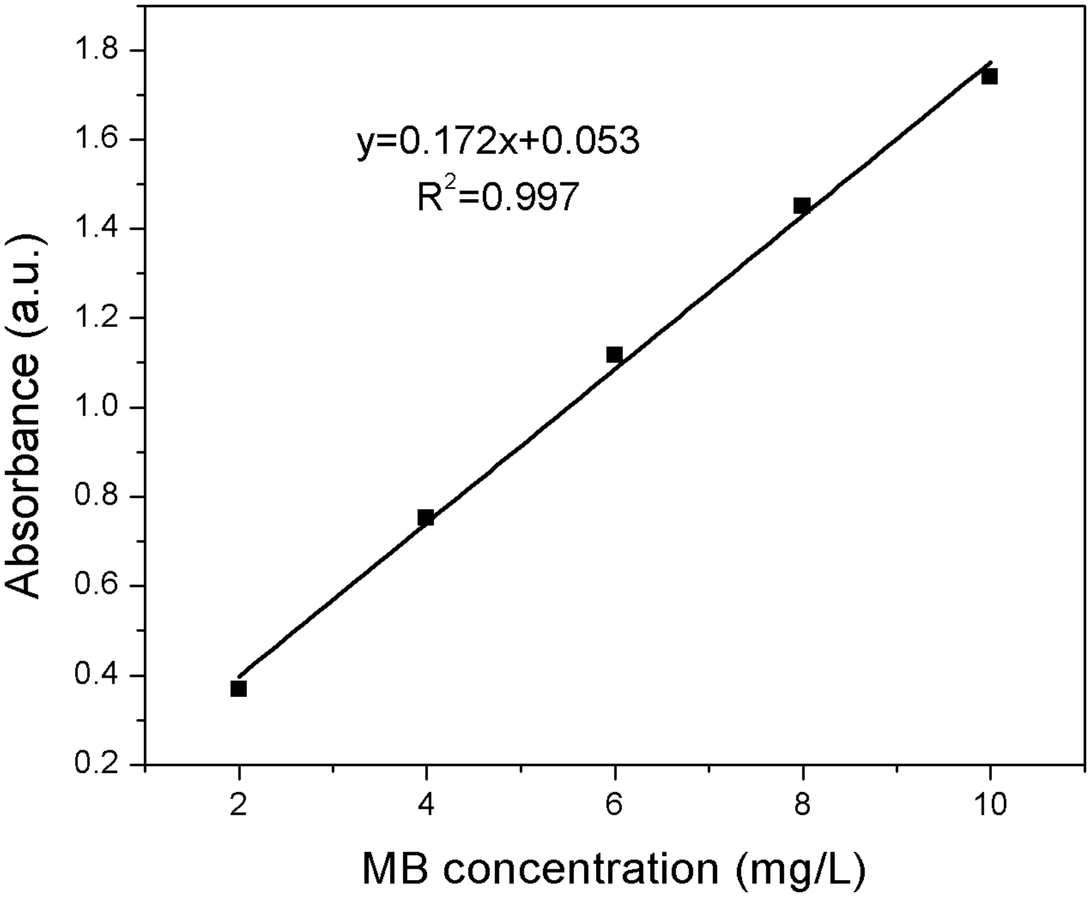

Figure 3.8: Calibration curve for methylene blue (MB) dye

The experiment for NiO/TNTs was conducted under clear sky condition at University of Malaya, Kuala Lumpur (latitude 101 ° 39' E and longitude 3 ° 7' N) between 11.00 am and 6.30 pm in April (2012).While the experiment for SnO_2/TNTs was carried out between 11.00 am and 5.00 pm in May (2012). Solar light intensity was measured using LT Lutron LX-101 Lux meter of 1000 × 100 lx and the average light intensity over the duration of clear sky weather condition was found to be 87 940 and 97 220 lux for NiO/TNTs and SnO_2/TNTs, respectively. Additionally, the influence of solar irradiation conditions such as clear sky (97 220 lux), partly cloudy (72 910 lux) and cloudy sky (54 520 lux) was studied for SnO_2/TNTs.

(b) GO/Ag-TNTs

The photocatalytic activity of GO/Ag-TNTs was evaluated based upon the removal of MB and 2-chlorophenol (2-CP) in aqueous solutions. For comparison, the photocatalytic activities of control, TNTs, Ag-TNTs and GO/TNTs were investigated. The experimental setup was illustrated in Fig. 3.9.

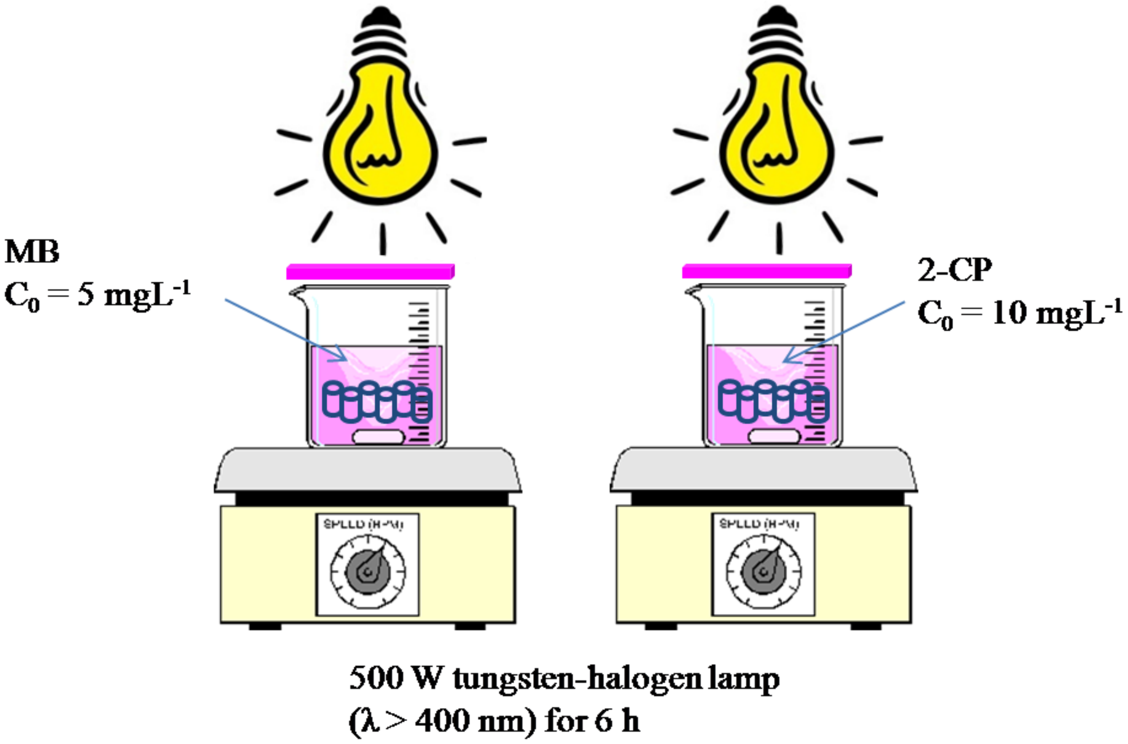

Figure 3.9: Schematic of experimental setup adopted for the photocatalytic degradation of MB and 2-CP for GO/Ag-TNTs under artificial visible light irradiation

The prepared photocatalysts were immersed in a glass beaker containing 100 mL aqueous solutions for MB (5 mgL^{-1}) and 200 mL aqueous solutions for 2-CP (10 mgL^{-1}), respectively. Prior to photodegradation, the solutions were magnetically stirred in a dark for 1 h to establish an adsorption-desorption equilibrium. A 500 W tungsten-halogen lamp was used as visible light source with any UV light below 400 nm was removed with a high-pass filter (FSQ-GG400, Newport Corp.). The dye samples were collected at regular interval, then analyzed for residual MB concentration with visible spectrophotometer (Spectroquant® Pharo 100, Merck) at λ_{max} = 664 nm. Similarly, 2-CP samples were withdrawn at regular interval, centrifuged and analyzed for residual concentration with ultra performance liquid chromatography (UPLC) (ACQUITY UPLC H Class, Waters) equipped with C18 column (50 mm × 2.1 mm × 1.7 µm). The mobile phase was acetonitrile (ACN) and water in the ratio 60:40 with a flow rate of 0.4 mL min^{-1}. The calibration curve adopted for quantification of 2-CP is shown in Fig. 3.10. All photocatalytic experiments were carried out for duration of 6 h.

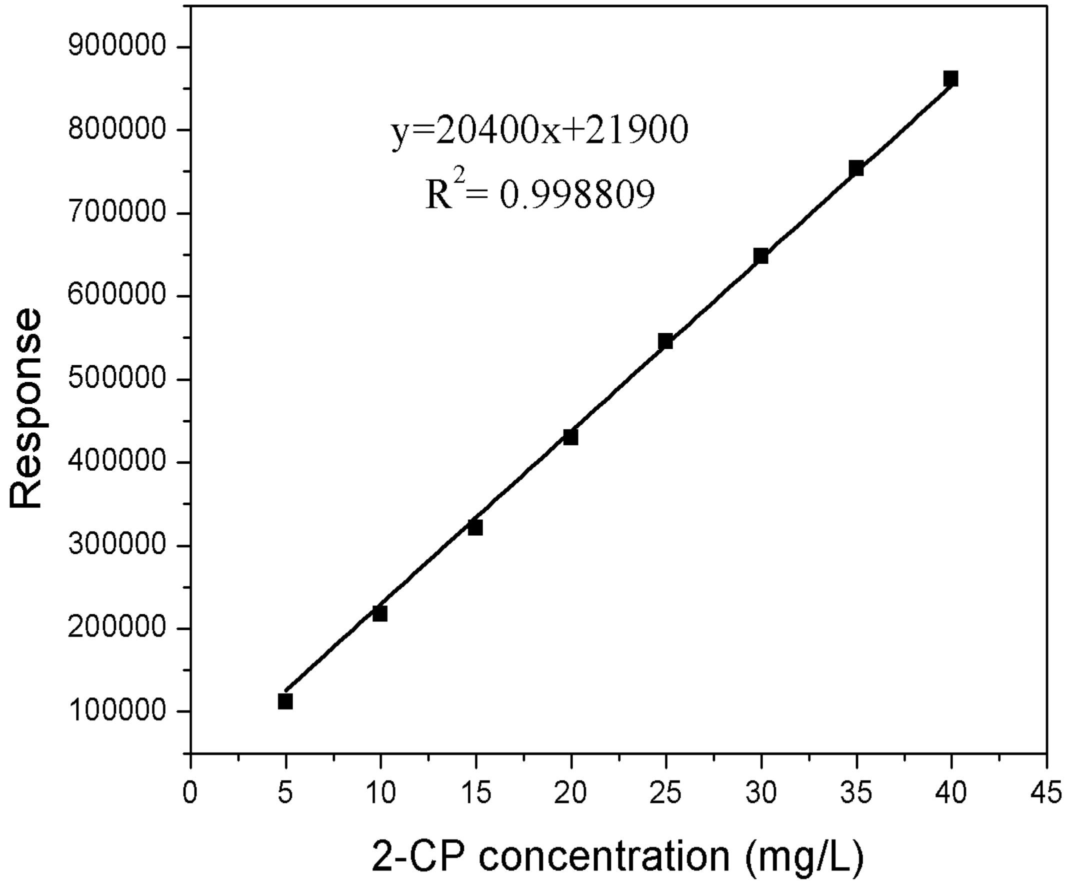

Figure 3.10: Adopted calibration curve for quantification of 2-CP

3.4.2 Photocatalytic Conversion of Carbon Dioxide (CO_2)

A dedicated gas phase photoreactor was fabricated to evaluate the photocatalytic activity of RGO/Pt-TNTs. The photograph of the reaction chamber and schematic of the complete experimental setup are illustrated in Fig. 3.11 and Fig. 3.12, respectively. A 500 W tungsten-halogen lamp was used as visible light source, mounted with high-pass UV light filter (FSQ-GG400, Newport Corp). Synthesized samples with size 1.0 × 1.0 cm was placed into the reaction chamber with a total volume of 9.8 mL. Highly purified CO_2 (99.99%) was humidified through water bubbling and then introduced into the reactor. Prior to the gas conversion, the reactor was purged with CO_2 at a flowrate of 300 mL min^{-1} for 1 h and then the flow rate was maintained at 100 mL min^{-1} throughout the gas conversion experiments. The products were collected at regular interval and analyzed for the CH_4 yield using gas chromatograph (Clarus 680, Perkin Elmer) equipped with a 30 m × 0.25 mm capillary column (Elite-1, Perkin Elmer) and flame ionization detector (FID). One point calibration was adopted for quantification of CH_4 using standard gas (CH_4, 100 ppm) with average percentage relative standard deviation (%RSD) < 3 and the summary data is shown in Table 3.2.

Figure 3.11: Photograph of the reaction chamber adopted for CO_2 gas conversion

Table 3.2: Summary of data for GC calibration using standard gas (CH_4, 100 ppm)

File Name	Time (min)	Methane area (µV.s)	Adjusted Amount
std 1	1.98	254751	0.25
std 2	1.98	266201	0.27
std 3	1.98	265545	0.27
std 4	1.98	256051	0.26
std 5	1.98	265419	0.27
std 6	1.98	258914	0.26
std 7	1.98	259842	0.26
std 8	1.98	258849	0.26
std 9	1.98	269136	0.27
	1.98	261634	0.26
	0.07	Average % RSD =2	1.93

RSD is between 0-3%

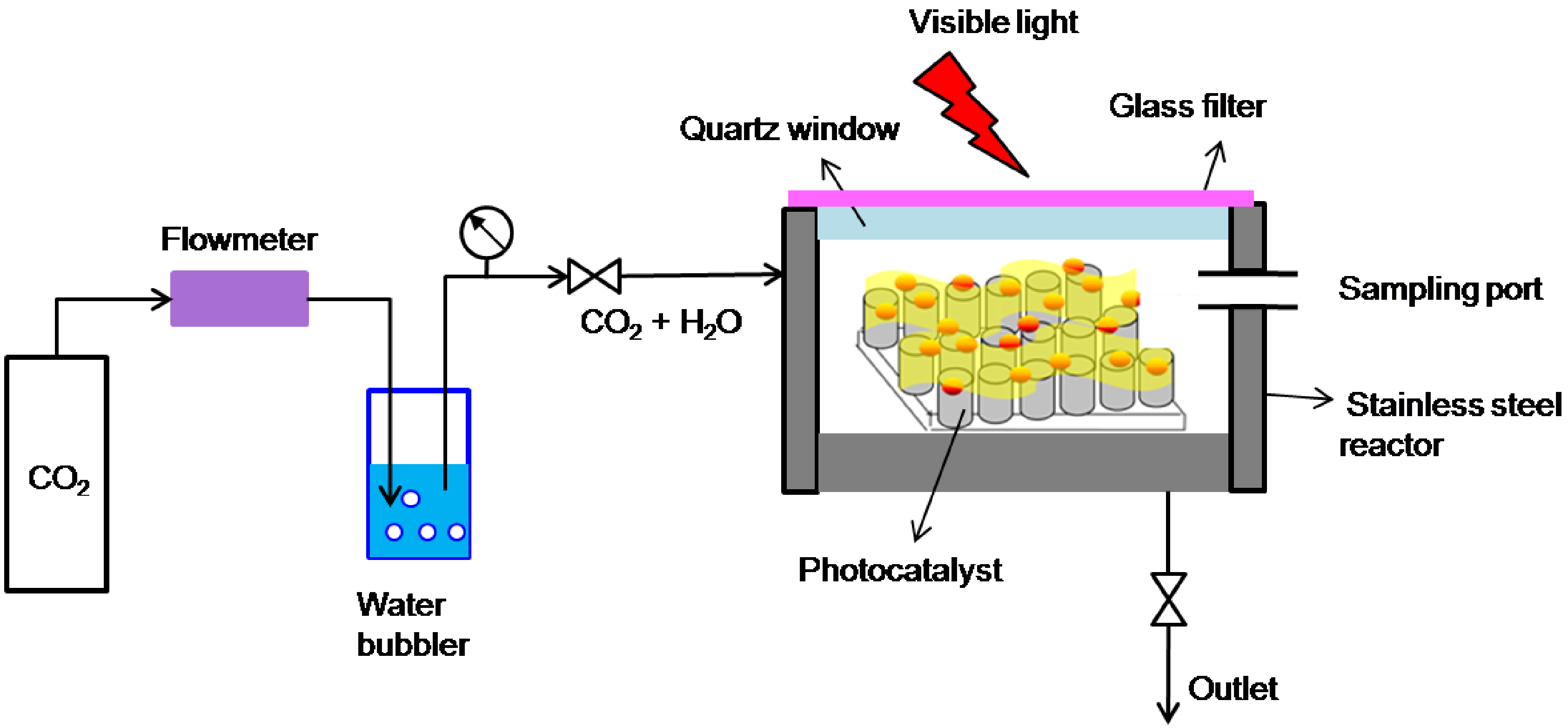

Figure 3.12: Schematic of complete experimental setup for photoreduction of CO_2 with H_2O

CHAPTER 4

RESULTS AND DISCUSSION

This chapter consolidates the findings that succeeded the adopted objectives of the thesis in an appropriate sequence. The preceding section describes the limelight of the tailored TNTs, and the overhauled constraints experienced while tailoring. This follows with sections devoted to explicit the robustness of the prepared modified TNTs from the mashing-up of semiconductors to conducting carbon materials and noble metals engulfed TNTs for both environmental cleanup and energy conversion.

4.1 TiO_2 Nanotube Arrays (TNTs)

The target of obtaining self organized and highly ordered nanotubular structures featuring absence of clog on the top of the TNTs was significantly achieved. The portrayed FESEM unveils the successful preparation of TNTs. Fig. 4.1(a-b) shows the morphological images of TNTs obtained directly after the electrochemical anodization in NH_4F/ethylene glycol (EG) electrolyte. It is observed that the top surface of the TNTs was covered by multiple layers of TiO_2 bunches (Fig. 4.1a) with a tube length ranged between 11 and 12 µm (Fig. 4.1b).

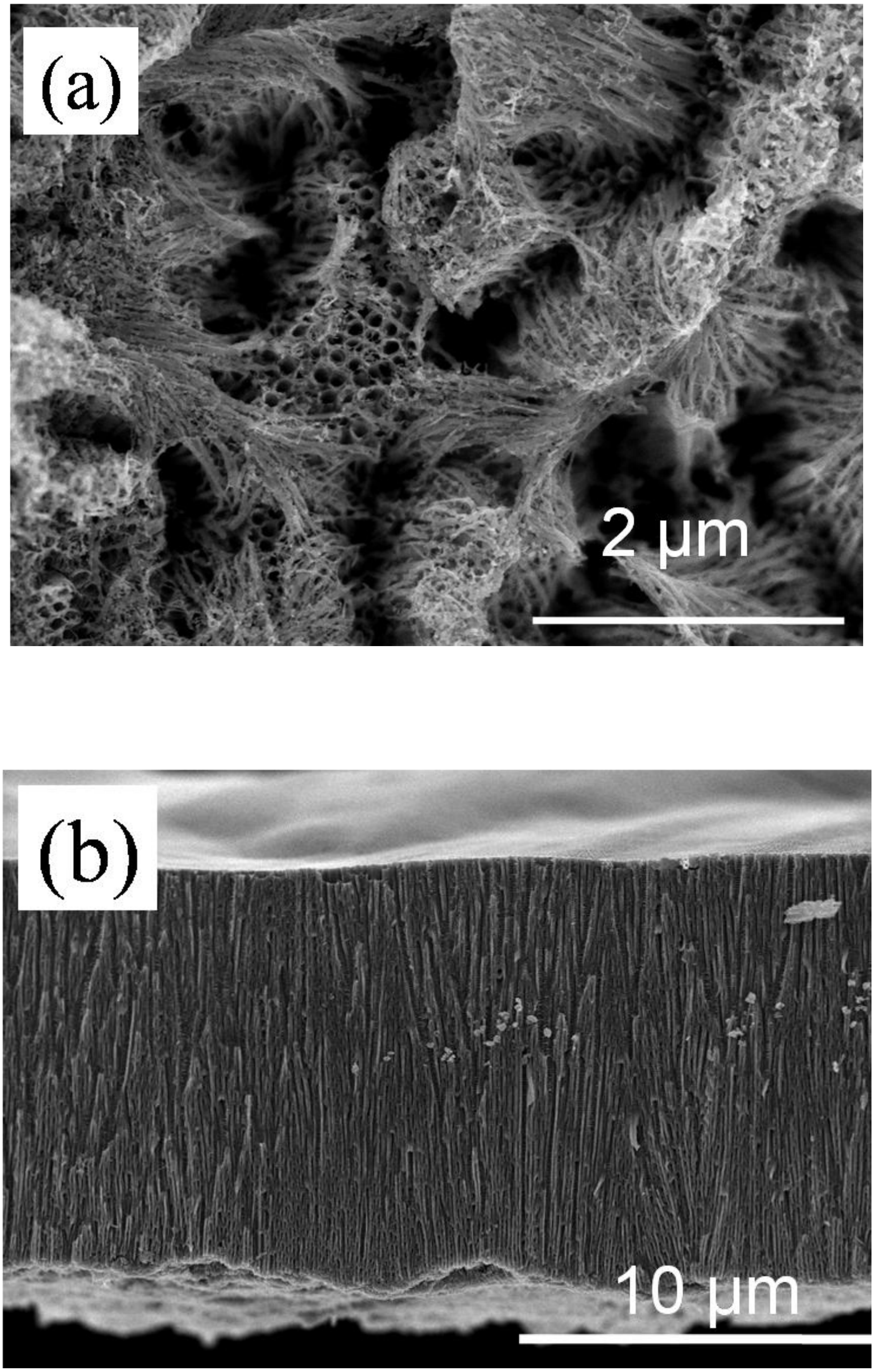

Figure 4.1: FESEM images of TNTs covered with bunches (a) top-view and (b) side view

This formation of the titania bunches was mainly induced by the over-etching effect of TNTs occurred on its surface of top section. This induced the tube wall to become very thin and the derived capillary force bent the tubes, leading to bunches formation on the surface of TNTs (Zhu et al., 2007). Thus formed bunches hindered and suppressed the charge-carriers transport and surface area for photoreaction, respectively. According to Lim and Choi (Lim and Choi, 2007), nanowires (titania bunches) originated from the vertical splitting of nanotube arrays and the morphology of nanotubes was strongly influenced by the applied potential and water content of the electrolytes. Thus, it was debundled by increasing water content in the electrolyte solution. The presence of water content either 10 or 20 wt% resulted in a successful debundling. The images obtained after the debundling of TNTs in EG electrolyte containing 10 and 20 wt% water content are shown in Fig. 4.2(a-b) and Fig. 4.2(c-d), respectively.

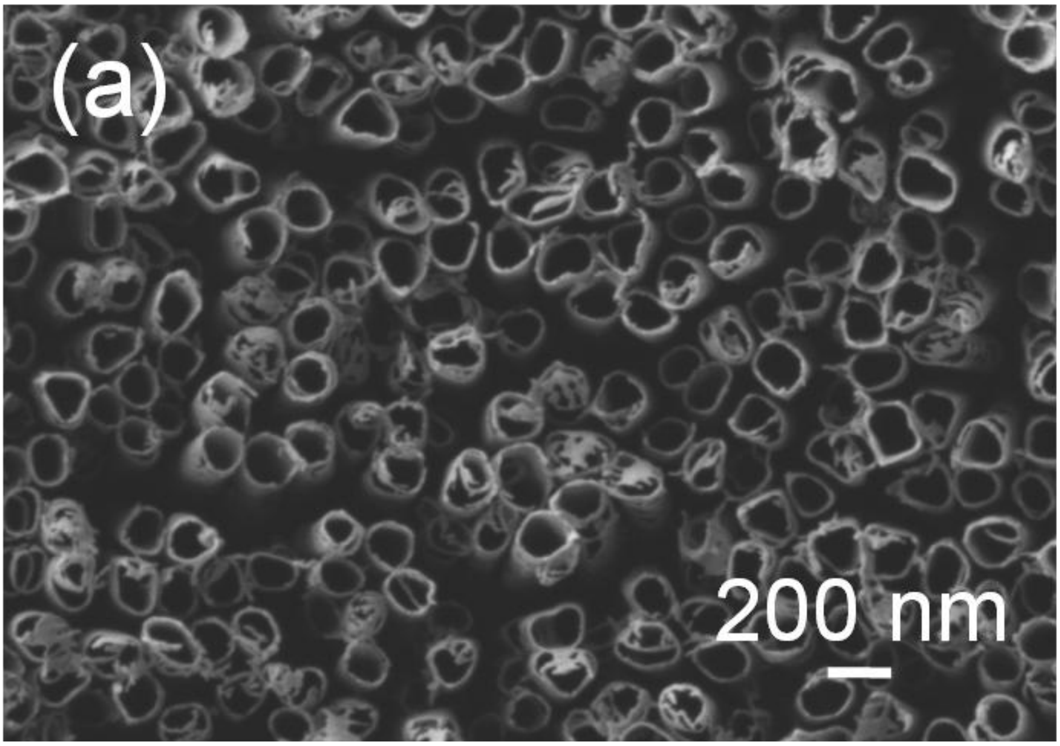

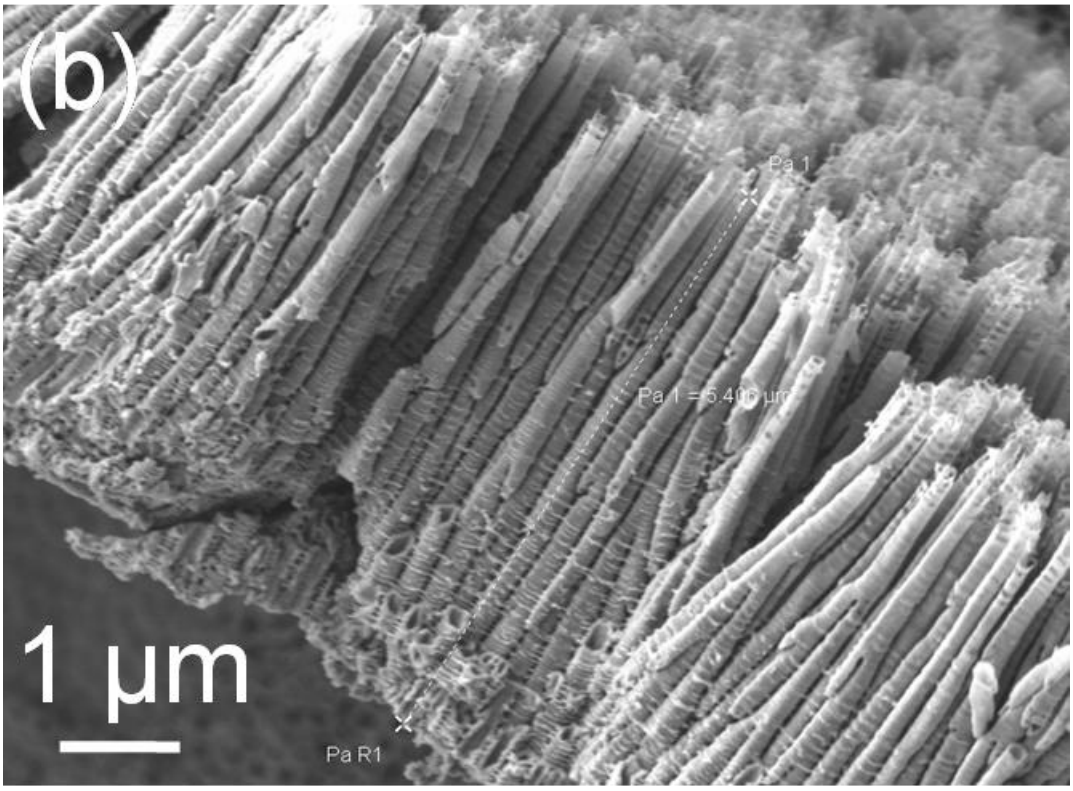
(b)
Pa 1
Pa 1 = 5.406 µm
1 µm
Pa R1

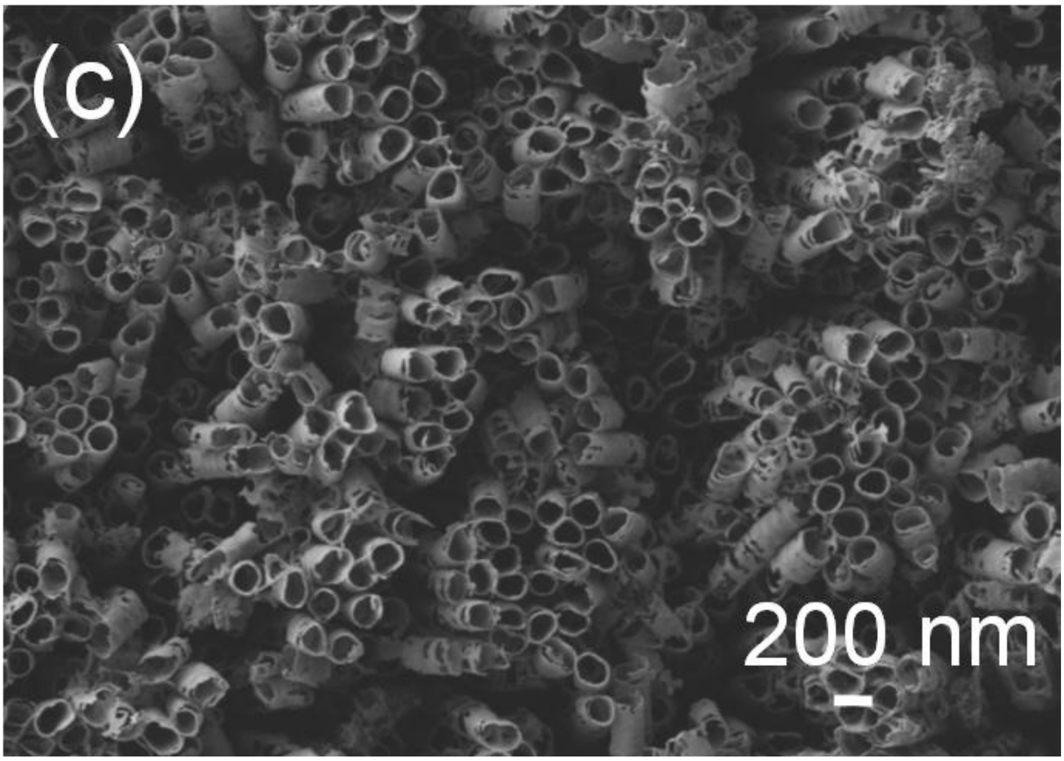
(c)
200 nm

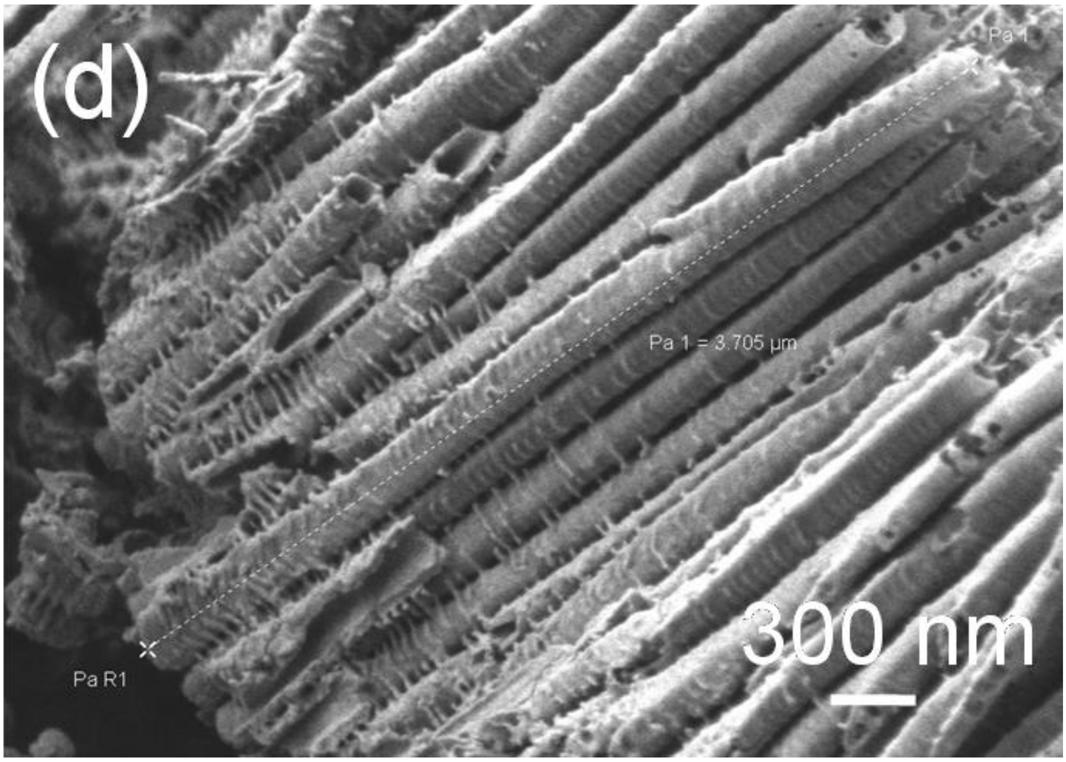

Figure 4.2: FESEM top-view and cross sectional images of TNTs synthesized in EG electrolyte containing (a-b) 10 wt% and (c-d) 20 wt% water content

The tube length was in the order of 5.4 µm and 3.7 µm for above mentioned water content, respectively. Moreover, it can be observed that the top portion of the tube mouths was highly fragile with non aligned tubular structure due to rapid dissolution rate. This rapid dissolution rate was attributed to the higher water content in the electrolyte. Although a surge in water content can resolve the cluster formation of titania, it led to anxiety of the tubular strength and orientation. Hence, a thermal treatment was considered for an hour after anodization followed by ultrasonication in ethanol for 30 min. The technique resulted in bunches free TNTs without disturbing the tubular structure by distorting and dispersing gray colour bunches into ethanol via ultrasonication and seen in Fig. 4.3(a)-(b).

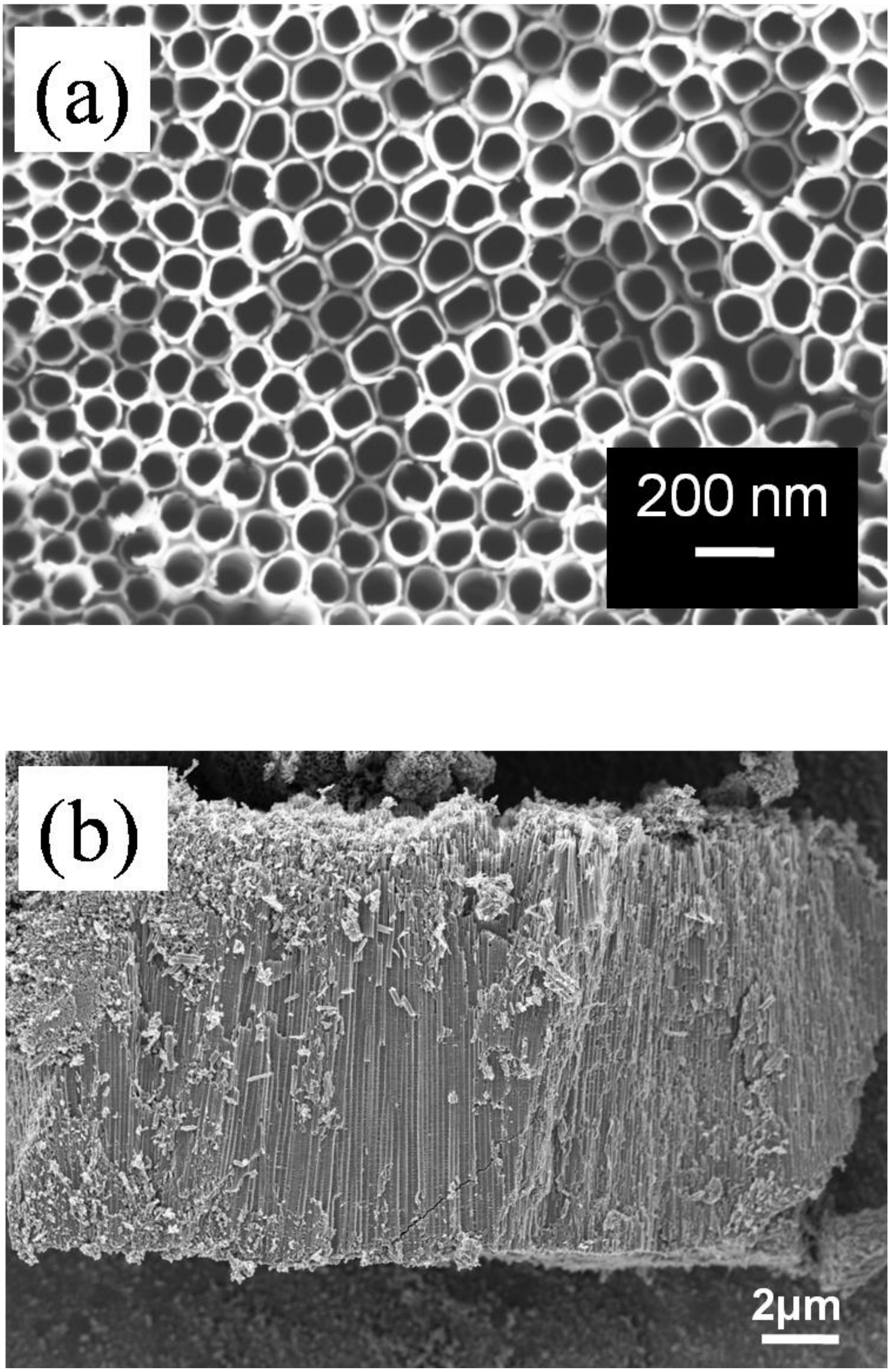

Figure 4.3: FESEM (a) top-view and (b) cross sectional images of bunches free TNTs after ultrasonication

The resulted one-dimensional vertical nanotube arrays possessed good alignment and close packing. They exhibited geometry with tube diameter of 109 nm, wall thickness of 15 nm and the tube length ranged between 7 and 10 µm. Thus derived bunches free TNTs was employed as backbone for subsequent modifications. The complete physicochemical properties of the studied TNTs were elaborated in the following semiconductors mash-up sections.

4.2 Mashing-up: NiO/TNTs Binary Semiconductor Composites

NiO semiconductor with dominant high p-type concentration was considered for the mashing-up with TNTs, speculating it can hanker higher hole mobility economically (Zhang et al., 2010b). In addition, NiO contributed for the separation of electron and hole pairs through the electric junction field and anchored the interfacial charge transfer (Chen et al., 2008; Ku et al., 2011; Chen et al., 2005b). To best of our knowledge, this is the first report that revealed the photocatalytic activity of the NiO/TNTs under solar-light illumination. The study demonstrated the successful loading of NiO on TNTs based on their physicochemical and photocatalytic performance.

The top and cross sectional view of the NiO/TNTs (0.5 M) is shown in Fig. 4.4a and Fig. 4.4b, respectively. The morphological structure of TNTs was not affected by the loading of NiO. Despite increasing the NiO to 2.5 M, the nanotubular structure remained unaffected (Fig. 4.4c). The EDS analysis in Fig. 4.5 confirmed the presence of Ni, O and Ti in NiO/TNTs. This spectrum was performed over different spots across the nanotubes to obtain very reliable Ni peaks. Table 4.1 shows the weight percentage of elemental composition for the adopted NiO concentration in TNTs.

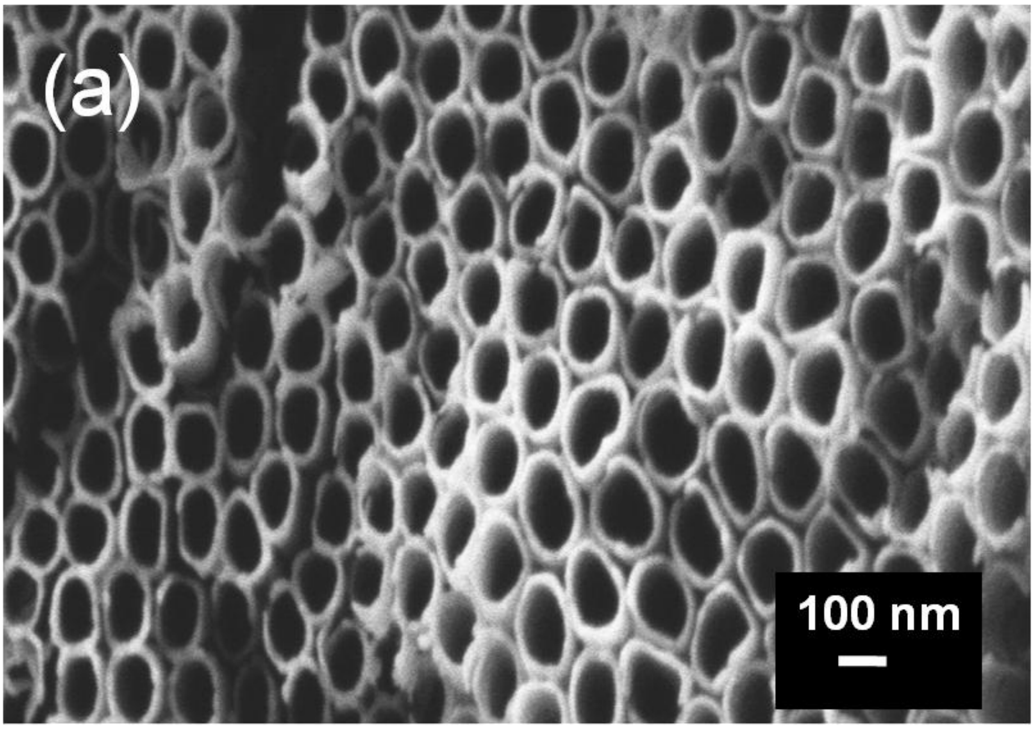
(a)
100 nm

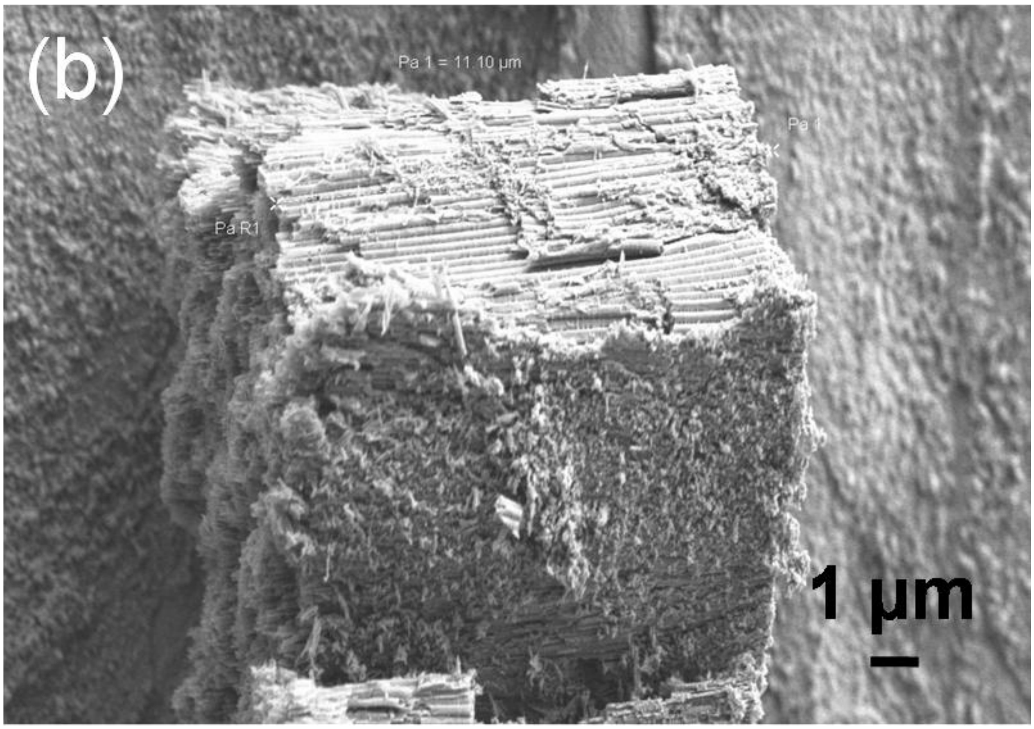
(b)
Pa 1 = 11.10 µm
Pa 1
Pa R1
1 µm

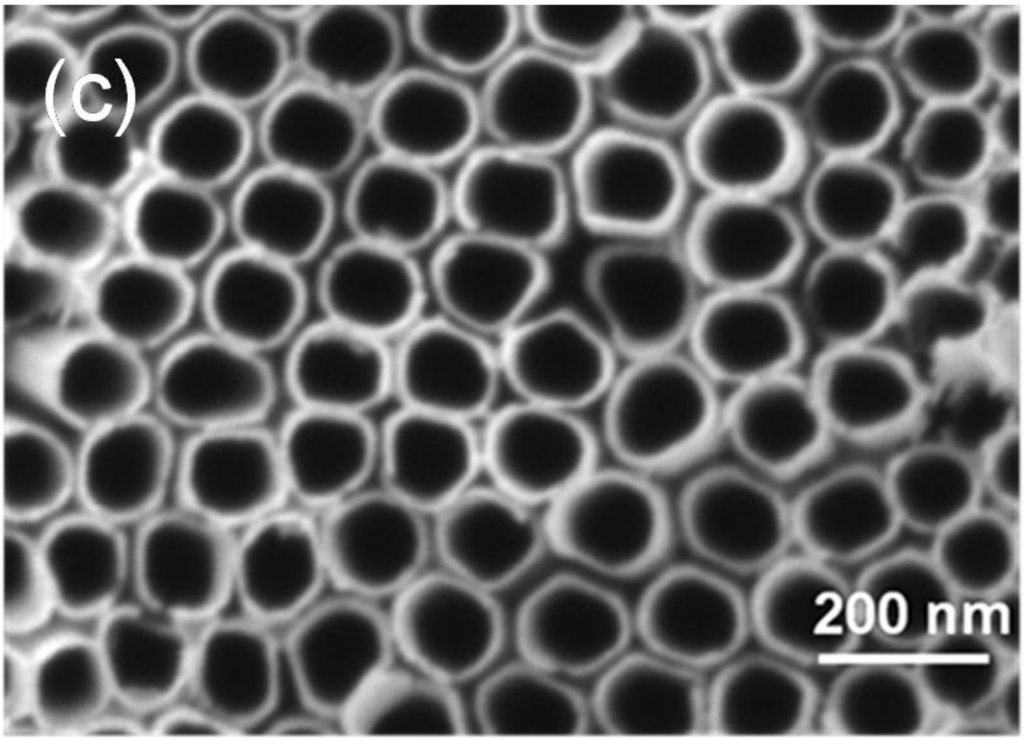

Figure 4.4: (a-b) Top-view and cross-sectional images of NiO/TNTs (0.5 M), and (c) top-view of NiO/TNTs (2.5 M)

Table 4.1: Elemental composition of NiO/TNTs with various loading conditions

		EDS		
		Elemental composition (wt%)		
Sample	**$Ni(NO_3)_2.6H_2O$ (M)**	**Ti**	**O**	**Ni**
TNTs	0	58.6	41.4	0
NiO/TNTs (0.5 M)	0.5	59.3	39.9	0.8
NiO/TNTs (1.5 M)	1.5	58.9	40.1	1
NiO/TNTs (2.5 M)	2.5	59.1	37.5	3.4

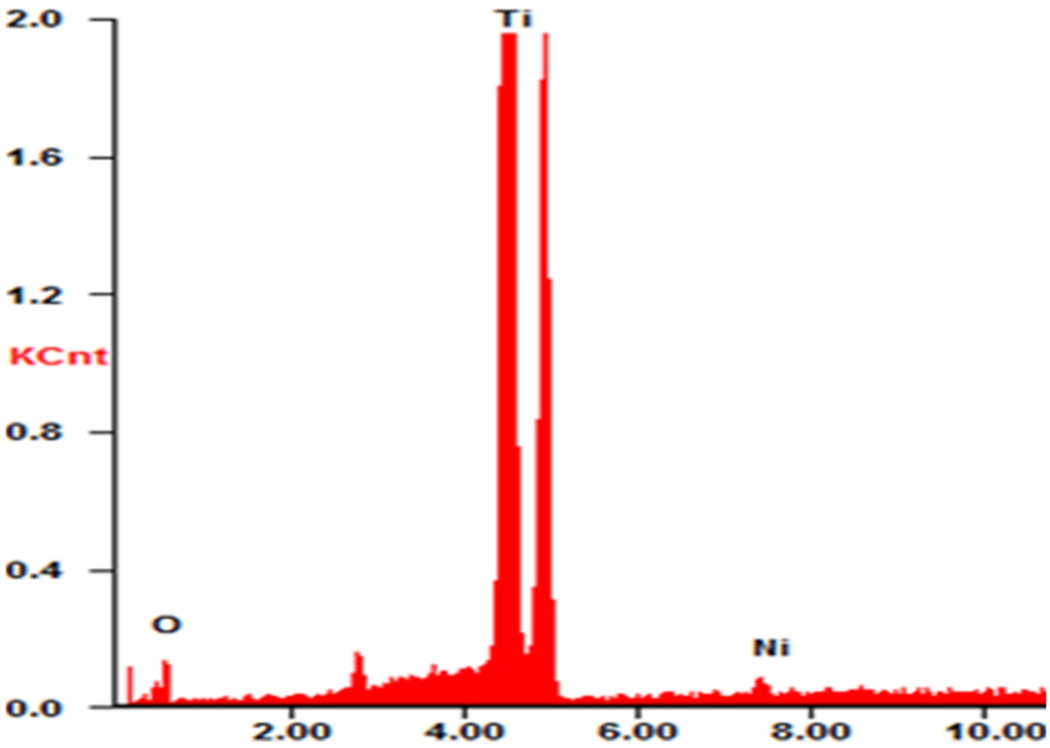

Figure 4.5: EDX of NiO/TNTs (0.5 M)

The uniform dispersion of the NiO NPs on the TNTs surface was confirmed by STEM analysis. The obtained STEM image as shown in Fig. 4.6a clarifies the homogeneous distribution of the NPs along the hollow structure of nanotubes. The image shows that the formed NPs ranged between 29.8 and 40.6 nm. The precious loading of NiO on the nanotubes was confirmed by performing EDX analysis (Fig. 4.6b). The existence of NiO in the prepared samples was further established through a lattice fringe obtained from HRTEM shown in Fig. 4.6c. A tangible evidence of crystalline nature of both TiO_2 and NiO was observed through lattice fringes of two planes with spacing of 0.35 nm and 0.48 nm, corresponding to the (1 0 1) plane of anatase TiO_2 (JCPDS no. 21-1272) and (1 1 1) NiO (JCPDS no. 89-5881).

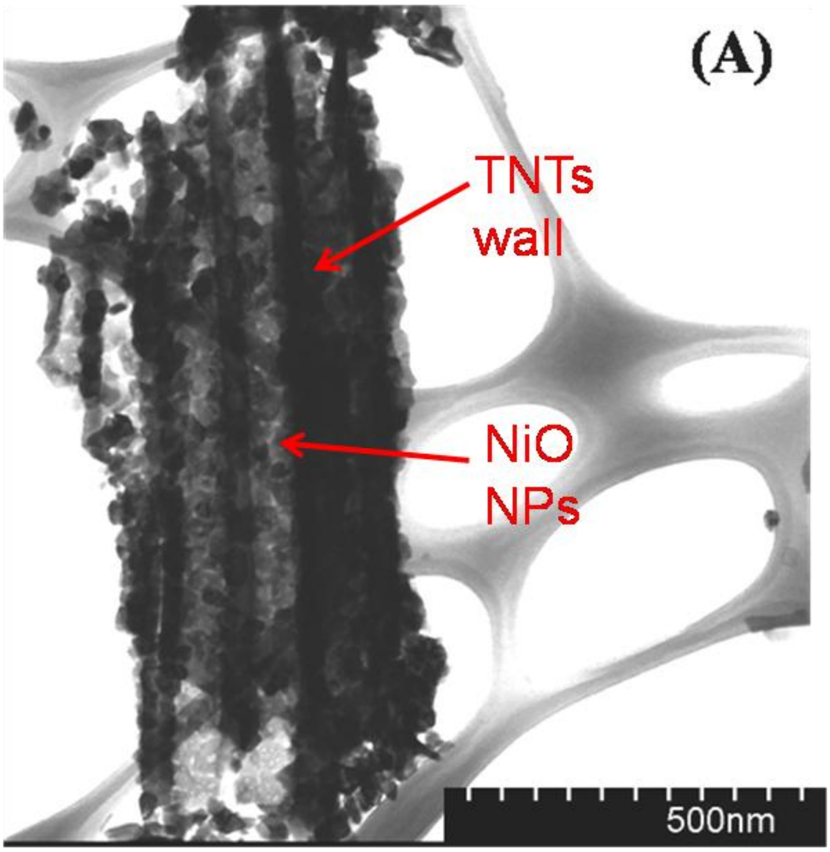
(A)
TNTs wall
NiO NPs
500nm

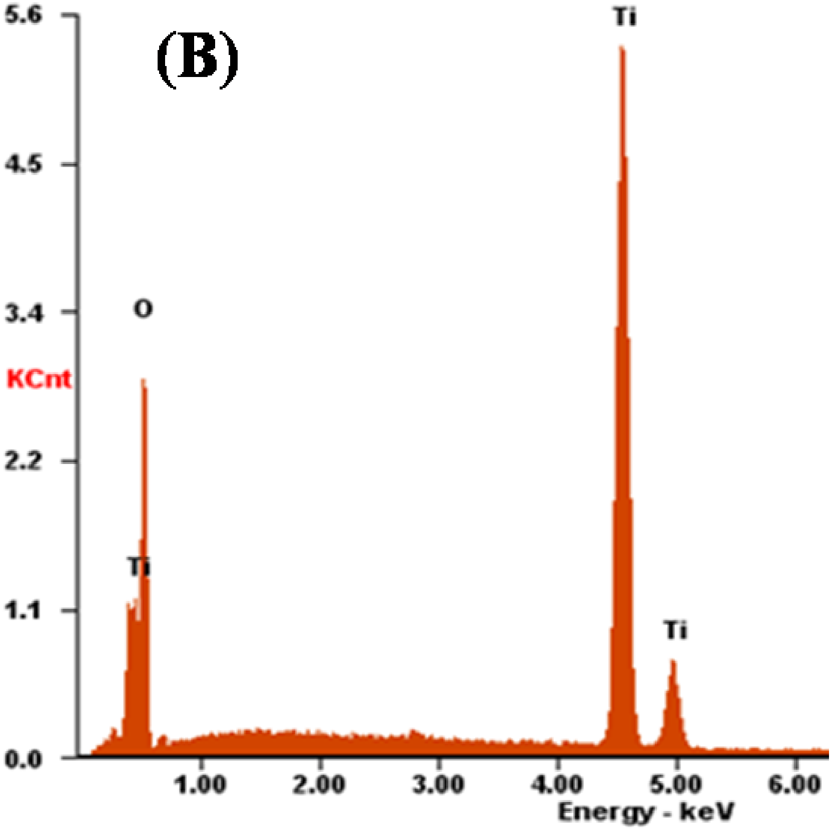
(B)
5.6
4.5
3.4
KCnt
2.2
1.1
0.0
O
Ti
Ti
Ti
1.00
2.00
3.00
4.00
5.00
6.00
Energy - keV

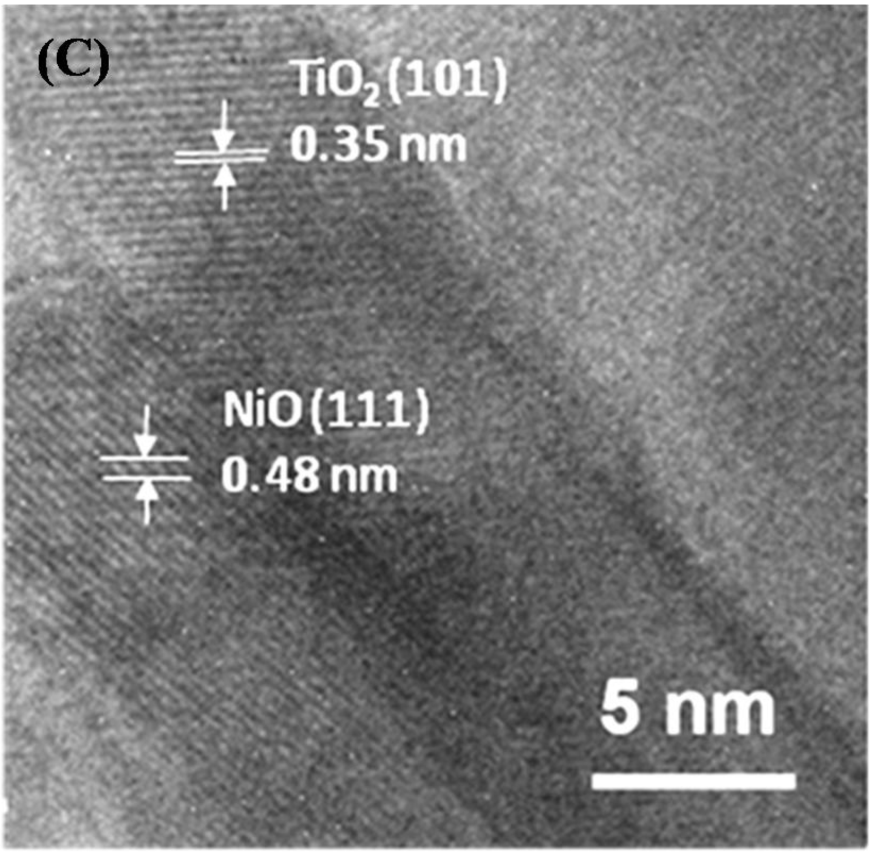

Figure 4.6: (a) STEM image, (b) EDX on top openings of nanotubes area and (c) HRTEM image of NiO/TNTs (0.5 M)

Fig. 4.7 depicts the XRD patterns of NiO/TNTs (0.5 M), NiO/TNTs (2.5 M) and TNTs. Since both low and higher NiO loading on TNTs reflected similar crystalline structure, the median NiO loading was not performed. However, irrespective of NiO loading, all the samples exhibited a complete anatase phase that disclosed the absence of phase change in anatase after the loading of varying concentration of NiO. There was an additional Ti peaks observed in the obtained crystallographic pattern, attributed to Ti substrate adopted as attachment for nanostructure layer. The peaks of tetragonal TiO_2 anatase phase (JCPDS no. 21-1272) appeared at 25.3 °, 36.9 °, 37.8 °, 48.0 °, 53.9 °, 55.1 °, 62.7 °, 68.8 ° and 75.0 °, corresponding to miller indices (1 0 1), (1 0 3), (0 0 4), (2 0 0), (1 0 5), (2 1 1), (2 0 4), (1 1 6) and (2 1 5), respectively. No peak associated with crystalline phase of NiO was detected. This was due to: (i) the adopted Ni cations (0.72

Å) were well substituted into the Ti cations (0.68 Å) in anatase TiO_2 lattice due to their similar ionic radii (ii) sound and uniform dispersion of NiO particles on TNTs surface (Vijayan et al., 2010; Li and Shang, 2010) and (iii) adopted lower NiO concentration that limited its detection.

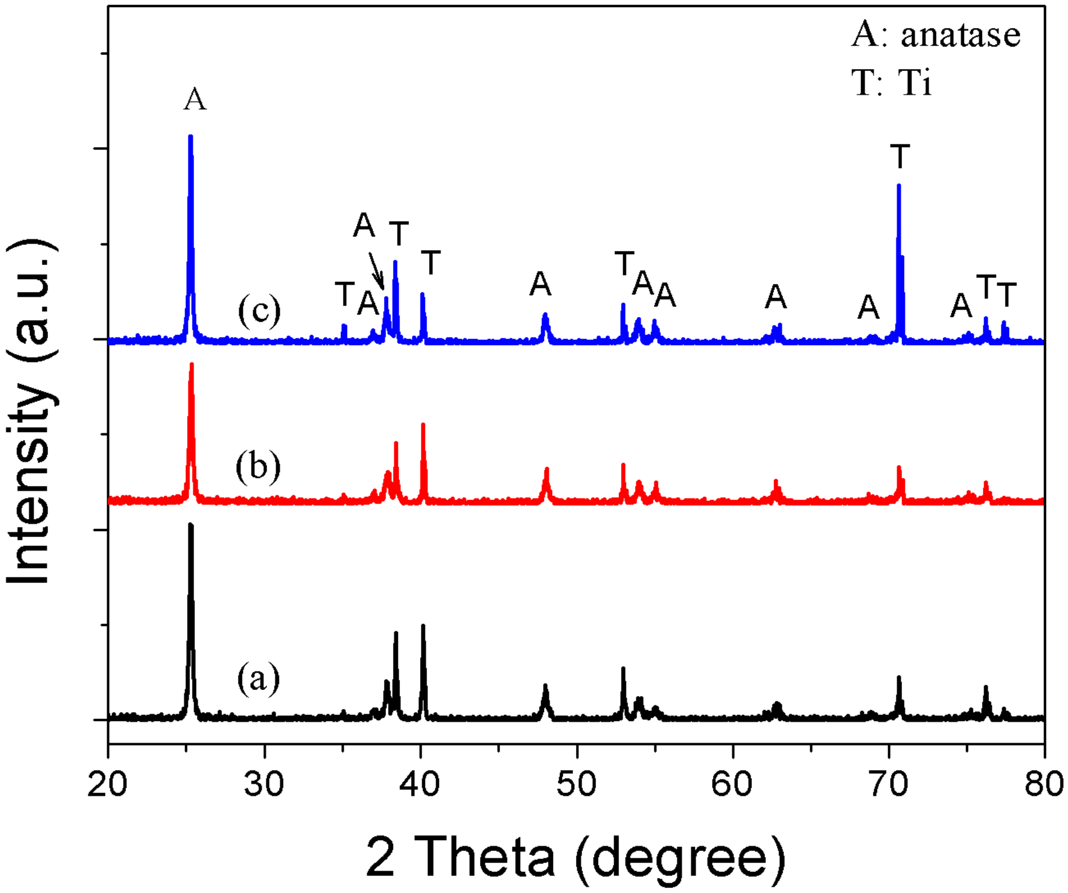

Figure 4.7: X-ray diffraction pattern of photocatalysts (a: TNTs; b: 0.5 M NiO/TNTs; c: 2.5 M NiO/TNTs)

The average crystallite sizes of TiO_2 anatase were calculated using Scherrer equation:

$$D = \frac{K\lambda}{\beta \cos\theta} \tag{4.1}$$

where β is the full width half maximum (FWHM) for the 2θ peak, K is the shape factor taken as 0.89 for calculations, λ is the wavelength of X-ray (0.154 nm), and θ is the diffraction angle. The lattice parameters were measured using (1 0 1) and (2 0 0) in anatase crystal planes by using Bragg's equations:

$$d_{(h\,k\,l)} = \frac{\lambda}{2\sin\theta} \tag{4.2}$$

Formula for tetragonal system is as follows:

$$d_{h\,k\,l}^{-2} = h^2a^{-2} + k^2b^{-2} + l^2c^{-2} \tag{4.3}$$

where $d_{(h\,k\,l)}$ is the distance between crystal planes of (h k l), λ is the X-ray wavelength, θ is the diffraction angle of crystal plane (h k l), h k l is the crystal index and a, b and c are lattice parameters (in anatase form, a=b≠c). The calculated crystallite sizes and lattice parameters of the samples are summarized in Table 4.2.

Table 4.2: Lattice parameters for TNTs and NiO/TNTs samples with different concentrations

Sample	Crystallite size (nm)[a]	Cell parameters a=b, c (Å)[b]
TNTs	33.81	3.7868, 9.5102
NiO/TNTs (0.5 M)	34.54	3.7828, 9.5184
NiO/TNTs (2.5 M)	34.10	3.7872, 9.5438

[a] Measured by (Eq. 4.1)

[b] Estimated according to (Eq. 4.2) and (Eq. 4.3)

The table vindicates that the calculated crystallite grain sizes and lattice parameters were not much influenced by NiO loading. Obviously the non subjected median point will also bear the similar structure irrefutably. The lattice parameters of all samples remained almost unchanged along a-and b-axis, whereas the c-axis parameter underwent a slight surge with ascent in NiO concentration. This provokes that a minor fractions of Ti^{4+} was replaced by Ni^{2+} substitutionally (Kim et al., 2006). This is also visualized from the non apparent peak broadening in the diffraction patterns of NiO/TNTs (Fig. 4.8). Further ascending the NiO loading to 2.5 M led to an increased crystallite size of anatase phase to 34.10 nm, suggesting that NiO loading never caused any suppression on titania crystal growth.

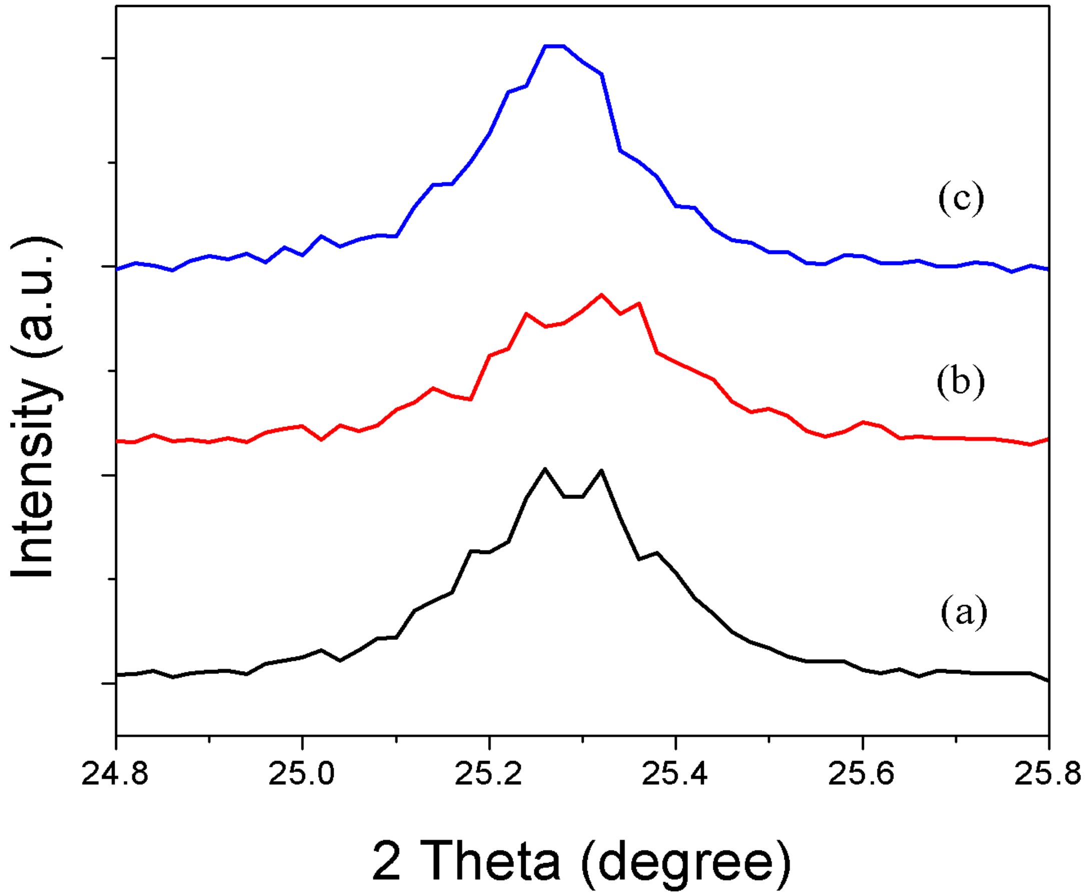

Figure 4.8: Enlarged XRD peaks of crystal plane (1 0 1) (a: TNTs; b: 0.5 M NiO/TNTs; c: 2.5 M NiO/TNTs)

Raman spectra of mashed-up semiconductor are depicted in Fig. 4.9. Four distinct Raman peaks at 145 (E_g), 399 (B_{1g}), 519 (A_{1g} + B_{1g}) and 639 cm^{-1} (E_g) are observed for the studied samples. All these peaks clearly attributed to the anatase phase of titania. The absence of NiO or any other related oxidation state of Ni was well correlated with diffraction findings.

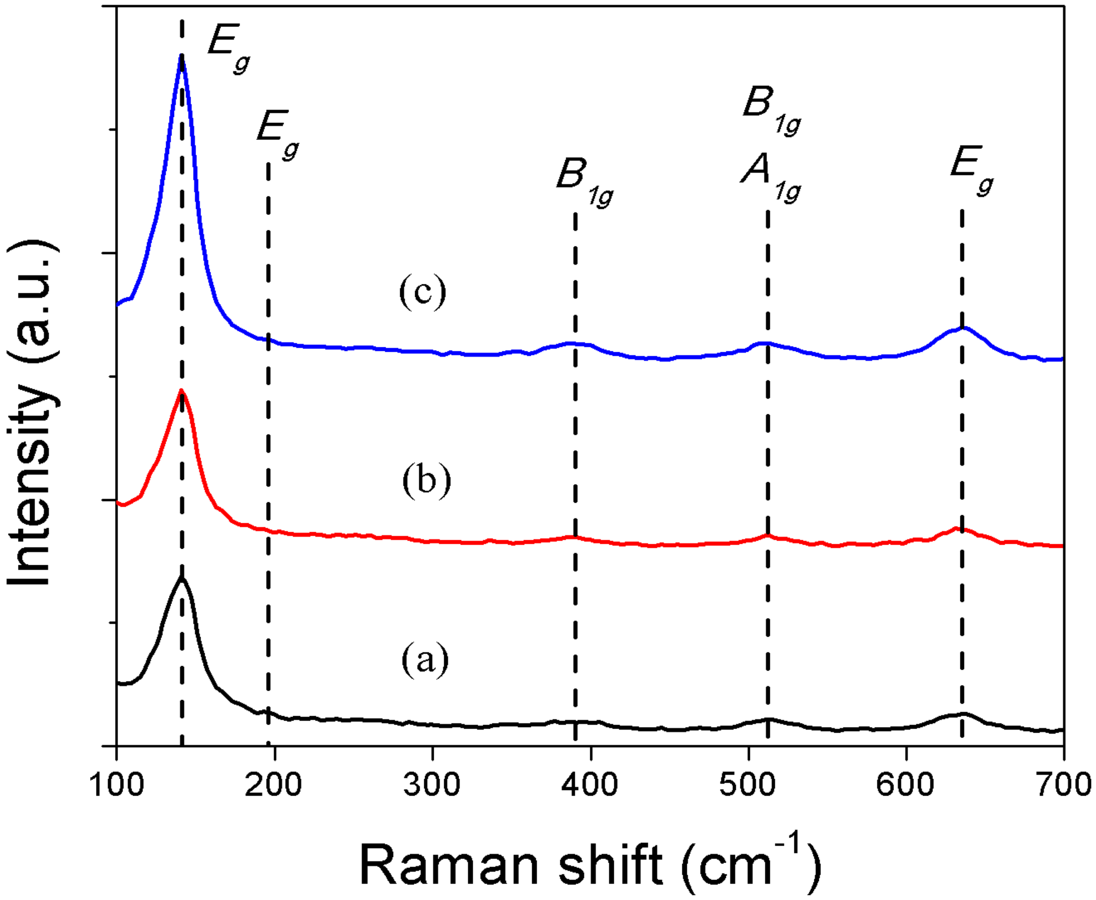

Figure 4.9: Raman spectra of photocatalysts (a: TNTs; b: 0.5 M NiO/TNTs; c: 2.5 M NiO/TNTs)

The prior and foremost challenge in upgrading the properties of titania is to shift the absorption spectrum towards the visible region that promote efficient solar driven photocatalysis. The diffuse reflectance spectra (DRS) of prepared samples are slated in

Fig. 4.10. All samples exhibited an absorption band lower than 390 nm (UV region) due to the charge transfer from O 2p valence band to Ti 3d conduction band (Fuerte et al., 2002). It can be seen that NiO/TNTs (0.5 M) did not show a significant red-shifted absorption edge towards visible region due to its marginal increase of NiO concentrations compared to that of TNTs. Meanwhile, the samples that bear NiO concentrations of 1.5 M and 2.5 M displayed a radical shift towards the visible region. NiO/TNTs (2.5 M) showed a distinct hump between 450 and 515 nm which was explained by the crystal field splitting of $3d^8$ orbital and charge transfer from Ni^{2+} to Ti^{4+}, respectively (Lin et al., 2006). In the junction region of NiO/TNTs, the overlap of CB of 3d level in Ti^{4+} with d-level of Ni^{2+} enabled charge transfer transitions between electrons in d-level of Ni^{2+} and the CB of TiO_2. It also contributed for a positive plunge in the energy gap between Ti 3d and O 2p states of TiO_2 (Lin et al., 2006; Mor et al., 2007) and swept absorption in visible region. This revealed the good agreement between the semiconductors in consequence of the inter-dispersion of the two oxides (Ku et al., 2011).

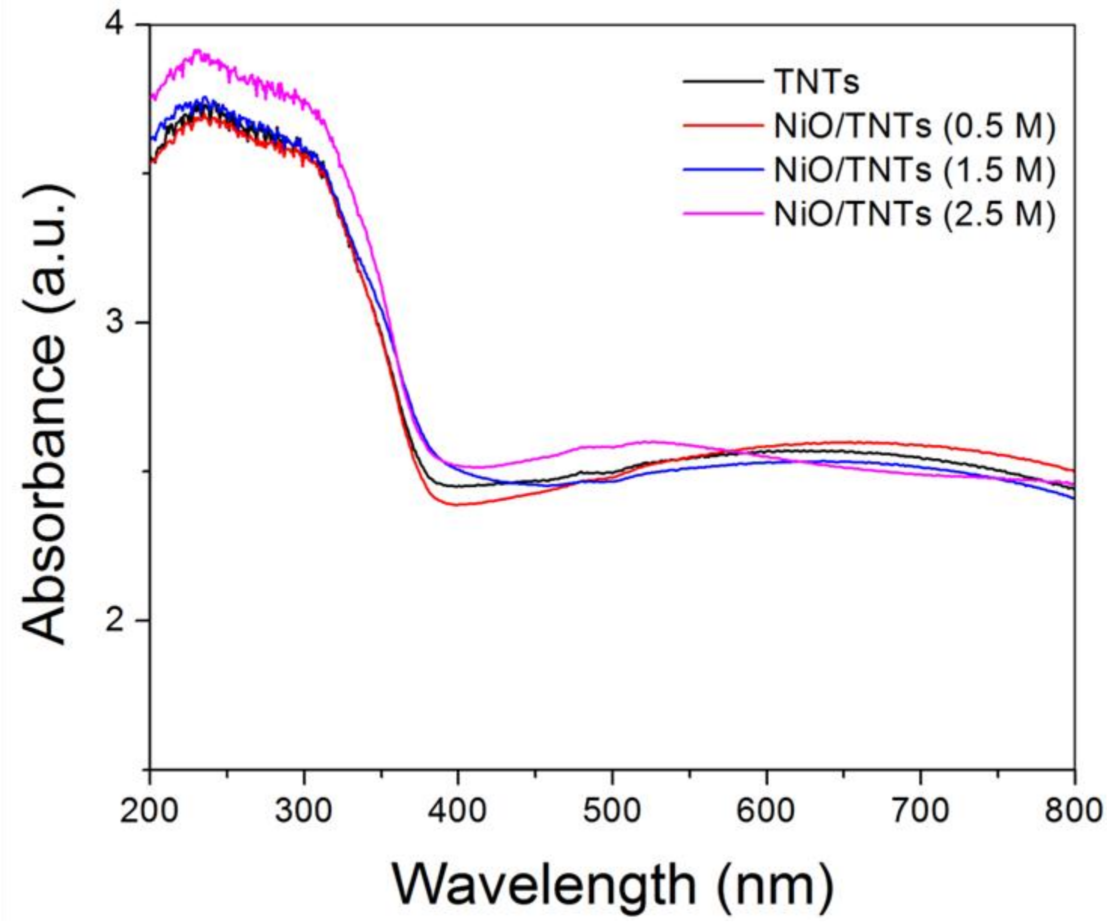

Figure 4.10: UV-visible absorption spectra of pure TNTs and different concentrations of NiO/TNTs (concentrations in molarity)

The variations in chemical composition and oxidation state of prepared photocatalysts were analyzed through X-ray photoelectron spectroscopy (XPS). The fully scanned version of the spectra is presented on Fig. 4.11a, indicating Ti, O and Ni elements existed in the prepared NiO/TNTs heterostructures. The spectra of Ni 2p, O 1s and Ti 2p core levels of the NiO/TNTs exist as: (1) Ti 2p region (450–470 eV); (2) Ni 2p region (850–890 eV); and (3) O 1s region (520–540 eV). As shown in Fig. 4.11b, there are two peaks observed at 458.4 eV (Ti $2p_{3/2}$) and 464.1 eV (Ti $2p_{1/2}$), both correspond to Ti^{4+} observed in the TiO_2 (Choi and Kang, 2007). Thus disclose that a large fraction of Ni^{2+} ions segregated as a separate NiO and as a dominant phase, while the residue fraction was incorporated substitutionally into TiO_2 lattice. The obtained

XPS spectra of O 1s core level was fitted to quad nature of chemical states (Fig. 4.11c). The peaks at 529.7, 530.8, 531.9 and 533.2 eV were assigned to oxygen atom of TiO_2, NiO, Ni_2O_3 and adsorbed water, respectively. The Ni 2p spectra in Fig. 4.11d were mapped into four peaks including NiO ($2p_{3/2}$), NiO ($2p_{1/2}$), Ni_2O_3 ($2p_{3/2}$) and Ni_2O_3 ($2p_{1/2}$). The binding energy of 855.6 eV and 873.1 eV corresponded to Ni^{2+} in NiO (Sasi and Gopchandran, 2007) and the binding energies of 856.3 eV and 874.1 eV specified the presence of Ni^{3+} in Ni_2O_3 (Shrestha et al., 2010). A summary of surface elemental composition of NiO/TNTs (0.5 M) is tabulated in Table 4.3.

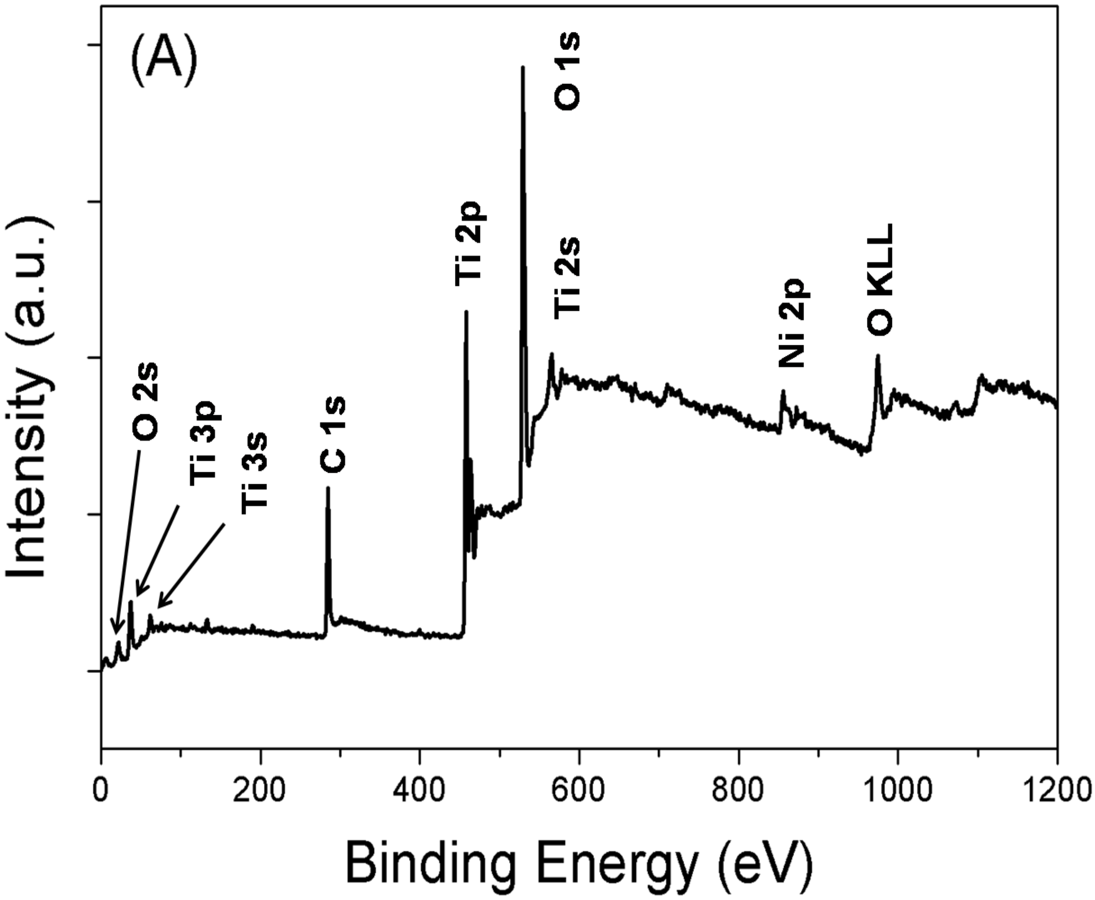

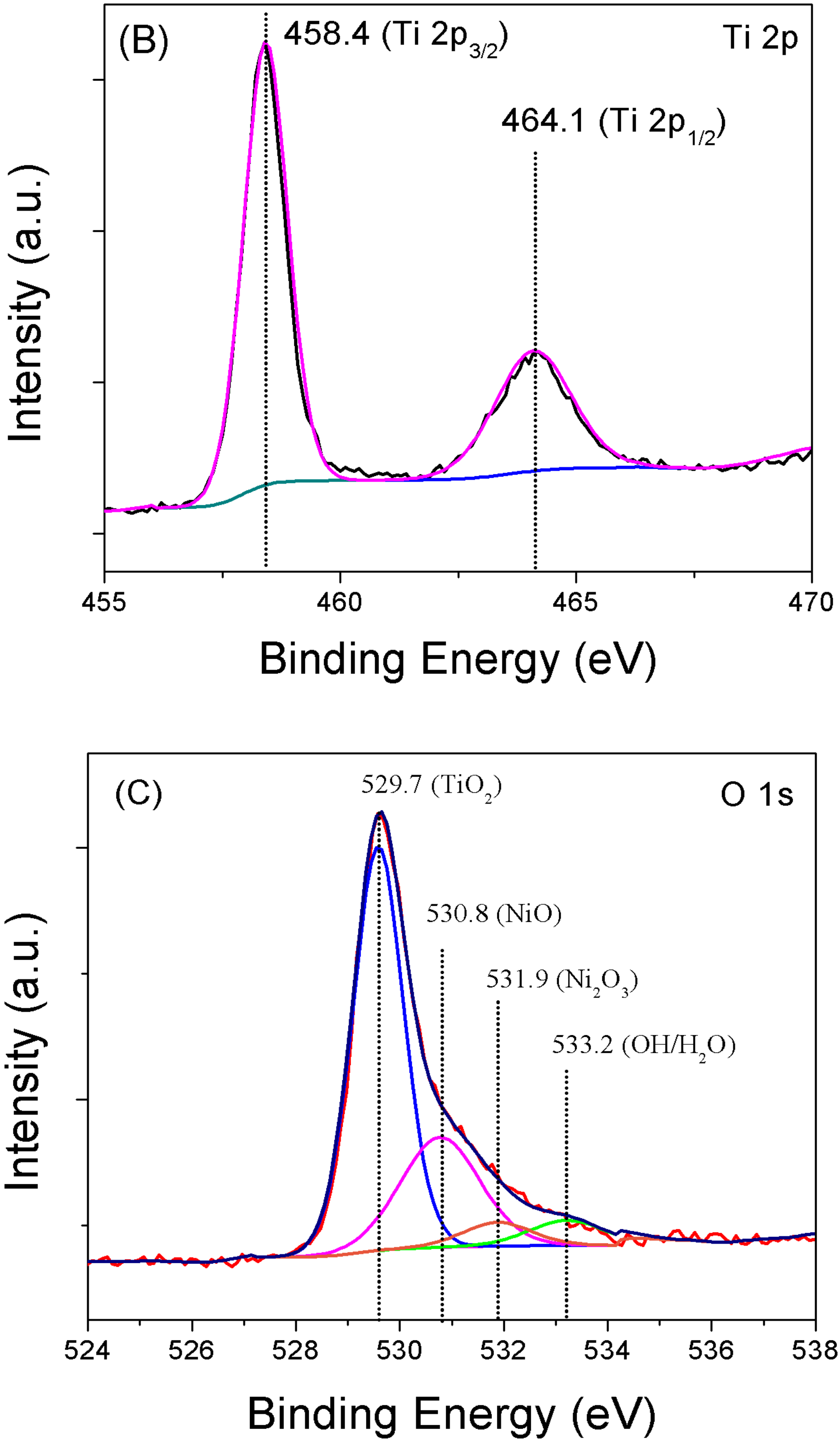
(B)
458.4 (Ti 2p$_{3/2}$)
Ti 2p
464.1 (Ti 2p$_{1/2}$)
Intensity (a.u.)
455
460
465
470
Binding Energy (eV)
(C)
529.7 (TiO$_2$)
O 1s
530.8 (NiO)
531.9 (Ni$_2$O$_3$)
533.2 (OH/H$_2$O)
Intensity (a.u.)
524
526
528
530
532
534
536
538
Binding Energy (eV)

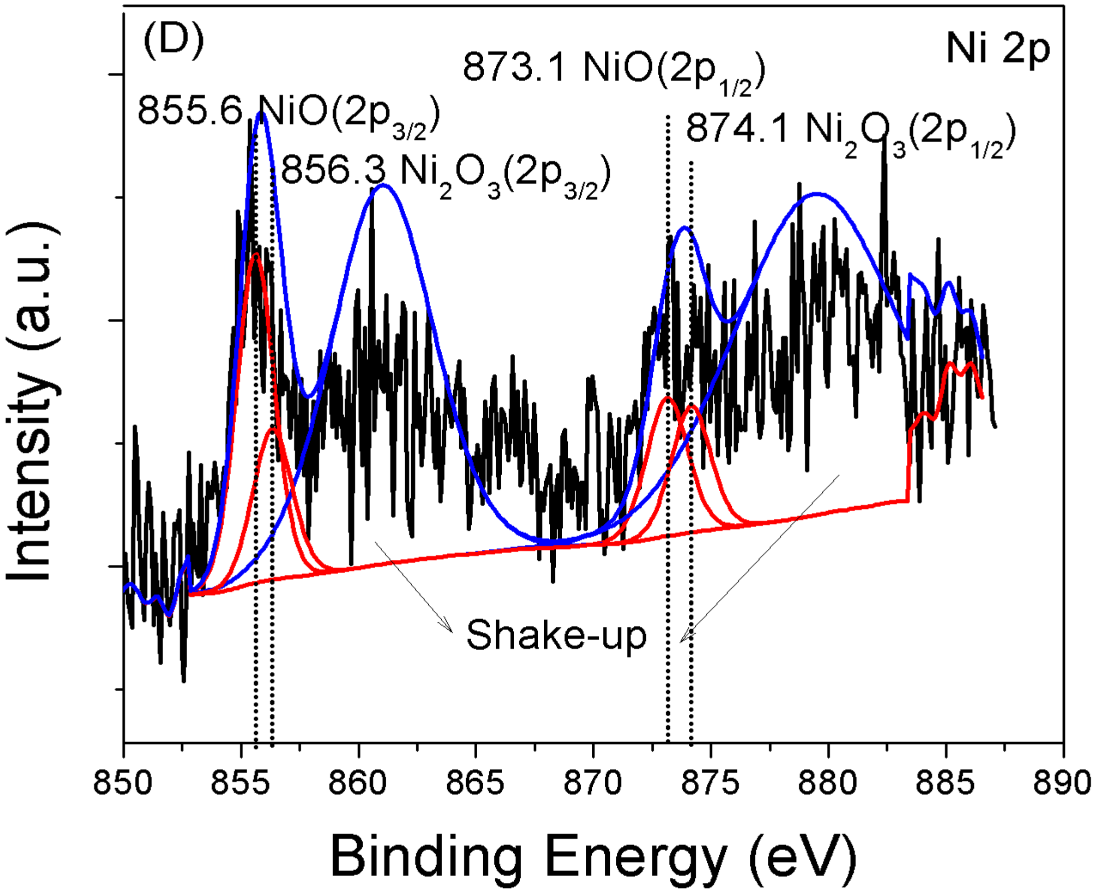

Figure 4.11: XPS spectra of NiO/TNTs (0.5 M) (a) fully scanned spectra (b) Ti 2p peak (c) O 1s peak and (d) Ni 2p peak

Table 4.3: Surface elemental concentration, Ti, O and Ni species concentration from XPS analysis for NiO/TNTs (0.5 M)

Sample	Surface elemental concentration (atom%)					Ni (%)		O (%)		Ti (%)
	Ti	O	Ni	C	Ni/Ti	Ni^{2+}	Ni^{3+}	$O_{lattice}$	O_{absorb}	Ti^{4+}
NiO/TNTs (0.5 M)	21.44	56.91	1.82	19.83	0.08	62.46	37.54	94.25	5.75	100

Fig. 4.12 shows the solar-light-induced photocatalytic activity of the NiO/TNTs. The initial concentration (C_0) was the MB concentration after adsorption-desorption equilibrium. Regardless of NiO concentrations, almost similar percentage (50.8 to 51.7%) of dye removal was achieved under dark conditions, while control resulted in 43.25%. The brilliant adsorption capability was attributed to the large surface area of nanotubes, which enabled MB molecules to diffuse freely inside NiO/TNTs (Ahmed, 2012). The photocatalytic reactions of all samples followed pseudo first-order reaction kinetics, which is expressed by equation:

$$\ln\left(\frac{C}{C_0}\right) = -kt \tag{4.4}$$

where k is the first-order reaction constant, C_0 and C are the initial and the final concentrations of MB dye, respectively. The derived kinetic parameters and MB degradation efficiency are shown in Table 4.4, and the respective plots are illustrated in Fig. 4.13.

Table 4.4: Photodegradation of MB dye for studied samples under solar light irradiation

Sample	**MB degraded**[a] **$(C_0\text{-}C)/C_0$ (%)**	**k**[b] **(min^{-1})**
Control[c]	43.65	0.001
TNTs	68.35	0.002
NiO/TNTs (0.5 M)	86.11	0.004
NiO/TNTs (1.5 M)	86.18	0.004
NiO/TNTs (2.5 M)	86.29	0.004

[a] After reaction for 7.5 h

[b] Apparent rate constant deduced from linear fitting of $\ln(C/C_0)$ versus reaction time

[c] The control was the photolysis of MB dye

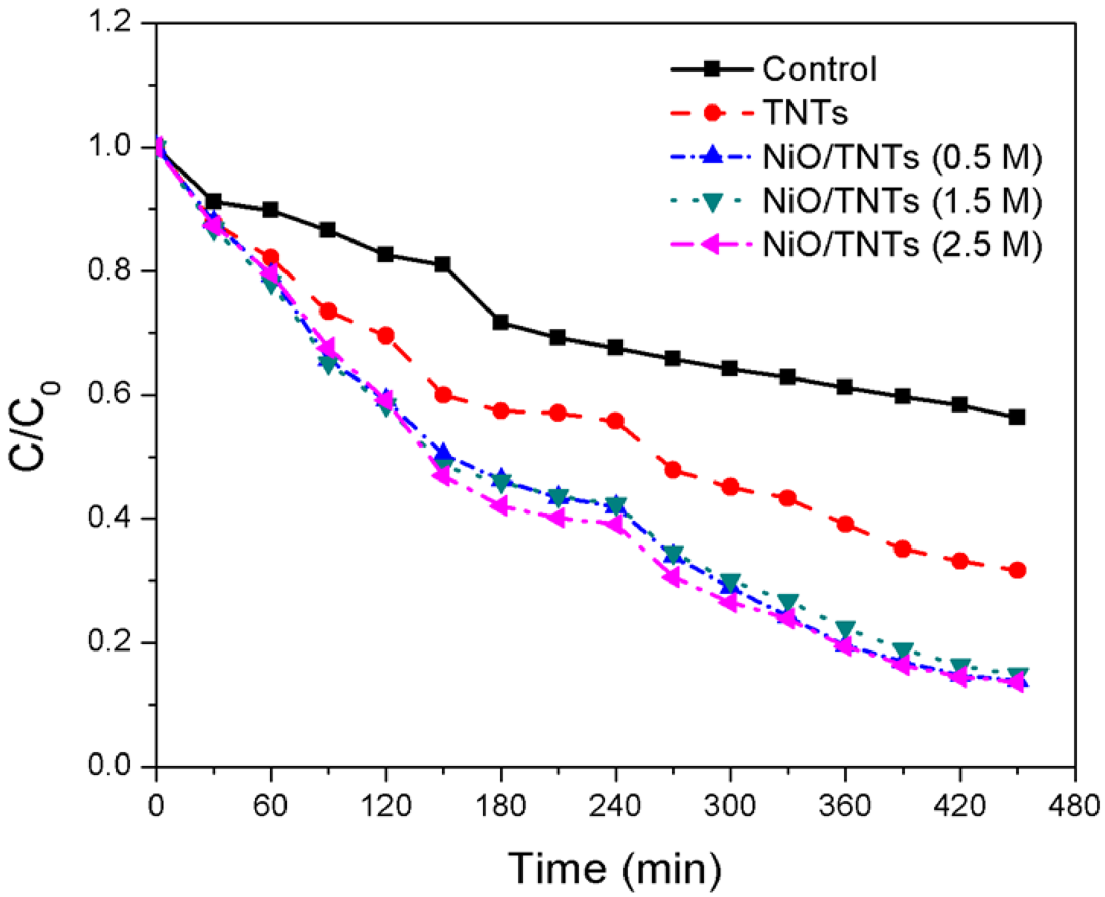

Figure 4.12: Photocatalytic degradation of MB over control, TNTs and NiO/TNTs with varying NiO concentrations under solar light irradiation

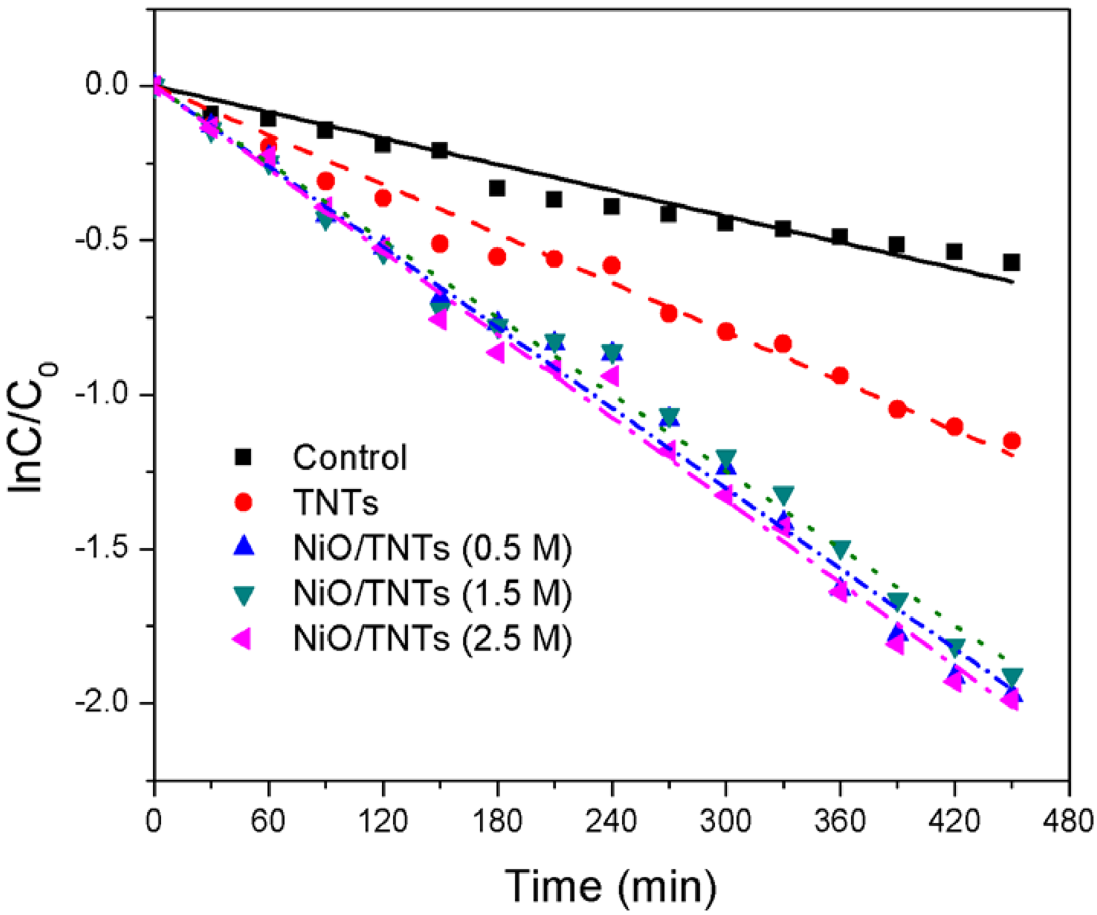

Figure 4.13: Kinetic plot over control, TNTs and NiO/TNTs with varying NiO concentrations under solar light irradiation

All mashed-up samples exhibited higher degradation efficiency than the control. The loading of NiO in TNTs resulted in a doubled reaction rate (0.004 min^{-1}) with 86% of MB removal than that of TNTs (k = 0.002 min^{-1}) with 68% MB removal. In the initial degradation phase of NiO/TNTs (2.5 M), a greater reaction rate was observed over the others (0.5 and 1.5 M). This could be attributed to the distinct hump observed in the diffuse reflectance spectra (Fig. 4.10) of NiO/TNTs (2.5 M). However, the solar-light-induced activities of all NiO/TNTs samples started to slow down and reached an identical MB degradation (86%) towards the end of reaction. The increase in degradation efficiency of NiO/TNTs was mainly due to the efficient electron-hole pairs separation and visible light absorption. The presence of NiO developed a p-n junction to separate electron-hole pairs effectively. While the enhancement of visible light absorption was due to the charge transfer transition from the electron donor levels formed by the 3d orbitals of substituted Ni^{2+} to the CB of TiO_2 (Niishiro et al., 2005). Further, Ni_2O_3 had a dark colour and it facilitated the absorption of visible light (Shrestha et al., 2010). The other contributing factor is the presence of Ni_2O_3 created Ni^{2+} vacancies in NiO that lowered the electrical resistance of NiO (Sasi and Gopchandran, 2007).

A competitive adsorption on the active sites between the reactant and the intermediate products declined the degradation rate towards the end of reaction (Konstantinou and Albanis, 2004). Hence, the accessibility of reactant to the active sites was deteriorated, resulting in a non-significant difference of degradation efficiency for all NiO/TNTs samples towards the end of the reaction. In addition, an almost similar Ni content in 0.5 M NiO/TNTs (0.8 wt%) and 1.5 M NiO/TNTs (1 wt%) could also result in a non-significant difference of degradation rate for both samples. Overall, it can be concluded that the loading of NiO effectively improved solar-light-induced photocatalytic activity. Though the sample with higher NiO concentration possessed better solar light absorption properties, it had no direct effect to the enhancement of photocatalytic activity.

The degradation mechanism of MB over NiO/TNTs and the effect of p-n junction are illustrated in Fig. 4.14. In presence of solar irradiation, the electrons were excited from VB of TiO_2 to the CB. As vindicated in crystalline phase and surface chemical analysis, key fragment of Ni^{2+} ions segregated as separate NiO NPs on the surface of TNTs whereas the remainder were incorporated substitutionally into TiO_2 lattice. When the segregated NiO NPs and TiO_2 integrated, a p-n-junction was formed between p-type NiO (p-NiO) and n-type TiO_2 (n-TiO_2). At the poise, a negative charge and positive charge was formed in between p-NiO and n-TiO_2 region, respectively.

When the p-n junction was stimulated by photons, the photogenerated holes jumped to VB of NiO NPs (negative field), while the electrons jumped to CB of TiO_2 (positive field) (Chen et al., 2008; Chen et al., 2005b). Therefore, the electrons on the TiO_2 surface were scavenged by the oxygen (O_2) adsorbed on TiO_2 surface or dissolved oxygen in MB solution to produce superoxide radical anion $^{\bullet}O_2^{-}$ (Konstantinou and Albanis, 2004). Meanwhile, the photogenerated holes in VB of NiO NPs oxidized the organic molecule in MB solution forming R^+, or reacting with OH^- or H_2O then oxidized to $^{\bullet}OH$ radicals. When Ti^{4+} in TiO_2 lattice was replaced with Ni^{2+}, the overlap of the CB of 3d level in Ti^{4+} with d-level of Ni ions (Mor et al., 2007) can induce the charge transfer transitions between Ni^{2+} d electrons and the CB of TiO_2 at lower band gap energy. Electron was excited at this lower energy level into TiO_2 CB and further reacted with O_2 adsorbed on TiO_2 surface, leading to the formation of $^{\bullet}OH$ radicals. The resulting robust oxidizing agent (standard redox potential +2.8 V) actively degraded MB dye.

In a summary, the presence of NiO well contributed for solar-light harvesting properties of TNTs, however MB degradation rate decelerated towards the end of reaction. The degradation efficiency of MB was found to be independent of NiO concentration. Therefore, another potential semiconductor, SnO_2 was examined for its potential to overcome the setback of NiO. The neglected influence of solar irradiation condition was also considered in the successive section.

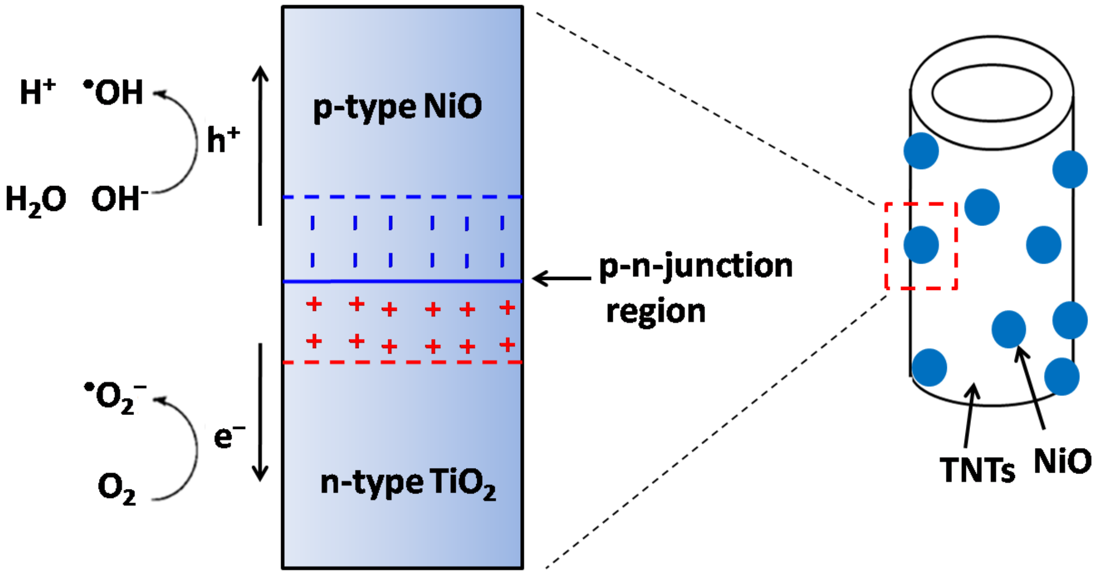

Figure 4.14: Schematic diagram of electron transport in NiO/TNTs photocatalyst under solar light irradiation

4.3 Mashing-up: SnO_2/TNTs Binary Semiconductor Composites

Nanosized SnO_2 was considered as mash-up material, anticipating the following pros derived from it: (i) the SnO_2 could lay a foundation for generation of Sn^{4+} species and could extend the photo-responding range, and (ii) SnO_2 NPs could serve as an electron collector to facilitate rapid separation of photogenerated charges before recombination. Thus attained material chemistry and photocatalytic performance of achieved SnO_2/TNTs composite is discussed below.

Fig. 4.15(a)-(c) portraits the various morphological images of SnO_2/TNTs captured at various SnO_2 loadings. It is apparent that variation in loading of SnO_2 did not either disintegrate the structure or cling on the openings of TNTs. The chemical characterization spectrum obtained from energy-dispersive X-ray spectroscopy (EDX) is displayed in Fig. 4.16 and demonstrated that prepared SnO_2/TNTs was a constituent of Sn, Ti and O. Its chemical characterization is tabulated in Table 4.5, reflecting the weight percentage of Sn in the samples ascended with the increased loading of SnO_2.

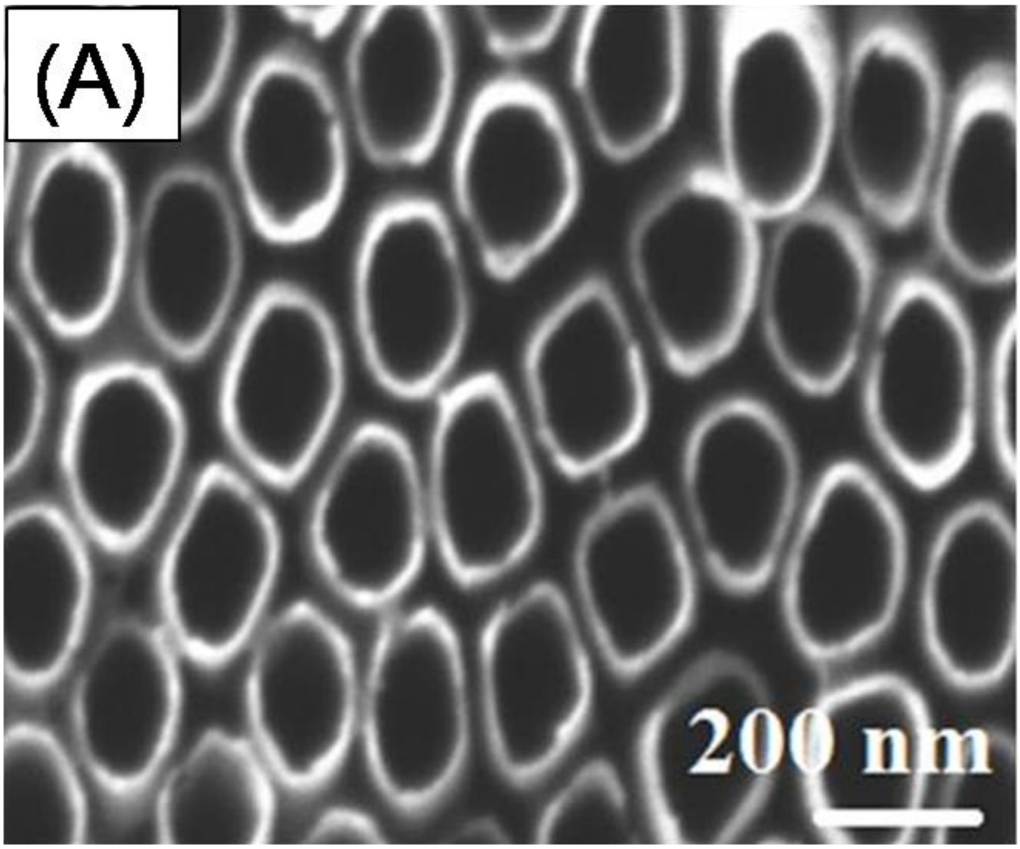
(A)
200 nm

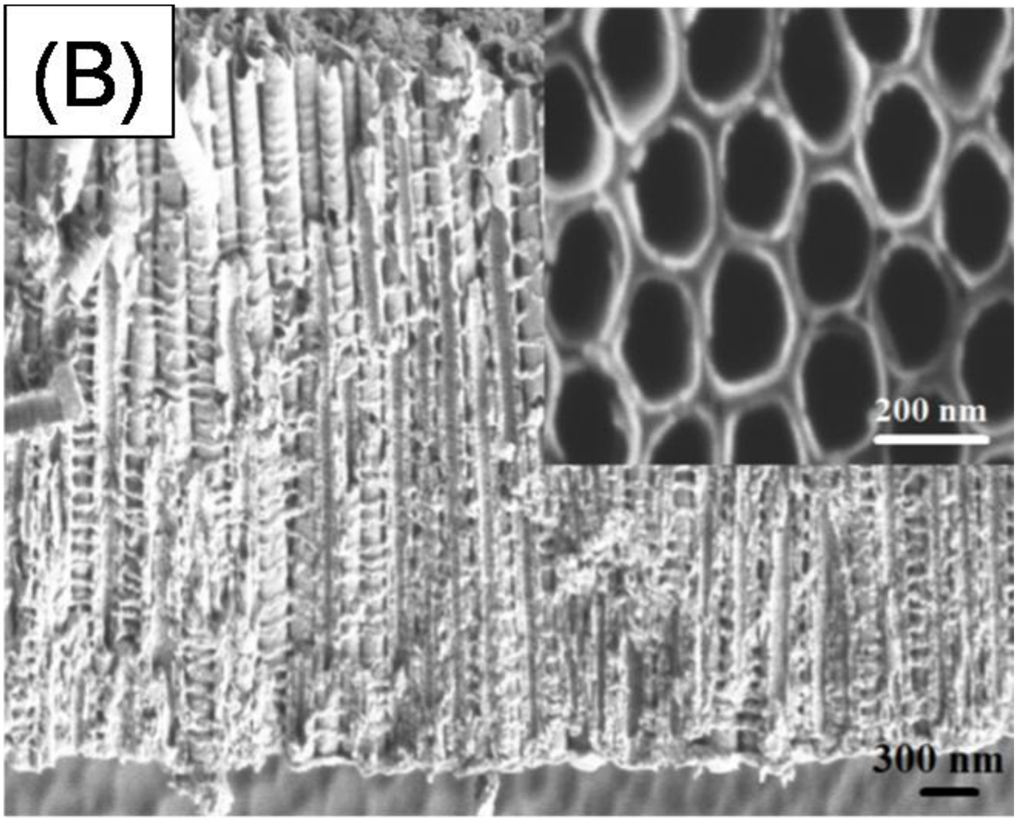
(B)
200 nm
300 nm

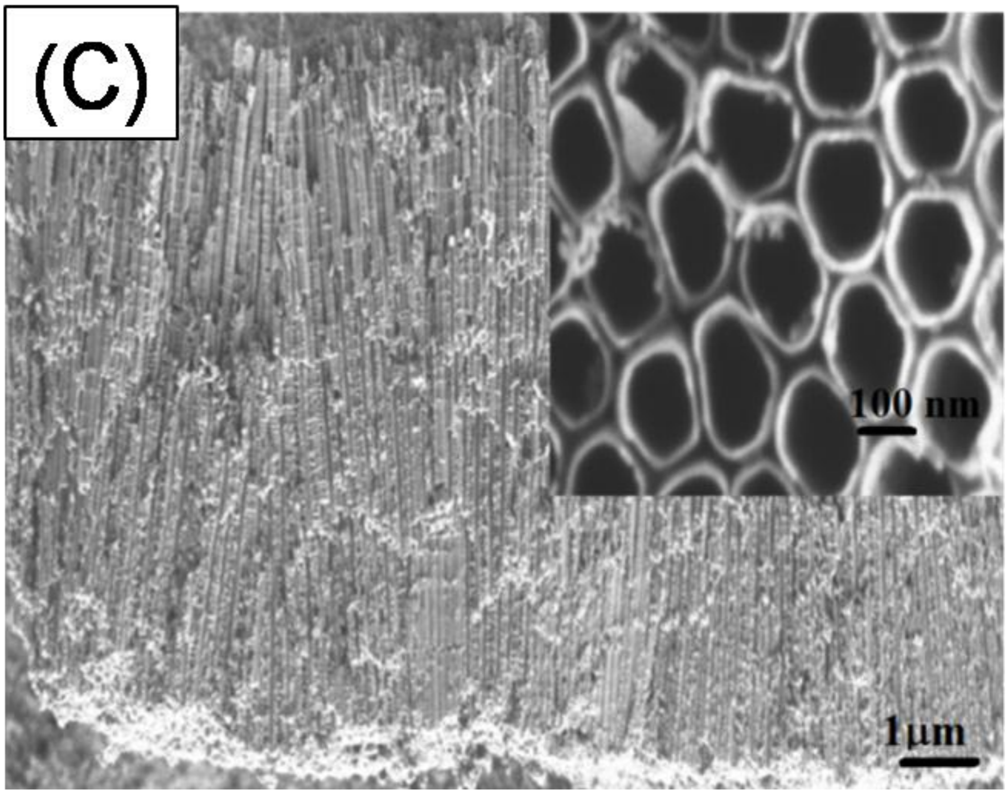

Figure 4.15: FESEM images of sample (a) top view of 1.59 Sn, cross-sectional view of (b) 2.25 Sn, and (c) 2.84 Sn. Insets show in (b) and (c) is the top view of 2.25 Sn and 2.84 Sn

Table 4.5: Elemental composition of TNTs, 1.59 Sn, 2.25 Sn and 2.84 Sn

	EDS		
	Elemental composition (wt%)		
Sample	**Ti**	**O**	**Sn**
TNTs	54.84	45.17	0
1.59 Sn	43	55.4	1.59
2.25 Sn	55.4	42.7	2.25
2.84 Sn	66.26	30.96	2.84

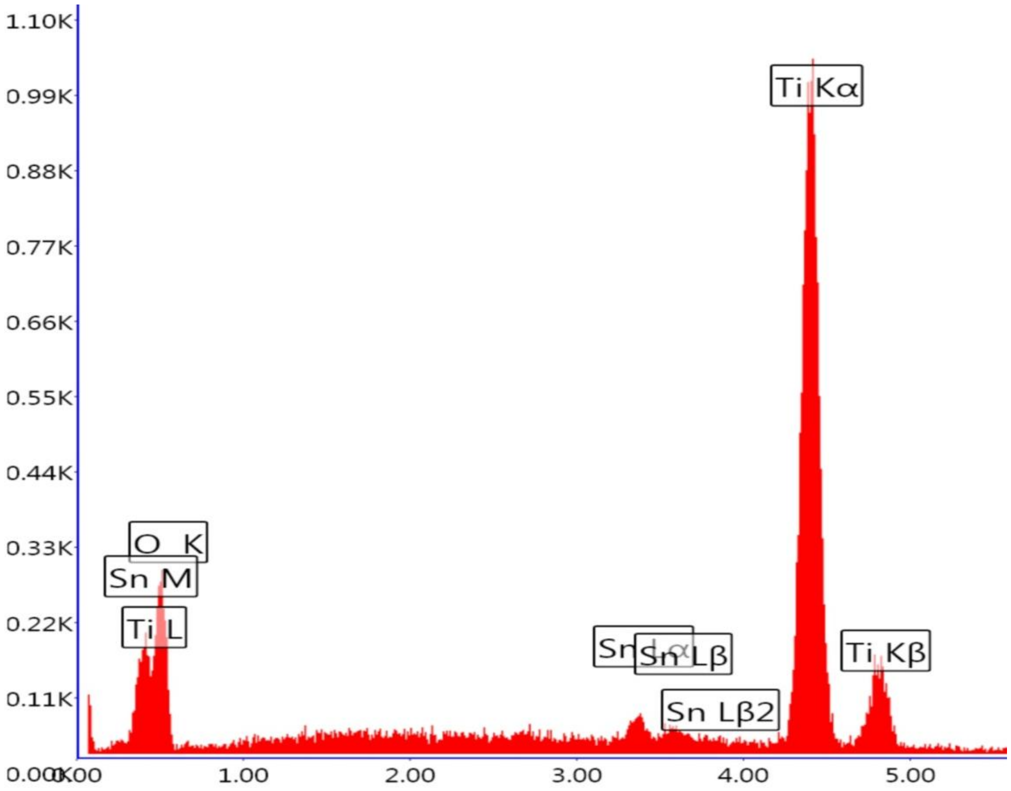

Figure 4.16: EDX of 1.59 Sn

The particles size ascribing SnO_2 as NPs and its loading onto the TNTs are clearly described through acquired HRTEM image shown in Fig. 4.17a. The loaded NPs were found to be ≤ 5 nm with uniform distribution. Clear evidence on crystallinity of TiO_2 and SnO_2 was spotted in Fig. 4.17a (inset) and Fig. 4.17b, respectively. The lattice fringes with 0.35 nm and 0.33 nm spacing are assigned to the (1 0 1) and (1 1 0) plane of anatase TiO_2 and SnO_2, respectively (Kang et al., 2008; He et al., 2006).

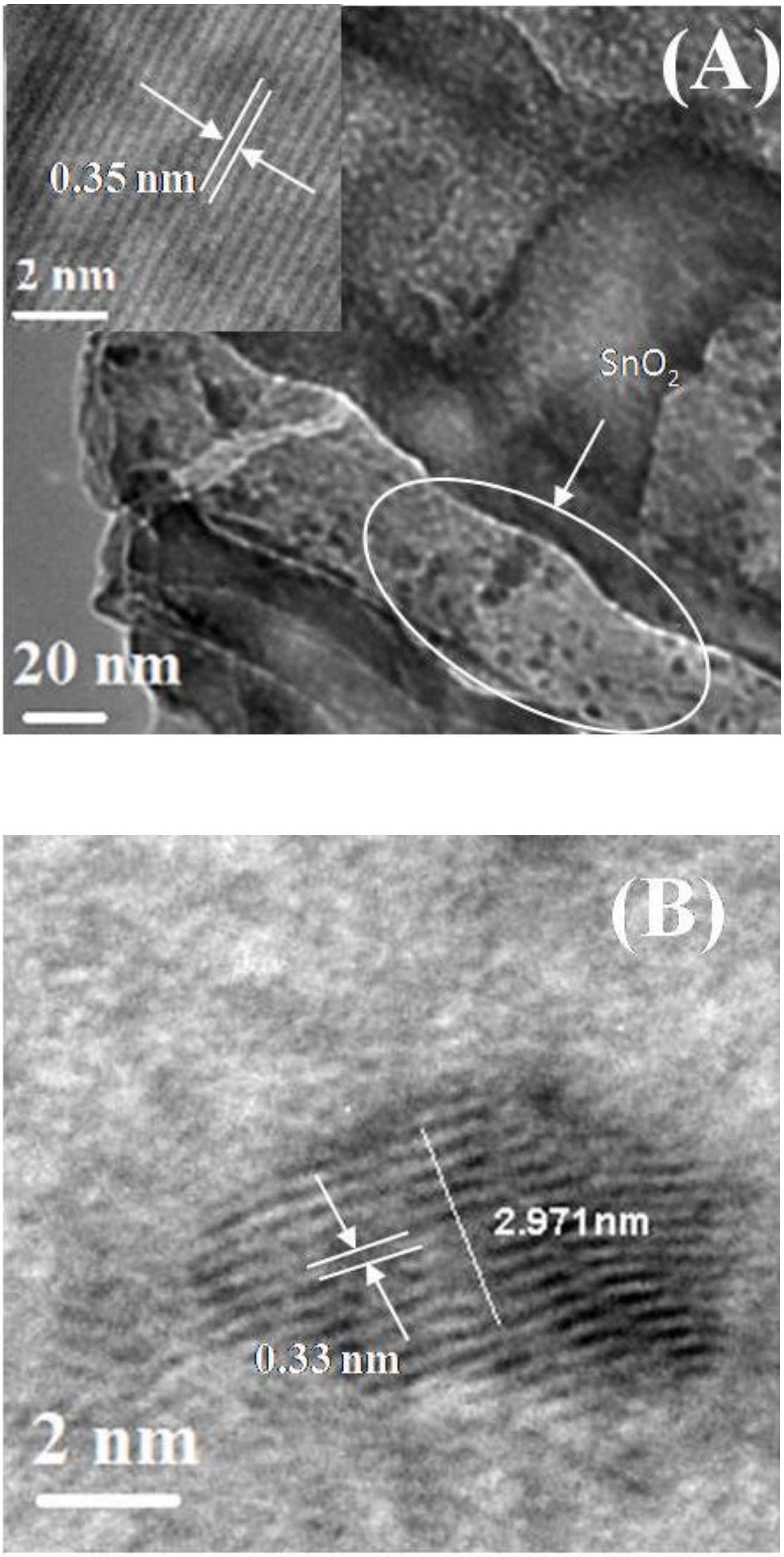

Figure 4.17: (a) HRTEM image of single nanotube loaded with SnO_2, and (b) HRTEM image of the circle area in (a). Inset shows the HRTEM image of pure TNTs

The diffraction patterns of the obtained samples are shown in Fig. 4.18. The prepared samples exhibited diffractions that were denoted to anatase phase. This clearly implies that the loading of SnO_2 never influenced the phase changes. The evident peaks of tetragonal TiO_2 anatase phase (JCPDS no. 21-1272) were noticed at 25.3°, 36.9°, 37.8°, 48.0°, 53.9°, 55.1°, 62.7°, 68.8° and 75.0°, corresponding to (1 0 1), (1 0 3), (0 0 4), (2 0 0), (1 0 5), (2 1 1), (2 0 4), (1 1 6) and (2 1 5) crystal planes, respectively. As seen in the samples of previous section, the crystalline phase of SnO_2 with adopted loading was also not captured in phase analysis. This was owing to high dispersion of SnO_2 NPs in TNTs in relatively insignificant concentration (Sakthivel et al., 2004; Ku et al., 2011). The calculated average crystallite sizes of TiO_2 anatase are reported in Table 4.6.

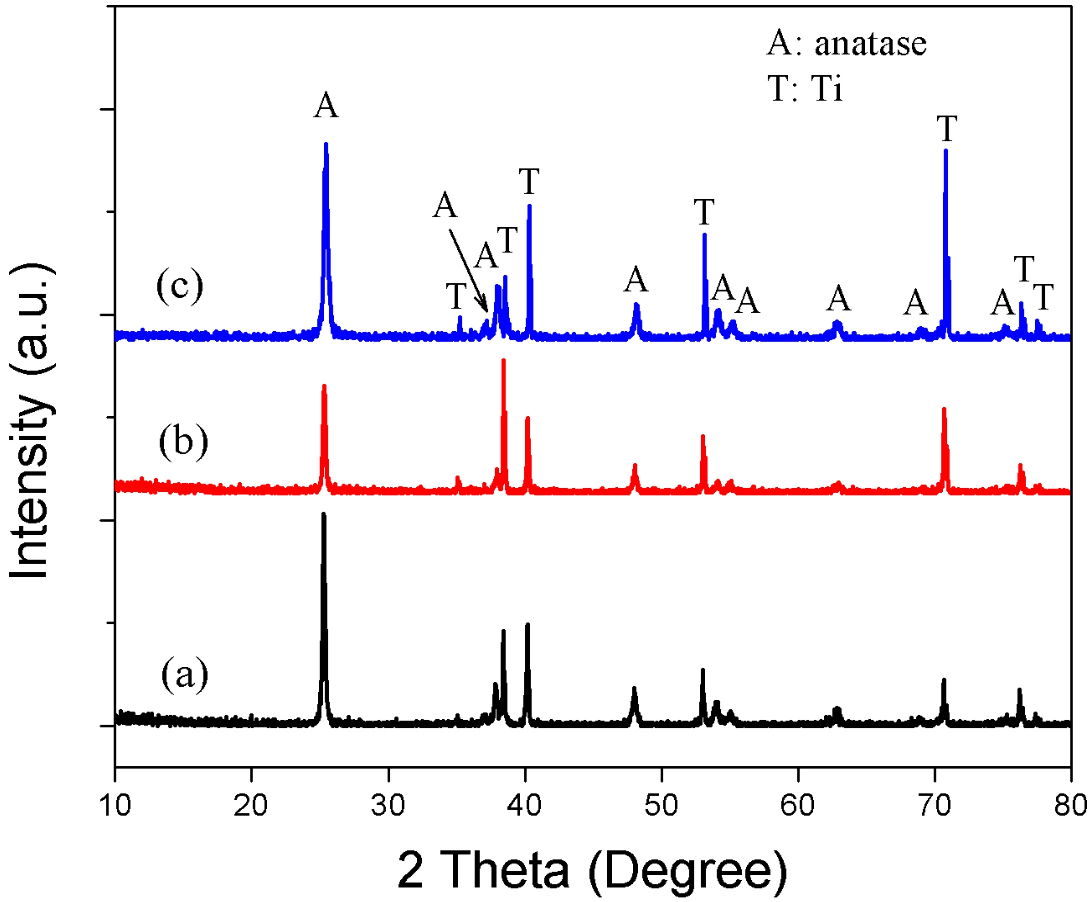

Figure 4.18: X-ray diffraction pattern of photocatalysts (a: TNTs; b: 1.59 Sn; c: 2.84 Sn)

Table 4.6: Calculated average crystallite size and lattice parameters for TNTs, 1.59 Sn and 2.84 Sn

Sample	**Crystallite size (nm)[a]**	**Cell parameters a=b, c (Å)[b]**
TNTs	34.50	3.7868, 9.5102
1.59 Sn	33.35	3.7863, 9.4308
2.84 Sn	25.00	3.7764, 9.3196

[a] Measured by (Eq. 4.1)
[b] Estimated according to (Eq. 4.2) and (Eq. 4.3)

It was well observed that lattice parameters and crystallite size of TiO_2 decreased with increased SnO_2 concentration. As seen in Fig. 4.19, a notable shift was observed at (1 0 1) towards higher angles with increasing loading level of SnO_2 and further altered the lattice parameters. In addition, SnO_2/TNTs exhibited lower anatase peak intensity than that of TNTs due to the lower crystallinity in titania discouraged by SnO_2 loading. This anomaly was owing to the replacement of Ti^{4+} (r_{ion}= 0.68 Å) with Sn^{4+} (r_{ion}= 0.69 Å) that possessed the similar ionic radii. The SnO_2 protagonised as an intercalation caused structural strain and disorder in TiO_2 crystalline lattice, inhibited crystal growth and descended the crystallite size of TiO_2 (Singhal et al., 2010; Santara et al., 2011).

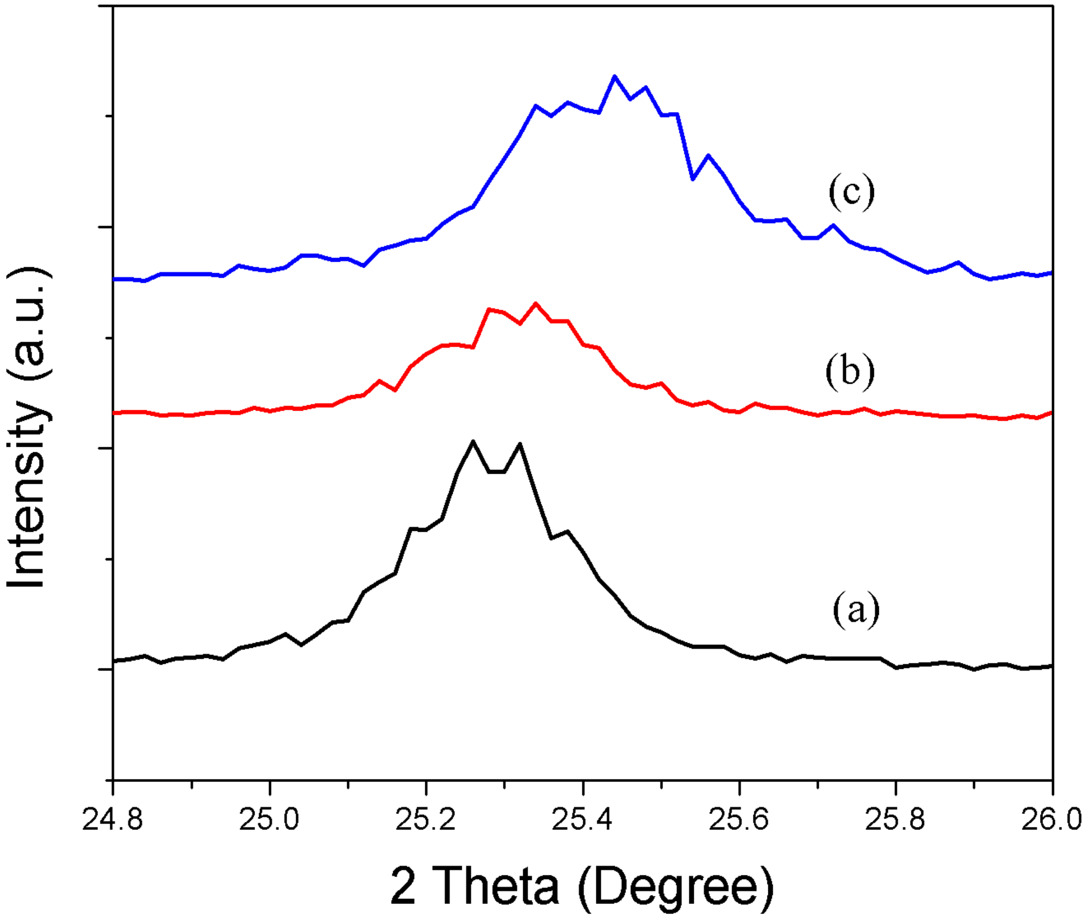

Figure 4.19: Enlarged region of XRD peak in a range of 24.8– 26 °(a: TNTs; b: 1.59 Sn; c: 2.84 Sn)

Fig. 4.20 illustrates the light harvesting properties through diffuse reflectance spectra (DRS) for prepared photocatalysts. Unfortunately, the sample with lower SnO_2 concentration (1.59 Sn) replicated a similar trend as shown by TNTs, whereas both of 2.25 and 2.84 Sn greatly stimulated towards visible region. The stimulation was appreciated by doping energy level of Sn^{4+} located below the CB of TNTs that assisted charge-transfer between them (Wang et al., 2011a). Though the semiconductor loading in both cases promoted visible light shift, the obtained inference prickled the analysis to move other way round by calculating the band gap energy.

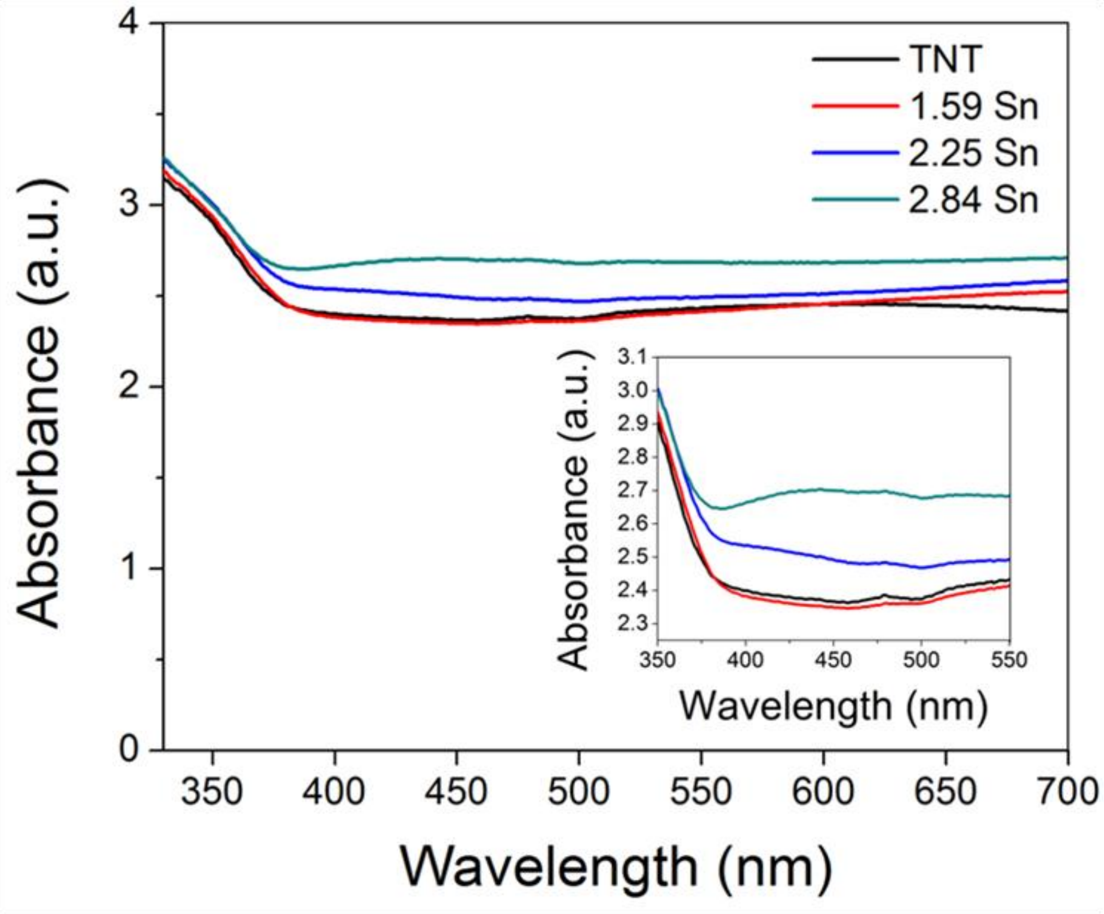

Figure 4.20: UV-visible absorption spectra of TNTs, 1.59 Sn, 2.25 Sn and 2.84 Sn. Inset shows the enlarged region of wavelength in a range of 340−700 nm

This band gap calculation was ratified through Tauc plot, a method that is accredited for its determination. It was obtained by plotting (F(R). hν)$^{1/2}$ against hν, where Kubelka-Munck function F(R) is derived from equation as below:

$$F(R) = (1-R)^2 / 2R \tag{4.5}$$

where R is diffuse reflectance, and hν is the photon energy. The band gap energies were determined by extrapolating the maximum slope of the curve to the photon energy axis. The obtained plot along with the calculated band gap energy is shown in Fig. 4.21. This obtained band gap energy was in consistent with the optical shift seen in the inset of Fig. 4.20, where the lower shift had a higher band gap while the higher shift resulted in narrower band gap energy. Therefore, it is well evident that the optical shift towards visible region plays pivotal role in narrowing the band gap energy.

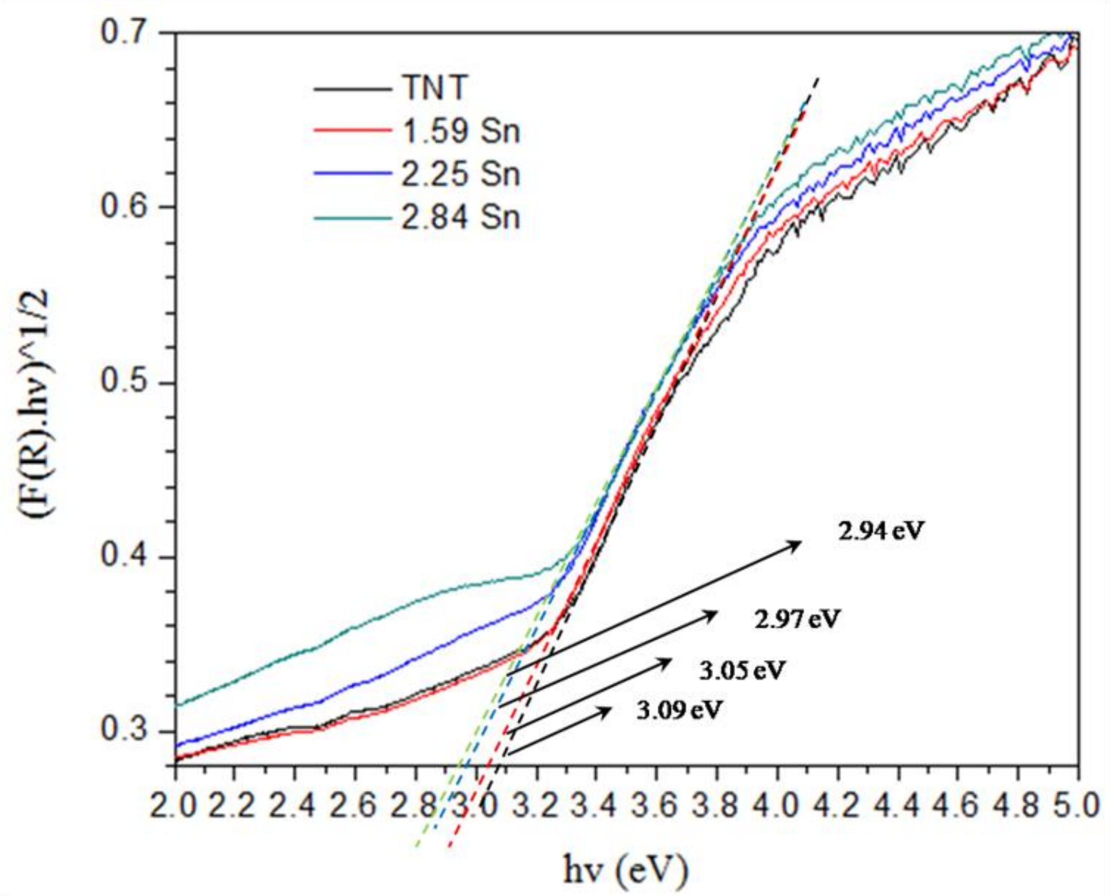

Figure 4.21: Tauc plots of TNTs, 1.59 Sn, 2.25 Sn and 2.84 Sn

The analysis was then extended to Raman spectroscopy with specific samples and the obtained spectra with shifts are illustrated in Fig. 4.22. The intention in performing this analysis is to confirm the occurrence of phase change arisen by SnO_2 loading. All the perceived peaks for both TNTs and 1.59 Sn at 144, 197, 399, 519 and 639 cm^{-1} were assigned to $E_{g(1)}$, $E_{g(2)}$, $B_{1g(1)}$, A_{1g} $B_{1g(2)}$ and $E_{g(3)}$ modes of the anatase phase, respectively (Ohsaka et al., 1979). This result was consistent with crystallographic patterns and confirmed the formation of a bulk anatase phase after annealing treatment. Those peaks related to SnO_2 or other oxidation state of Sn was not detected in the spectra of SnO_2/TNTs samples. This specified the high dispersion of SnO_2 on TiO_2 surface (Xiaoyuan et al., 2008) which corresponded to the XRD inference. The E_g mode of anatase (144 cm^{-1}) (inset, Fig. 4.22) in 1.59 Sn exhibited lower and broader peak, further it red shifted to higher frequency region. Besides, few broader peaks were also observed at 399, 519 and 639 cm^{-1} in this sample. This occurrence was due to the breakdown of long-range translational crystal symmetry induced by Sn^{4+} substitution defects (Pal et al., 2012).

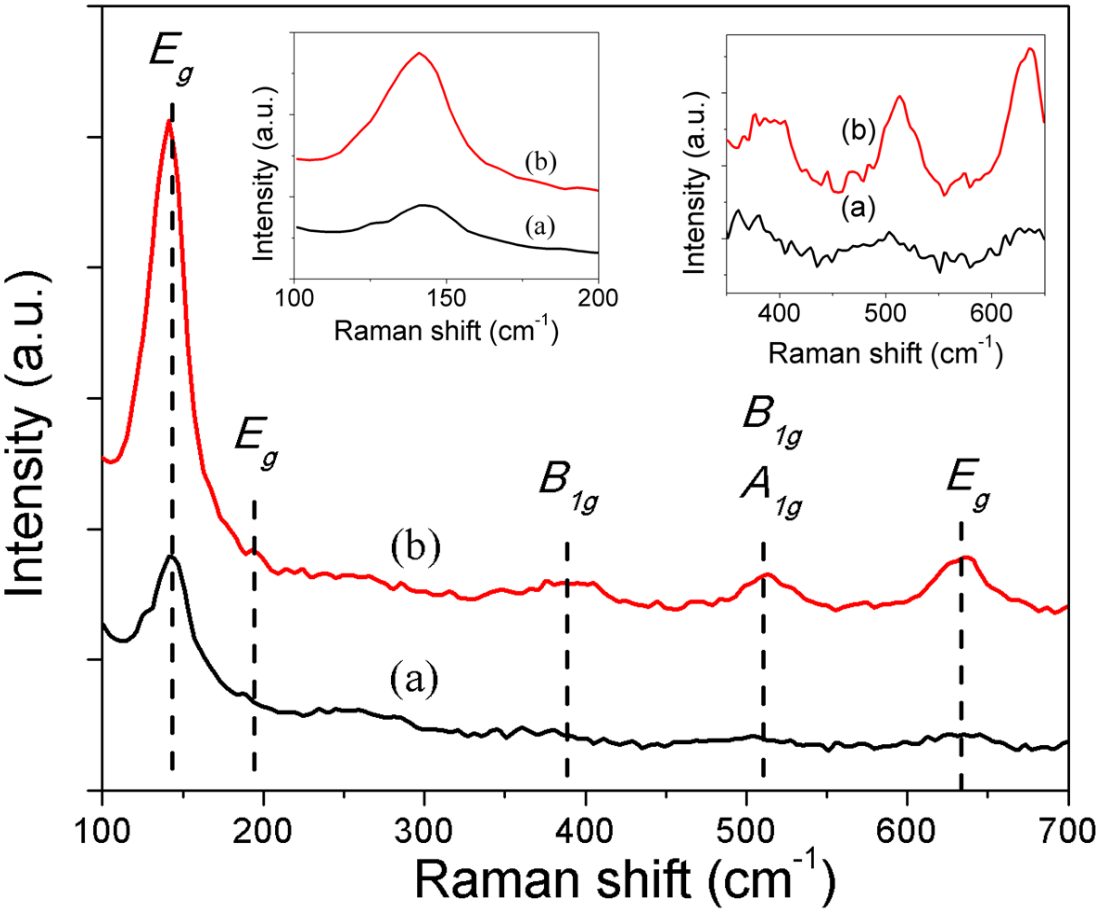

Figure 4.22: Raman spectra of (a) 1.59 Sn (b) TNTs. Insets show the enlarged region of Raman shift in a range of 100–200 cm^{-1} and 350–650 cm^{-1}

Fig. 4.23a displays the wide-scan spectra obtained from mono-energetic X-rays causing photoelectrons emitted from the sample surface. The recorded spectra symbolized the presence of Ti, O, C and Sn elements in the SnO_2/TNTs. A high-resolution XPS shown in Fig. 4.23b depicts O 1s core level between 520 and 540 eV was fitted to trival chemical states. The peaks at 529.9, 531.3 and 532.8 eV were assigned to crystal lattice oxygen of Ti-O, Sn-O and adsorbed water, respectively. Sn $3d_{5/2}$ peak was found at 486.1 eV and the Sn $3d_{3/2}$ peak was seen at 494.5 eV as conveyed in Fig. 4.23c. The splitting of Sn 3d doublet at 8.41 eV confirmed the valence state of Sn is +4. Fig. 4.23d reveals the presence of binary peaks at 458.1 eV (Ti $2p_{3/2}$) and 463.9 eV (Ti $2p_{1/2}$), corresponded to Ti^{4+}. The non-stoichiometric nature of TiO_2

(Ti^{4+}) surface was ascertained by the presence of TiO (Ti^{2+}) and Ti_2O_3 (Ti^{3+}) peaks. The presence of Ti^{2+} was detected at peak 460 eV. The two shoulder like peaks with lower binding energy on Ti $2p_{3/2}$ (456.9 eV) and Ti $2p_{1/2}$ (462.2 eV) were assigned to Ti^{3+}, generated from the replacement of Ti^{4+} (0.68 Å) by Sn^{4+} (0.69 Å) with similar ionic radii, leading to stoichiometry changes in TiO_2 lattice.

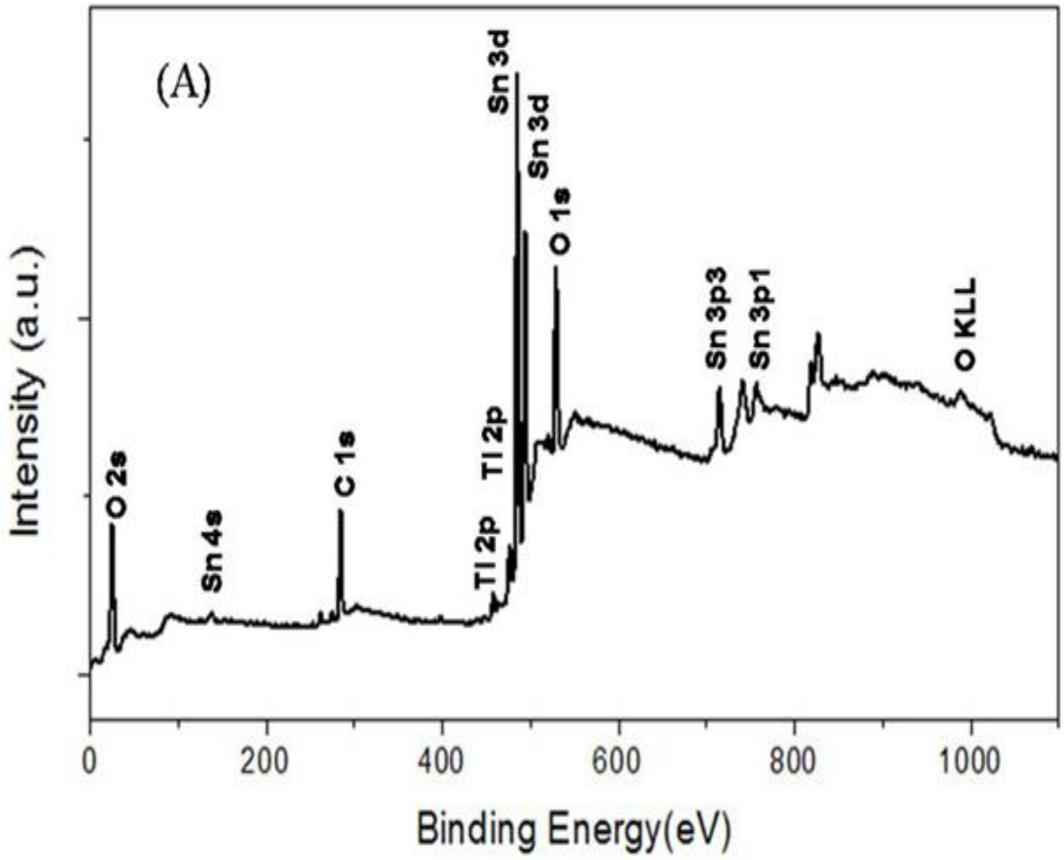

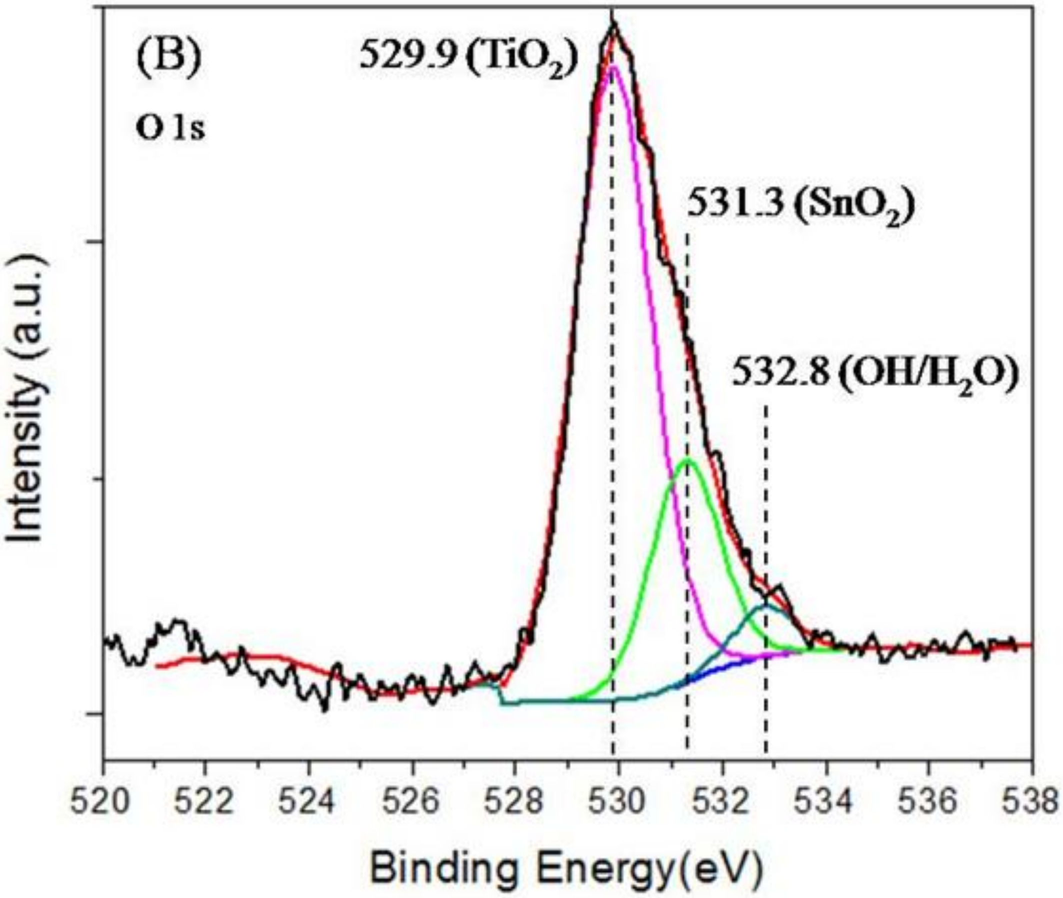
(B)
O 1s
529.9 (TiO$_2$)
531.3 (SnO$_2$)
532.8 (OH/H$_2$O)
Intensity (a.u.)
520
522
524
526
528
530
532
534
536
538
Binding Energy(eV)

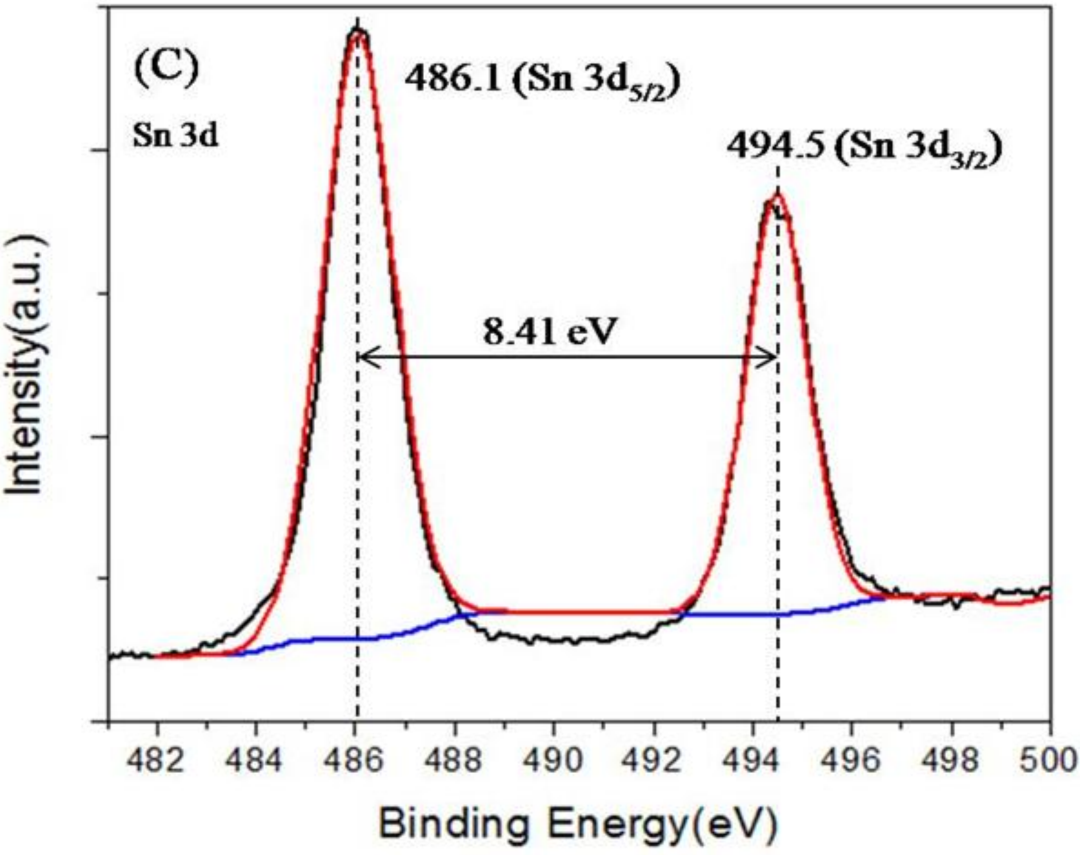
(C)
Sn 3d
486.1 (Sn 3d$_{5/2}$)
494.5 (Sn 3d$_{3/2}$)
8.41 eV
Intensity(a.u.)
482
484
486
488
490
492
494
496
498
500
Binding Energy(eV)

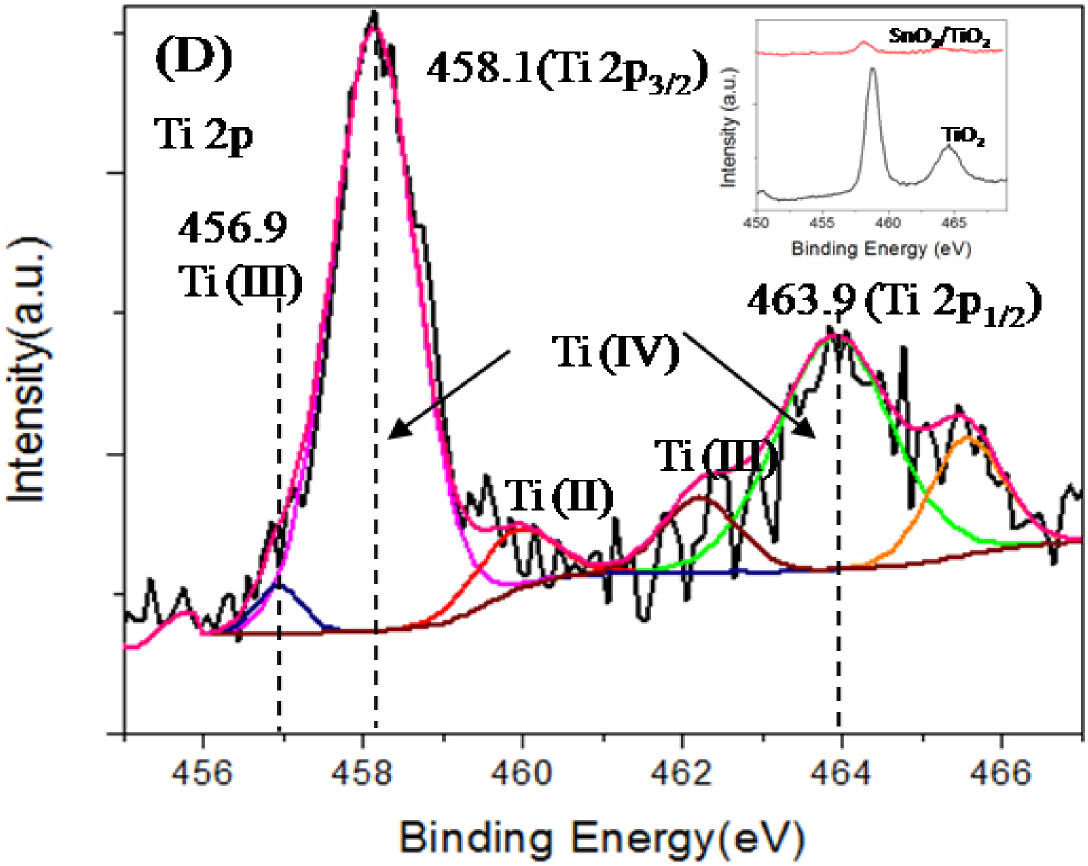

Figure 4.23: XPS spectra of 1.59 Sn (a) fully scanned spectra (b) O 1s peak (c) Sn 3d peak (d) Ti 2p peak. Inset in (d) shows the enlarged region of binding energy in a range of 450–470 eV

Interestingly, the binding energies for Ti $2p_{3/2}$ and Ti $2p_{1/2}$ shifted towards lower side with the substitution of Sn^{4+} compared to that of pure TNTs (inset, Fig. 4.23d). This phenomenon was interrelated to the existence of Ti with lower valence (Ti^{2+}, Ti^{3+}) arisen from the oxygen vacancies after SnO_2 loading (Kaleji and Sarraf-Mamoory, 2012). These XPS results also in agreement with XRD results (Fig. 4.19) which showed SnO_2/TNTs samples shifted towards higher angle compared to that of TNTs. Both results confirmed that SnO_2 was successfully loaded in TiO_2 lattice in substitution mode and accompanied by oxygen vacancy formation which contributed to the visible responsive (Xiong et al., 2012) and electron-hole pairs separation (Xiao et al., 2011).

The photocatalytic activity of fabricated SnO_2/TNTs samples was evaluated by degrading MB dye under solar irradiation at clear sky condition shown in Fig. 4.24. The initial concentration (C_0) was considered as the MB concentration after adsorption-desorption equilibrium. In the dark reaction, all SnO_2/TNTs samples irrespective of SnO_2 concentration exhibited an excellent adsorption capacity of ~40%. Since the photocatalytic principle is dependent on the surface phenomena, such good adsorption property could facilitate the enhancement of photocatalytic performance in the presence of solar light. The blank experiment in the absence of photocatalyst achieved 46.5% of dye removal through sensitization effect of dye. The photocatalytic reactions for all samples followed pseudo first-order reaction kinetics (Eq. 4.4). The kinetic plot and photocatalytic results are depicted in Fig. 4.25 and Table 4.7, respectively.

Table 4.7: MB solar photodegradation efficiency and derived kinetics

Sample	**MB degraded**[a] **(C_0-C)/C_0 (%)**	**k**[b] **(min^{-1})**
Control[c]	46.5	0.002
TNTs	65.4	0.003
1.59 Sn	84.0	0.005
2.25 Sn	84.2	0.005
2.84 Sn	84.0	0.005

[a] After reaction for 6 h

[b] Apparent rate constant deduced from linear fitting of ln(C/C_0) versus reaction time

[c] The control was the photolysis of MB dye

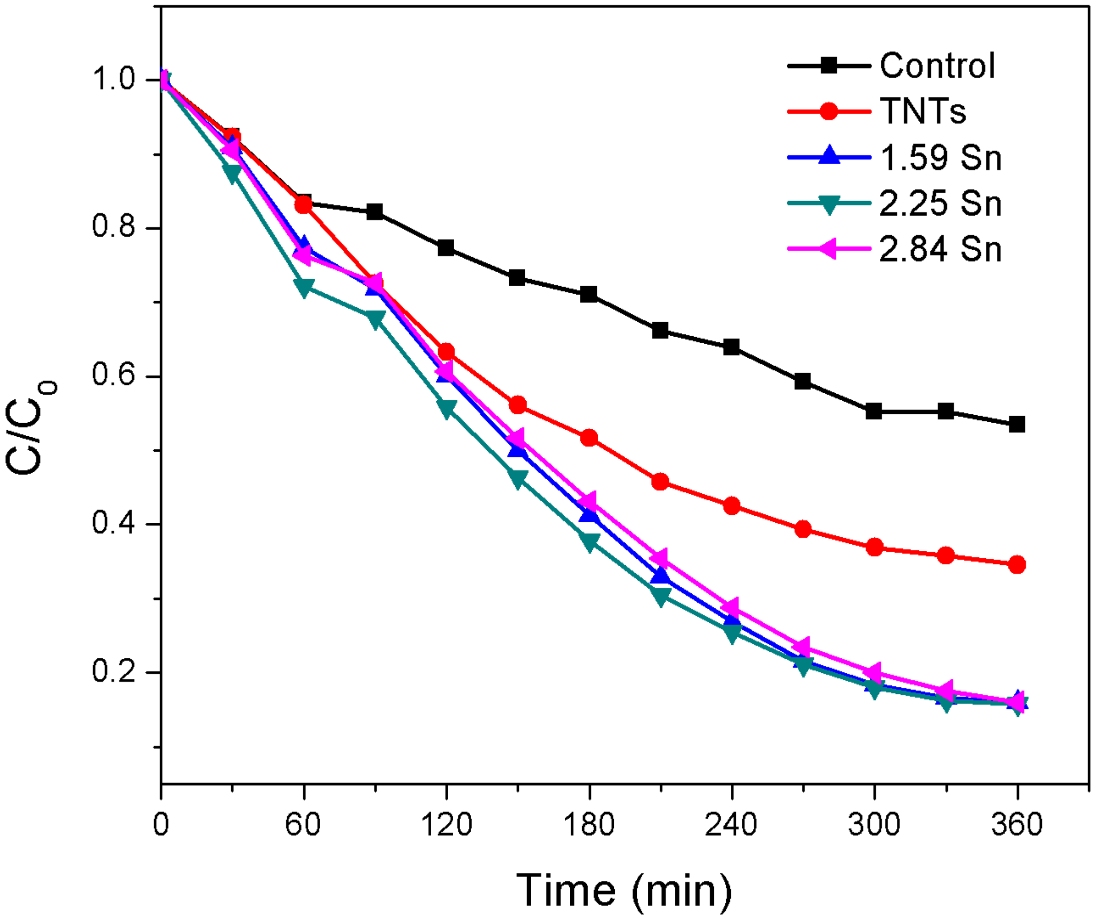

Figure 4.24: Solar photocatalytic degradation of MB as a function of reaction time

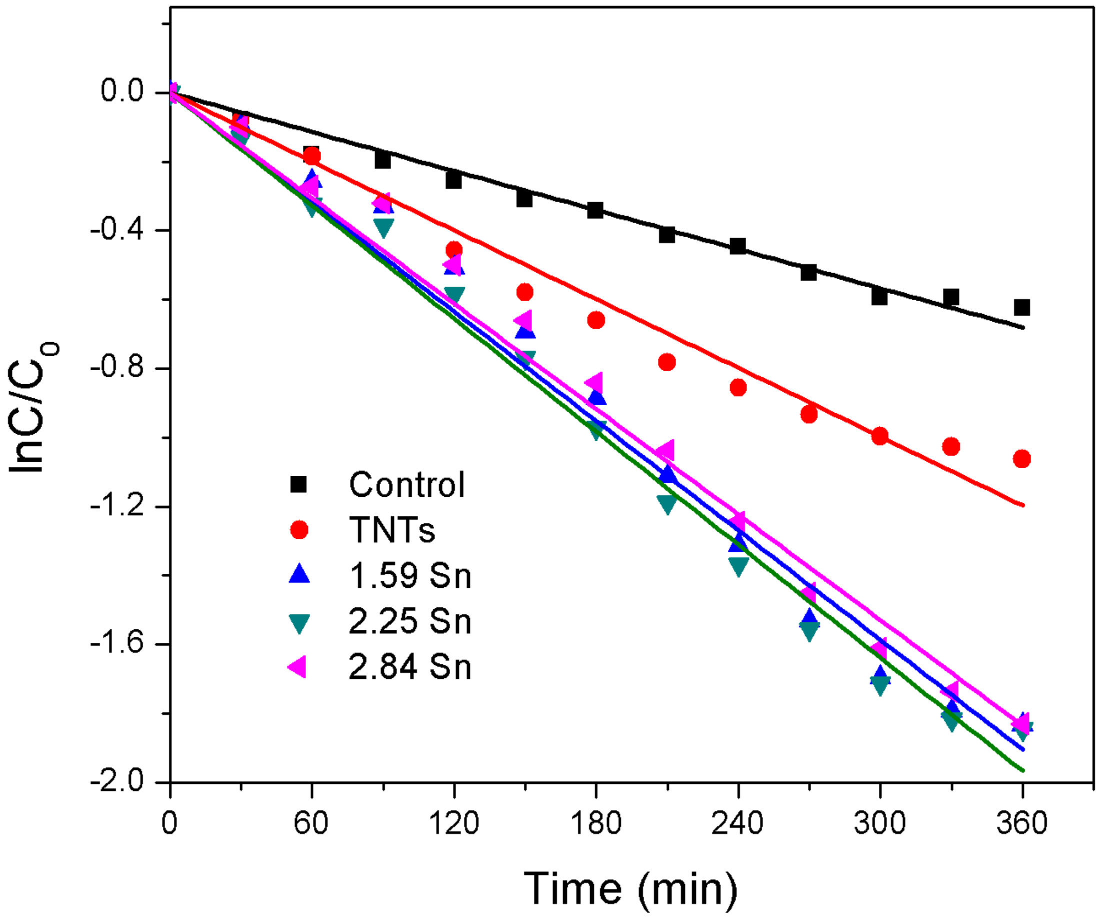

Figure 4.25: Corresponding variation of ln(C/C$_0$) with degradation time

The loading of SnO_2 in TNTs drastically ascended the photodegradation efficiency of MB over TNTs. In the initial phase of degradation reaction, Sn with 2.25 achieved higher MB removal rate compared to that of 1.59 Sn. However, degradation efficiency competence of both 1.59 Sn and 2.25 Sn plunged and reached nearly identical degradation efficiency (84%) after 210 min of reaction time. This was again contributed by a competitive adsorption on the active sites between the reactant and the intermediate products and thus affecting the accessibility of reactant to the active sites (Konstantinou and Albanis, 2004). This led to an insignificant difference of degradation efficiency for all mashed-up samples. It is noteworthy that step-up of SnO_2 loading to 2.84 wt% did not result in appreciable degradation efficiency instead they exhibited a vice versa efficiency than that of those samples with lower SnO_2 concentrations (1.59 and 2.25).

The deposition of SnO_2 on TNTs sowed a space charge layer that played a pivotal role in separation of photoinduced electron-hole pairs. Further increase in the concentration of SnO_2, the surface barriers surged and the electron-hole pairs within the region were efficiently separated by the electric field. But when in excess, the existence of SnO_2 particles on the TiO_2 surface blocked the active sites of TiO_2 and diminished the adsorption of reactant. It housed the recombination centers of photoinduced electron-hole pairs (Huang et al., 2012) and thereby deteriorated the photocatalytic activity.

The influence of sky conditions on the MB degradation efficiency and the kinetic plots are shown in Fig. 4.26 and Fig. 4.27(a-c), respectively. As shown in Fig. 4.27(a-c), all photodegradation process under various light intensity followed apparent first-order kinetics. The highest dye removal was observed for the clear sky weather condition, with 84% degradation efficiency and reaction rate of 0.005 min^{-1}. The efficiency fell to 78.8% ($k = 0.004$ min^{-1}) and 73% ($k = 0.003$ min^{-1}) at partly cloudy and cloudy sky condition, respectively. Thus reveals the robust influence of irradiation conditions on degradation efficiency of solar driven photocatalysis.

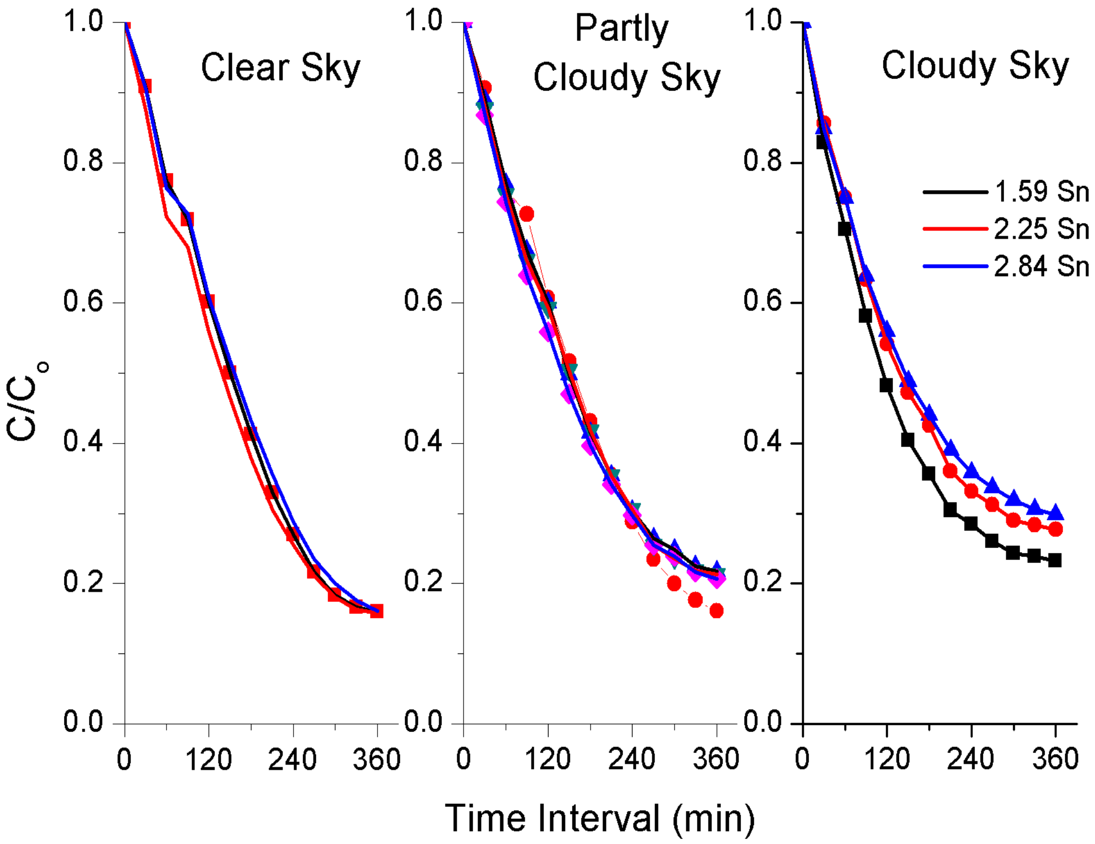

Figure 4.26: Solar photocatalytic degradation profile of MB against time recorded for the samples with influence of sky conditions

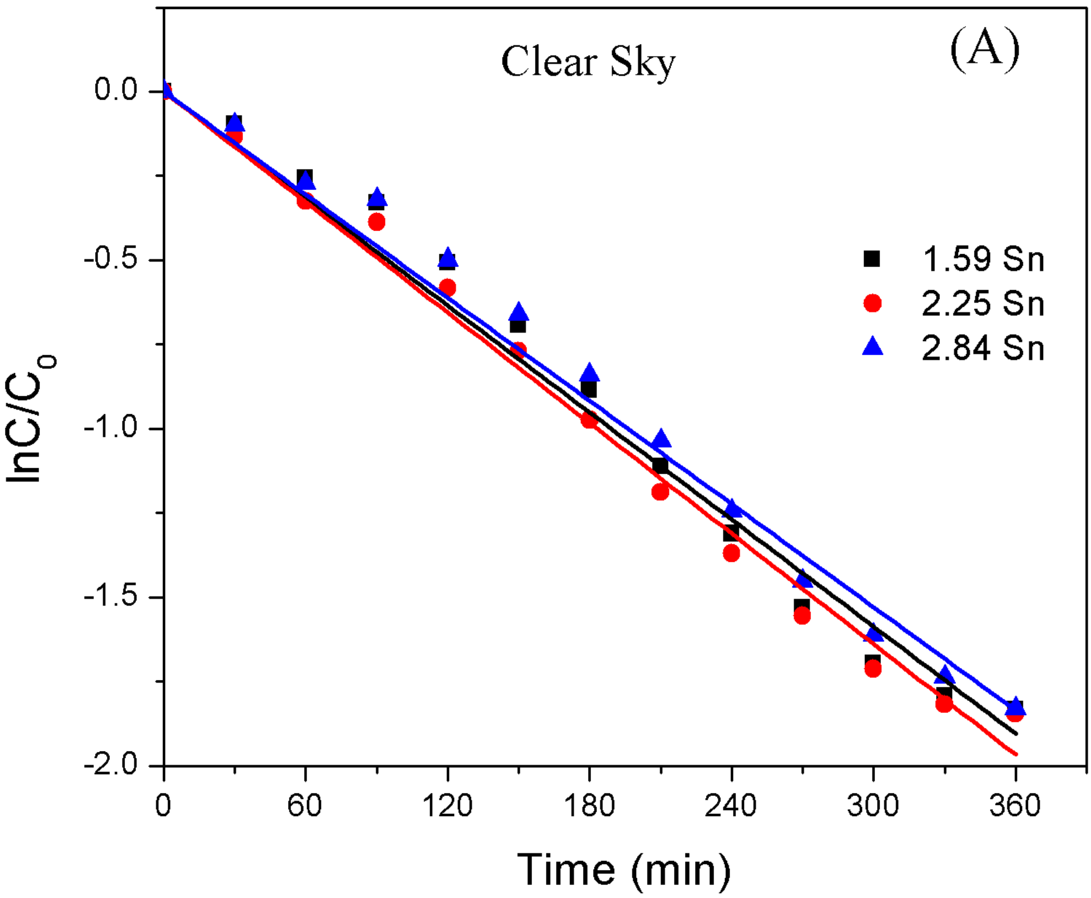
Clear Sky
(A)
1.59 Sn
2.25 Sn
2.84 Sn
lnC/C$_0$
0.0
-0.5
-1.0
-1.5
-2.0
0
60
120
180
240
300
360
Time (min)

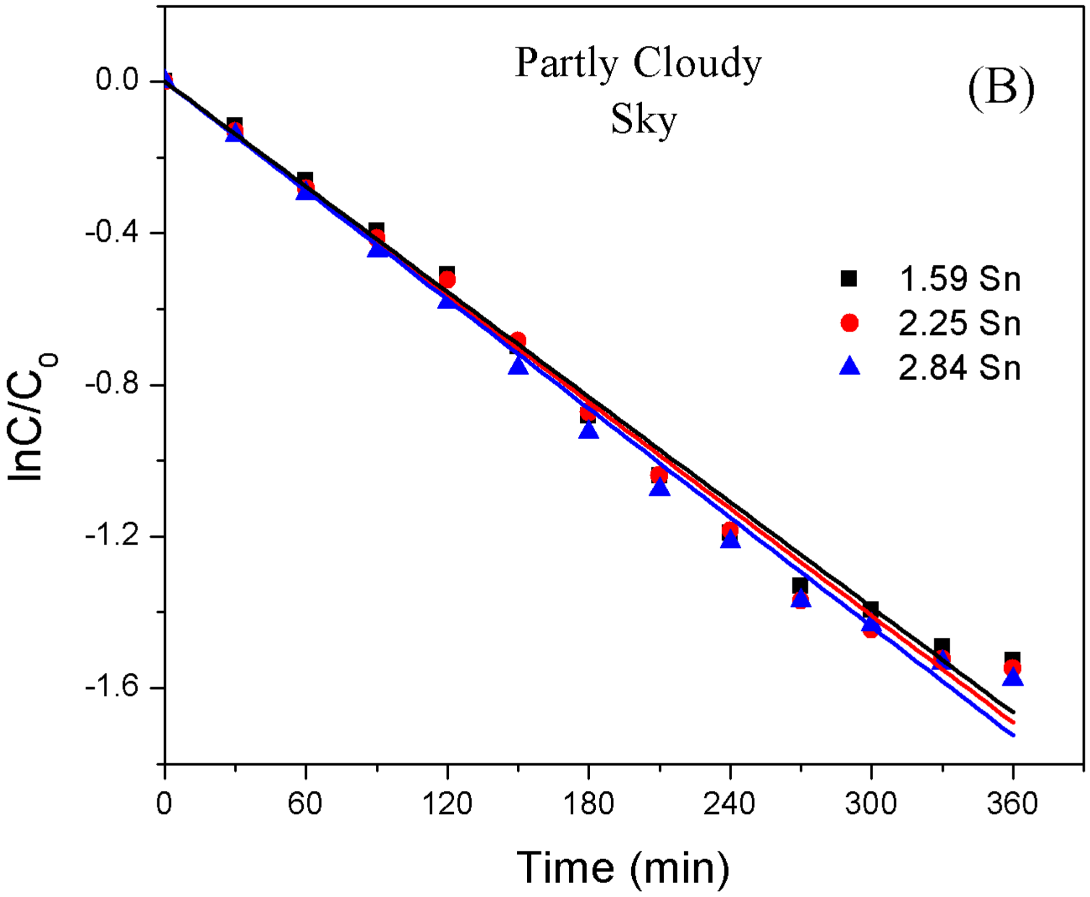
Partly Cloudy Sky
(B)
1.59 Sn
2.25 Sn
2.84 Sn
lnC/C$_0$
0.0
-0.4
-0.8
-1.2
-1.6
0
60
120
180
240
300
360
Time (min)

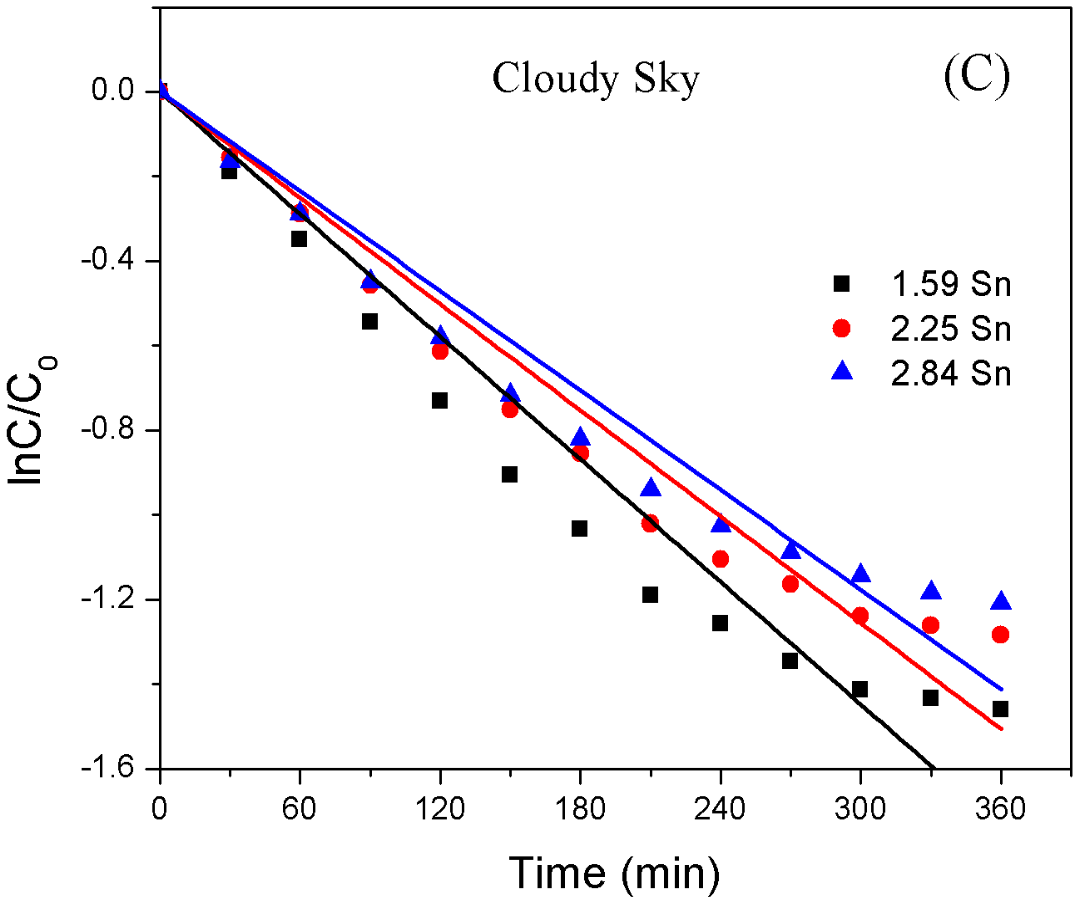

Figure 4.27: (a-c) Kinetic fit of MB as a function of degradation time

The proposed degradation mechanism of MB over SnO_2/TNTs is illustrated in Fig. 4.28. The Sn^{4+} ions obtained from the SnO_2 were incorporated into TiO_2 lattice in substitution mode and created Sn^{4+} doping energy level located at 0.4 eV below the CB of TNTs (Wang et al., 2011a). When TNTs was irradiated with solar light, the excited electrons transferred from VB of TNTs to Sn^{4+} doping energy level. Meanwhile the excited electron at the CB of TNTs could also fall into Sn^{4+} doping energy level (Cao et al., 2004). The CB of SnO_2 (E_{CB} = 0 V) was lower than that of the TiO_2 (E_{CB} = -0.5 V) (Vinodgopal and Kamat, 1995) and thus promoting the electron transfer from CB of TNTs to SnO_2. Besides, SnO_2 also trapped electrons injected from the photoexcited MB (MB*) due to the lower CB of SnO_2 compared to that of the working function of excited MB. Thus, SnO_2 served as an electron reservoir for the reduction process with oxidant.

The O_2 adsorbed on TNTs surface or dissolved in water was reduced by the electrons trapped at Sn^{4+} doping energy level and CB of SnO_2 to produce superoxide radical anion $^{\bullet}O_2^{-}$. The holes were injected from VB of SnO_2 to TNTs VB and oxidized the organic molecule in MB solution to form R^{+}. They also reacted with OH^{-} or H_2O, oxidizing them into $^{\bullet}OH$ radicals. The surface defects Ti^{3+} as identified in XPS analysis also easily reacted with O_2 adsorbed on TiO_2 surface, leading to the formation of radicals such as $^{\bullet}O_2^{-}$, $HO_2^{\bullet}$, and $^{\bullet}OH$ (Xiong et al., 2012) to effectively oxidize MB to harmless end-products.

Although the considered elements served as potential semiconductor candidate, it never yielded an exemplary supposition as either solar or visible light photocatalyst. Hence, the hunt for the most promising candidate for the prospective visibility nature continued again without any conciliation. The research spirit gloomed the thesis towards the other direction by promoting the localized surface plasmon resonance (LSPR) phenomenon shown by the noble metal for superior visible light harvesting potential. It is also well known that the carbon in the form of GO or RGO exhibited a uniqueness to promote electron mobility. These conceived concepts were engulfed, experimented the ability of the developed photocatalysts for visible light photocatalysis. Owing to the unsteady and uncertainty issues posed by the solar light, the source was replaced by a lamp that produced visible light without any uncertainty in the intensity. This is vital to obtain more accurate repeatability results for successive study and also to elucidate the said behaviour of noble metal.

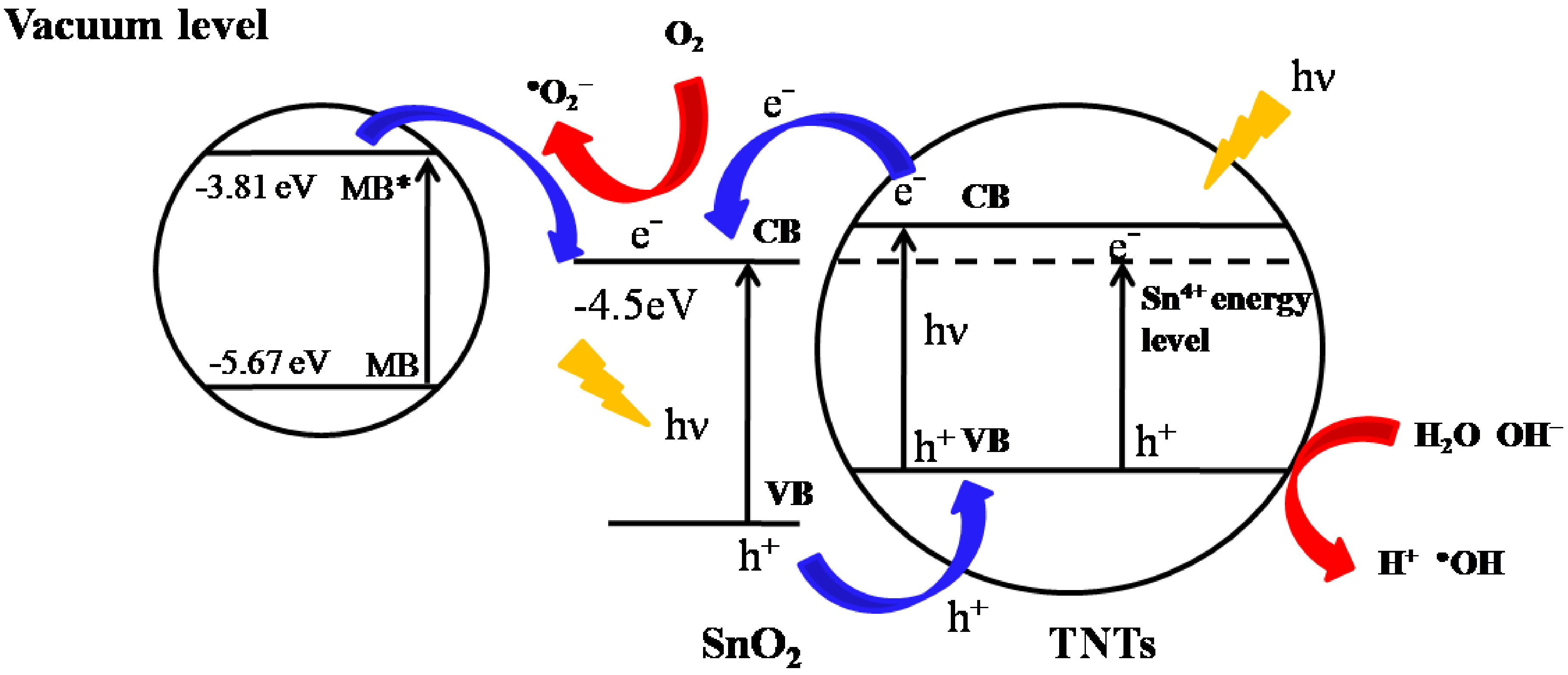

Figure 4.28: Schematic diagram of charge transfer in SnO_2/TNTs photocatalyst under solar light irradiation

4.4 Engulfing of Conducting Carbon Material and Noble Metal: GO/Ag-TNTs Ternary Composite

This section aimed to enhance photocatalytic performance of TNTs by using Ag and GO as an electron transfer channel or electron sink to reduce the recombination of photogenerated electron-hole pairs. Recent years, there are few reports that disclosed GO as an electron sink to inhibit electron-hole pairs recombination (Gao et al., 2012; Song et al., 2012), but indeed the role of GO could vary according to the pollutants genera. The present initiative offered several advantages over previous reports, including (1) deposition of Ag particles onto the surface of TNTs instead of GO to draw more conclusive results of comparison, (2) a low cost and a facile assembly method to deposit GO onto Ag/TNTs, (3) the photocatalytic activities were examined by comparing the degradation between methylene blue (MB) and 2-chlorophenol (2-CP), considering that photocatalyst could respond differently to genera of pollutants. The exhibited physical chemistry and the photocatalysis were detailed successively.

The cross-sectional image in Fig. 4.29a revealed the tube length ranging from 8−9 µm. The sizes and shape of the photodeposited Ag particles distributed over the TNTs are illustrated in Fig. 4.29b. The chemical composition was distinct from the nanotubes and was endorsed to the Ag NPs with average particle size of ~100 nm (Fig. 4.29c). The adequate deposition of the Ag NPs on and into the surface of the nanotubes was deliberated in Fig. 4.29d. GO/Ag-TNTs sample was excelled with a sheet of GO coating the most surface of the TNTs and is clarified in Fig. 4.29e. When closely observed, the GO had a flake-like structure with wrinkles which was consistent with the earlier reports (Zhang et al., 2011; Wang et al., 2012a; Zhang et al., 2010a). This wrinkles seems to be the characteristic features of GO when it was not conformally coated on the surface of TNTs (Pandey et al., 2011).

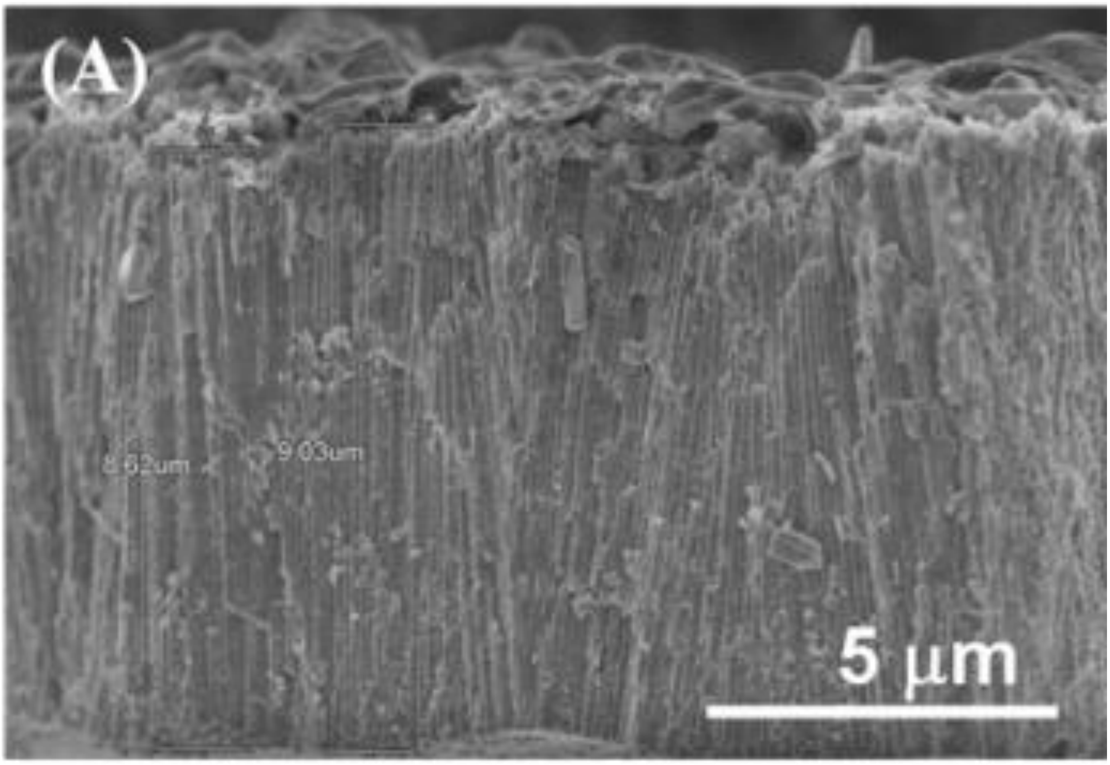
(A)
8.62um
9.03um
5 µm

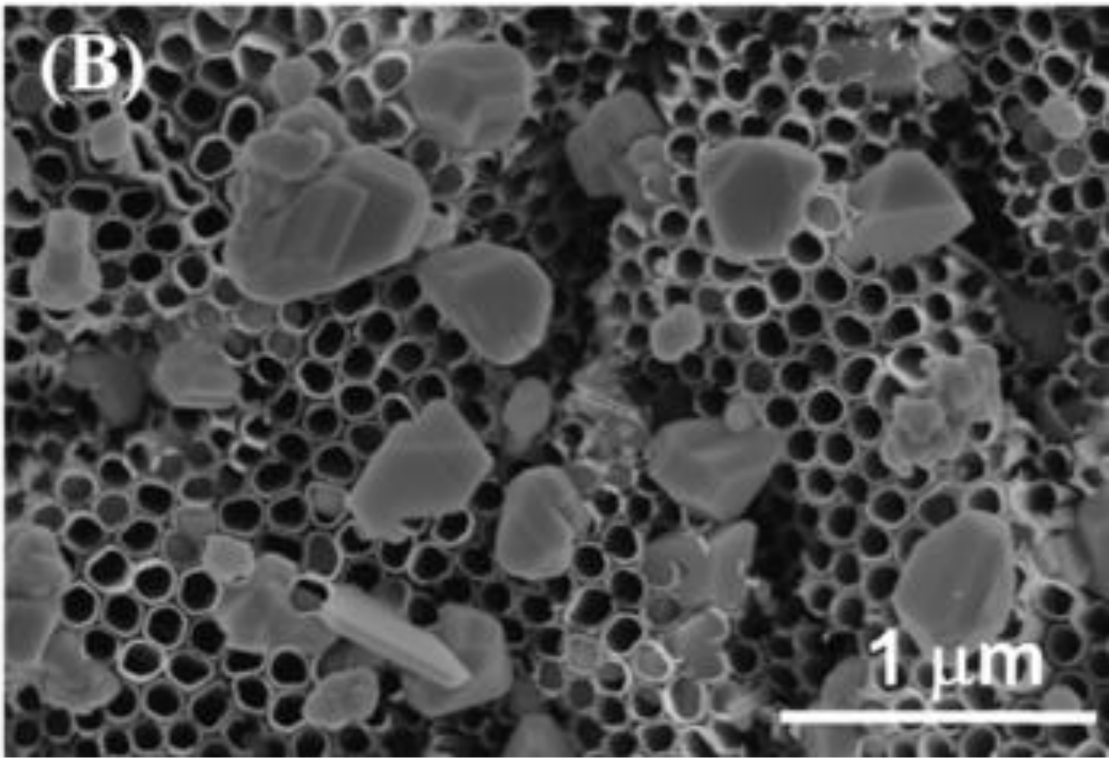
(B)
1 µm

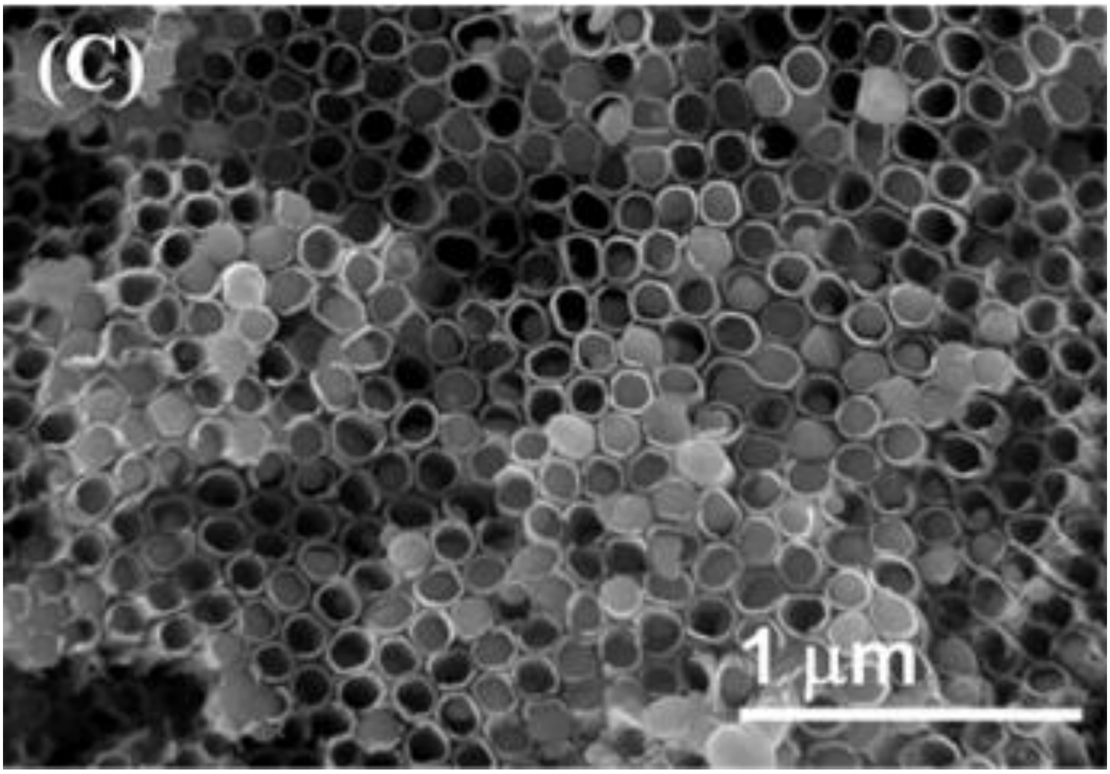
(C)
1 μm

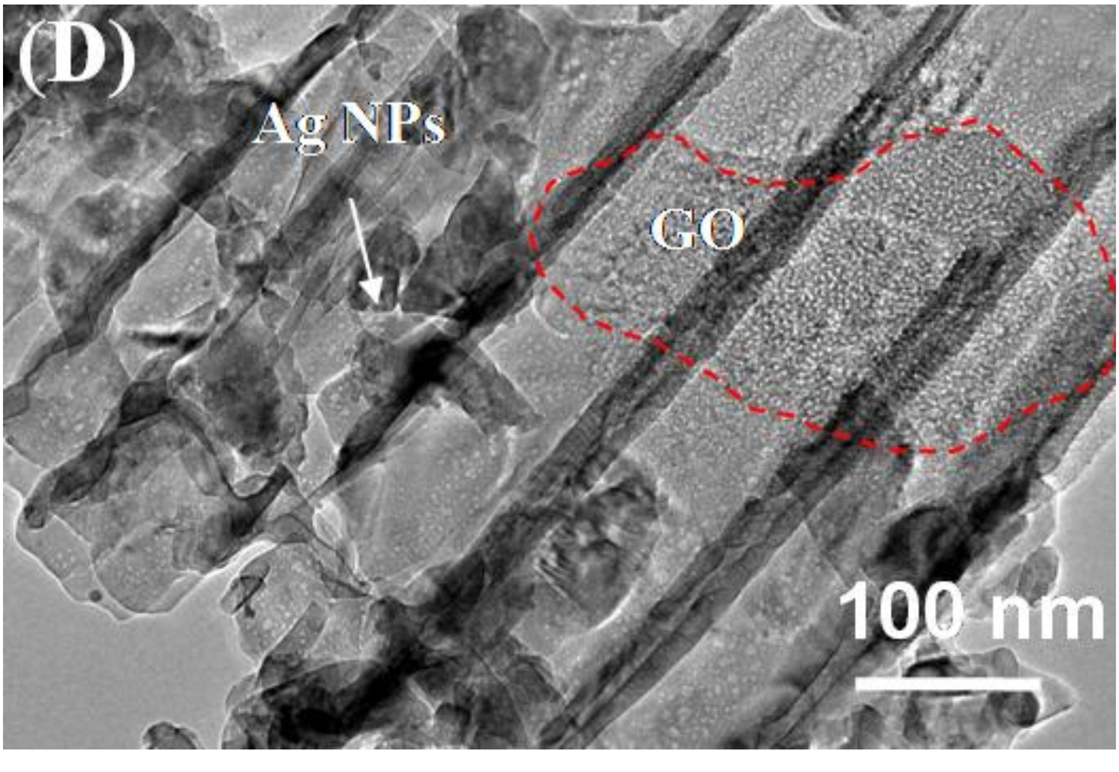
(D)
Ag NPs
GO
100 nm

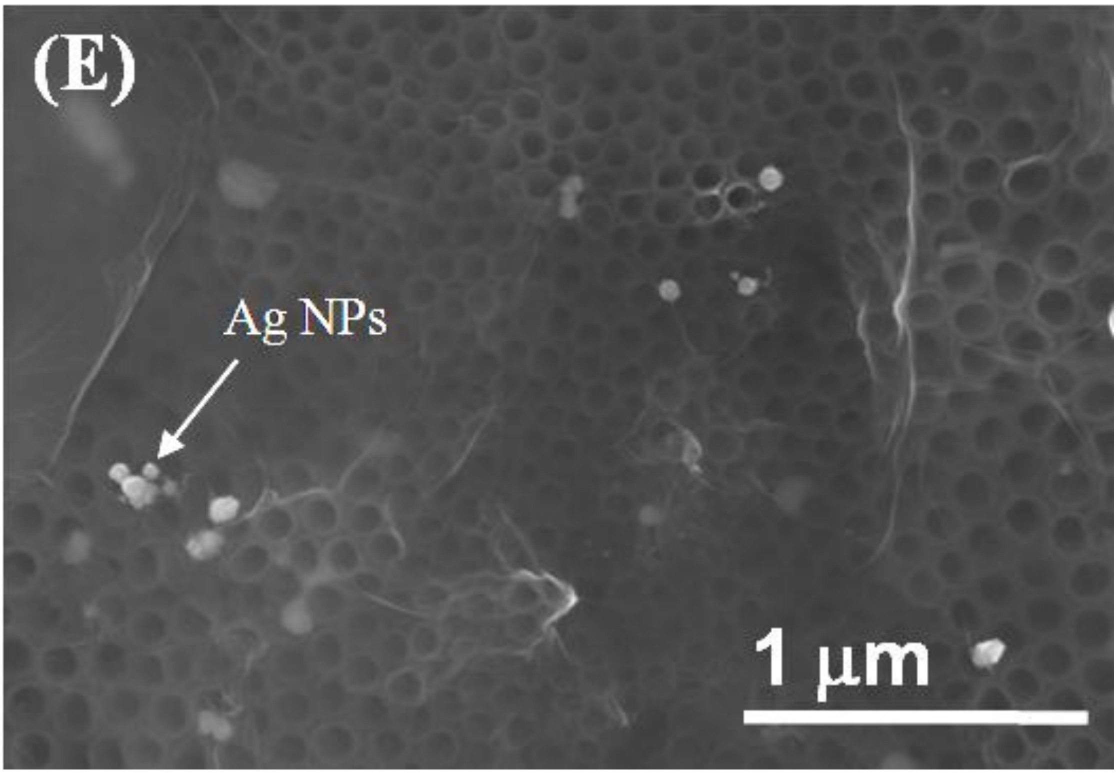

Figure 4.29: FESEM images of the (a) cross-section of GO/Ag-TNTs, top view of Ag-TNTs (b) without sonication, (c) with sonication, (d) HRTEM image of Ag NPs dispersed on and into surface of TNTs, and (e) top view of GO/Ag-TNTs

Fig. 4.30 corresponds the EDX spectrum of the prepared photocatalyst, unveils the presence of the elements like C, Ag, O and Ti with their atomic weight percentage of the engulfed nanotubes in GO/Ag-TNTs. The presence of engulfed Ag in the TiO_2 lattice was clearly visualized by the lattice fringes acquired from high resolution TEM image. The image pertaining to it is displayed in Fig. 4.31. The identified lattice fringes of 0.24 nm and 0.35 nm spacing were complimented to Ag (1 1 1) and anatase titania (1 0 1) planes, respectively (Shah et al., 2013; Ren et al., 2010).

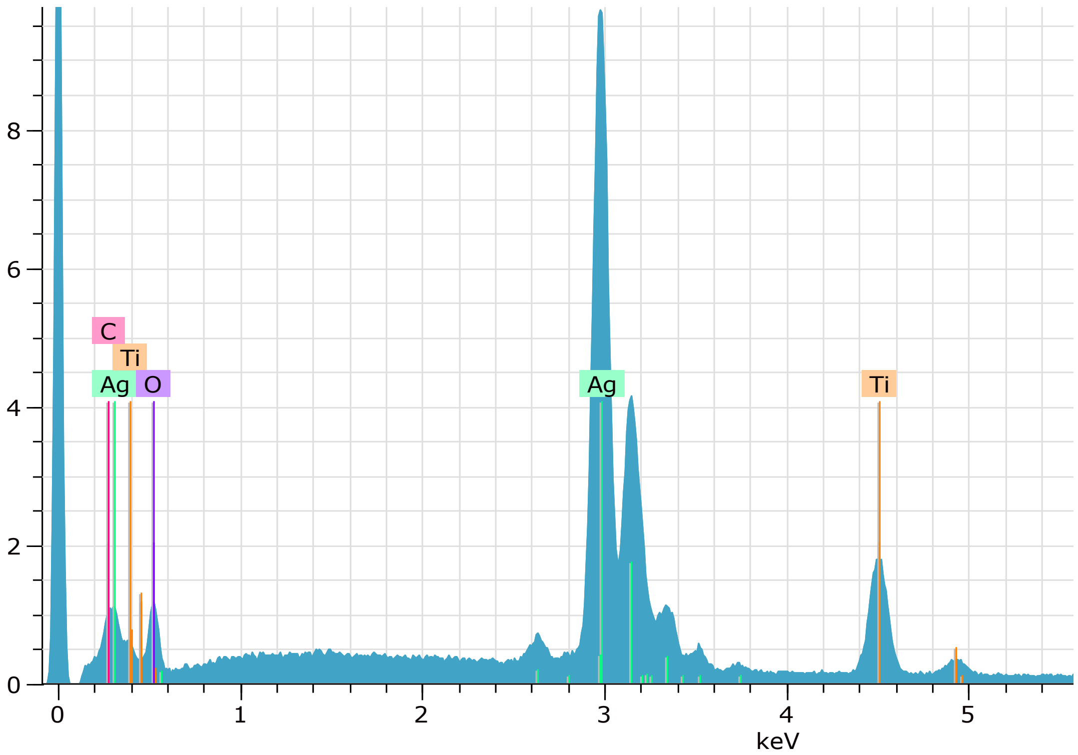

Figure 4.30: EDX of GO/Ag-TNTs

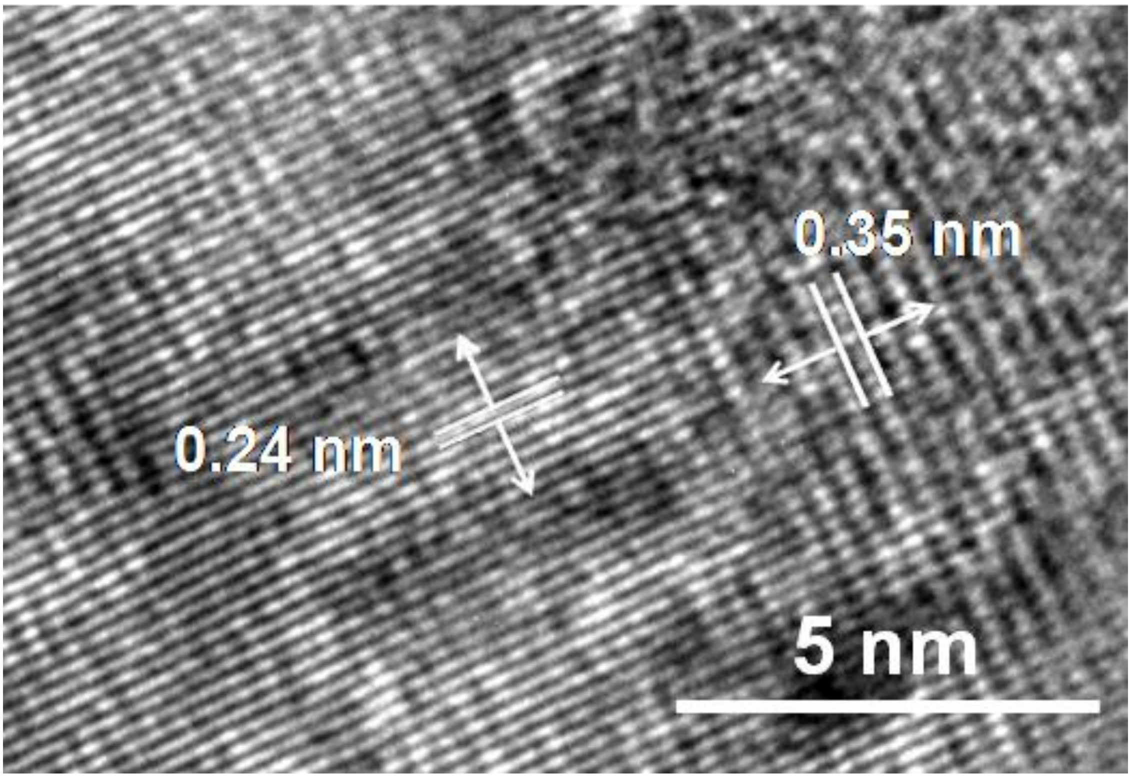

Figure 4.31: HRTEM images of GO/Ag-TNTs showing fringes of TiO_2 and Ag

The morphology was succeeded with a phase and crystalline analysis and the obtained crystallography diffraction pattern is depicted in Fig. 4.32. The derived diffraction peaks of TNTs tagged to the pristine anatase phase and the same was also seen in both Ag-TNTs and GO/Ag-TNTs. A binary obvious peaks designated to tetragonal anatase phase (JCPDS no. 21-1272) appeared at 25.3 ° and 48.0 °, corresponded to (1 0 1) and (2 0 0) crystal planes, respectively. Additionally, Ag-TNTs and GO/Ag-TNTs showed peaks at 38.1 °, 44.3 °, 64.4 ° and 77.4 ° assigned to (1 1 1), (2 0 0), (2 2 0) and (3 1 1) planes of face centered cubic (FCC) Ag (JCPDS no. 65-2871). A (0 0 2) diffraction peak at 10.6 ° was observed for GO, indicating complete oxidization of natural graphite to GO through *d*-spacing expansion from 3.37 Å to 8.6 Å. This also indicates the introduction of oxygen-containing groups on the GO sheets (Zhang et al., 2011). However, there was no peak ascribed to GO can be observed in the sample of GO/Ag-TNTs due to the low amount of GO which was below the detection limit of XRD (Wang et al., 2013e; Wang et al., 2012c). The average crystallite sizes of TiO_2 anatase and Ag particles were calculated using Scherrer equation (Eq. 4.1). There was no significant change in the crystallite size of anatase TiO_2 in pure TNTs (33.81 nm) and GO/Ag-TNTs (33.12 nm), proving that a large portion of Ag particles with crystallite size of 45.16 nm were not incorporated in TiO_2 lattice, but deposited on the surface of the matrix. After revealing the detailed phase, crystalline analysis of the samples was subjected to optical properties spectroscopically.

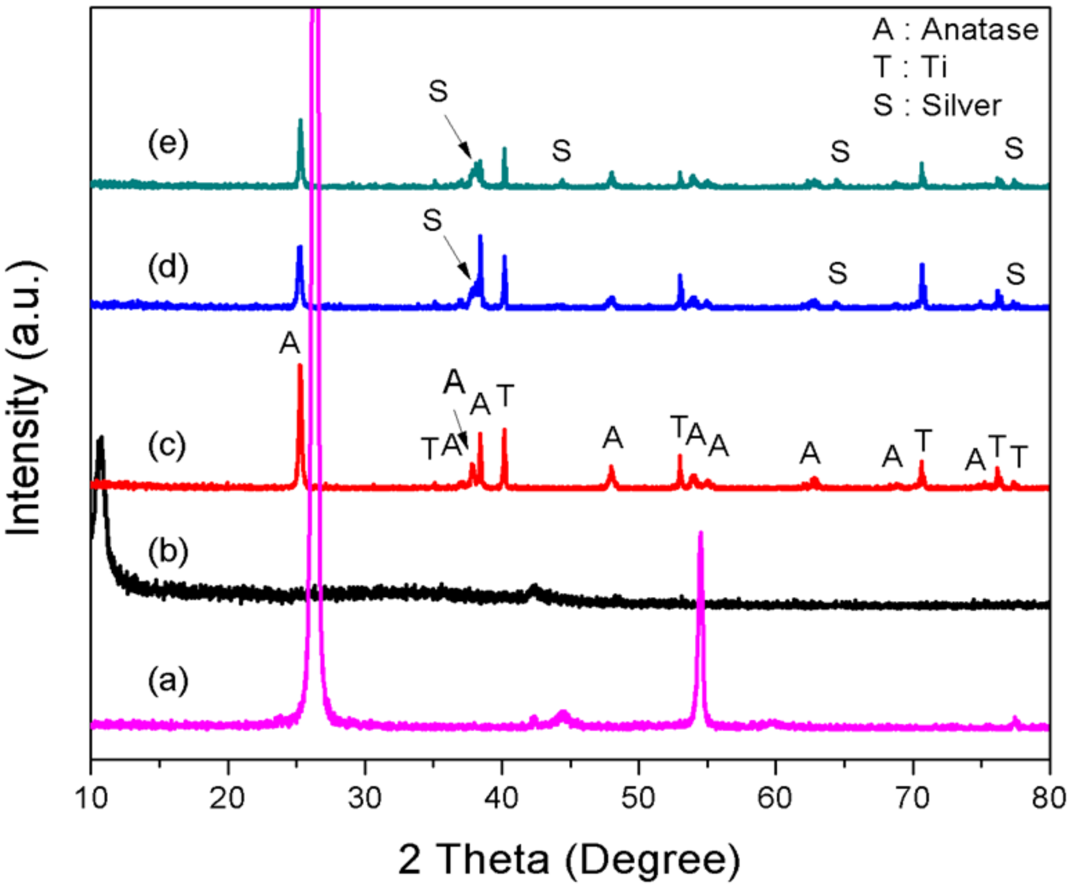

Figure 4.32: X-ray diffraction patterns of (a) graphite (b) GO (c) TNTs (d) Ag-TNTs and (e) GO/Ag-TNTs

The spectroscopic response was described with UV-vis diffuse reflectance spectra (UV-DRS) and the spectrum is recorded in Fig. 4.33. The TNTs showed an expected absorption lower than 380 nm (UV region) due to the charge transfer from O 2p valence band to Ti 3d conduction band (Fuerte et al., 2002). A broad absorption peak at approximately 460 nm was observed for Ag-TNTs, which was attributed to the surface plasmon absorption of Ag NPs (Liu et al., 2012). This pristinely showed the presence of metallic Ag NPs on the surface of TNTs. In addition, GO/Ag-TNTs exhibited higher light absorption capacities in the entire visible region due to the presence of GO.

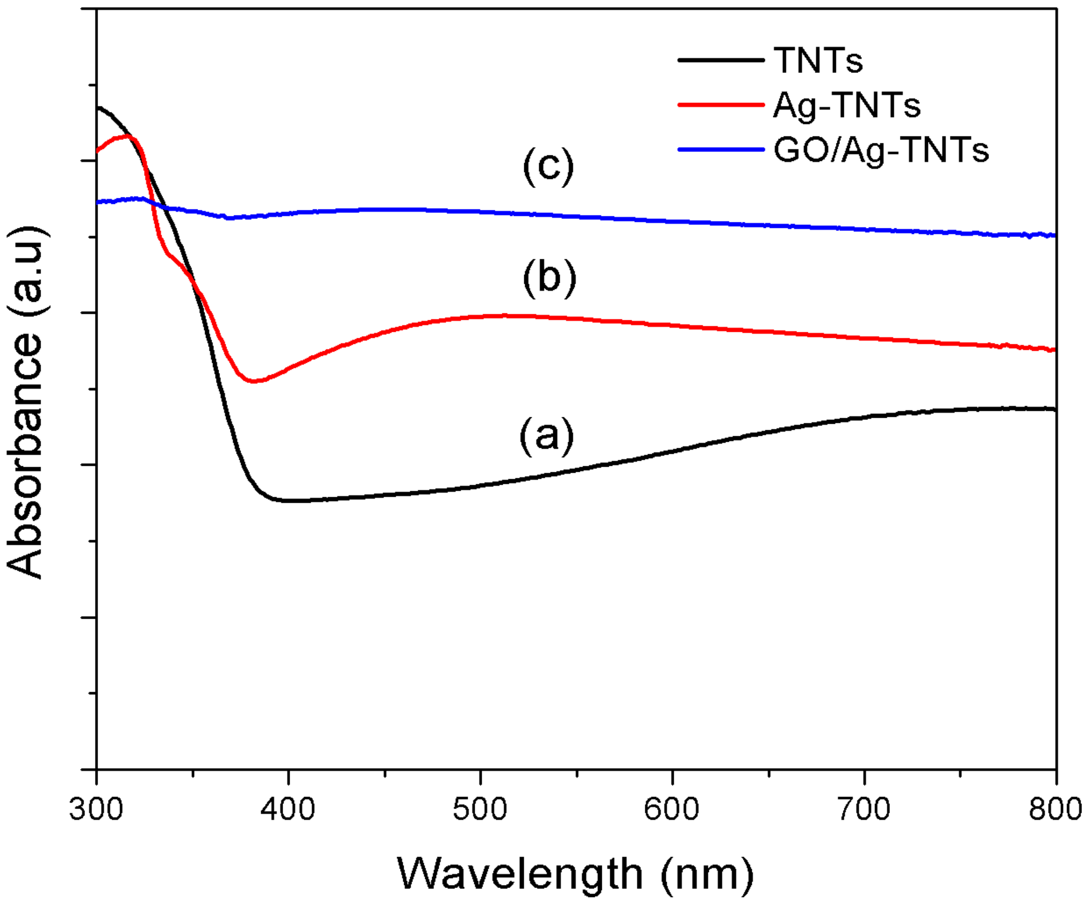

Figure 4.33: UV-visible absorption spectra of (a) TNTs (b) Ag-TNTs and (c) GO/Ag-TNTs

The spectroscopic analysis was further extended to Raman and is pictorial expressed in Fig. 4.34. A distinct quadric Raman shift showing the anatase TiO_2 was registered at bands 145 (E_g), 399 (B_{1g}), 519 (A_{1g} + B_{1g}) and 639 cm^{-1} (E_g) for all the studied samples. This observed Raman shift further proved that all the combinations of synthesized samples resulted in anatase phase without any phase of other impurities. It is expected that GO and its composite expressed a binary shift at around 1595 cm^{-1} and 1350 cm^{-1}, corresponding to the G- and D-bands, respectively. The appeared G-band near 1595 cm^{-1} was unique characteristic of sp^2 hybridized carbon materials, which could provide information on the in-plane vibration of sp^2-bonded carbon domains (Ni et al., 2008; Chen et al., 2010). Whereas, the D-band that appeared at around 1350 cm^{-1}

indicated the presence of sp^3 defects within the hexagonal graphitic structure (Graf et al., 2007) assigned to structural defects, amorphous carbon or edges that break the symmetry and selection rule (Long et al., 2013). This was well proved that a minor I_D/I_G peak intensity ratio corresponded to the lower defects of the graphitized structures. In comparison between the obtained spectra of the samples, GO and GO/Ag-TNTs resulted in broader G-band promoted by the isolated double bonds (Wang et al., 2013b). The increased disorder in GO and GO/Ag-TNTs was reflected through comparable sharper D-band Raman shift. After the oxidation of graphite, the ratio of I_D/I_G increased to 0.91, designated the formation of large sp^3 domain in the sample of GO. The D- and G-band of GO/Ag-TNTs were roughly at the similar position to that of GO. However, the ratio of I_D/I_G for GO/Ag-TNTs was 0.95 which was marginally higher than GO, showing a negligible decline of graphitic domains.

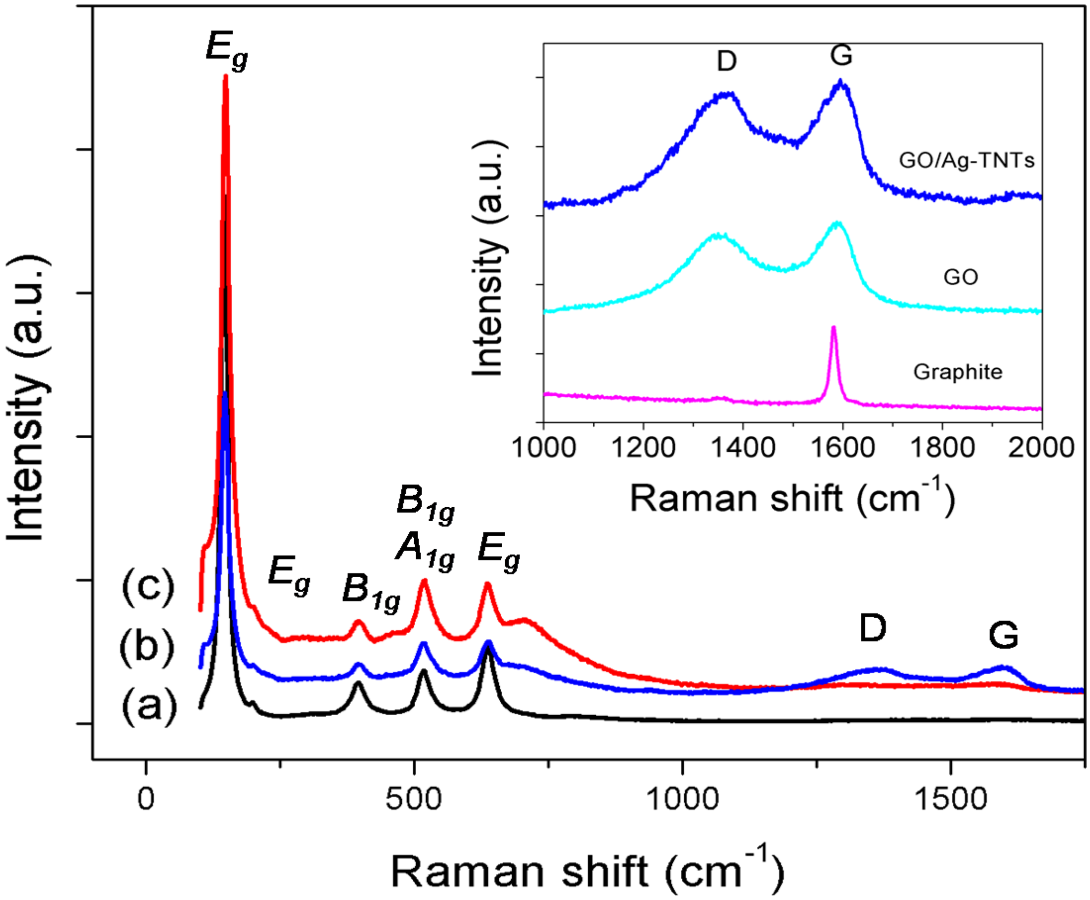

Figure 4.34: Raman spectra of (a) TNTs (b) GO/Ag-TNTs and (c) Ag-TNTs. The inset is the D- and G-band of graphite, GO and GO/Ag-TNTs

After exploring the information from Raman, the analysis was continued with FTIR analysis to characterize the carbon species in the prepared samples. The obtained results are depicted in Fig. 4.35. The unalloyed GO exhibited many strong absorption peaks corresponding to the stretching of hydroxyl group (3300 cm^{-1}) and C=O groups in carbonyl and carboxyl moieties (1720 cm^{-1}). The C=C vibrational bands were displayed by unoxidized graphitic domains and stretching deformation of intercalated water (1620 cm^{-1}). Besides, carboxyl group (1375 cm^{-1}), epoxide C-O-C or phenolic C-O-H stretching vibrations (1220 cm^{-1}), and C-O stretching vibrations in epoxy or alkoxy groups (1045 cm^{-1}) were also denoted (Shah et al., 2013; Xu et al., 2008; Guo et al., 2009). For GO alloyed sample, most of these groups were retained with a significant decrease in the peak intensity due to the lower GO utilized in the synthesis. The disappearance of C-O stretching band at wavenumber 1220 cm^{-1} suggests that epoxide or phenolic groups in GO reacted with the surface hydroxyl groups of Ag-TNTs and led to Ti-O-C bonds. The absorption peaks appeared at 800 cm^{-1} can be assigned as a combination of Ti-O-Ti vibration in crystalline TiO_2 and Ti-O-C vibration (Sakthivel and Kisch, 2003).

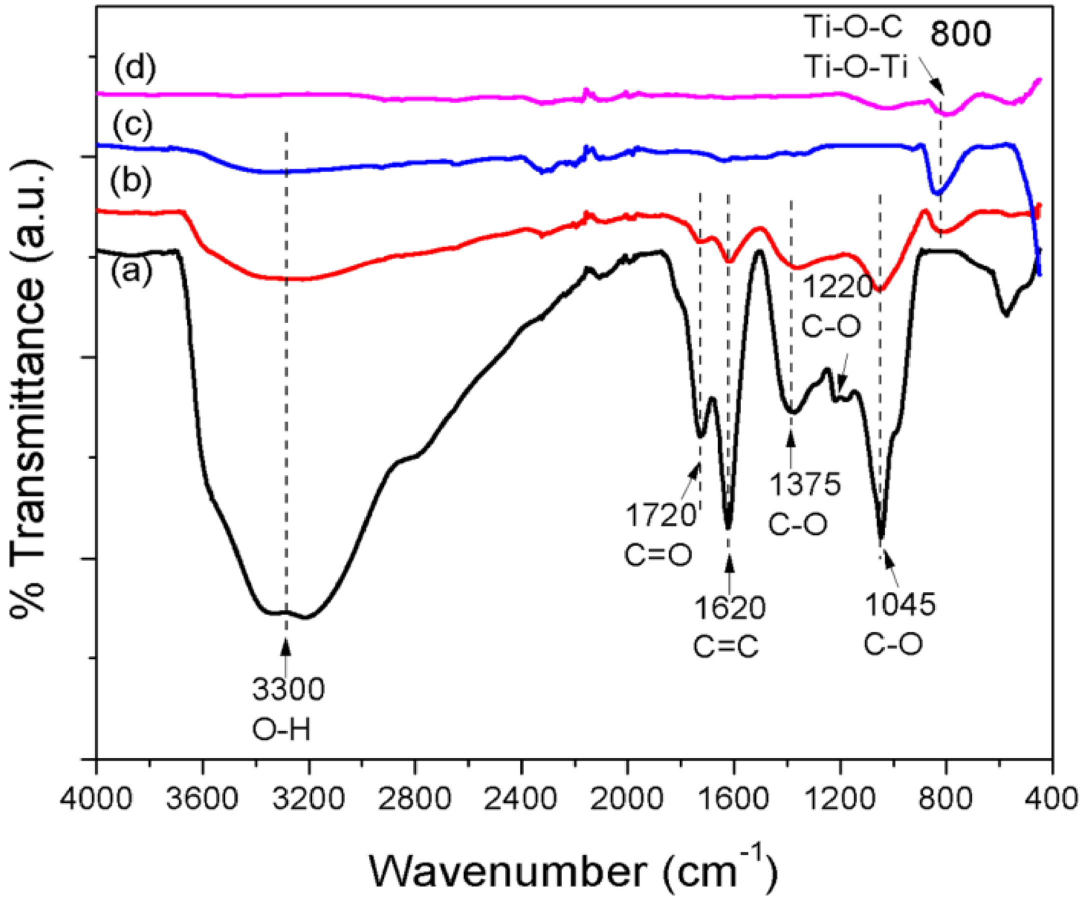

Figure 4.35: Absorption and emission Fourier transform infrared spectra of (a) GO (b) GO/Ag-TNTs (c) TNTs and (d) Ag-TNTs

In order to understand the recombination phenomenon exerted by the samples, a PL analysis was carried out and the obtained spectra are shown in Fig. 4.36. This PL emission intensity was correlated to the recombination rate of excited electron-hole pairs. In general, lower intensity attributes to greater number of transferred or trapped excited electrons, whereas the higher intensity cites to the vice versa effect i.e., quicker recombination rate. The emission peak of GO/Ag-TNTs and Ag-TNTs were obviously quenched as compared to that of TNTs. The quenching behaviour revealed that both the GO and Ag trapped electron or transferred electron to suppress electron-hole pairs recombination. The effective charge carrier separation extended the reactive electron-hole pairs lifetimes and enhanced the photocatalytic activity of GO/Ag-TNTs.

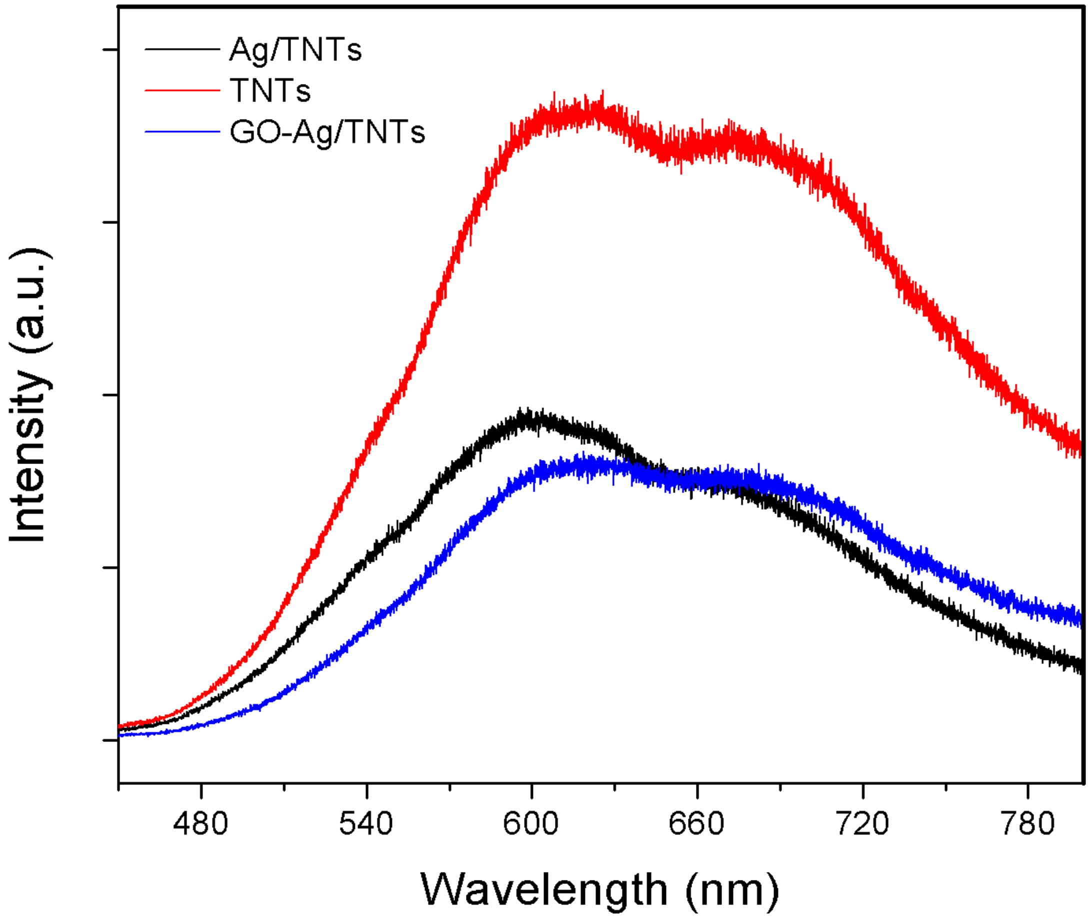

Figure 4.36: Photoluminescence spectra of studied samples

A high-resolution XPS was performed to determine the chemical composition and oxidation state of GO/Ag-TNTs as shown in Fig. 4.37(a-c). From the Fig. 4.37a, two peaks were observed at binding energies 459 eV (Ti $2p_{3/2}$) and 464.6 eV (Ti $2p_{1/2}$), corresponded to Ti^{4+} in anatase phase. The presence of Ag NPs were signified by peaks centered at 368.2 eV and 374.2 eV, assigned to Ag $3d_{5/2}$ and Ag $3d_{3/2}$, respectively (Fig. 4.37b). As shown in Fig. 4.37c, the C 1s XPS signals were deconvoluted into three components. The peak at 284.5 eV was assigned to the sp^2 carbon atoms of GO. The peaks at higher binding energies were assigned to the oxygenated carbon species of GO, such as C-OH, C=O and COOH (Zhang et al., 2011; Shah et al., 2013). The interaction between GO and TNTs could be ascertained by the existence of Ti-C (281 eV) and Ti-O-C (288.7 eV) signals. The former one was attributed to the formation of Ti-C bond in the interface between GO and TNTs. The coordination between carboxyl groups of GO and $Ti(OH)_x$ form Ti-O-C bond (Akhavan et al., 2009). The results deployed by these spectra expressed the influence of oxygenated groups of GO retained in GO/Ag-TNTs and the formation of Ti-O-C bond. All these obtained inference correlated in good agreement with the FTIR findings.

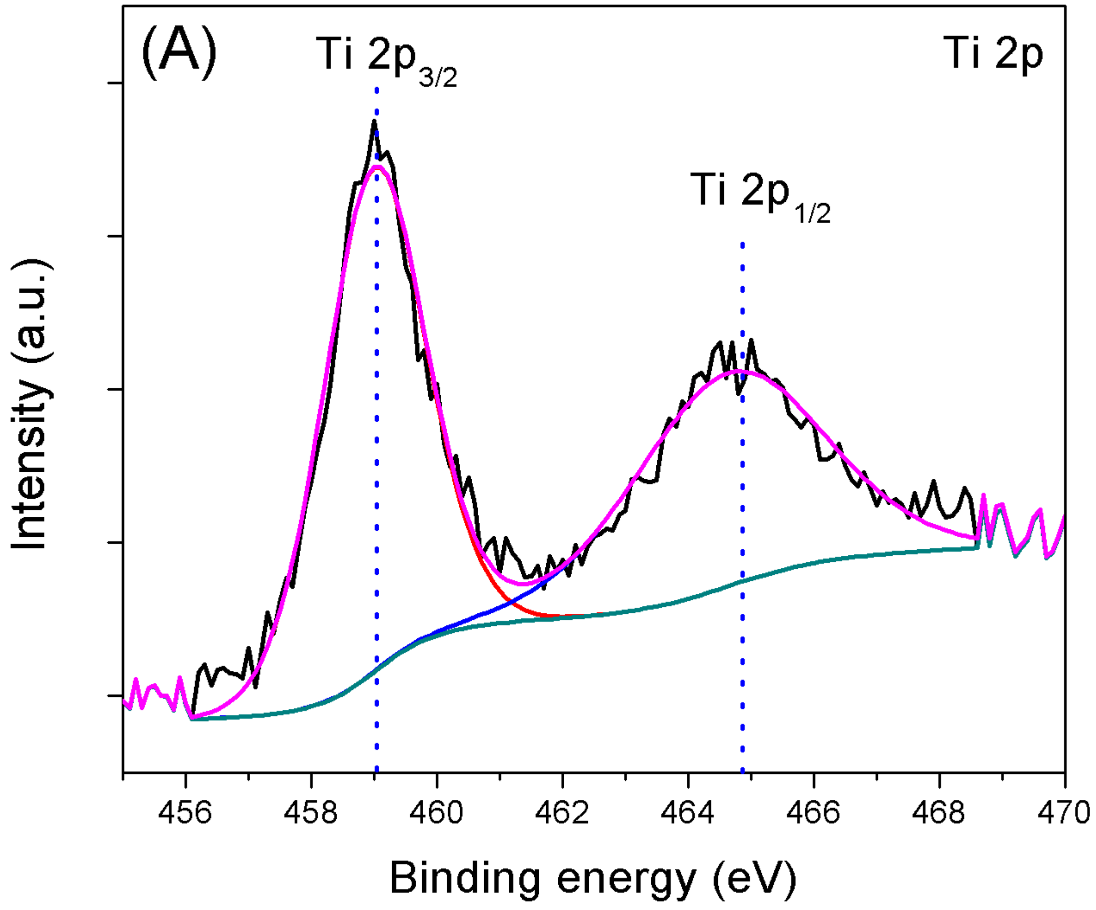
(A)
Ti 2p$_{3/2}$
Ti 2p
Ti 2p$_{1/2}$
Intensity (a.u.)
456
458
460
462
464
466
468
470
Binding energy (eV)

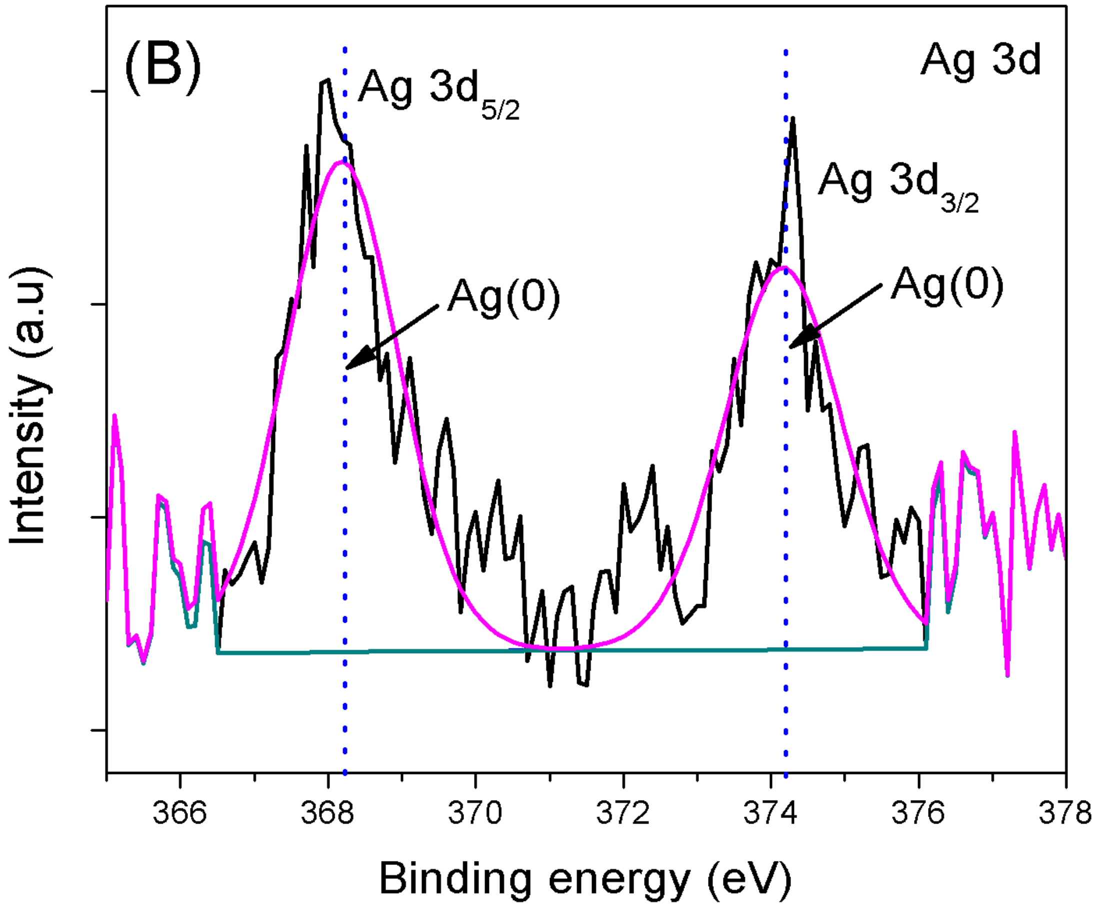
(B)
Ag 3d$_{5/2}$
Ag 3d
Ag 3d$_{3/2}$
Ag(0)
Ag(0)
Intensity (a.u)
366
368
370
372
374
376
378
Binding energy (eV)

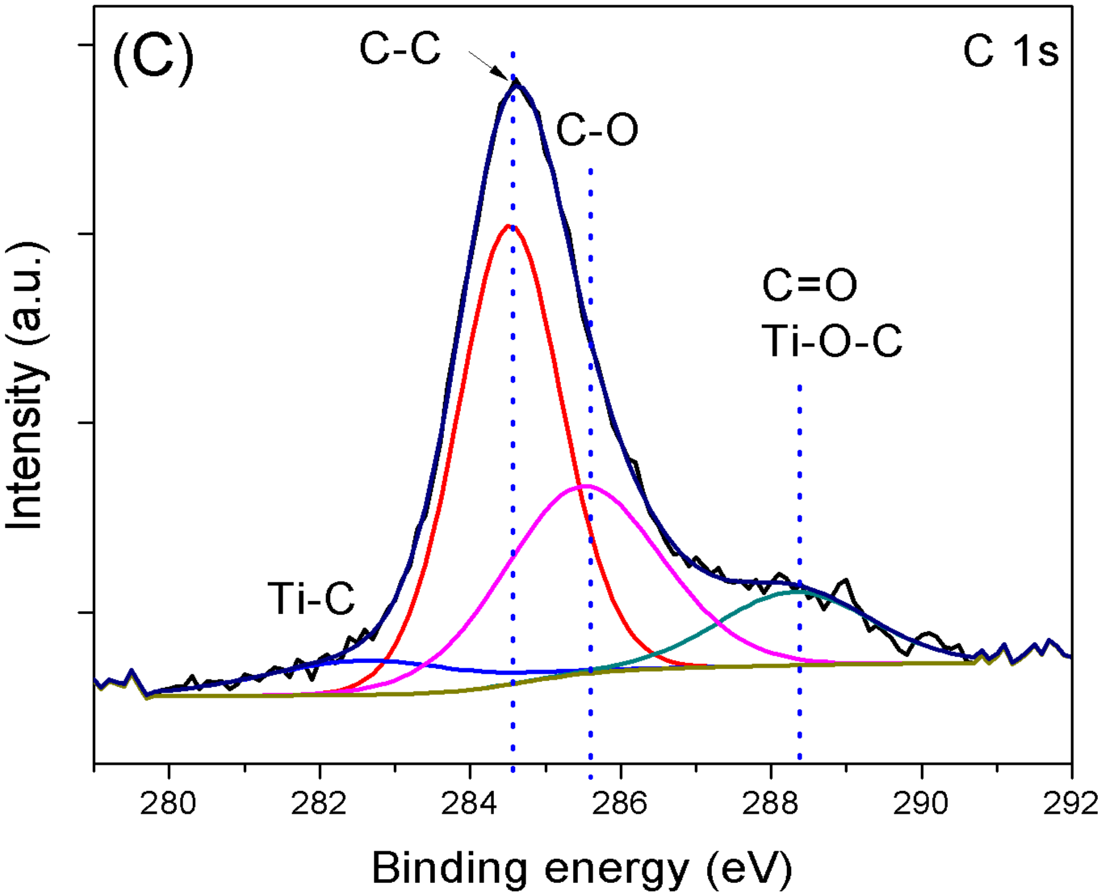

Figure 4.37: Core level XPS spectra of (a) Ti 2p (b) Ag 3d and (c) C 1s of GO/Ag-TNTs

The photocatalytic activity of the prepared GO engulfed samples was evaluated by adopting MB and 2-CP as model pollutants of different genera aided by visible light and the obtained profile is depicted in Fig. 4.38 and Fig. 4.39. It is clear from the figures that dark adsorption process in both GO/TNTs and GO/Ag-TNTs exhibited an adsorption capacity of 34% for MB, a heterocyclic aromatic compound and 12% for chlorinated compound, 2-CP, which was higher than the other samples. The reason for the high adsorption capacity of MB on the surface of GO was attributed to the strong π-π stacking interactions between the benzene rings of MB and the surface of GO (Wu et al., 2011). A significant decrease in the adsorption capacity of MB was observed for GO/Ag-TNTs after the first run, while it remained almost unchanged from the second to sixth run (Fig. 4.40). It can be explained that the chemisorption which was irreversible played a dominant role at first. After many runs, there was almost only physical adsorption and therefore, MB adsorption rate was almost remained constant. On the other hand, physical adsorption was dominant in the case of 2-CP since there was an insignificant loss in the adsorption capacity after many runs.

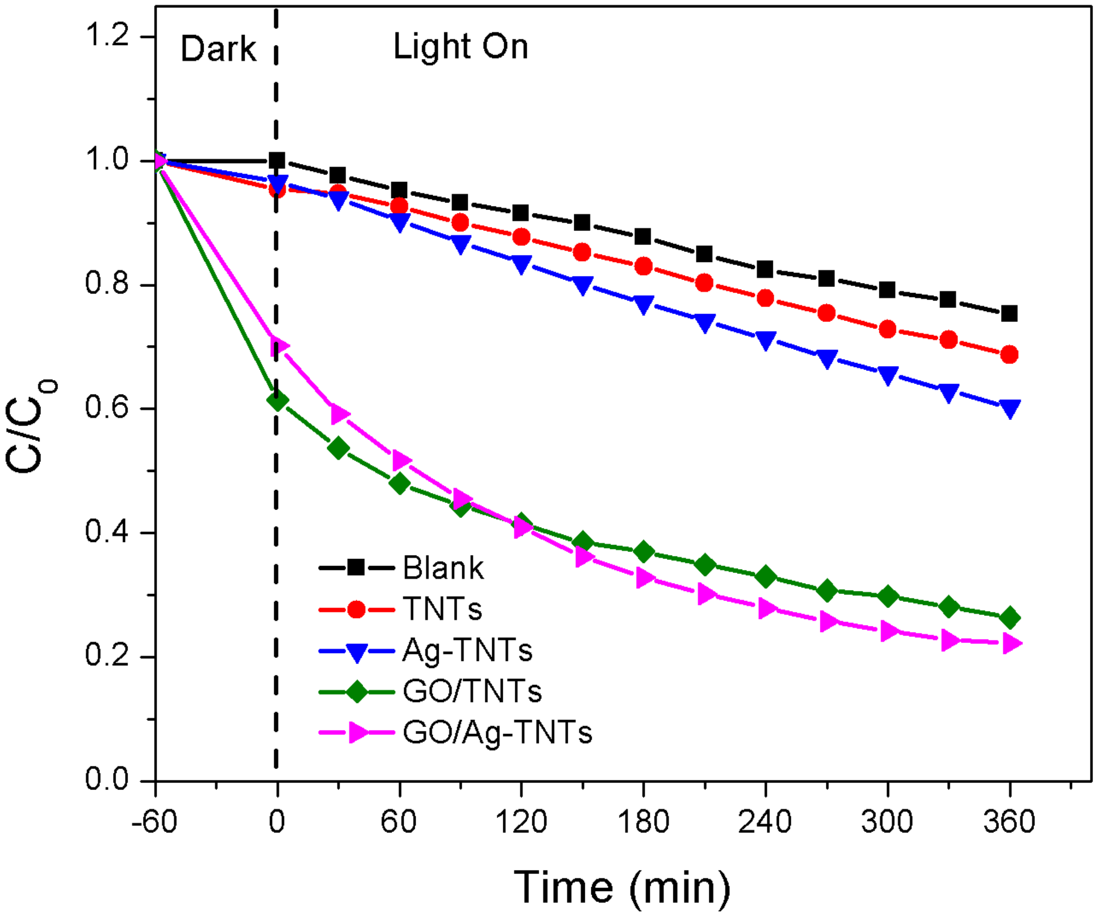

Figure 4.38: Photocatalytic degradation rates of MB for blank, TNTs, Ag-TNTs, GO/TNTs and GO/Ag-TNTs

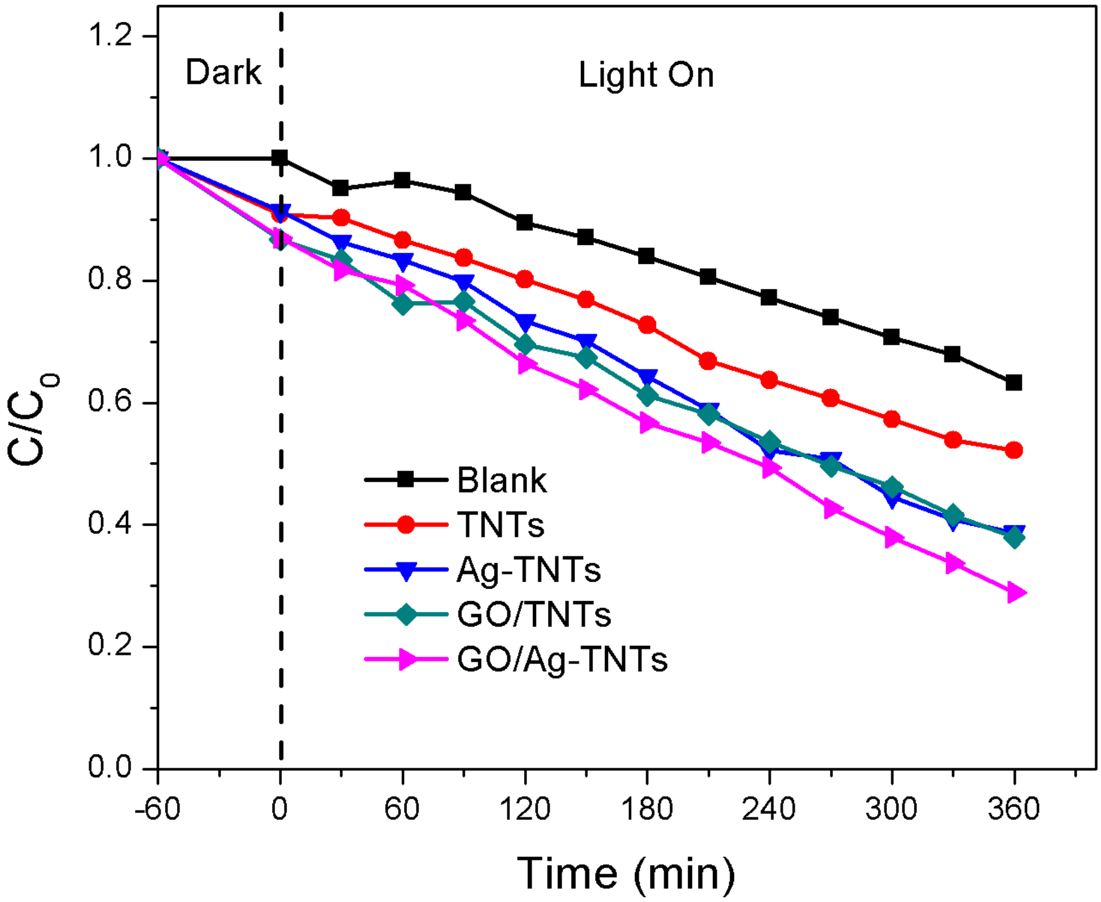

Figure 4.39: Photocatalytic degradation rates of 2-CP for studied samples

The initial concentration (C_0) was considered as the concentration of MB and 2-CP after adsorption-desorption equilibrium. As shown in Fig. 4.38, the degradation efficiency of MB followed an order of GO/Ag-TNTs (68.3%) > GO/TNTs (57.2%) > Ag-TNTs (37.6%) > TNTs (27.9%) > blank (24.7%), while the 2-CP followed an order of GO/Ag-TNTs (66.8%) > Ag-TNTs (57.7%) > GO/TNTs (56.2%) > TNTs (42.6%) blank (36.8%) as seen in Fig. 4.39. These results enlightened that the degradation efficiency of both MB and 2-CP was comparable in the first run and also improved remarkably in the presence of GO, mainly with the coexistence of Ag and GO. In most cases, GO sheets were used as an electron sink to facilitate photogenerated electrons separation and store the separated electrons (Wang et al., 2011b). The suggested degradation mechanism of MB in Fig. 4.41 describes that GO could accumulate the electrons injected from the photogenerated MB because of π-conjugated network and higher work function of GO than that of the excited MB. However, the injected electron could recombine with the surface adsorbed $MB^{\bullet +}$ to lower the degradation efficiency. Besides that, the direct transfer of photogenerated electrons from GO to TNTs was confined by limited contact between GO and TNTs. Therefore, the photocatalytic activity of GO/TNTs was truncated compared to that of GO/Ag-TNTs.

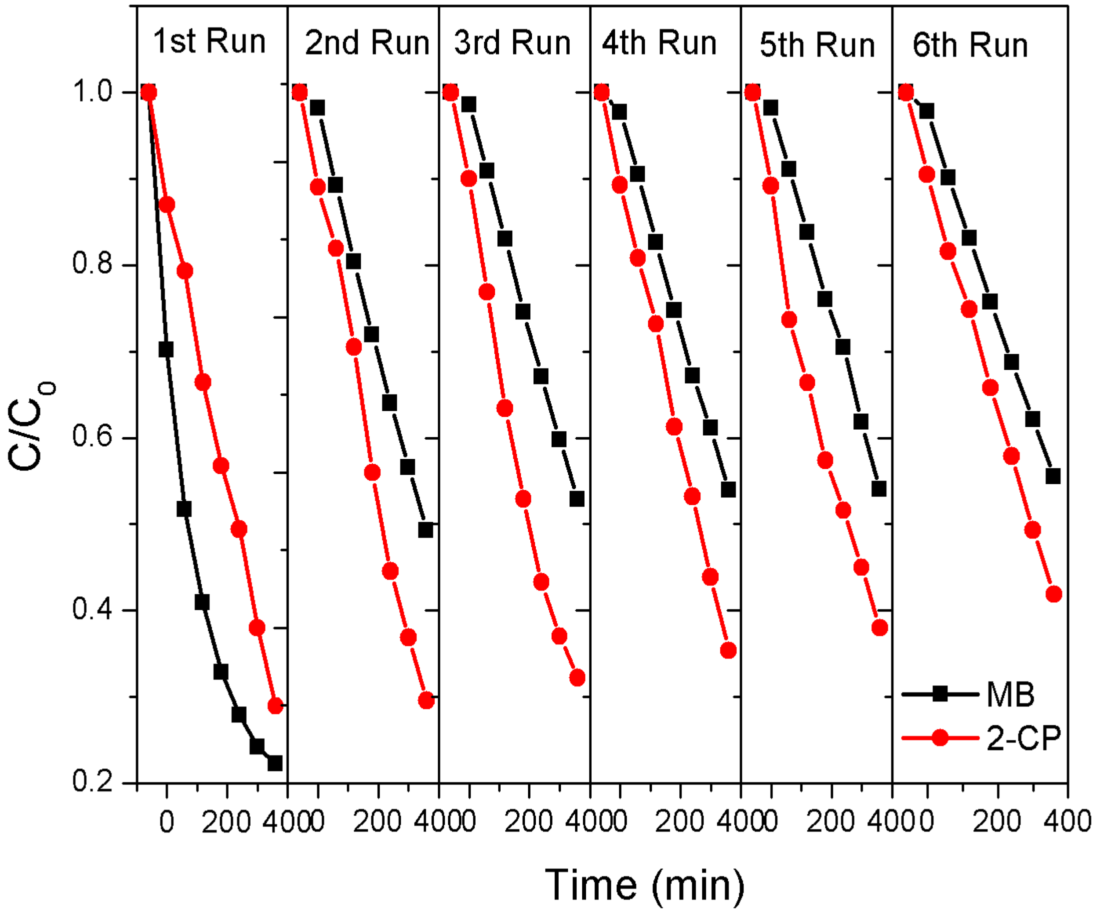

Figure 4.40: Recycled photocatalytic degradation rates of MB and 2-CP for GO/Ag-TNTs

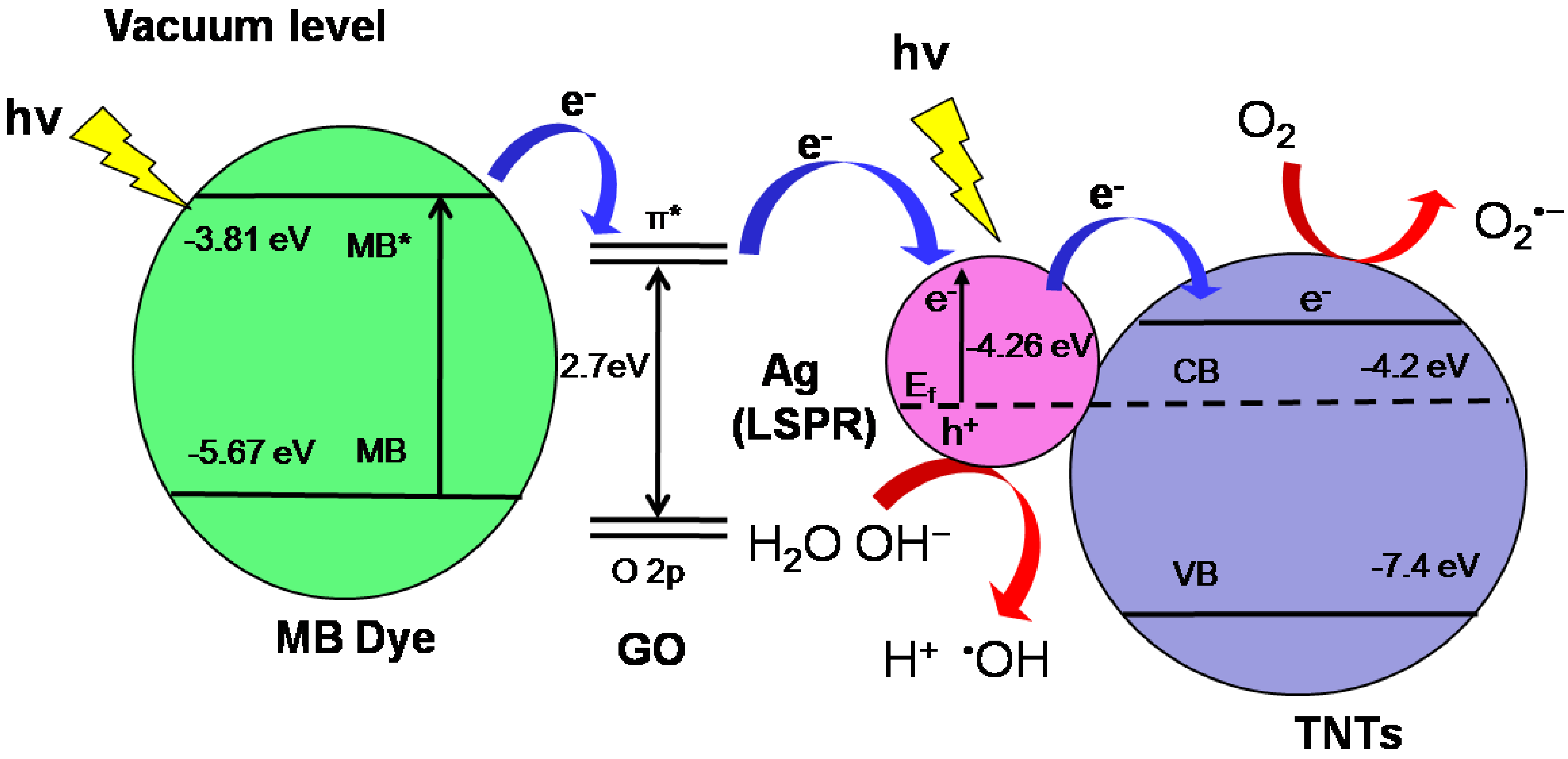

Figure 4.41: Schematic representation of electron transfer and degradation mechanism of MB

Ag NPs were deposited onto the surface of TNTs prior to the decoration of GO to overcome these limitations. Ag NPs were able to absorb visible light due to the existence of a localized surface plasmon resonance (LSPR) (Zielińska-Jurek et al., 2011), resulted in a better degradation efficiency for Ag-TNTs (37.6% for MB and 57.7% for 2-CP) than that of TNTs (27.9% for MB and 42.6% for 2-CP). The Ag NPs also possessed higher work function (4.26 eV) than GO and located below the CB of TNTs (4.2 eV) (Yeh et al., 2011; Hensel et al., 2010; Lin et al., 2009). Band gap energy (E_g) of GO was mainly formed by the anti-bonding of π* orbital as CB with a higher energy level and the O 2p orbital as a VB (Yeh et al., 2010; Yeh et al., 2013). It was also reported that Ag^+ could be reduced in graphene/TiO_2 photocatalytic systems (Lightcap et al., 2010). This disclosed the higher energy level of anti-bonding π* orbital that facilitated the electrons transfer from graphene to Ag^+, concluding the injection of electrons from the excited GO to Ag NPs (Moon et al., 2012).

Moreover, when Ag NPs and TNTs were in contact, a Schottky barrier was formed at the interface. The Ag NPs overcame the energy barrier at the interface of Ag/TiO_2 upon LSPR-excitation to inject electrons from Ag NPs into the CB of TiO_2 under the irradiation of visible light (Fan et al., 2014; Chen et al., 2014; Su et al., 2012; He et al., 2013; Wang et al., 2013c; Eom et al., 2014). Herein, the electrons generated by the LSPR effect in Ag NPs diffused into the CB of TNTs. The TNTs protagonisted as an electron reservoir by capturing the electrons transferred from the GO and Ag to further increase the degradation efficiency of MB. GO emerged as an electron-accepting mediator between the MB and Ag NPs (Min and Lu, 2011; Mou et al., 2011). Alternatively, the excited MB could also transfer electrons to TNTs and Ag due to its submissive work function (3.81 eV) than Ag (4.26 eV) and lying above the CB of TNTs (4.2 eV). However, this electron transfer rate was gentle because of the blocking effect shown by the deposited GO on nanotube as visualized in FESEM and perhaps decreased the effective area of Ag-TNTs for the electron transfer.

For the degradation of MB, GO/Ag-TNTs demonstrated a tremendous decreasing trend by 27% after the first run and followed by a significant loss of 36.7% after the sixth run (Fig. 4.40). It can be argued that the active sites of the GO could be undesirably occupied by the adsorbed MB through chemisorption which could not be eluted, resulting in decreased photocatalytic activity after the first run. The involvement of certain functional groups on the surface of GO in the adsorption of MB is shown in Fig. 4.42. The FTIR of GO/Ag-TNTs before and after the adsorption of MB was demonstrated to ascertain the possible involvement of the functional groups on the surface of GO in the adsorption of MB. It could be inferred that chemical bonding between MB and related groups of GO took place based on following reasons: 1) After adsorption, the stretching vibration adsorption band of OH groups at 3300 cm^{-1} was broadening and offset; 2) The bands at 1620 and 1375 cm^{-1} were shifted to 1579 and 1343 cm^{-1} with broadening. This clarifies the involvement of -OH, -C=C and C-O group in the adsorption of MB onto GO. FTIR results unmasked the role played by some functional groups on the surface of GO in the adsorption of MB. Hence, it is foreseen that the active sites of the GO could be undesirably occupied by the adsorbed MB through chemisorptions undoubtedly.

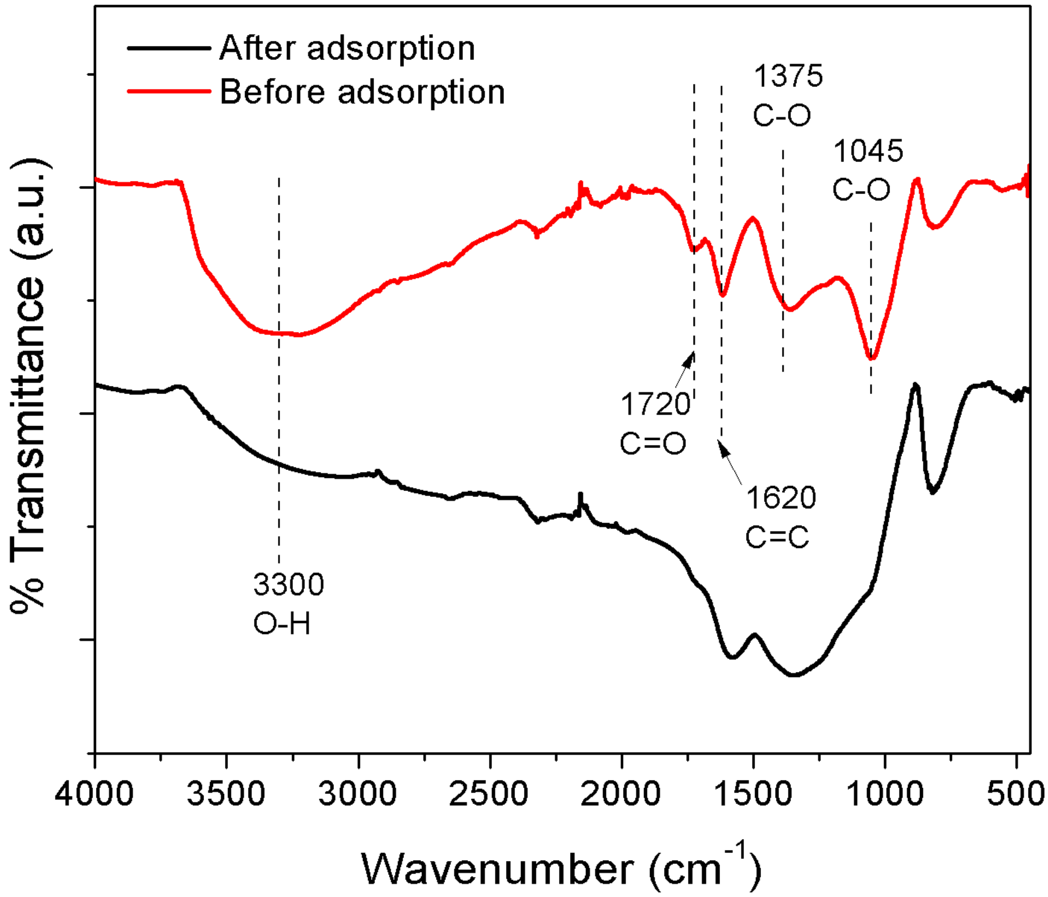

Figure 4.42: FTIR spectra of GO/Ag-TNTs before and after the adsorption of MB

In contrast, GO/Ag-TNTs showed a greater stability on reusability of 2-CP with 19.5% loss through physical adsorption that can be eluted. It was well established that 4-chlorophenol (4-CP) and other derivatives of phenolic compounds robustly degraded under visible irradiation due to the charge transfer surface complex formation between the phenolic compound and TNTs (Kim and Choi, 2005). Such a surface complex promoted the visible light excitation through ligand-to-metal charge transfer (LMCT) between the 2-CP (ligand) and the Ti^{4+} site on the TNTs surface (Wang et al., 2003; Tachikawa et al., 2004). Since 2-CP is one of the derivatives of phenolics, the surface complex formation acknowledged the 2-CP degradation as metaphorized in Fig. 4.43. Thus clarifies the higher degradation efficiency of 2-CP (42.6%) than that of MB (27.9%) for TNTs. The electrons jumped from TNTs/2-CP surface complex to CB of

TNTs. These electrons were subsequently injected to Ag NPs and finally to GO which served as an electron sink to facilitate the separation of the excited electrons. On the other hand, the instigation of LSPR in the Ag NPs anchored the movement of electrons to the CB of TNTs (Fan et al., 2014; Chen et al., 2014; Su et al., 2012; He et al., 2013; Wang et al., 2013c; Eom et al., 2014). All these electrons closely reacted with O_2, yielding superoxide radical anion $^{\bullet}O_2^{-}$. While the photogenerated holes oxidized the organic molecule in MB or 2-CP to form R^{+}, or reacted with OH^{-} or H_2O and then further oxidizing them into $^{\bullet}OH$ radicals. The resulting healthy $^{\bullet}OH$ radicals were durable oxidizing agent that oxidized problematic MB dye and 2-CP to harmless end-products. The observed degradation data were fitted to the simple kinetic model and was seen in Fig. 4.44(a-b) and Fig. 4.45(a-b). The second order kinetic is expressed by equation:

$$\frac{1}{C} = kt + \frac{1}{C_0} \tag{4.6}$$

where k is the second-order reaction constant, C is the final concentrations of MB dye. The photocatalytic degradation of MB and 2-CP fitted to pseudo second-order reaction kinetics with a regression > 0.9, indicating the reaction rate is proportional to the product of the concentrations of two reactants, or to the square of the concentration of a single reactant. The occurred kinetic parameters are tabulated in Table 4.8, and Table 4.9, respectively.

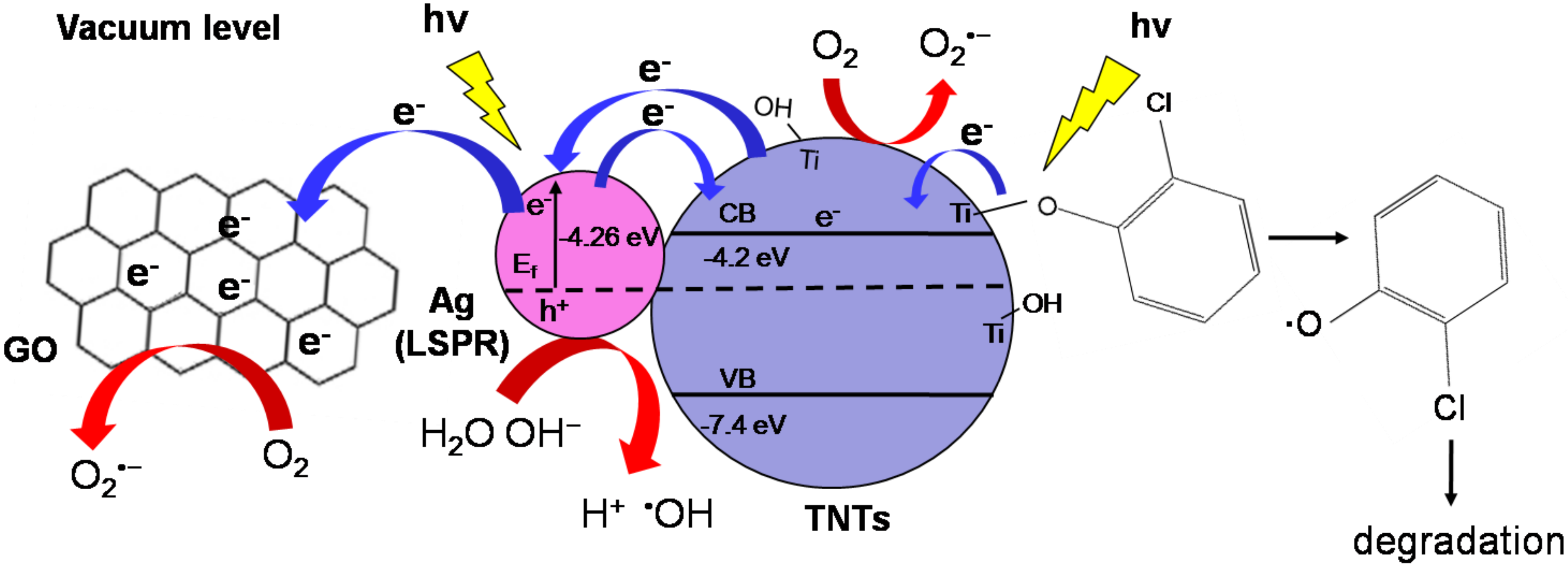

Figure 4.43: Schematic representation of electron transfer and degradation mechanism of 2-CP

Table 4.8: Obtained kinetic parameters on MB degradation

		1st Order Kinetic			
	Blank	**TNTs**	**Ag-TNTs**	**GO/TNTs**	**GO/Ag-TNTs**
R^2	0.99913	0.99328	0.99933	0.986	0.98645
k	0.00077615	0.000862308	0.00128	0.00255	0.00365
		2nd Order Kinetic			
R^2	0.99993	0.99962	0.99965	0.99961	0.99913
k	1.7641E-4	0.000210615	0.000323795	0.00121	0.00182

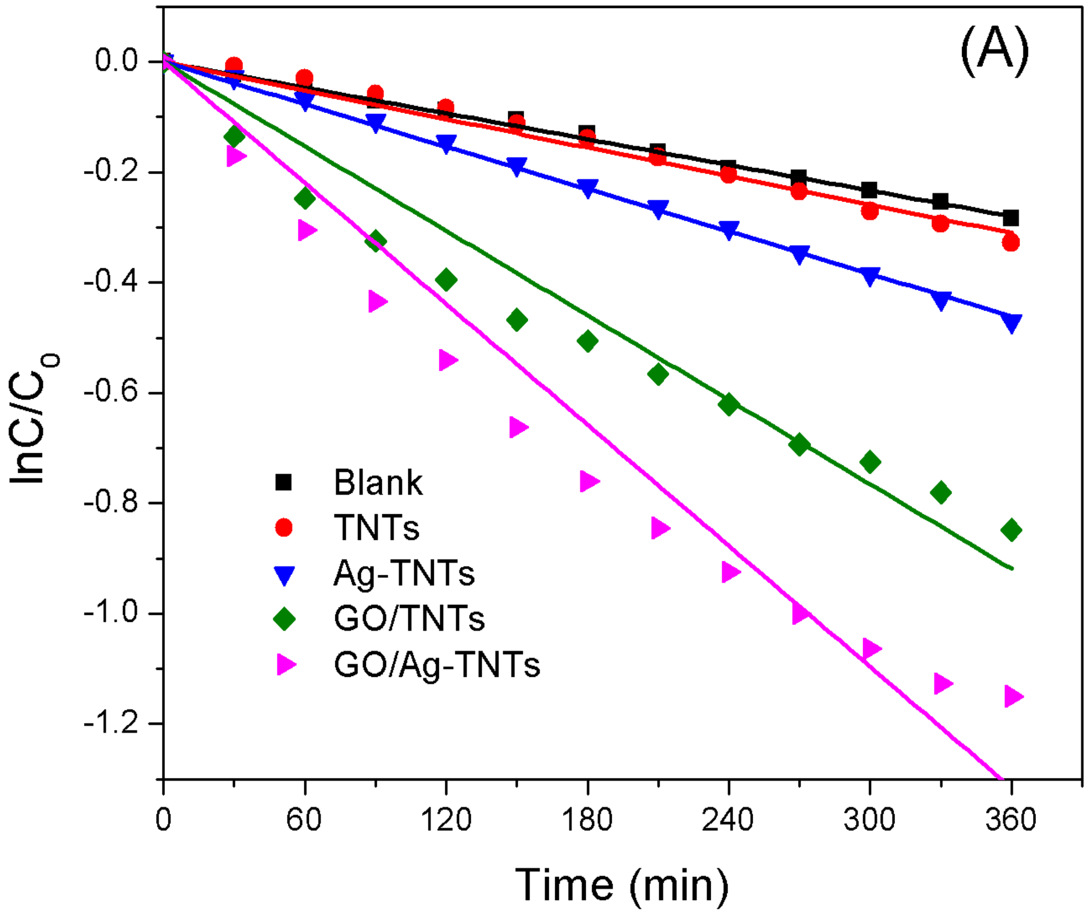

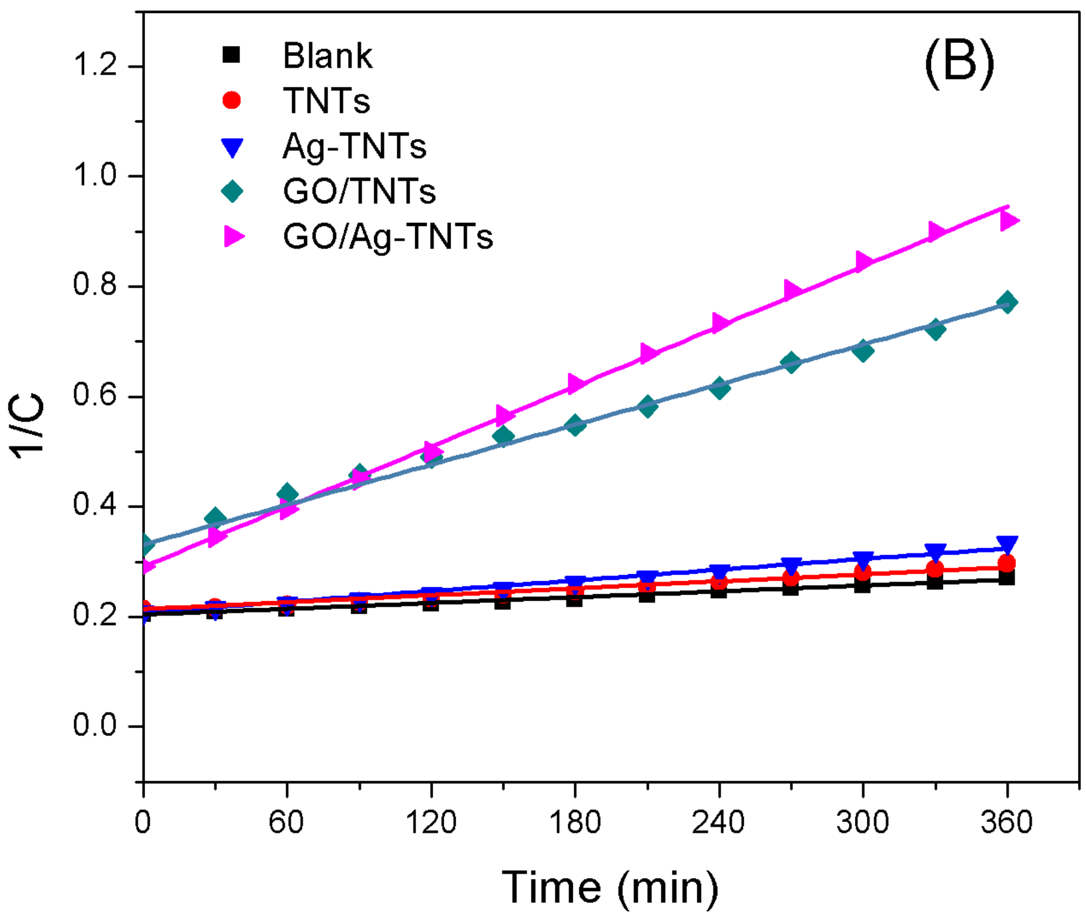

Figure 4.44: Fitted kinetic plots for MB degradation (a) first order and (b) second order

Table 4.9: Obtained kinetic parameters for 2-CP degradation

		1st Order Kinetic			
	Blank	**TNTs**	**Ag-TNTs**	**GO/TNTs**	**GO/Ag-TNTs**
R^2	0.98704	0.98724	0.9905	0.9917	0.98586
k	0.00113	0.00147	0.00226	0.00209	0.00285
		2nd Order Kinetic			
R^2	0.99859	0.99769	0.99318	0.99429	0.98598
k	0.00015	0.000215077	0.000393487	0.00034641	0.000543231

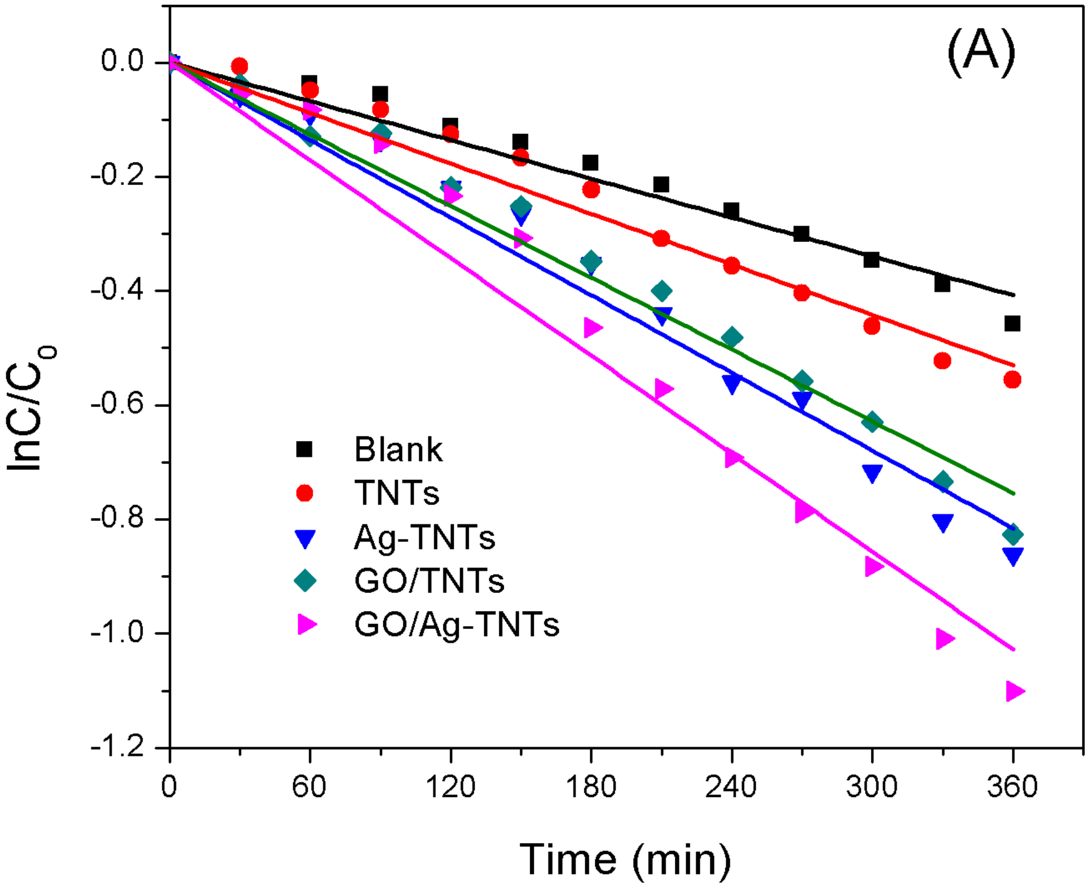
(A)
lnC/C$_0$
0.0
-0.2
-0.4
-0.6
-0.8
-1.0
-1.2
0
60
120
180
240
300
360
Time (min)
Blank
TNTs
Ag-TNTs
GO/TNTs
GO/Ag-TNTs

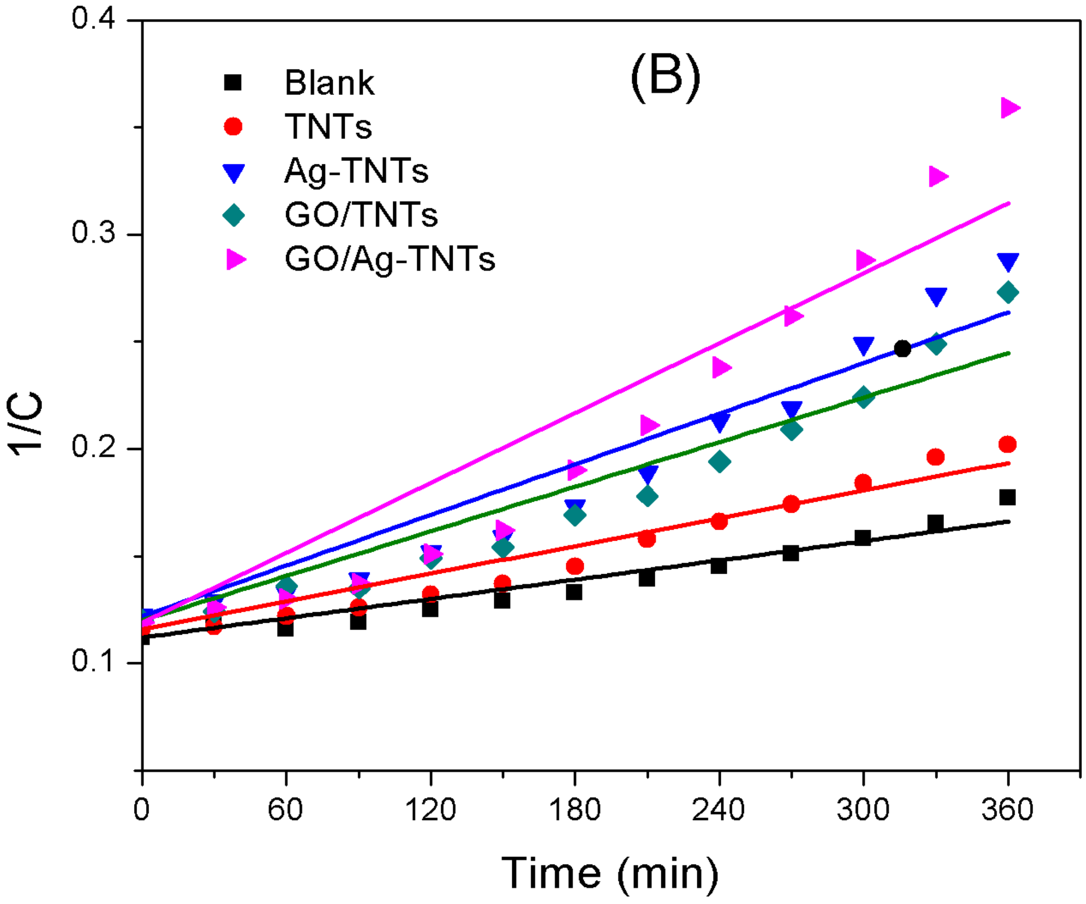

Figure 4.45: Fitted kinetic plots for 2-CP degradation (a) first order and (b) second order

Overall the consideration of the GO and Ag as an engulfing agent extended their support and emerged the TNTs with excellent visible light utilization, charge separation and reusability. The prepared photocatalyst proved its ability as a potential candidate for toxic organics removal. These prosperous outcomes laid a pathway with great motivation to implement them for anchoring "artificial photosynthesis" that addresses the greenhouse gases issue and alternative energy simultaneously. Therefore the thesis streamlined to the respective realm. This was approached more precisely by engulfing RGO and Pt as a foreign agent or impurities for TNTs.

4.5 Engulfing Conducting Carbon Material and Noble Metal: RGO/Pt-TNTs Ternary Composite

In recent years, studies devoted to graphene-TiO_2 nanocomposite are limited only to the organic pollutants photodegradation applications (Sun et al., 2014; Wang et al., 2013d; Shah et al., 2013) whereas photocatalytic conversion of CO_2 utilizing visible light are not widely considered. This encouraged the thesis direction towards the photocatalytic conversion of CO_2 to CH_4 with the help of RGO as a proficient electron trapper to overwhelm the recombination of photoinduced electron-hole pairs. Simultaneously, the employed Pt NPs empower the light absorption skill in visible region. To the best of our knowledge, this is the first accomplishment that employed engulfed RGO and Pt NPs with highly ordered TNTs for the “artificial photosynthesis process” i.e., photocatalytic conversion of CO_2 and H_2O to light hydrocarbon namely CH_4 excited by photons derived from visible light spectrum. Engulfing the RGO and Pt on TNTs shifted the material science paradigm of the TNTs and became a robust photocatalyst that could anchor the above said challenging task. The successfulness of the prepared combination is debated as below.

The anatomy of the prepared photocatalysts is shown in Fig. 4.46(a-b). Fig. 4.46a reveals the structural image of RGO/Pt-TNTs with a precious measurement on the geometry of the prepared nanotubes. The images ratify nanotube length as 8−9 μm. The observed anatomy signifies the two-dimensional transparent RGO sheets with wrinkles and engulfed the TNTs surface uniformly with Pt NPs (Fig. 4.46b). It is also diagnosed that the morphology of the TNTs remained unscuffed after the encapsulation of the impurities.

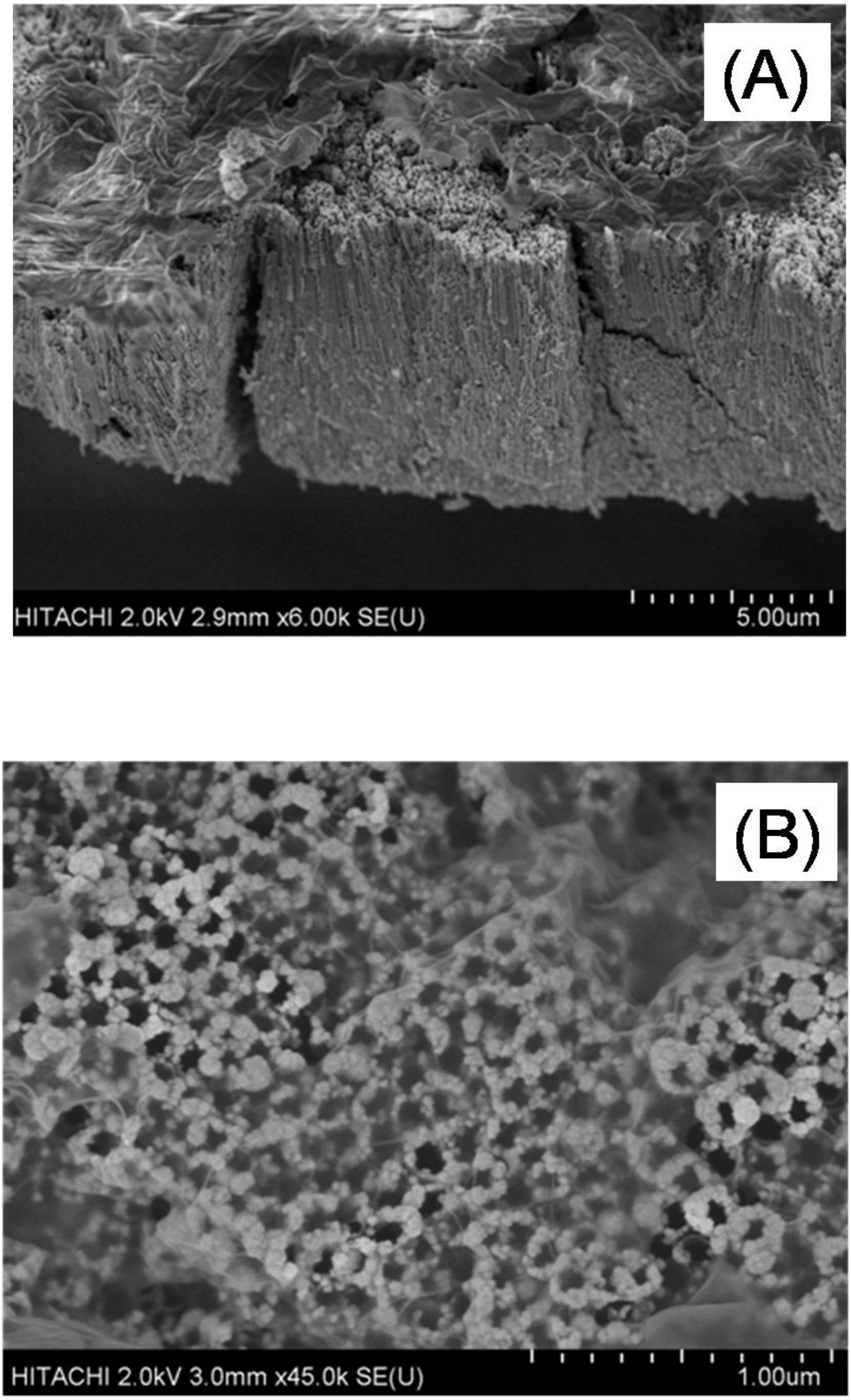

Figure 4.46: Electron microscopy images of: (a) cross-section of RGO/Pt-TNTs and (b) top view of RGO/Pt-TNTs

The presence of the specific elements in the composite was confirmed by obtained EDX spectrum, shown in Fig. 4.47. As illustrated in Fig. 4.48a, Pt NPs were fairly dispersed on the TNTs surface and inside the tubes. The synthesized Pt and TiO_2 were clearly identified by the lattice fringes recorded in the high resolution-transmission electron microscopy (HRTEM) image of RGO/Pt-TNTs (Fig. 4.48b). The lattice fringes with spacing of 0.23 nm and 0.35 nm were mapped to (1 1 1) and (1 0 1) planes of Pt and anatase TiO_2, respectively (Feng et al., 2011; Sim et al., 2013).

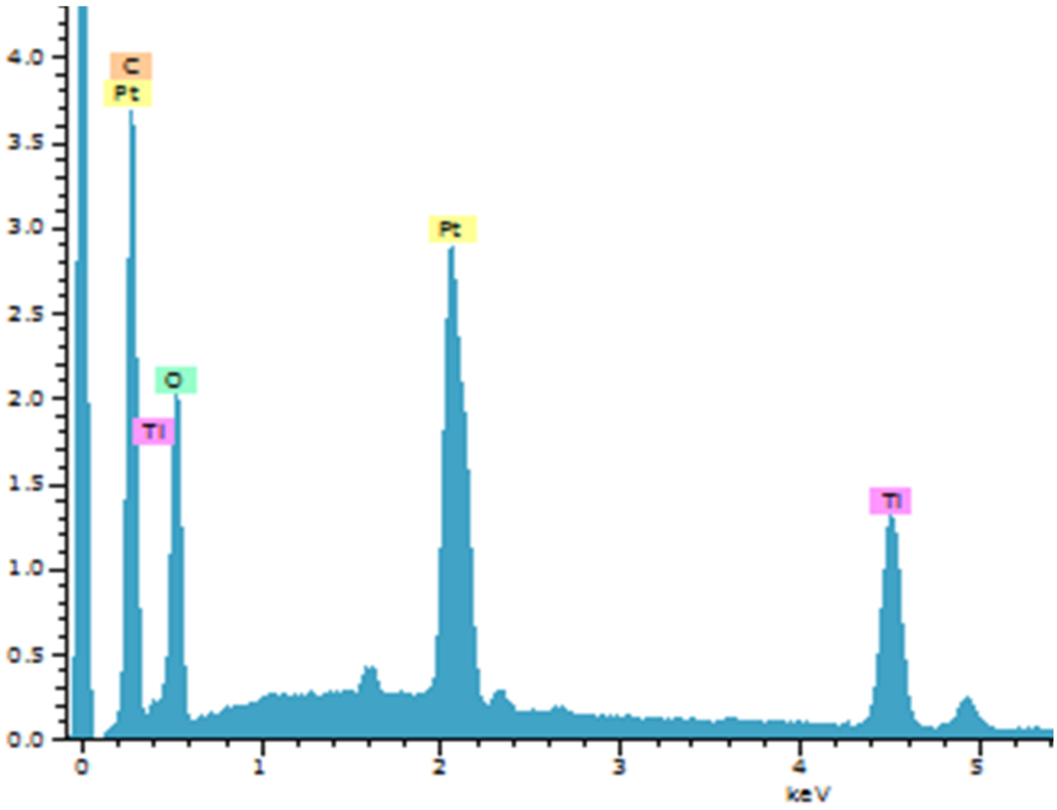

Figure 4.47: EDX of RGO/Pt-TNTs

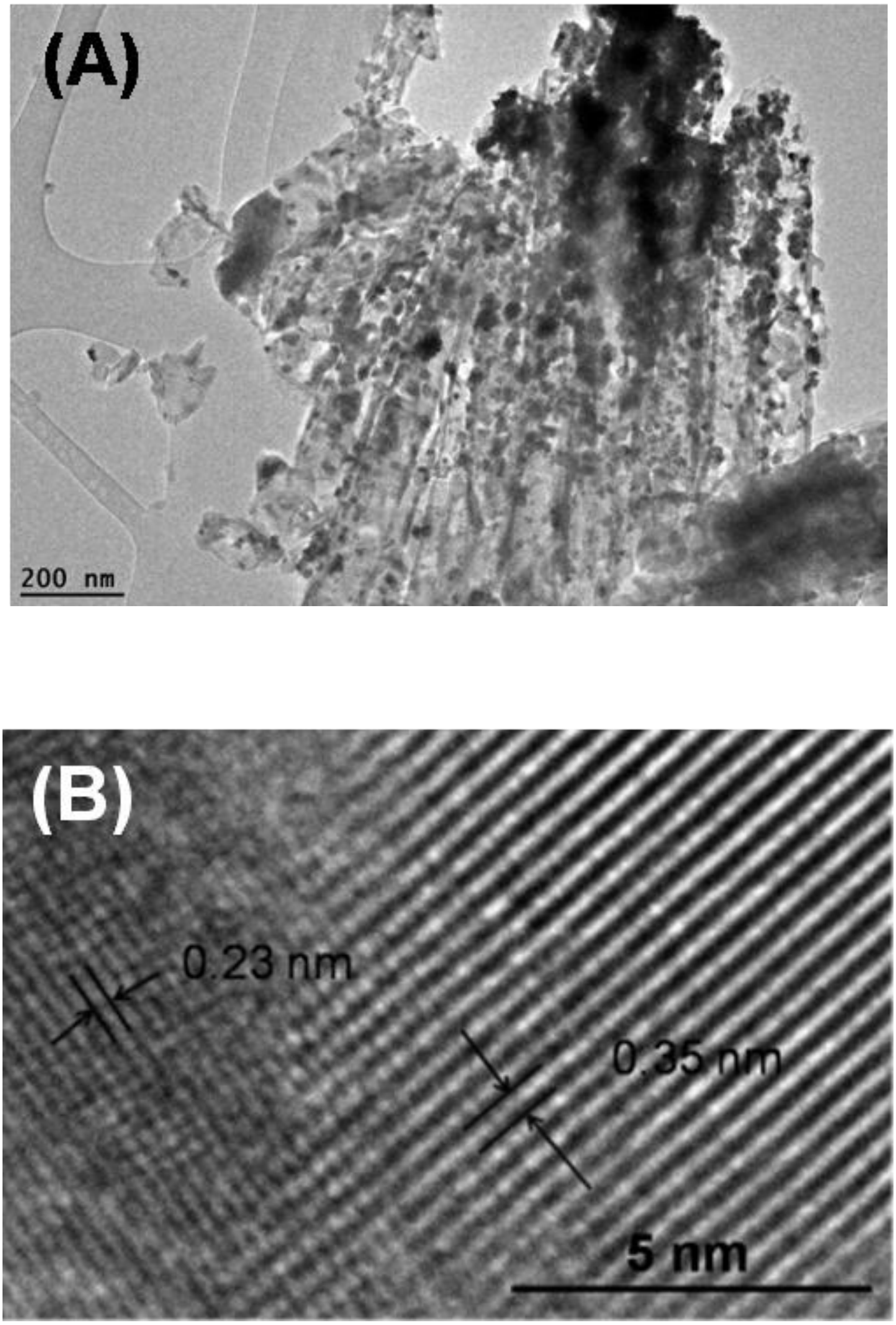

Figure 4.48: (a-b) High resolution electron microscopy images of RGO/Pt-TNTs

Fig. 4.49 depicts the XRD patterns of TNTs, Pt-TNTs and RGO/Pt-TNTs. The sharp diffraction peak at 25.3 ° correspond to (1 0 1) crystal plane of anatase TiO_2 (JCPDS no. 21-1272) was well observed for all TNTs based photocatalysts. Significant Pt peaks were observed for both Pt-TNTs and RGO/Pt-TNTs at 40 °, 46.2 ° and 67.4 ° assigned to (1 1 1), (2 0 0) and (2 2 0) planes of face centered Pt, respectively. The mean crystallite size of Pt was found to be 7.1 nm through Scherrer equation (Eq. 4.1). After the inclusion of Pt NPs onto TNTs matrix, insignificant change in the crystallite size of anatase TiO_2 in pure TNTs (18.59 nm) and RGO/Pt-TNTs (19.03 nm) was observed.

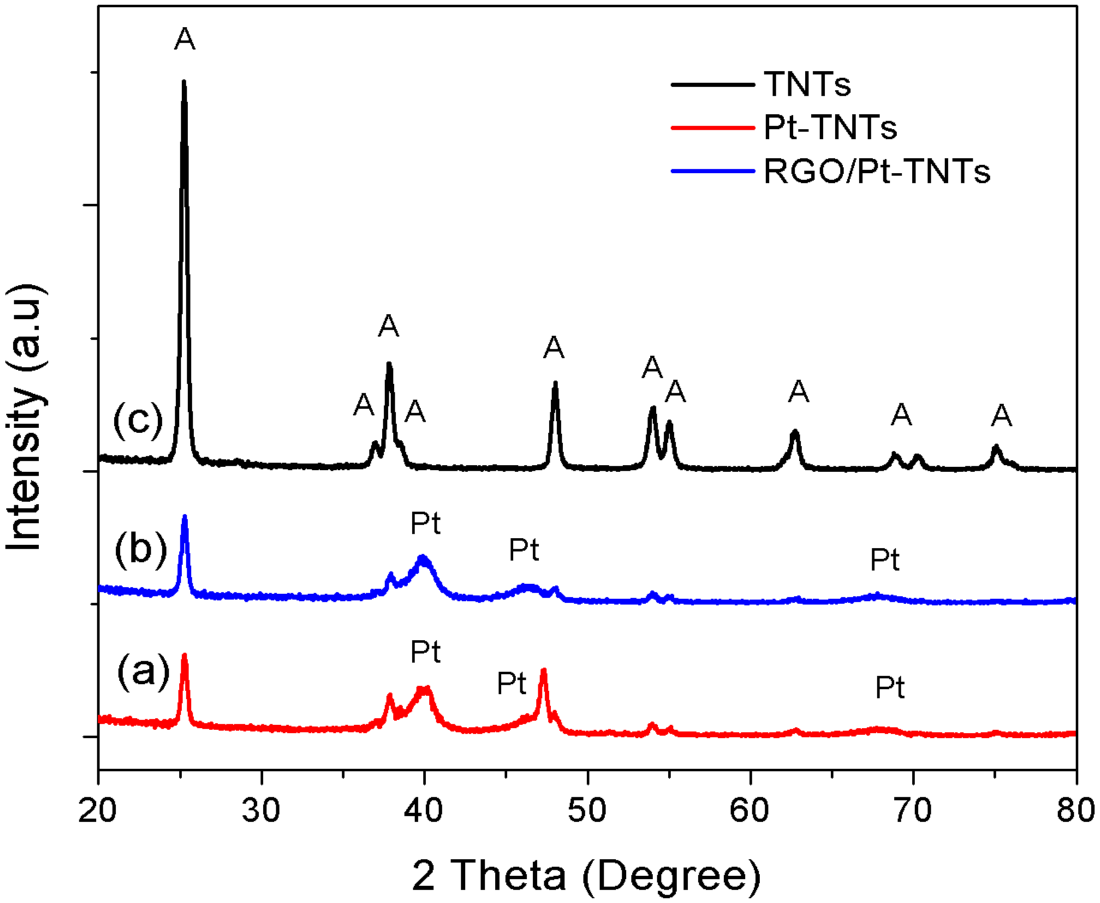

Figure 4.49: X-ray diffraction patterns of photocatalysts (a: Pt-TNTs; b: RGO/Pt-TNTs; c: TNTs)

The XRD patterns of graphite GO and RGO are shown in Fig. 4.50. A (0 0 2) diffraction peak at 10.1 ° was attributed to GO, indicating the pristine graphite was oxidized into GO by expanding the *d*-spacing from 3.35 Å to 8.75 Å. This is because the oxygen-containing groups were attached to the GO sheets and they still stacked with each other regularly (Zhang et al., 2011; Guo et al., 2013). After the rapid thermal reduction of GO, a peak at around 25 ° corresponding to an interlayer spacing of 0.35 nm was observed for RGO, which was slightly smaller than that of pristine graphite. There was no peak attributed to RGO can be observed in RGO/Pt-TNTs due to the similar effect seen in the preceding sections.

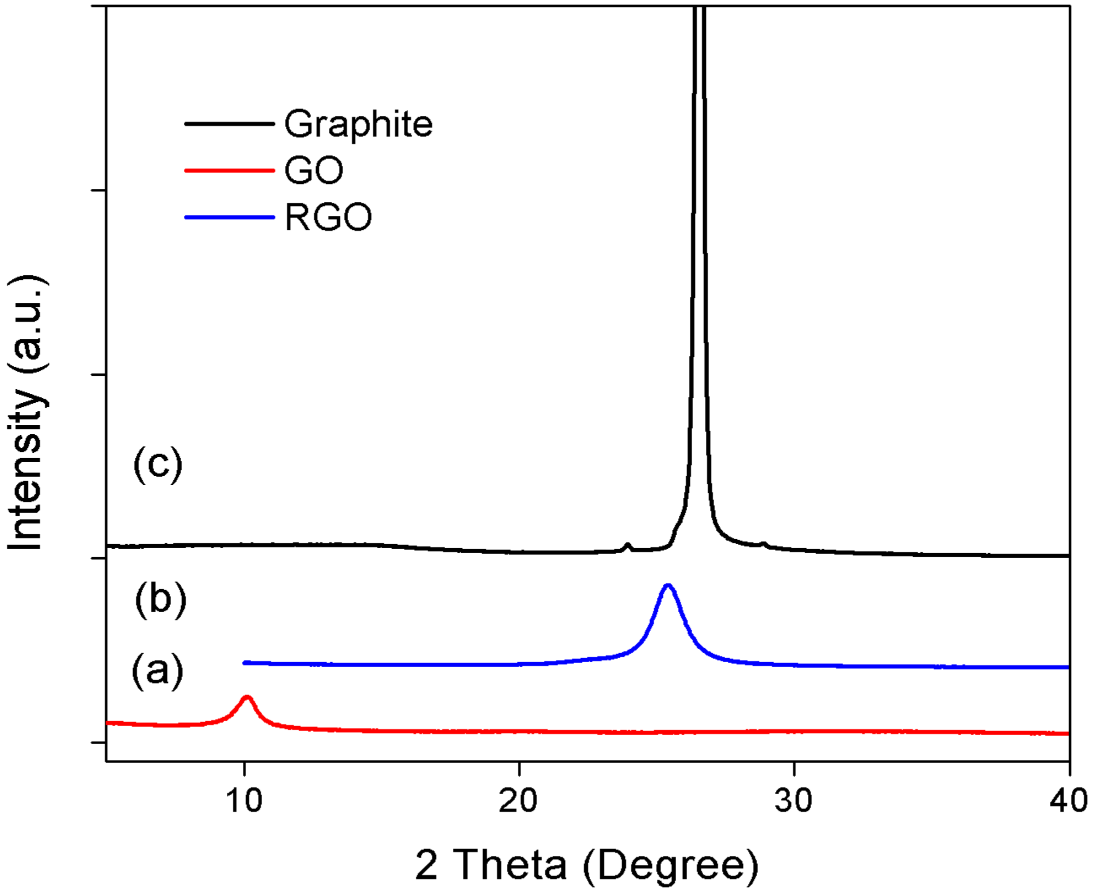

Figure 4.50: X-ray diffraction patterns of carbon materials (a: GO; b: RGO; c: Graphite)

The UV-visible diffuse reflectance spectra that endorse the visible light responsiveness characters of the photocatalyst are shown in Fig. 4.51a. The pure TNTs exhibited an ascended absorption band moderately around 380 nm (UV region) owing to the charge transfer from O 2p valence band to Ti 3d conduction band as seen in the preceding findings of the thesis (Fuerte et al., 2002). The expected surface plasmon band for Pt was clearly observed at around 450 nm as shown in Fig. 4.51b, and guided the absorption edge of Pt-TNTs shifted towards the visible spectrum. In RGO/Pt-TNTs, the dark appearance of carbon species from RGO played a great role reducing the light reflection (Zhang et al., 2010a; Yu et al., 2010) and thus, stepping up the absorption of visible spectrum.

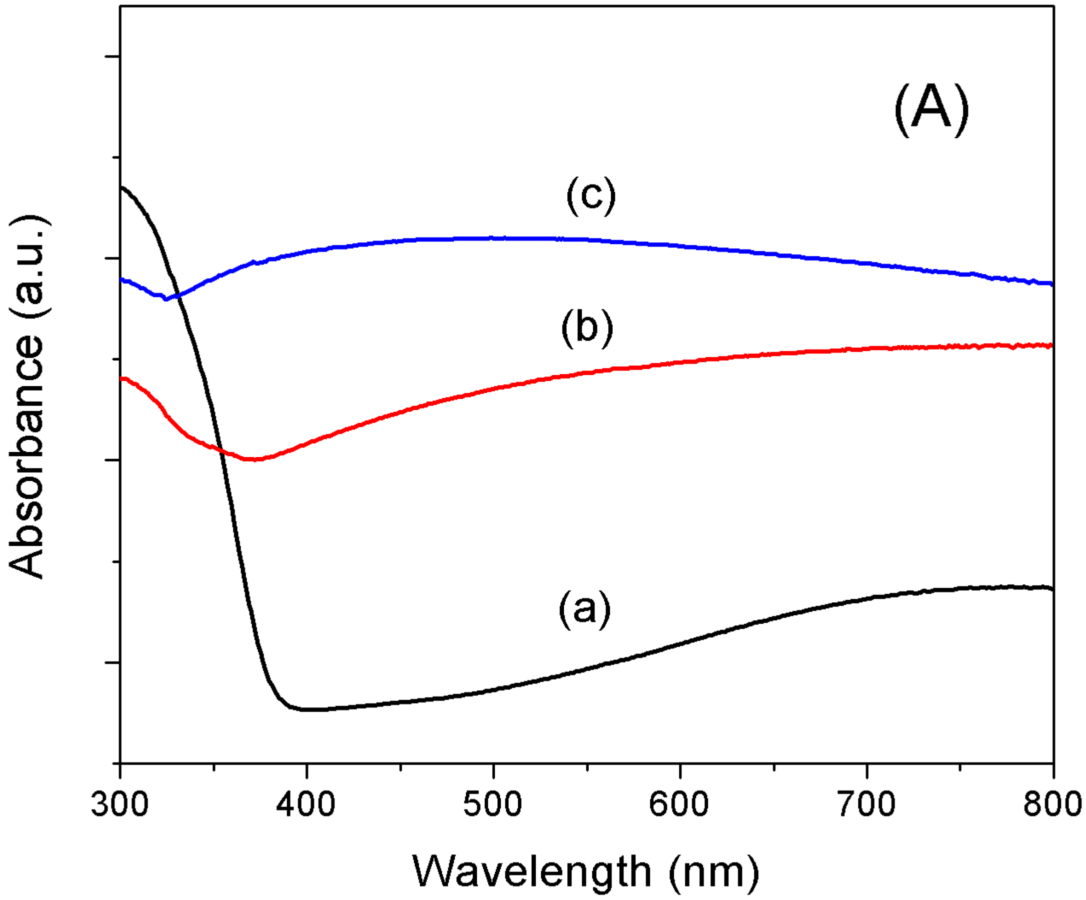

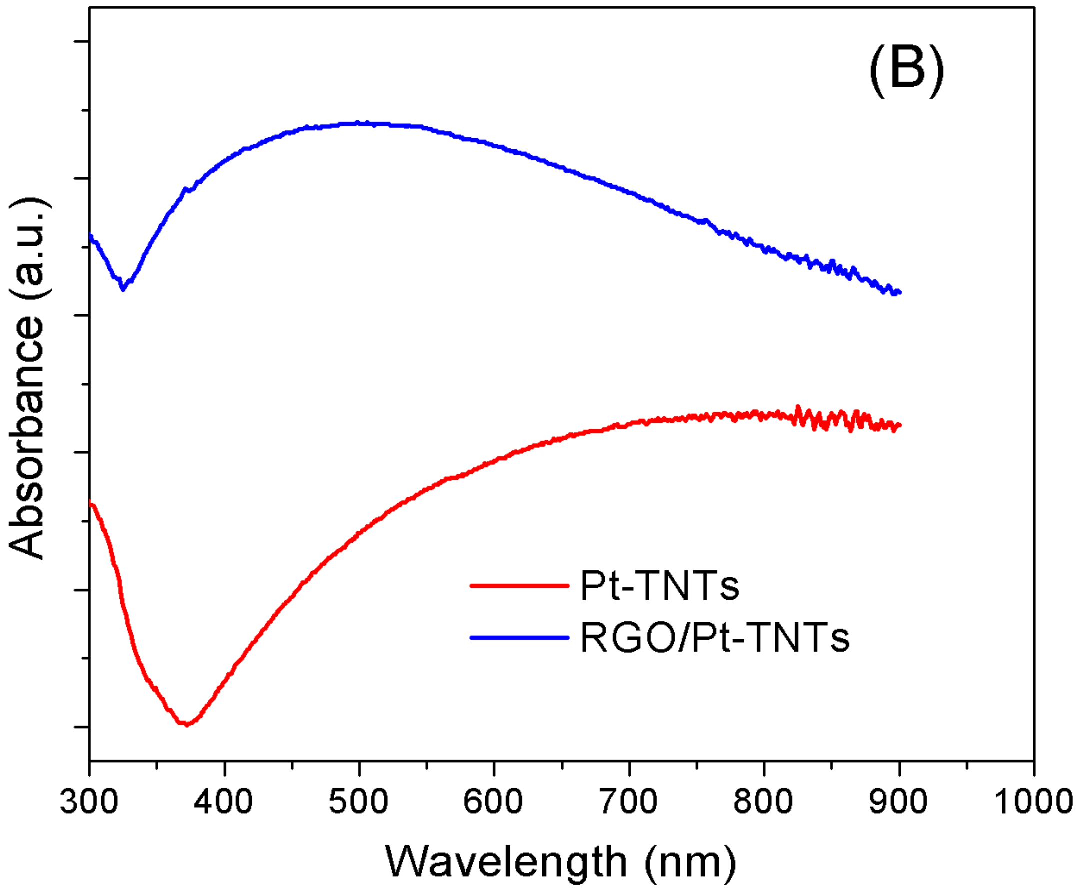

Figure 4.51: UV-visible absorption spectra of (a) photocatalysts (a: TNTs; b: Pt-TNTs; c: RGO/Pt-TNTs) and (b) enlarged absorption band for Pt-TNTs and RGO/Pt-TNTs

Fig. 4.52 depicts the FTIR spectra of the obtained samples. The spectrum of GO exhibited broad O-H stretching in the 3100−3400 cm^{-1}, C=O stretching vibrations in carbonyl and carboxyl moieties (1720 cm^{-1}), C=C skeletal vibration bands from unoxidized graphitic domains (1620 cm^{-1}), carboxyl group (1375 cm^{-1}), epoxide C-O-C or phenolic C-O-H stretching vibrations (1220 cm^{-1}), and C-O stretching vibrations in epoxy or alkoxy groups (1045 cm^{-1}) (Shah et al., 2013; Xu et al., 2008; Guo et al., 2009). For RGO, the peak corresponding to the stretching vibrations from the oxygen functional groups (O-H, C=O, C-O, C-O-C and C-O-H) was significantly diminished by deoxygenation. The absorption peaks appeared at 800 cm^{-1} was assigned to a combinatorial effect of Ti-O-Ti vibration in crystalline TiO_2 and Ti-O-C vibration as a result of the interaction between the functionalities in RGO and TNTs (Sakthivel and Kisch, 2003).

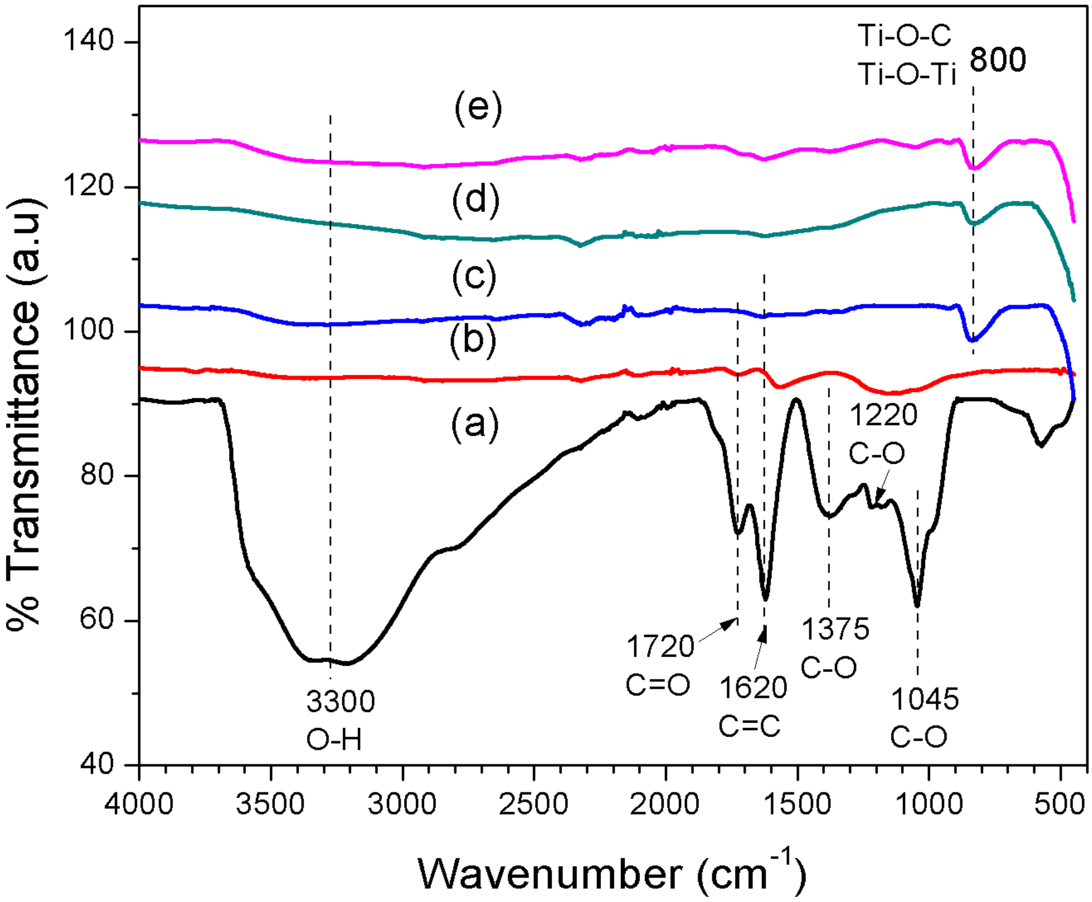

Figure 4.52: FTIR spectra of (a) GO (b) RGO (c) TNTs (d) Pt-TNTs and (e) RGO/Pt-TNTs

The analysis was carried to Raman spectroscopy in order to explicit the ordered and disordered crystal structures of carbon based materials. As usual, the anatase of TiO_2 was double confirmed in the Raman spectra and peaks at the corresponding wavenumber are seen in Fig. 4.53a. A typical Raman spectra exhibited by the carbon materials (Fig. 4.53b) unveiled the prominent peaks at 1350 cm^{-1} and 1600 cm^{-1}, corresponding to the D- and G-bands, respectively. The significance of this attained G-and D-band was well clarified in the previous section and the same was observed here. The in-plane vibrational mode involving sp^2-bonded carbon atoms, whilst D-band is known as the sp^3 defects arising from the disruption in the sp^2 bonding that includes vacancies, heptagon and pentagon rings, edge effect and etc. (Chen et al., 2010; Bajpai et al., 2012). In comparison to graphite, GO registered a sharper D-band due to the introduction of oxygenated groups. Their G-band broadened because of the enhanced isolated double bonds (Wang et al., 2013b). The I_D/I_G peak intensity ratio was calculated to characterize the level of defect in RGO. When GO was reduced to RGO, the ratio of I_D/I_G decreased from 0.75 to 0.60, indicating the partial restoration of sp^2-hybridized network due to the removal of oxygenated functional groups that elevated the defect level.

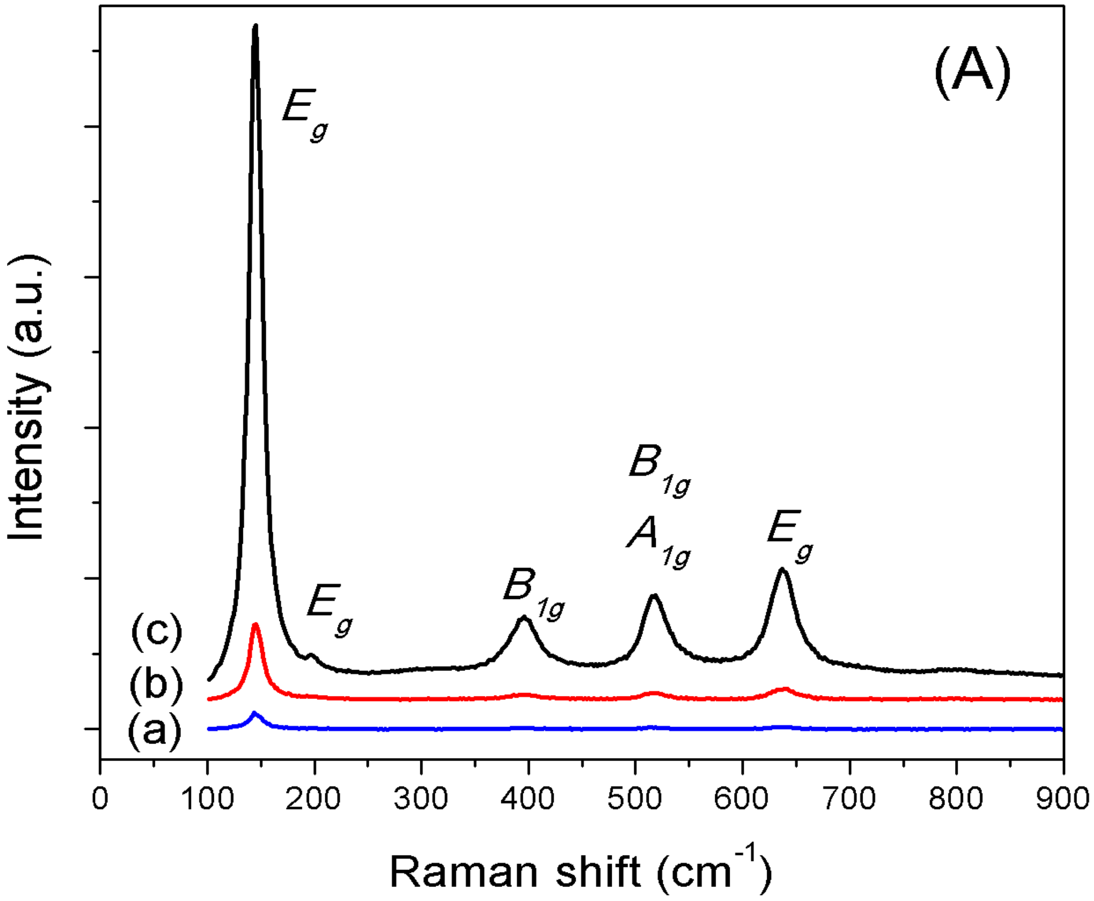

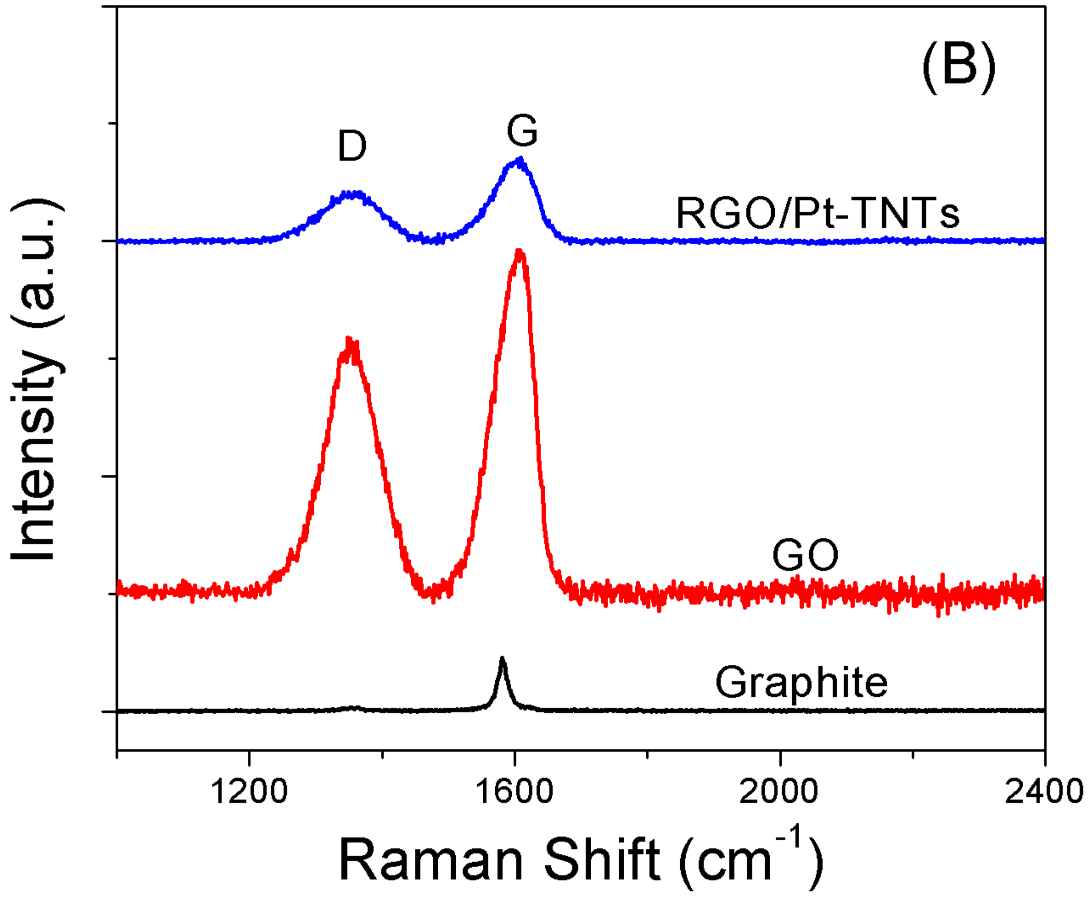

Figure 4.53: Raman spectra of anatase TiO_2 in (a) photocatalysts (a: RGO/Pt-TNTs; b: Pt-TNTs; c: TNTs) and (b) D- and G-band of graphite, GO and RGO/Pt-TNTs

The light emission spectra from the prepared photocatalysts after the absorption of photons are presented in Fig. 4.54. The shown spectrum reveals the significance of the engulfed impurities. The inclusion of Pt and the combined LSPR accredited the separation and recombination properties. The additional consideration of the RGO stimulated suppression of the recombination of the photogenerated electron-hole pairs. This proved the physical and chemical influence of both RGO and Pt as an efficient electrons trapper to overcome the predominant recombination principle exerted by the electron-hole pairs. Naturally this will reflect a boon effect in the photocatalytic performance.

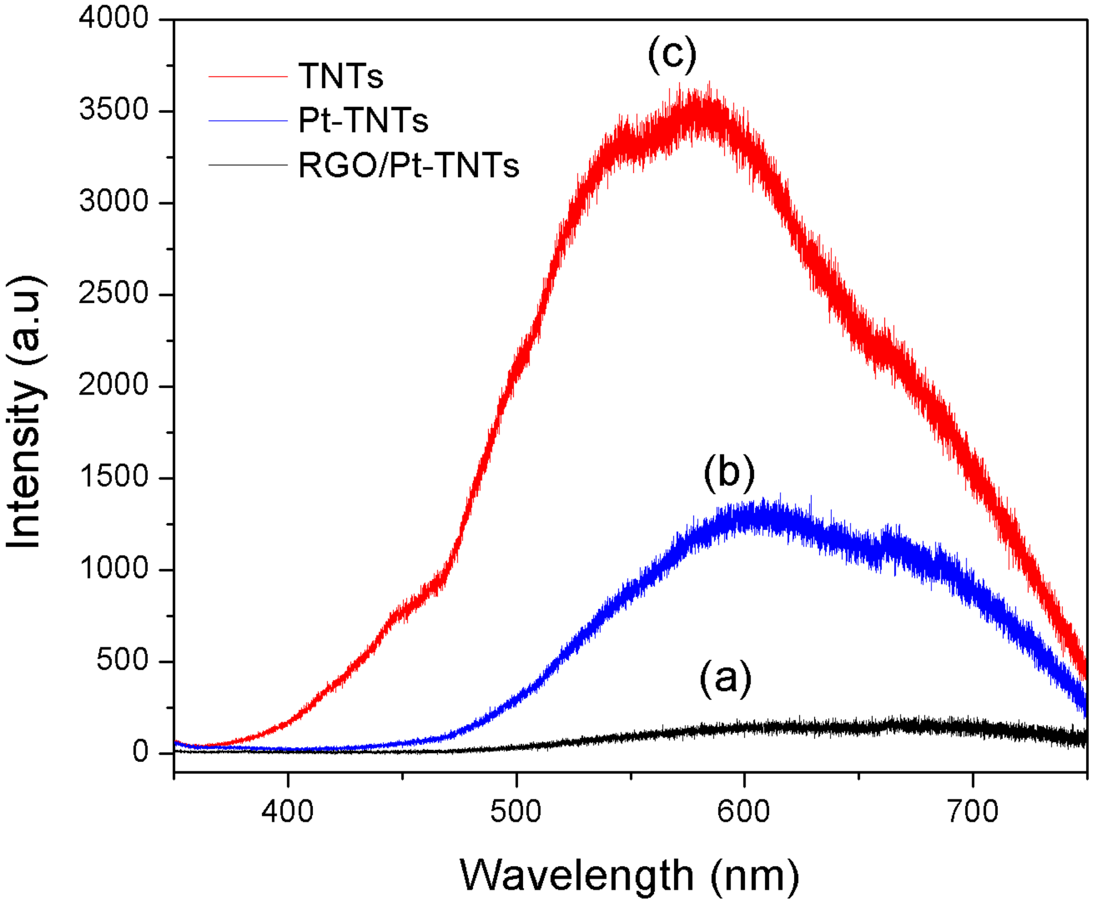

Figure 4.54: Photoluminescence spectra of TNTs, Pt-TNTs and RGO/Pt-TNTs

The chemical states of C, Ti and Pt in RGO/Pt-TNTs were investigated by XPS and the obtained results are depicted in Fig. 4.55. As shown in Fig. 4.55a, the C 1s spectra of RGO/Pt-TNTs was deconvoluted into three peaks with binding energies at 284.4, 285 and 288.4 eV, attributable to the sp^2 hybridized carbon, sp^3 hybridized carbon and C=O oxygenated carbon species, respectively. The disappearance of some oxygenated carbon species at higher binding energies such as C-OH, C=O and COOH suggests that the oxygen-containing functional groups were removed to a great extent for RGO. The absence of peak correlated to Ti-C and Ti-O-C bonds proved the physical attachment of RGO to the surface of TNTs (Akhavan et al., 2010). The deconvolution result of Pt 4f (Fig. 4.55b) shows that the peaks at binding energies 70.9, 71.4 and 74.4 eV were assigned to Pt^0, while peak at 75.3 eV was attributed to Pt^{4+}. The chemical states of Pt NPs were mainly Pt^0 (90.2%), with less than 9.8% of Pt^{4+}. From Fig. 4.55c, there were two peaks observed at 459 eV (Ti $2p_{3/2}$) and 464 eV (Ti $2p_{1/2}$), both corresponded to Ti^{4+} in pure anatase. From the obtained detailed chemical configuration, the visible light absorption properties of RGO/Pt-TNTs cannot be correlated to the Pt impurity (Pt^{4+}), oxygen vacancies and Ti^{3+} ions. Hence, the insight from the analysis suggested that the LSPR effect of Pt NPs more likely contributed for the visible light enhancement.

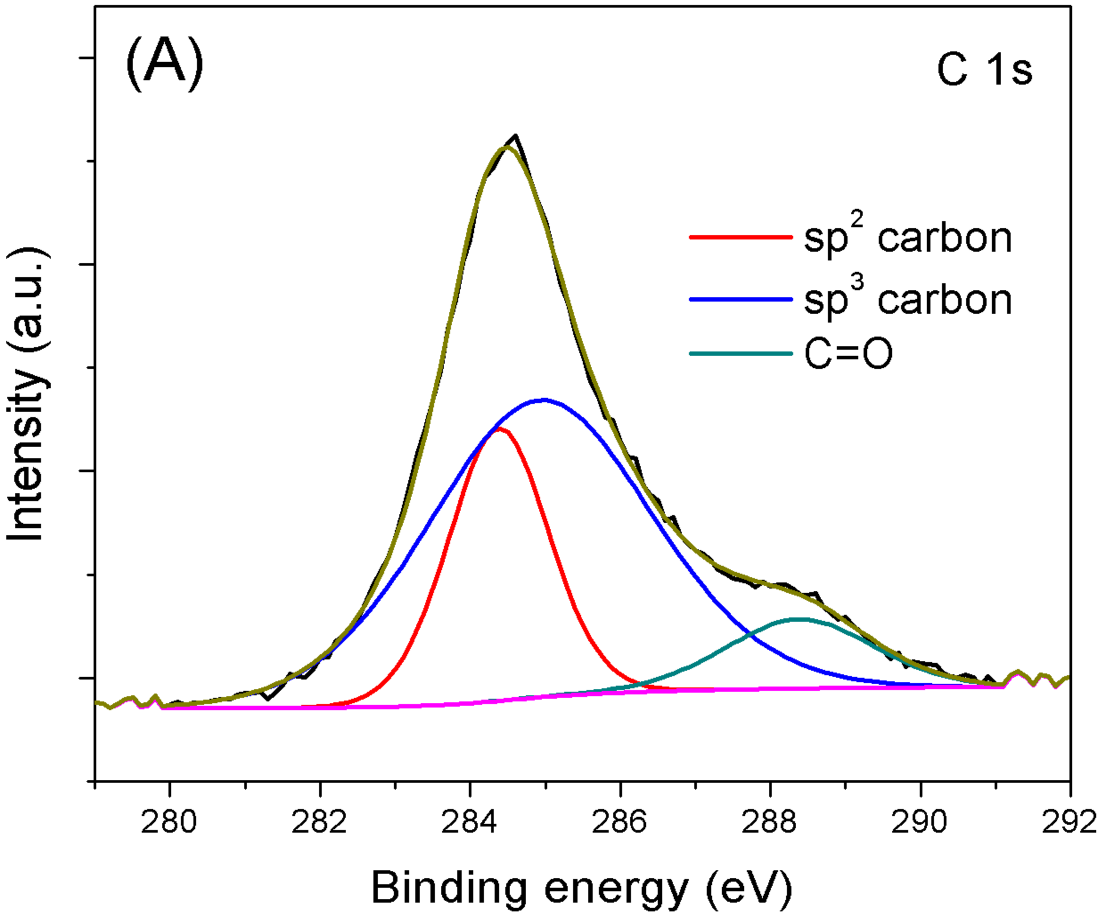

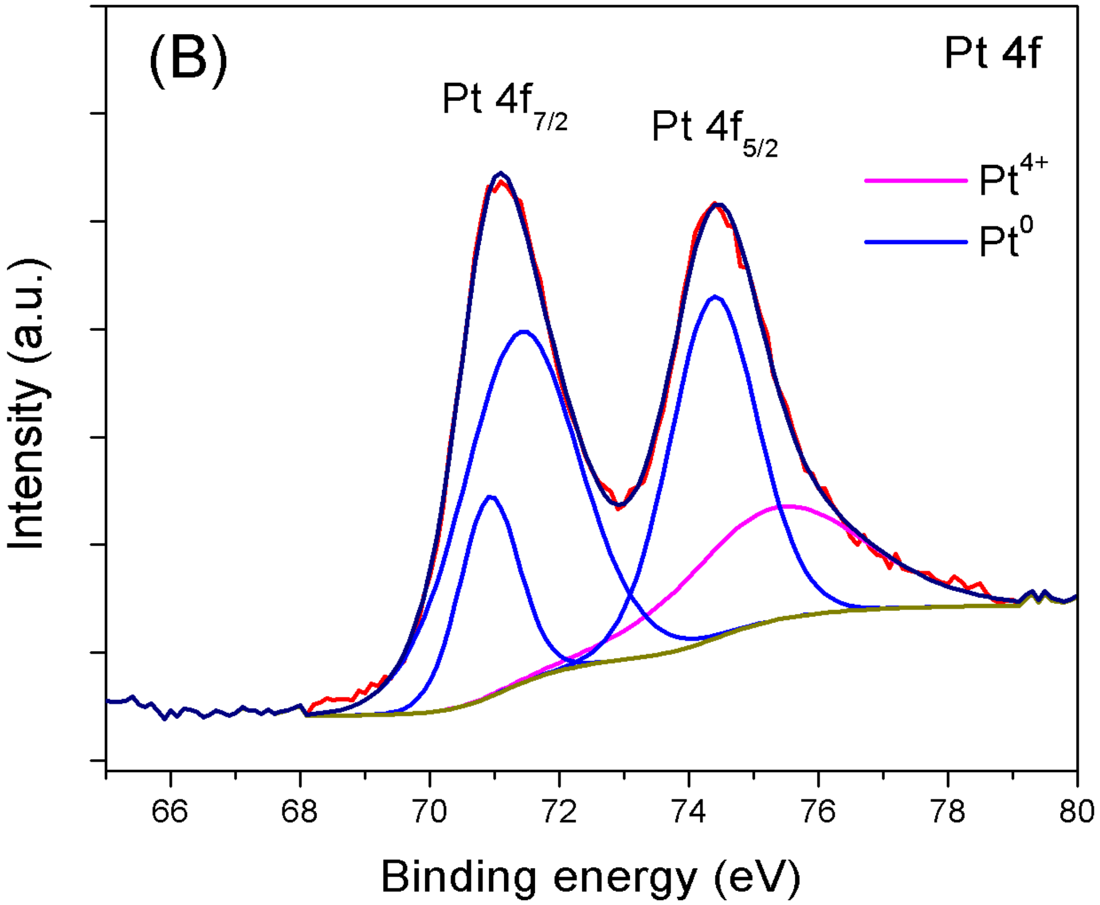
(B)
Pt 4f
Pt 4f$_{7/2}$
Pt 4f$_{5/2}$
Pt^{4+}
Pt^{0}
Intensity (a.u.)
66
68
70
72
74
76
78
80
Binding energy (eV)

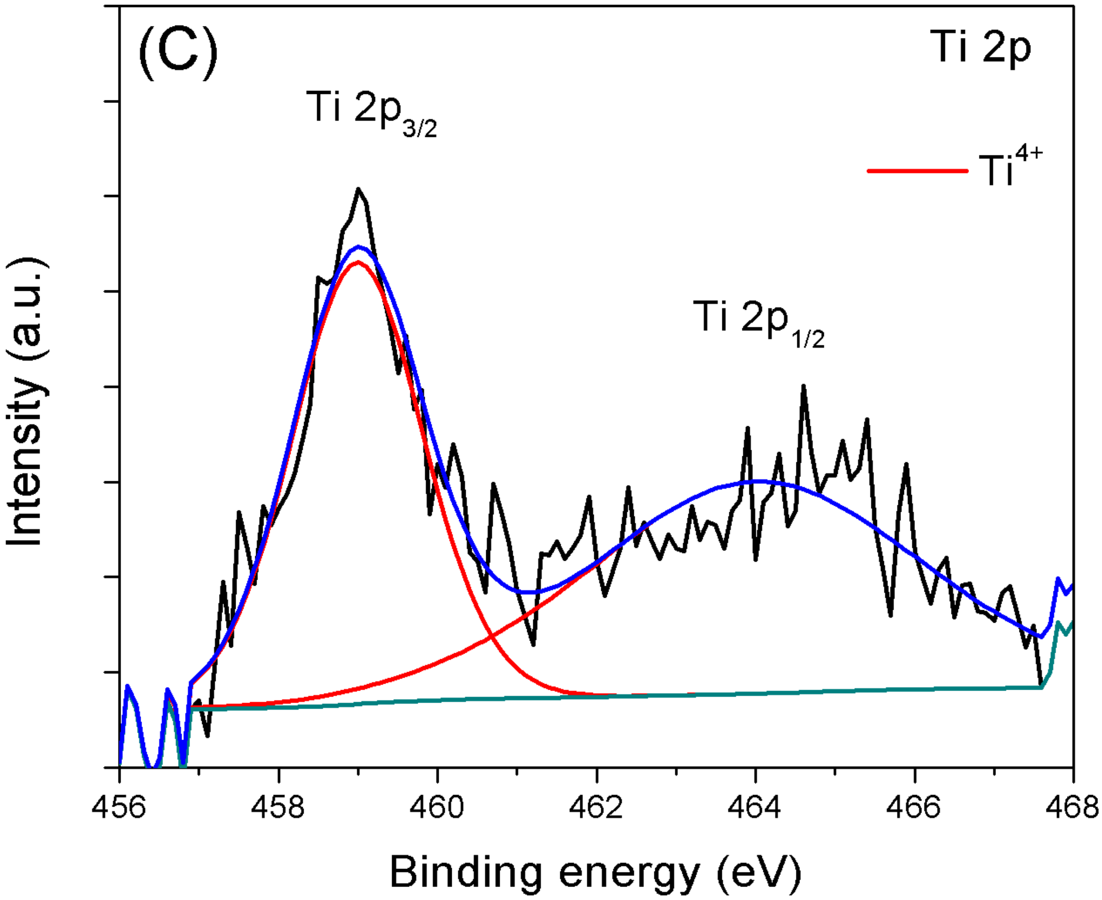

Figure 4.55: Core level XPS spectra of (a) C 1s, (b) Pt 4f and (c) Ti 2p of RGO/Pt-TNTs

The photocatalytic activities of all the prepared photocatalysts were evaluated for the conversion of inorganic CO_2 with water vapour (H_2O) to CH_4 and the reaction was driven by the photons contributed from the visible light irradiation. The formation of CH_4 was not detected either in the absence of light irradiation or photocatalyst, ratifying that CH_4 was not produced as a consequence of photo-decomposition of organic residues in the photocatalyst. It also further vindicates that reduction of CO_2 occurred solely in the presence of photocatalyst and light irradiation. The product formed in the challenging reaction is shown in Fig. 4.56. It was evident from the figure that product (CH_4) rate increased with irradiation time and peaked a maximum following ascending order TNTs (1.39 ppm) < RGO-TNTs (1.40 ppm) < Pt-TNTs (1.42

ppm) < RGO/Pt-TNTs (2 ppm). Further 4 h of reaction time, CH_4 formation started to decline, this was dominantly expressed by both pure TNTs and RGO-TNTs than that of the rest of combinations. This phenomenon was defeated by loading Pt NPs that speculated to generate more electrons for the CO_2 photoreduction process owing to the LSPR. The contact between Pt NPs and TNTs resulted in a better average CH_4 production rate for Pt-TNTs (1.26 ppm cm^{-2} h^{-1}) compared to that of TNTs (1 ppm cm^{-2} h^{-1}) and RGO-TNTs (1.07 ppm cm^{-2} h^{-1}) (see Fig. 4.57). In the absence of Pt NPs, the presence of RGO in RGO-TNTs resulted in a similar effect as seen in TNTs, because the RGO seldom contributed for the visible light absorption.

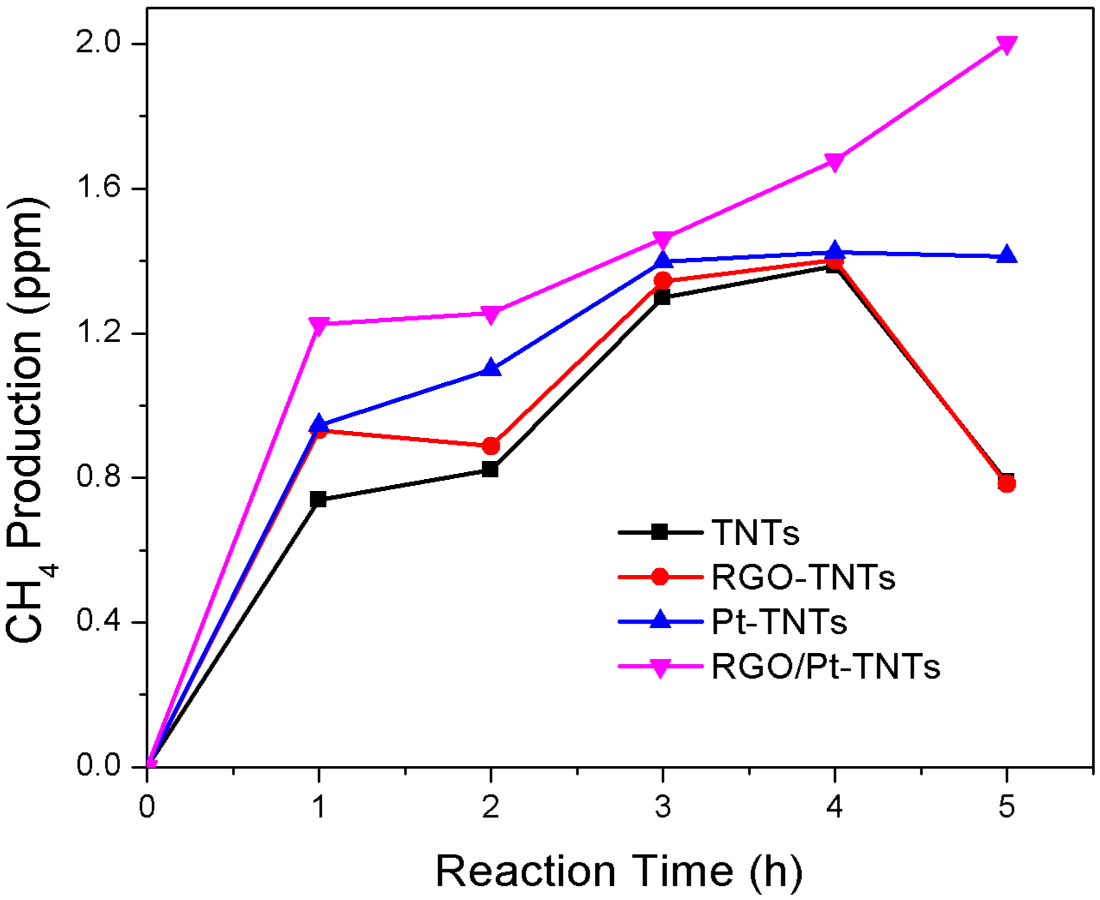

Figure 4.56: Time dependence on the production rate of CH_4

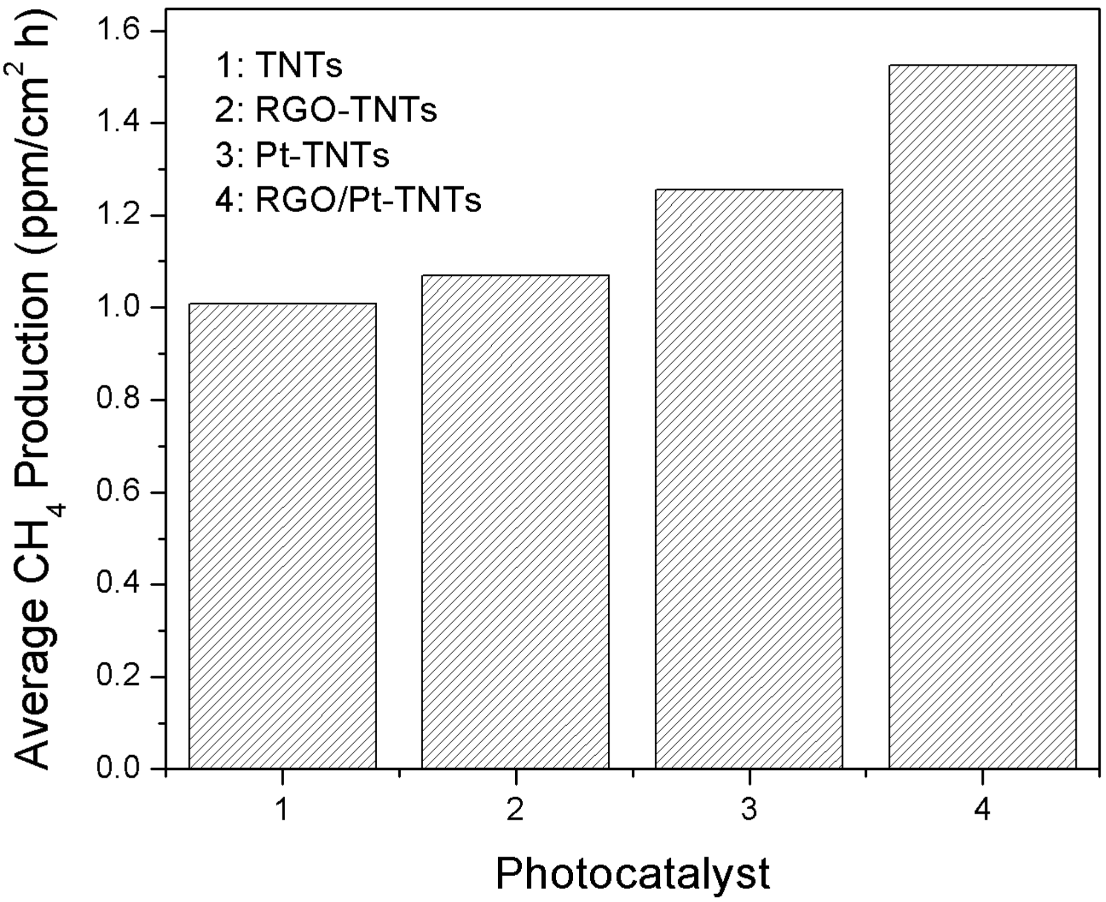

Figure 4.57: Average production rate of CH_4 of prepared samples

Where else the presence of Pt in the Pt-TNTs equalized the Fermi level (E_f) of TNTs to the working function of Pt NPs and thus the CB of TNTs became lower, facilitating electrons transfer from Pt NPs to CB of TNTs (Fig. 4.58). In the interface between Pt NPs and TNTs, the electron collision further excited the electron from VB to the CB of TNTs and left a hole at VB (Zhang et al., 2013). The electric field in the space-charge layer induced the holes transfer towards Pt NPs, where the oxidation reaction of surface absorbed species occurred. For the oxidation reaction, the adsorbed water molecules were oxidized to form hydrogen ions (H^+) and oxygen (O_2). It is generally believed that the electron-hole pairs recombination time (10^{-9} s) is much faster than the adsorption kinetic of the CO_2 molecules on TiO_2 (Woan et al., 2009; Hoffmann et al., 1995). These deficiencies were conquered by depositing RGO sheets onto the surface of Pt-TNTs to prolong the lifetime of electron-hole pairs. The RGO is well known for its two-dimensional and planar π-conjugation structure endorses the Pt-TNTs with outstanding electron conductivity (Xiang et al., 2011; Wang et al., 2008). In addition, the favourable work function of RGO (-4.42 eV) and CB of TNTs (-4.2 eV) promoted the electrons transfer from TNTs to RGO (Yang et al., 2010). As shown in Fig. 4.58, RGO sheets furnished a rapid pathway to trap the electrons from TNTs, leading to enhanced separation of charge carriers. The electrons trapped at RGO sites initially reacted with CO_2 to form CO, simultaneously hydrogen ions obtained through oxidation competed with CO_2 for the quenching of electrons and produced hydrogen. As-produced CO then reacted with hydrogen ion through reduction process to yield CH_4. When engulfing of Pt NPs and RGO onto TNTs was ultimate, the average CH_4 production rate increased steadily to 1.52 ppm cm^{-2} h^{-1} without any decline towards the end of reaction. The prolonged lifetime of the electrons and high adsorption capacity of the CO_2 molecules on the surface of RGO with large specific surface area contributed for such promising response.

In a summary, the initially developed binary composite nanophotocatalyst had poise in pros and cons. All these concerns were successfully overhauled by identifying appropriate impurities that sowed for the development of ternary composite. This harvested an incredible ternary composite photocatalyst that drastically transited the physical and chemical nature of the traditional photocatalyst with pivotal applications in both environmental cleanup and greenhouse gas reduction.

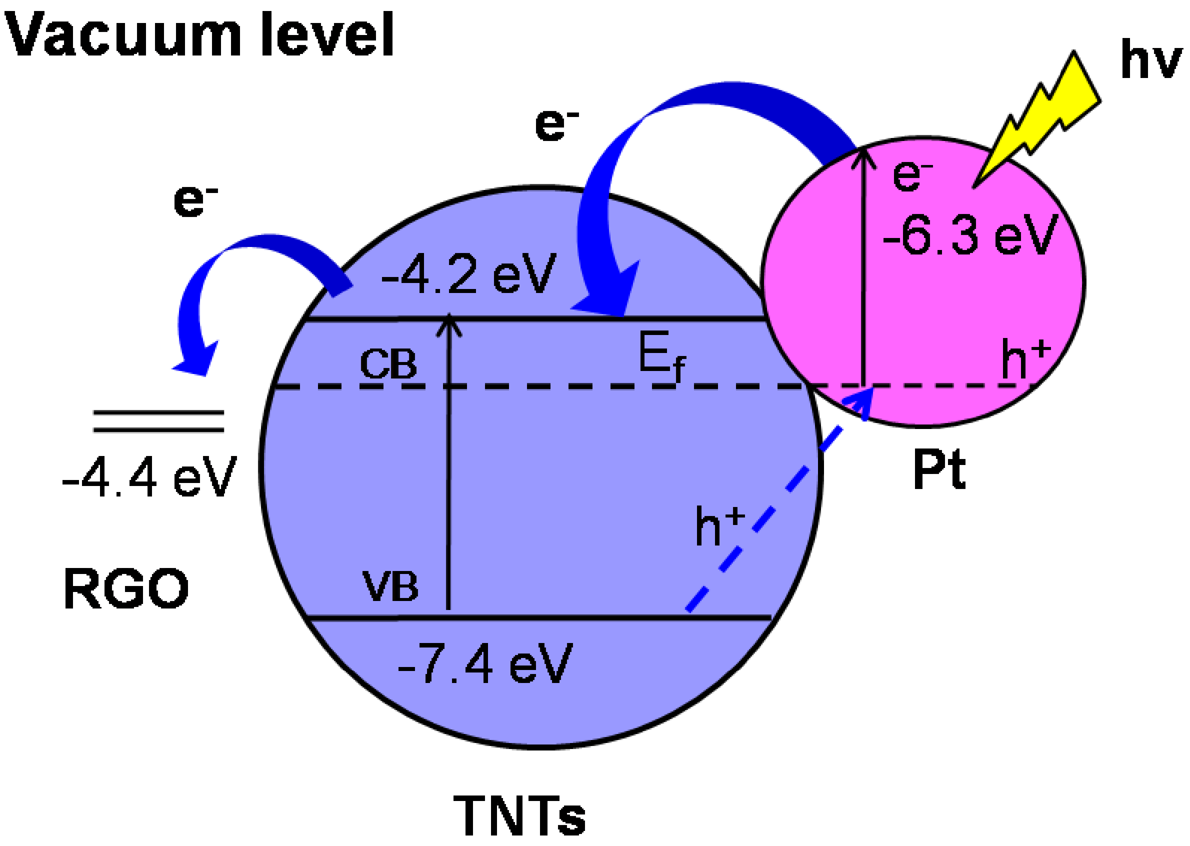

Figure 4.58: Schematic diagram of electron transfer and separation in RGO/Pt-TNTs

CHAPTER 5

CONCLUSIONS AND RECOMMENDATIONS

5.1 Conclusions

The foremost aim of this thesis was to develop highly ordered TNTs, which is solar and visible-light-active for cleanup and energy applications. The foresaid goal was successfully achieved by fabricating binary and ternary composite of different genera using TiO_2 nanotube arrays (TNTs) as a spinal. The most conclusive findings drawn from the thesis are listed below:

- The preliminary phase of modification resulted in binary composite with a simple mashing-up of the semiconductors, NiO and SnO_2. The substitutional introduction of the cations generated from semiconductors well endorsed the shift towards the visible light spectrum.

- The existed electric field at the p-n junction of NiO/TNTs binary composite played a crucial role in promoting superior charge carrier separation.

- The variation in the semiconductors loadings showed appreciable changes in the optical performance whereas an insignificant phenomenon was reflected for the solar photocatalytic activity.

- The prevailed issues in the mashing-up phase were upbeated successfully by engulfing Ag and GO onto the surface of TNTs through photodeposition followed by impregnation.

- The chosen conducting carbon material as an electron acceptor engulfant significantly suppressed the electron-hole pair recombination and was portraited by photoluminescence spectrum.

- The engulfed noble metal contributed exemplary visible light harvesting nature through the notable and distinctive plasmon effect.

- The acknowledgement of both noble and carbon compound contributed for a marvelous photocatalytic performance by degrading different genera of pollutants with a promising durability nature.

- The proposed degradation mechanism explicited the unique behaviour attributed to the pollutants genera.

- The final phase compiled the novelty and feasibility of photocatalytic conversion of CO_2 under visible-light irradiation. The developed RGO/Pt-TNTs ternary composite prototyped this challenging natural photoreaction to an energy derivate.

- Despite of the fact that the concentration of the product (CH_4) seemed to be negligible the realism of the making the successfulness of this artificial photosynthesis was a great accomplishment undoubtedly.

5.2 Recommendations

The following recommendations are taken into considerations for future research works.

- For the primary work, Lux meter was used to record the solar light intensity throughout the experiment. However, it was not capable to record the solar spectra over the spectrum region. Instead, the application of solar radiometers would give a clear picture of the radiations of solar spectrum. This can further provide a simulation platform for studying the influence of the radiation.

- The amount of hydroxyl radicals ($^{\bullet}$OH) and superoxide radical anion ($^{\bullet}$O$_2^{-)}$ could be quantitatively analysed for additional information on the surface reactions.

- For the real time implications and industrially feasibility, a scale-up study could necessitate in an appropriate reactor with hydrodynamics.

- The scale up could be considered by combining the developed technology with other oxidation techniques such as electrocatalysis, sonocatalysis/Fenton process, biodegradation and wetland technology to improve the total degradation efficiency of treating large quantities of wastewater (in real systems).

References

Abdelsayed, V., Moussa, S., Hassan, H. M., Aluri, H. S., Collinson, M. M., & El-Shall, M. S. (2010). Photothermal deoxygenation of graphite oxide with laser excitation in solution and graphene-aided increase in water temperature. *The Journal of Physical Chemistry Letters, 1*, 2804−2809.

Addamo, M., Bellardita, M., Di Paola, A., & Palmisano, L. (2006). Preparation and photoactivity of nanostructured anatase, rutile and brookite TiO_2 thin films. *Chemical Communication, 47*, 4943−4945.

Ahmed, M. A. (2012). Synthesis and structural features of mesoporous NiO/TiO_2 nanocomposites prepared by sol-gel method for photodegradation of methylene blue dye. *Journal of Photochemistry and Photobiology A: Chemistry, 238*, 63−70.

Akhavan, O., Abdolahad, M., Abdi, Y., & Mohajerzadeh, S. (2009). Synthesis of titania/carbon nanotube heterojunction arrays for photoinactivation of *E. Coli* in visible light irradiation. *Carbon, 47*, 3280−3287.

Akhavan, O., Abdolahad, M., Esfandiar, A., & Mohatashamifar, M. (2010). Photodegradation of graphene oxide sheets by TiO_2 nanoparticles after a photocatalytic reduction. *The Journal of Physical Chemistry C, 114*, 12955−12959.

Allam, N. K., Shankar, K., & Grimes, C. A. (2008). Photoelectrochemical and water photoelectrolysis properties of ordered TiO_2 nanotubes fabricated by Ti anodization in fluoride-free HCl electrolytes. *Journal of Materials Chemistry, 18*, 2341−2348.

An, H., Zhou, J., Li, J., Zhu, B., Wang, S., Zhang, S., … Huang, W. (2009). Deposition of Pt on the stable nanotubular TiO_2 and its photocatalytic performance. *Catalysis Communications, 11*, 175−179.

Bai, H., Li, C., & Shi, G. (2011). Functional composite materials based on chemically converted graphene. *Advanced Materials, 23*, 1089−1115.

Bajpai, R., Roy, S., Rafiee, J., Koratkar, N., & Misra, D. S. (2012). Graphene supported nickel nanoparticle as a viable replacement for platinum in dye sensitized solar cells. *Nanoscale, 4*, 926−930.

Barron, A. R., & Hamilton, C. E. (20 Jun, 2009). *Graphene*. Retrieved from http://cnx.org/contents/790bacf3-6512-4957-bbed-ac887a4fca7c@4.

Binitha, N. N., Yaakob, Z., Reshmi, M. R., Sugunan, S., Ambili, V. K., & Zetty, A. A. (2009). Preparation and characterization of nano-silver doped mesoporous titania photocatalysts for dye degradation. *Catalysis Today, 147*, S76−S80.

Cai, Q., Paulose, M., Varghese, O. K., & Grimes, C. A. (2005). The effect of electrolyte composition on the fabrication of self-organized titanium oxide nanotube arrays by anodic oxidation. *Journal of Materials Research, 20*, 230−236.

Cao, Y., He, T., Zhao, L., Wang, E., Yang, W., & Cao, Y. (2009). Structure and phase transition behavior of Sn^{4+}-doped TiO_2 nanoparticles. *The Journal of Physical Chemistry C, 113*, 18121−18124.

Cao, Y., Yang, W., Zhang, W., Liu, G., & Yue, P. (2004). Improved photocatalytic activity of Sn^{4+} doped TiO_2 nanoparticulate films prepared by plasma-enhanced chemical vapor deposition. *New Journal of Chemistry, 28*, 218−222.

Chang, S. Y., Chen, S. F., & Huang, Y. C. (2011). Synthesis, structural correlations, and photocatalytic properties of TiO_2 nanotube/SnO_2-Pd nanoparticle heterostructures. *The Journal of Physical Chemistry C, 115*, 1600−1607.

Chen, C., Cai, W., Long, M., Zhou, B., Wu, Y., Wu, D., & Feng, Y. (2010). Synthesis of visible-light responsive graphene oxide/TiO_2 composites with p/n heterojunction. *ACS nano, 4*, 6425−6432.

Chen, J., Wiley, B., McLellan, J., Xiong, Y., Li, Z. Y., & Xia, Y. (2005a). Optical properties of Pd-Ag and Pt-Ag nanoboxes synthesized via galvanic replacement reactions. *Nano Letters, 5*, 2058−2062.

Chen, S. F., Zhang, S. J., Liu, W., & Zhao, W. (2008). Preparation and activity evaluation of p-n junction photocatalyst NiO/TiO_2. *Journal of Hazardous Materials*, *155*, 320−326.

Chen, X., & Mao, S. S. (2007). Titanium dioxide nanomaterials: synthesis, properties, modifications, and applications. *Chemical Rev*iews, *107*, 2891−2959.

Chen, X., Schriver, M., Suen, T., & Mao, S. S. (2007). Fabrication of 10 nm diameter TiO_2 nanotube arrays by titanium anodization. *Thin Solid Films, 515*, 8511−8514.

Chen, Y., Crittenden, J. C., Hackney, S., Sutter, L., & Hand, D. W. (2005b). Preparation of a novel TiO_2-based p-n junction nanotube photocatalyst. *Environmental Science and Technology, 39*, 1201−1208.

Chen, Z., Fang, L., Dong, W., Zheng, F., Shen, M., & Wang, J. (2014). Inverse opal structured Ag/TiO_2 plasmonic photocatalyst prepared by pulsed current deposition and its enhanced visible light photocatalytic activity. *Journal of Materials Chemistry A, 2*, 824−832.

Cheng, J., Zhang, M., Wu, G., Wang, X., Zhou, J., & Cen, K. (2014). Photoelectrocatalytic reduction of CO_2 into chemicals using Pt-modified reduced graphene oxide combined with Pt-modified TiO_2 nanotubes. *Environmental Science & Technology, 48*, 7076−7084.

Choi, H. J., & Kang, M. (2007).Hydrogen production from methanol/water decomposition in a liquid photosystem using the anatase structure of Cu loaded TiO_2. *International Journal of Hydrogen Energy, 32*, 3841−3848.

Choi, W., Termin, A., & Hoffmann, M. R. (1994). Role of metal-ion dopants in quantum-sized TiO_2-correlation between photoreactivity and charge-carrier recombination dynamics. *The Journal of Physical Chemistry A, 98*, 13669−13679.

Cong, Y. Q., Li, Z., Zhang, Y., Wang, Q., & Xu, Q. (2012). Synthesis of α-Fe_2O_3/TiO_2 nanotube arrays for photoelectro-Fenton degradation of phenol. *Chemical Engineering Journal, 191*, 356−363.

Daghrir, R., Drogui, P., & Robert, D. (2013). Modified TiO_2 for environmental photocatalyric applications: a review. *Industry & Engineering Chemistry Research, 52*, 3581−3599.

De Jongh, P. E., & Vanmaekelbergh, D. (1996). Trap-limited electronic transport in assemblies of nanometer-size TiO_2 particles. *Physical Review Letters, 77*, 3427−3430.

Eom, H., Jung, J. Y., Shin, Y., Kim, S., Choi, J. H., Lee, E., Jeong, J. H., & Park, I. (2014). Strong localized surface plasmon resonance effects of Ag/TiO_2 core-shell nanowire arrays in UV and visible light for photocatalytic activity. *Nanoscale, 6*, 226−234.

Fan, W., Jewell, S., She, Y., & Leung, M. K. (2014). *In situ* deposition of Ag-Ag_2S hybrid nanoparticles onto TiO_2 nanotube arrays towards fabrication of photoelectrodes with high visible light photoelectrochemical properties. *Physical Chemistry Chemical Physics, 16*, 676−680.

Fang, D., Huang, K., Liu, S., & Li, Z. (2008). Electrochemical properties of ordered TiO_2 nanotube loaded with Ag nano-particles for lithium anode material. *Journal of Alloys and Compounds, 464*, L5−L9.

Feng, X., Sloppy, J. D., LaTempa, T. J., Paulose, M., Komarneni, S., Bao, N., & Grimes, C. A. (2011). Synthesis and deposition of ultrafine Pt nanoparticles within high aspect ratio TiO_2 nanotube arrays: application to the photocatalytic reduction of carbon dioxide. *Journal of Materials Chemistry, 21*, 13429−13433.

Fuerte, A., Hernández-Alonso, M. D., Maira, A. J., Martınez-Arias, A., Fernández-Garcıa, M., Conesa, J. C., ... Munuera, G. (2002). Nanosize Ti–W mixed oxides: effect of doping level in the photocatalytic degradation of toluene using sunlight-type excitation. *Journal of Catalysis, 212*, 1−9.

Fujishima, A., & Honda, K. (1972). Electrochemical photolysis of water at a semiconductor electrode. *Nature, 238*, 37−38.

Galian, R. E., & Pérez-Prieto, J. (2010). Catalytic processes activated by light. *Energy & Environmental Science, 3*, 1488−1498.

Gao, J., Ren, X., Chen, D., Tang, F., & Ren, J. (2007). Bimetallic Ag-Pt hollow nanoparticles: synthesis and tunable surface plasmon resonance. *Scripta Materialia, 57*, 687−690.

Gao, X., Jang, J., & Nagase, S. (2010). Hydrazine and thermal reduction of graphene oxide: reaction mechanisms, product structures, and reaction design. *The Journal of Physical Chemistry C, 114*, 832−842.

Gao, Y. Y., Pu, X. P., Zhang, D. F., Ding, G. Q., Shao, X., & Ma, J. (2012). Combustion synthesis of graphene oxide-TiO_2 hybrid materials for photodegradation of methyl orange. *Carbon, 50*, 4093−4101.

Gong, D. W., Grimes, C. A., Varghese, O. K., Hu, W., Singh, R. S., Chen, Z., & Dickey, E. C. (2001). Titanium oxide nanotube arrays prepared by anodic oxidation. *Journal of Materials Research, 16*, 3331−3334.

Graf, D., Molitor, F., Ensslin, K., Stampfer, C., Jungen, A., Hierold, C., & Wirtz, L. (2007). Spatially resolved Raman spectroscopy of single-and few-layer graphene. *Nano Letters, 7*, 238−242.

Grimes, C. A., & Mor, G. K. (2009). *Nanotube arrays: synthesis, properties and application*. New York, USA: Springer.

Guo, H. L., Wang, X. F., Qian, Q. Y., Wang, F. B., & Xia, X. H. (2009). A green approach to the synthesis of graphene nanosheets. *ACS nano, 3*, 2653−2659.

Guo, H., Peng, M., Zhu, Z., & Sun, L. (2013). Preparation of reduced graphene oxide by infrared irradiation induced photothermal reduction. *Nanoscale, 5*, 9040−9048.

Guo, J., Fu, W., Yang, H., Yu, Q., Zhao, W., Zhou, X., ... Li, M. (2010). A NiO/TiO_2 junction electrode constructed using self-organized TiO_2 nanotube arrays for highly efficient photoelectrocatalytic visible ligh activations. *Journal of Physics D: Applied Physics, 43*, 245202−245209.

Hahn, R., Macak, J. M., & Schmuki, P. (2007). Rapid anodic growth of TiO_2 and WO_3 nanotubes in fluoride free electrolytes. *Electrochemistry Communications, 9*, 947−952.

Haruta, M. (2005). Catalysis: Gold rush. *Nature, 437*, 1098−1099.

He Jr, H., Wu, T. H., Hsin, C. L., Li, K. M., Chen, L. J., Chueh, Y. L., ... Wang, Z. L. (2006). Beaklike SnO_2 nanorods with strong photoluminescent and field-emission properties. *small, 2*, 116−120.

He, X., Cai, Y., Zhang, H., & Liang, C. (2011). Photocatalytic degradation of organic pollutants with Ag decorated free-standing TiO_2 nanotube arrays and interface electrochemical response. *Journal of Materials Chemistry, 21*, 475−480.

He, Y., Basnet, P., Murph, S. E. H., & Zhao, Y. (2013). Ag nanoparticle embedded TiO_2 composite nanorod arrays fabricated by oblique angle deposition: toward plasmonic photocatalysis. *ACS Applied Materials & Interfaces, 5*, 11818−11827.

Hensel, J., Wang, G., Li, Y., & Zhang, J. Z. (2010). Synergistic effect of CdSe quantum dot sensitization and nitrogen doping of TiO_2 nanostructures for photoelectrochemical solar hydrogen generation. *Nano Letters, 10*, 478−483.

Hernández-Alonso, M. D., Fresno, F., Suárez, S., & Coronado, J. M. (2009). Development of alternative photocatalyst to TiO_2: challenges and opportunities. *Energy & Environmental Science, 2*, 1231−1257.

Ho, P. F., & Chi, K. M. (2004). Size-controlled synthesis of Pd nanoparticles from β-diketonato complexes of palladium. *Nanotechnology, 15*, 1059−1064.

Hoffmann, M. R., Martin, S. T., Choi, W., & Bahnemann, D. W. (1995). Environmental applications of semiconductor photocatalysis. *Chemical Reviews, 95*, 69−96.

Hou, L. R., Yuan, C. Z., & Peng, Y. (2007). Synthesis and photocatalytic property of SnO_2/TiO_2. *Journal of Hazardous Materials, B139*, 310−315.

Hou, Y., Li, X., Zhao, Q., Quan, X., & Chen, G. (2010). Electrochemically assisted photocatalytic degradation of 4-chlorophenol by $ZnFe_2O_4$-modified TiO_2 nanotube array electrode under visible light irradiation. *Environmental Science & Technology, 44*, 5098−5103.

Hou, Y., Li, X., Zou, X., Quan, X., & Chen, G. (2009). Photoeletrocatalytic activity of a Cu_2O-loaded self-organized highly oriented TiO_2 nanotube array electrode for 4-chlorophenol degradation. *Environmental Science & Technology, 43,* 858−863.

Huang, J. Y., Zhang, K. Q., & Lai, Y. K. (2013). Fabrication, modification, and emerging applications of TiO_2 nanotube arrays by electrochemical synthesis: a review. *International Journal of Photoenergy, 2013*, 1−19.

Huang, J., Cheuk, W., Wu, Y., Lee, F. S., & Ho, W. (2012). Fabrication of Bi-doped TiO_2 spheres with ultrasonic spray pyrolysis and investigation of their visible-light photocatalytic properties. *Journal of Nanotechnology, 2012*, 1−7.

Huang, L. H., Sun, C., & Liu, Y. L. (2007). Pt/N-codoped TiO_2 nanotubes and its photocatalytic activity under visible light. *Applied Surface Science, 253*, 7029−7035.

Huang, Y. C., Chang, S. Y., Lin, C. F., & Tseng, W. J. (2011). Synthesis of ZnO nanorod grafted TiO_2 nanotube 3-D arrayed heterostructure as supporting platform for nanoparticle deposition. *Journal of Materials Chemistry, 21*, 14056−14061.

Hummers Jr, W. S., & Offeman, R. E. (1958). Preparation of graphitic oxide. *Journal of the American Chemical Society, 80*, 1339−1339.

Ihara, T., Miyoshi, M., Iriyama, Y., Matsumoto, O., & Sugihara, S. (2003). Visible-light-active titanium oxide photocatalyst realized by an oxygen-deficient structure and by nitrogen doping. *Applied Catalysis B: Environmental, 42*, 403−409.

Indrakanti, V. P., Kubicki, J. D., & Schobert, H. H. (2009). Photoinduced activation of CO_2 on Ti-based heterogeneous catalysts: current state, chemical physics-based insights and outlook. *Energy & Environmental Science, 2*, 745−758.

Jiao, J., Tang, J., Gao, W., Kuang, D., Tong, Y., & Chen, L. (2015). Plasmonic silver nanoparticles matched with vertically aligned nitrogen-doped titanium dioxide nanotube arrays for enhanced photoelectrochemical activity. *Journal of Power Sources, 274*, 464−470.

Kaleji, B. K., & Sarraf-Mamoory, R. (2012). Nanocrystalline sol–gel TiO_2-SnO_2 coatings: preparation, characterization and photo-catalytic performance. *Materials Research Bulletin, 47*, 362−369.

Kaneco, S., Shimizu, Y., Ohta, K., & Mizuno, T. (1998). Photocatalytic reduction of high pressure carbon dioxide using TiO_2 powders with a positive hole scavenger. *Journal of Photochemistry and Photobiology A: Chemistry*, *115*, 223−226.

Kang, S. H., Sung, Y. E., & Smyrl, W. H. (2008). The effectiveness of sputtered PtCo catalysts on TiO_2 nanotube arrays for the oxygen reduction reaction. *Journal of the Electrochemical Society, 155*, B1128−B1135.

Kim, D. H., Park, H. S., Kim, S. J., & Lee, K. S. (2006). Synthesis of novel TiO_2 by mechanical alloying and heat treatment-derived nanocomposite of TiO_2 and $NiTiO_3$. *Catalysis Letters, 106*, 29−33.

Kim, S., & Choi, W. (2005). Visible-light-induced photocatalytic degradation of 4-chlorophenol and phenolic compounds in aqueous suspension of pure titania: demonstrating the existence of a surface-complex-mediated path. *The Journal of Physical Chemistry B, 109*, 5143−5149.

Kočí, K., Matějů, K., Obalová, L., Krejčíková, S., Lacný, Z., Plachá, D., ... Ŝolcová, O. (2010). Effect of silver doping on the TiO_2 for photocatalytic reduction of CO_2. *Applied Catalysis B: Environmental*, 96, 239−244.

Konstantinou, I. K., & Albanis, T. A. (2004). TiO_2-assisted photocatalytic degradation of azo dyes in aqueous solution: kinetic and mechanistic investigations: a review. *Applied Catalysis B: Environmental, 49*, 1−14.

Krejčíková, S., Matějová, L., Kočí, K., Obalová, L., Matěj, Z., Čapek, L., & Šolcová, O. (2012). Preparation and characterization of Ag-doped crystalline titania for photocatalysis applications. *Applied Catalysis B: Environmental, 111*, 119−125.

Ku, Y., Lin, C. N., & Hou, W. M. (2011). Characterization of coupled NiO/TiO_2 photocatalyst for the photocatalytic reduction of Cr(VI) in aqueous solution. *Journal of Molecular Catalysis A: Chemical, 349*, 20−27.

Kudo, A., & Miseki, Y. (2009). Heterogeneous photocatalyst materials for water splitting. *Chemical Society Reviews, 38*, 253−278.

Lai, Y. K., Huang, J. Y., Zhang, H. F., Subramaniam, V. P., Tang, Y. X., Gong, D. G., ... Lin, C. J. (2010a). Nitrogen-doped TiO_2 nanotube array films with enhanced photocatalytic activity under various light sources. *Journal of Hazardous Materials, 184*, 855−863.

Lai, Y., Lin, Z., Zheng, D., Chi, L., Du, R., & Lin, C. (2012). CdSe/CdS quantum dots co-sensitized TiO_2 nanotube array photoelectrode for highly efficient solar cells. *Electrochimica Acta, 79*, 175−181.

Lai, Y., Zhuang, H., Xie, K., Gong, D., Tang, Y., Sun, L., … Chen, Z. (2010b). Fabrication of uniform Ag/TiO_2 nanotube array structures with enhanced photoelectrochemical performance. *New Journal of Chemistry, 34*, 1335−1340.

Langhammer, C., Yuan, Z., Zorić, I., & Kasemo, B. (2006). Plasmonic properties of supported Pt and Pd nanostructures. *Nano Letters, 6*, 833−838.

Li, F. B., & Li, X. Z. (2002). The enhancement of photodegradation efficiency using Pt-TiO_2 catalyst. *Chemosphere, 48*, 1103−1111.

Li, P., Zhao, G., Li, M., Cao, T., Cui, X., & Li, D. (2012). Design and high efficient photoelectric-synergistic catalytic oxidation activity of 2D macroporous SnO_2 1D TiO_2 nanotubes. *Applied Catalysis B: Environmental*, *111*, 578−585.

Li, Q., & Shang, J. K. (2010). Composite photocatalyst of nitrogen and fluorine codoped titanium oxide nanotube arrays with dispersed palladium oxide nanoparticles for enhanced visible light photocatalytic performance. *Environmental Science & Technology, 44*, 3493−3499.

Li, Y., Wang, W. N., Zhan, Z., Woo, M. H., Wu, C. Y., & Biswas, P. (2010). Photocatalytic reduction of CO_2 with H_2O on mesoporous silica supported Cu/TiO_2 catalysts. *Applied Catalysis B: Environmental, 100*, 386−392.

Lightcap, I. V., Kosel, T. H., & Kamat, P. V. (2010). Anchoring semiconductor and metal nanoparticles on a two-dimensional catalyst mat. storing and shuttling electrons with reduced graphene oxide. *Nano Letters, 10*, 577−583.

Lim, J. H., & Choi, J. (2007). Titanium oxide nanowires originating from anodically grown nanotubes: the bamboo-splitting model. *small, 3*, 1504−1507.

Lin, C., Song, Y., Cao, L., & Chen, S. (2013). TiO_2 nanotubes/ZnO/CdS ternary nanocomposites: preparation, characterization and photocatalysis. *Journal of the Chinese Advanced Materials Society, 1*, 188−199.

Lin, D., Wu, H., Zhang, R., & Pan, W. (2009). Enhanced photocatalysis of electrospun Ag-ZnO heterostructured nanofibers. *Chemistry of Materials, 21*, 3479−3484.

Lin, Y. J., Chang, Y. H., Yang, W. D., & Tsai, B. S. (2006). Synthesis and characterization of ilmenite $NiTiO_3$ and $CoTiO_3$ prepared by a modified Pechini method. *Journal of Non-Crystalline Solids, 352*, 789−794.

Lin, Z. Q., Lai, Y. K., Hu, R. G., Li, J., Du, R. G., & Lin, C. J. (2010). A highly efficient ZnS/CdS@TiO_2 photoelectrode for photogenerated cathodic protection of metals. *Electrochimica Acta, 55*, 8717−8723.

Linsebigler, A. L., Lu, G., & Yates Jr, J. T. (1995). Photocatalysis on TiO_2 surfaces: principles, mechanisms, and selected results. *Chemical Reviews, 95*, 735−758.

Liu, B. S., He, X., Zhao, X. J., & Zhao, Q. N. (2006). The surface states and the electron-hole pairs recombination of TiO_2 nanopowders. *Spectroscopy and Spectral Analysis, 26*, 208−212.

Liu, C., Teng, Y., Liu, R., Luo, S., Tang, Y., Chen, L., & Cai, Q. (2011). Fabrication of graphene films on TiO_2 nanotube arrays for photocatalytic application. *Carbon, 49*, 5312−5320.

Liu, H., Liu, G., & Zhou, Q. (2009). Preparation and characterization of Zr doped TiO_2 nanotube arrays on the titanium sheet and their enhanced photocatalytic activity. *Journal of Solid State Chemistry, 182*, 3238−3242.

Liu, J., Sun, Y., & Li, Z. (2012). Ag loaded flower-like $BaTiO_3$ nanotube arrays: Fabrication and enhanced photocatalytic property. *CrystEngComm, 14*, 1473−1478.

Liu, L., Lv, J., Xu, G., Wang, Y., Xie, K., Chen, Z., & Wu, Y. (2013). Uniformly dispersed CdS nanoparticles sensitized TiO_2 nanotube arrays with enhanced visible-light photocatalytic activity and stability. *Journal of Solid State Chemistry, 208*, 27−34.

Liu, Z., Liu, Q., Huang, Y., Ma, Y., Yin, S., Zhang, X., … Chen, Y. (2008). Organic photovoltaic devices based on a novel acceptor material: graphene. *Advanced Materials, 20*, 3924−3930.

Loh, K. P., Bao, Q., Ang, P. K., & Yang, J. (2010). The chemistry of graphene. *Journal of Materials Chemistry, 20*, 2277−2289.

Long, M., Qin, Y., Chen, C., Guo, X., Tan, B., & Cai, W. (2013). Origin of visible light photoactivity of reduced graphene oxide/TiO_2 by in situ hydrothermal growth of undergrown TiO_2 with graphene oxide. *The Journal of Physical Chemistry C, 117*, 16734−16741.

Ma, Q., Liu, S. J., Weng, L. Q., Liu, Y., & Liu, B. (2010). Growth, structure and photocatalytic properties of hierarchical Cu-Ti-O nanotube arrays by anodization. *Journal of Alloys and Compounds, 501*, 333−338.

Macak, J. M., & Schmuki, P. (2006). Anodic growth of self-organized anodic TiO_2 nanotubes in viscous electrolytes. *Electrochimica Acta, 52*, 1258−1264.

Macak, J. M., Sirotna, K., & Schmuki, P. (2005a). Self-organized porous titanium oxide prepared in Na_2SO_4/NaF electrolytes. *Electrochimica Acta, 50*, 3679−3684.

Macak, J. M., Tsuchiya, H., Taveira, L., Aldabergerova, S., & Schmuki, P. (2005b). Smooth anodic TiO_2 nanotubes. *Angewandte Chemie International Edition, 44*, 7463−7465.

Mills, A., & Le Hunte, S. (1997). An overview of semiconductor photocatalysis. *Journal of Photochemistry and Photobiology A: Chemistry, 108*, 1−35.

Min, S., & Lu, G. (2011). Dye-sensitized reduced graphene oxide photocatalysts for highly efficient visible-light-driven water reduction. *The Journal of Physical Chemistry C, 115*, 13938−13945.

Mkhoyan, K. A., Contryman, A. W., Silcox, J., Stewart, D. A., Eda, G., Mattevi, C., ... Chhowalla, M. (2009). Atomic and electronic structure of graphene-oxide. *Nano Letters, 9*, 1058−1063.

Mohamed, A. E. R., & Rohani, S. (2011). Modified TiO_2 nanotube arrays (TNTAs): progressive strategies towards visible light responsive photoanode, a review. *Energy & Environmental Science, 4*, 1065−1086.

Mohapatra, S. K., Kondamudi, N., Banerjee, S., & Misra, M. (2008). Functionalization of self-organized TiO_2 nanotubes with Pd nanoparticles for photocatalytic decomposition of dyes under solar light illumination. *Langmuir, 24*, 11276−11281.

Moon, G. H., Kim, H. I., Shin, Y., & Choi, W. (2012). Chemical-free growth of metal nanoparticles on graphene oxide sheets under visible light irradiation. *RSC Advances, 2*, 2205−2207.

Mor, G. K., Prakasam, H. E., Varghese, O. K., Shankar, K., & Grimes, C. A. (2007). Vertically oriented Ti−Fe−O nanotube array films: toward a useful material architecture for solar spectrum water photoelectrolysis. *Nano Letters, 7*, 2356−2364.

Mor, G. K., Shankar, K., Paulose, M., Varghese, O. K., & Grimes, C. A. (2005). Enhanced photocleavage of water using titania nanotube arrays. *Nano Letters, 5*, 191−195.

Mor, G. K., Varghese, O. K., Paulose, M., Mukherjee, N., & Grimes, C. A. (2003). Fabrication of tapered, conical-shaped titania nanotubes. *Journal of Materials Research, 18*, 2588−2593.

Mor, G. K., Varghese, O. K., Paulose, M., Shankar, K., & Grimes, C. A. (2006). A review on highly ordered, vertically oriented TiO_2 nanotube arrays: fabrication, material properties, and solar energy applications. *Solar Energy Materials & Solar Cells, 90*, 2011−2075.

Mou, Z., Dong, Y., Li, S., Du, Y., Wang, X., Yang, P., & Wang, S. (2011). Eosin Y functionalized graphene for photocatalytic hydrogen production from water. *International Journal of Hydrogen Energy, 36*, 8885−8893.

Mun, K. S., Alvarez, S. D., Choi, W. Y., & Sailor, M. J. (2010). A stable, label-free optical interferometric biosensor based on TiO_2 nanotube arrays. *ACS Nano, 4*, 2070−2076.

Murphy, A. B., Barnes, P. R. F., Randeniya, L. K., Plumb, I. C., Grey, I. E., Horne, M. D., & Glasscock, J. A. (2006). Efficiency of solar water splitting using semiconductor electrodes. *International Journal of Hydrogen Energy, 31*, 1999−2017.

Nah, Y. C., Paramasivam, I., & Schmuki, P. (2010). Doped TiO_2 and TiO_2 nanotubes: synthesis and applications. *ChemPhysChem, 11*, 2698−2713.

Nair, R. R., Blake, P., Grigorenko, A. N., Novoselov, K. S., Booth, T. J., Stauber, T., … Geim, A. K. (2008). Fine structure constant defines visual transparency of graphene. *Science, 320,* 1308−1308.

Neppolian, B., Bruno, A., Bianchi, C. L., & Ashokkumar, M. (2012). Graphene oxide based Pt-TiO_2 photocatalyst: ultrasound assisted synthesis, characterization and catalytic efficiency. *Ultrasonics Sonochemistry, 19*, 9−15.

Ni, Z., Wang, Y., Yu, T., & Shen, Z. (2008). Raman spectroscopy and imaging of graphene. *Nano Research, 1*, 273−291.

Niishiro, R., Kato, H., & Kudo, K. (2005). Nickel and either tantalum or niobium-codoped TiO_2 and $SrTiO_3$ photocatalysts with visible-light response for H_2 or O_2 evolution from aqueous solutions. *Physical Chemistry Chemical Physics, 7*, 2241−2245.

Nishimura, A., Komatsu, N., Mitsui, G., Hirota, M., & Hu, E. (2009). CO_2 reforming into fuel using TiO_2 photocatalyst and gas separation membrane. *Catalysis Today, 148,* 341−349.

Nolan, N. T., Seery, M. K., Hinder, S. J., Healy, L. F., & Pillai, S. C. (2010). A systematic study of the effect of silver on the chelation of formic acid to a titanium precursor and the resulting effect on the anatase to rutile transformation of TiO_2. *The Journal of Physical Chemistry C, 114*, 13026−13034.

Ohsaka, T., Yamaoka, S., & Shimomura, O. (1979). Effect of hydrostatic pressure on the Raman spectrum of anatase (TiO_2). *Solid State Communications, 30*, 345−347.

Pal, M., Pal, U., Jiménez, J. M. G. Y., & Pérez-Rodríguez, F. (2012). Effects of crystallization and dopant concentration on the emission behavior of TiO_2: Eu nanophosphors. *Nanoscale Research Letters, 7*, 1−12.

Palmisano, G., García-López, E., Marcì, G., Loddo, V., Yurdakal, S., Augugliaro, V., & Palmisano, L. (2010). Advances in selective conversions by heterogeneous photocatalysis. *Chemical Communications, 46*, 7074−7089.

Pan, D., Xi, C., Li, Z., Wang, L., Chen, Z., Lu, B., & Wu, M. (2013). Electrophoretic fabrication of highly robust, efficient, and benign heterojunction photoelectrocatalysts based on graphene-quantum-dot sensitized TiO_2 nanotube arrays. *Journal of Materials Chemistry A, 1,* 3551−3555.

Pandey, D. K., Chung, T. F., Prakash, G., Piner, R., Chen, Y. P., & Reifenberger, R. (2011). Folding and cracking of graphene oxide sheets upon deposition. *Surface Science, 605*, 1669−1675.

Paramasivam, I., Macak, J. M., & Schmuki, P. (2008). Photocatalytic activity of TiO_2 nanotube layers loaded with Ag and Au nanoparticles. *Electrochemistry Communications, 10*, 71−75.

Paulose, M., Prakasam, H. E., Varghese, O. K., Peng, L., Popat, K. C., Mor, G. K., … Grimes, C. A. (2007). TiO_2 nanotube arrays of 1000 µm length by anodization of titanium foil: phenol red diffusion. *Journal of Physical Chemistry C, 111*, 14992−14997.

Paulose, M., Shankar, K., Yoriya, S., Prakasam, H. E., Varghese, O. K., Mor, G. K., … Grimes, C. A. (2006). Anodic growth of highly ordered TiO_2 nanotube arrays to 134 µm in length. *The Journal of Physical Chemistry B, 110*, 16179−16184.

Prakasam, H. E., Shankar, K., Paulose, M., Varghese, O. K., & Grimes, C. A. (2007). A new benchmark for TiO_2 nanotube array growth by anodization. *The Journal of Physical Chemistry C, 111*, 7235−7241.

Rajeshwar, K. (1994). Photoelectrochemisty and the environment. *Journal of Applied Electrochemistry, 25*, 1067−1082.

Ramesha, G. K., & Sampath, S. (2009). Electrochemical reduction of oriented graphene oxide films: an in situ raman spectroelectrochemical study. *The Journal of Physical Chemistry C, 113*, 7985−7989.

Ren, C., Yang, B., Wu, M., Xu, J., Fu, Z., Guo, T., … Zhu, C. (2010). Synthesis of Ag/ZnO nanorods array with enhanced photocatalytic performance. *Journal of Hazardous Materials, 182*, 123−129.

Roy, S. C., Varghese, O. K., Paulose, M., & Grimes, C. A. (2010). Toward solar fuels: photocatalytic conversion of carbon dioxide to hydrocarbons. *ACS Nano, 4*, 1259−1278.

Ruan, C., Paulose, M., Varghese, O. K., Mor, G. K., & Grimes, C. A. (2005). Fabrication of highly ordered TiO_2 nanotube arrays using an organic electrolyte. *The Journal of Physical Chemistry B, 109*, 15754−15759.

Sakthivel, S., & Kisch, H. (2003). Daylight photocatalysis by carbon-modified titanium dioxide. *Angewandte Chemie International Edition, 42,* 4908−4911.

Sakthivel, S., Shankar, M. V., Palanichamy, M., Arabindoo, B., Bahnemann, D. W., & Murugesan, V. (2004). Enhancement of photocatalytic activity by metal deposition: characterisation and photonic efficiency of Pt, Au and Pd deposited on TiO_2 catalyst. *Water Research, 38*, 3001−3008.

Santara, B., Pal, B., & Giri, P. K. (2011). Signature of strong ferromagnetism and optical properties of Co doped TiO_2 nanoparticles. *Journal of Applied Physics*, *110*, 114322−114329.

Sasi, B., & Gopchandran, K. G. (2007). Nanostructured mesoporous nickel oxide thin films. *Nanotechnolog*y, *18*, 115613−115622.

Sasirekha, N., Basha, S. J. S., & Shanthi, K. (2006). Photocatalytic performance of Ru doped anatase mounted on silica for reduction of carbon dioxide. *Applied Catalysis B: Environmental, 62*, 169−180.

Schniepp, H. C., Li, J. L., McAllister, M. J., Sai, H., Herrera-Alonso, M., Adamson, D. H., ... Aksay, I. A. (2006). Functionalized single graphene sheets derived from splitting graphite oxide. *The Journal of Physical Chemistry B, 110*, 8535−8539.

Schulte, K. L., DeSario, P. A., & Gray, K. A. (2010). Effect of crystal phase composition on the reductive and oxidative abilities of TiO_2 nanotubes under UV and visible light. *Applied Catalysis B: Environmental, 97*, 354−360.

Seery, M. K., George, R., Floris, P., & Pillai, S. C. (2007). Silver-doped titanium dioxide nanomaterials for enhanced visible light photocatalysis. *Journal of Photochemistry and Photobiology A: Chemistry, 189*, 258−263.

Seger, B., & Kamat, P. V. (2009). Fuel cell geared in reverse: photocatalytic hydrogen production using a TiO_2/Nafion/Pt membrane assembly with no applied bias. *The Journal of Physical Chemistry C*, *113*, 18946−18952.

Serpone, N., Maruthamuthu, P., Pichat, P., Pelizzetti, E., & Hidaka, H. (1995). Exploiting the interparticle electron transfer process in the photocatalysed oxidation of phenol, 2-chlorophenol and pentachlorophenol: chemical evidence for electron and hole transfer between coupled semiconductors. *Journal of Photochemistry and Photobiology A: Chemistry, 85*, 247−255.

Shah, M. S. A. S., Zhang, K., Park, A. R., Kim, K. S., Park, N. G., Park, J. H., & Yoo, P. J. (2013). Single-step solvothermal synthesis of mesoporous Ag/TiO_2/reduced graphene oxide ternary composites with enhanced photocatalytic activity. *Nanoscale, 5*, 5093−5101.

Shankar, K., Mor, G. K., Prakasam, H. E., Yoriya, S., Paulose, M., Varghese, O. K., & Grimes, C. A. (2007). Highly-ordered TiO_2 nanotube arrays up to 220 μm in length: use in water photoelectrolysis and dye-sensitized solar cells. *Nanotechnology, 18*, 1−11.

Shrestha, N. K., Yang, M., Nah, Y. C., Paramasivam, I., & Schmuki, P. (2010). Self-organized TiO_2 nanotubes: visible light activation by Ni oxide nanoparticle decoration. *Electrochemistry Communications, 12*, 254−257.

Sim, L. C., Ng, K. W., Ibrahim, S., & Saravanan, P. (2013). Preparation of improved p-n junction NiO/TiO_2 nanotubes for solar-energy-driven light photocatalysis. *International Journal of Photoenergy, 2013*, 1−10.

Singhal, S., Chawla, A. K., Gupta, H. O., & Chandra, R. (2010). Influence of cobalt doping on the physical properties of $Zn_{0.9}Cd_{0.1}S$ nanoparticles. *Nanoscale Research Letters, 5*, 323−331.

Song, P., Zhang, X., Sun, M., Cui, X., & Lin, Y. (2012). Graphene oxide modified TiO_2 nanotube arrays: enhanced visible light photoelectrochemical properties. *Nanoscale, 4*, 1800−1804.

Su, C., Liu, L., Zhang, M., Zhang, Y., & Shao, C. (2012). Fabrication of Ag/TiO_2 nanoheterostructures with visible light photocatalytic function via a solvothermal approach. *CrystEngComm, 14*, 3989−3999.

Su, Y., & Deng, Y. (2011). Effect of structure on the photocatalytic activity of Pt-doped TiO_2 nanotubes. *Applied Surface Science, 257*, 9791−9795.

Sun, H. Q., Liu, S. Z., Liu, S. M., & Wang, S. B. (2014). A comparative study of reduced graphene oxide modified TiO_2, ZnO and Ta_2O_5 in visible light photocatalytic/photochemical oxidation of methylene blue. *Applied Catalysis B: Environmental, 146*, 162−168.

Sun, L., Li, J., Wang, C., Li, S., Lai, Y., Chen, H., & Lin, C. (2009). Ultrasound aided photochemical synthesis of Ag loaded TiO_2 nanotube arrays to enhance photocatalytic activity. *Journal of Hazardous Materials, 171*, 1045−1050.

Sun, Y., Wang, G., & Yan, K. (2011). TiO_2 nanotubes for hydrogen generation by photocatalytic water splitting in a two compartment photoelectrochemical cell. *International Journal of Hydrogen Energy, 36*, 15502−15508.

Tachikawa, T., Tojo, S., Fujitsuka, M., & Majima, T. (2004). Photocatalytic one-electron oxidation of biphenyl derivatives strongly coupled with the TiO_2 surface. *Langmuir*, *20*, 2753−2759.

Tang, Y., Luo, S., Teng, Y., Liu, C., Xu, X., Zhang, X., & Chen, L. (2012). Efficient removal of herbicide 2,4-dichlorophenoxyacetic acid from water using Ag/reduced graphene oxide co-decorated TiO_2 nanotube arrays. *Journal of Hazardous Materials, 241*, 323−330.

Taveira, L. V., Macak, J. M., Sirotna, K., Dick, L. F. P., & Schmuki, P. (2006). Voltage oscillations and morphology during the galvanostatic formation of self-organized TiO_2 nanotubes. *Journal of the Electrochemical Society, 153*, B137−B143.

Taveira, L. V., Macak, J. M., Tsuchiya, H., Dick, L. F. P., & Schmuki, P. (2005). Initiation and growth of self-organized TiO_2 nanotubes anodically formed in $NH_4F/(NH_4)_2SO_4$ electrolytes. *Journal of the Electrochemical Society, 152*, B405−B410.

Teh, C. M., & Mohamed, A. R. (2011). Role of titanium dioxide and ion doped titanium dioxide on photocatalytic degradation of organic pollutants (phenol compounds and dyes) in aqueous solutions: a review. *Journal of Alloys and Compounds, 509*, 1648−1660.

Timilsina, G. R., & Shrestha, A. (2009). Transport sector CO_2 emissions growth in Asia: underlying factors and policy options. *Energy Policy, 37*, 4523−4539.

Tomás, S. A., Luna-Resendis, A., Cortés-Cuautli, L. C., & Jacinto, D. (2009). Optical and morphological characterization of photocatalytic TiO_2 thin films doped with silver. *Thin Solid Films, 518*, 1337−1340.

Tseng. I. H., Wu, J. C. S., & Chou, H. Y. (2004). Effects of sol-gel procedures on the photocatalysis of Cu/TiO_2 in CO_2 photoreduction. *Journal of Catalysis, 221*, 432−440.

Varghese, O. K., Paulose, M., LaTempa, T. J., & Grimes, C. A. (2009). High-rate solar photocatalytic conversion of CO_2 and water vapor to hydrocarbon fuels. *Nano Letters, 9*, 731−737.

Vijayan, B. K., Dimitrijevic, N. M., Wu, J., & Gray, K. A. (2010). The effects of Pt doping on the structure and visible light photoactivity of titania nanotubes. *The Journal of Physical Chemistry C, 114*, 21262−21269.

Vinodgopal, K., & Kamat, P. V. (1995). Enhanced rates of photocatalytic degradation of an azo dye using SnO_2/TiO_2 coupled semiconductor thin films. *Environmental Science & Technology, 29,* 841−845.

Vinodgopal, K., Neppolian, B., Lightcap, I. V., Grieser, F., Ashokkumar, M., & Kamat, P. V. (2010). Sonolytic design of graphene-Au nanocomposites. Simultaneous and sequentical reduction of graphene oxide and Au (III). *The Journal of Physical Chemistry Letters, 1,* 1987−1993.

Wang, C., Thompson, R. L., Baltrus, J., & Matranga, C. (2010). Visible light photoreduction of CO_2 using $CdSe/Pt/TiO_2$ heterostructured catalysts. *The Journal of Physical Chemistry Letters, 1,* 48−53.

Wang, D. T., Li, X., Chen, J. F., & Tao, X. (2012a). Enhanced photoelectrocatalytic activity of reduced graphene oxide/TiO_2 composite films for dye degradation. *Chemical Engineering Journal, 198−199*, 547−554.

Wang, E., He, T., Zhao, L., Chen, Y., & Cao, Y. (2011a). Improved visible light photocatalytic activity of titania doped with tin and nitrogen. *Journal of Materials Chemistry, 21*, 144−150.

Wang, J., & Lin, Z. Q. (2010). Dye-sensitized TiO_2 nanotube solar cells with markedly enhanced performance via rational surface engineering. *Chemistry of Materials, 22*, 579−584.

Wang, M., Sun, L., Lin, Z., Cai, J., Xie, K., & Lin, C. (2013a). p–n Heterojunction photoelectrodes composed of Cu_2O-loaded TiO_2 nanotube arrays with enhanced photoelectrochemical and photoelectrocatalytic activities. *Energy & Environmental Science, 6,* 1211−1220.

Wang, P., Liu, Z. G., Chen, X., Meng, F. L., Liu, J. H., & Huang, X. J. (2013b). UV irradiation synthesis of an Au–graphene nanocomposite with enhanced electrochemical sensing properties. *Journal of Materials Chemistry A, 1,* 9189−9195.

Wang, P., Tang, Y., Dong, Z., Chen, Z., & Lim, T. T. (2013c). Ag–AgBr/TiO_2/RGO nanocomposite for visible-light photocatalytic degradation of penicillin G. *Journal of Materials Chemistry A, 1,* 4718−4727.

Wang, P., Wang, J., Wang, X. F., Yu, H. G., Yu, J. G., Lei, M., & Wang, Y. G. (2013d). One-step synthesis of easy-recycling TiO_2-rGO nanocomposite photocatalysts with enhanced photocatalytic activity. *Applied Catalysis B: Environmental, 132,* 452−459.

Wang, P., Zhai, Y., Wang, D., & Dong, S. (2011b). Synthesis of reduced graphene oxide-anatase TiO_2 nanocomposite and its improved photo-induced charge transfer properties. *Nanoscale, 3,* 1640−1645.

Wang, W. N., An, W. J., Ramalingam, B., Mukherjee, S., Niedzwiedzki, D. M., Gangopadhyay, S., & Biswas, P. (2012b). Size and structure matter: enhanced CO_2 photoreduction efficiency by size-resolved ultrafine Pt nanoparticles on TiO_2 single crystals. *Journal of the American Chemical Society, 134,* 11276−11281.

Wang, W. S., Wang, D. H., Qu, W. G., Lu, L. Q., & Xu, A. W. (2012c). Large ultrathin anatase TiO_2 nanosheets with exposed {001} facets on graphene for enhanced visible light photocatalytic activity. *The Journal of Physical Chemistry C, 116,* 19893−19901.

Wang, X., Zhi, L., & Müllen, K. (2008). Transparent, conductive graphene electrodes for dye-sensitized solar cells. *Nano Letters, 8*, 323−327.

Wang, Y., Hang, K., Anderson, N. A., & Lian, T. (2003). Comparison of electron transfer dynamics in molecule-to-nanoparticle and intramolecular charge transfer complexes. *The Journal of Physical Chemistry B, 107*, 9434−9440.

Wang, Y., Tang, Y., Chen, Y., Li, Y., Liu, X., Luo, S., & Liu, C. (2013e). Reduced graphene oxide-based photocatalysts containing Ag nanoparticles on a TiO_2 nanotube array. *Journal of Materials Science, 48*, 6203−6211.

Williams, G., Seger, B., & Kamat, P. V. (2008). TiO_2-graphene nanocomposites. UV-assisted photocatalytic reduction of graphene oxide. *ACS Nano, 2*, 1487−1491.

Woan, K., Pyrgiotakis, G., & Sigmund, W. (2009). Photocatalytic carbon-nanotube–TiO_2 composites. *Advanced Materials, 21*, 2233−2239.

Wu, J. C. S., Lin, H. M., & Lai, C. L. (2005). Photo reduction of CO_2 to methanol using optical-fiber photoreactor. *Applied Catalysis A: General, 296,* 194−200.

Wu, L., Li, F., Xu, Y. Y., Zhang, J. W., Zhang, D. Q., Li, G. S., & Li, H. X. (2015). Plasmon-induced photoelectrocatalytic activity of Au nanoparticles enhanced TiO_2 nanotube arrays electrodes for environmental remediation. *Applied Catalysis B: Environmental, 164*, 217−224.

Wu, Q., Ouyang, J., Xie, K., Sun, L., Wang, M., & Lin, C. (2012). Ultrasound-assisted synthesis and visible-light-driven photocatalytic activity of Fe-incorporated TiO_2 nanotube array photocatalysts. *Journal of Hazardous Materials, 199*, 410−417.

Wu, T., Cai, X., Tan, S., Li, H., Liu, J., & Yang, W. (2011). Adsorption characteristics of acrylonitrile, p-toluenesulfonic acid, 1-naphthalenesulfonic acid and methyl blue on graphene in aqueous solutions. *Chemical Engineering Journal, 173*, 144−149.

Xiang, Q., Yu, J., & Jaroniec, M. (2011). Enhanced photocatalytic H_2-production activity of graphene-modified titania nanosheets. *Nanoscale, 3*, 3670−3678.

Xiao, F. X. (2012a). Layer-by-layer self-assembly construction of highly ordered metal-TiO_2 nanotube arrays heterostructures (M/TNTs, M= Au, Ag, Pt) with tunable catalytic activities. *The Journal of Physical Chemistry C, 116*, 16487−16498.

Xiao, F. X. (2012b). Construction of highly ordered ZnO-TiO_2 nanotube arrays (ZnO/TNTs) heterostructure for photocatalytic application. *ACS Applied Materials & Interfaces, 4*, 7055−7063.

Xiao, F. X., Miao, J., Wang, H. Y., & Liu, B. (2013). Self-assembly of hierarchically ordered CdS quantum dots-TiO_2 nanotube array heterostructures as efficient visible light photocatalysts for photoredox applications. *Journal of Materials Chemistry A, 1*, 12229−12238.

Xiao, P., Zhang, Y., & Cao, G. (2011). Effect of surface defects on biosensing properties of TiO_2 nanotube arrays. *Sensors and Actuators B: Chemical, 155*, 159−164.

Xiaoyuan, J., Huijuan, L., & Xiaoming, Z. (2008). Catalytic activity of CuO-loaded $TiO_2/\gamma\text{-}Al_2O_3$ for NO Reduction by CO. *Journal of Materials Science, 43*, 6505−6512.

Xie, K. P., Sun, L., Wang, C. L., Lai, Y. K., Wang, M. Y., Chen, H. B., & Lin, C. J. (2010). Photoelectrocatalytic properties of Ag nanoparticles loaded TiO_2 nanotube arrays prepared by pulse current deposition. *Electrochimica Acta, 55*, 7211−7218.

Xiong, L. B., Li, J. L., Yang, B., & Yu, Y. (2012). Ti^{3+} in the surface of titanium dioxide: generation, properties and photocatalytic application. *Journal of Nanomaterials, 2012*, 1−13.

Xiong, Y., Chen, J., Wiley, B., Xia, Y., Yin, Y., & Li, Z. Y. (2005). Size-dependence of surface plasmon resonance and oxidation for Pd nanocubes synthesized via a seed etching process. *Nano Letters, 5*, 1237−1242.

Xu, J., Ao, Y., Chen, M., & Fu, D. (2010). Photoelectrochemical property and photocatalytic activity of N-doped TiO_2 nanotube arrays. *Applied Surface Science, 256*, 4397−4401.

Xu, Y., Bai, H., Lu, G., Li, C., & Shi, G. (2008). Flexible graphene films via the filtration of water-soluble noncovalent functionalized graphene sheets. *Journal of the American Chemical Society, 130,* 5856−5857.

Xu, Z., Yu, J., & Liu, G. (2011). Enhancement of ethanol electrooxidation on plasmonic Au/TiO_2 nanotube arrays. *Electrochemistry Communications, 13*, 1260−1263.

Yang, D. J., Park, H., Cho, S. J., Kim, H. G., & Choi, W. Y. (2008). TiO_2-nanotube-based dye-sensitized solar cells fabricated by an efficient anodic oxidation for high surface area. *Journal of Physics and Chemistry of Solids, 69*, 1272−1275.

Yang, N., Zhai, J., Wang, D., Chen, Y., & Jiang, L. (2010). Two-dimensional graphene bridges enhanced photoinduced charge transport in dye-sensitized solar cells. *ACS Nano, 4*, 887−894.

Yeh, T. F., Chan, F. F., Hsieh, C. T., & Teng, H. (2011). Graphite oxide with different oxygenated levels for hydrogen and oxygen production from water under illumination: the band positions of graphite oxide. *The Journal of Physical Chemistry C, 115*, 22587−22597.

Yeh, T. F., Cihlář, J., Chang, C. Y., Cheng, C., & Teng, H. (2013). Roles of graphene oxide in photocatalytic water splitting. *Materials Today, 16*, 78−84.

Yeh, T. F., Syu, J. M., Cheng, C., Chang, T. H., & Teng, H. (2010). Graphite oxide as a photocatalyst for hydrogen production from water. *Advanced Functional Materials, 20*, 2255−2262.

Yin, Y., Jin, Z., Hou, F., & Wang, X. (2007). Synthesis and morphology of TiO_2 nanotube arrays by anodic oxidation using modified glycerol-based electrolytes. *Journal of the American Ceramic Society, 90*, 2384−2389.

Yoriya, S., Mor, G. K., Sharma, S., & Grimes, C. A. (2008). Synthesis of ordered arrays of discrete, partially crystalline titania nanotubes by Ti anodization using diethylene glycol electrolytes. *Journal of Materials Chemistry, 18*, 3332−3336.

Yoriya, S., Paulose, M., Varghese, O. K., Mor, G. K., & Grimes, C. A. (2007). Fabrication of vertically oriented TiO_2 nanotube arrays using dimethyl sulfoxide electrolytes. *The Journal of Physical Chemistry C, 111*, 13770−13776.

Yu, H., Chen, S., Fan, X., Quan, X., Zhao, H., Li, X., & Zhang, Y. (2010). A structured macroporous silicon/graphene heterojunction for efficient photoconversion. *Angewandte Chemie International Edition, 49*, 5106−5109.

Yu, J., Dai, G., & Huang, B. (2009). Fabrication and characterization of visible-light-driven plasmonic photocatalyst Ag/AgCl/TiO_2 nanotube arrays. *The Journal of Physical Chemistry C, 113*, 16394−16401.

Yuan, J., Zhang, C., Li, C., Chen, M., & Shangguan, W. (2011, January). Pt-CdS/TiO_2 nanotube catalyst for photocatalytic reduction of CO_2 with water under visible light irradiation. In *MRS Proceedings* (Vol. 1326, pp. mrss11−1326). Cambridge University Press.

Yui, T., Kan, A., Saitoh, C., Koike, K., Ibusuki, T., & Ishitani, O. (2011). Photochemical reduction of CO_2 using TiO_2: effects of organic adsorbates on TiO_2 and deposition of Pd onto TiO_2. *ACS Applied Materials and Interfaces, 3*, 2594−2600.

Zhang, H., Lv, X., Li, Y., Wang, Y., & Li, J. (2009). P25-graphene composite as a high performance photocatalyst. *ACS Nano, 4*, 380−386.

Zhang, J., Xiong, Z., & Zhao, X. S. (2011). Graphene-metal-oxide composites for the degradation of dyes under visible light irradiation. *Journal of Materials Chemistry, 21*, 3634−3640.

Zhang, X. Y., Li, H. P., Cui, X. L., & Lin, Y. (2010a). Graphene/TiO_2 nanocomposites: synthesis, characterization and application in hydrogen evolution from water photocatalytic splitting. *Journal of Materials Chemistry, 20*, 2801−2806.

Zhang, X., Chen, Y. L., Liu, R. S., & Tsai, D. P. (2013). Plasmonic photocatalysis. *Reports on Progress in Physics, 76*, 046401.

Zhang, X., Han, F., Shi, B., Farsinezhad, S., Dechaine, G. P., & Shankar, K. (2012). Photocatalytic conversion of diluted CO_2 into light hydrocarbons using periodically modulated multiwalled nanotube arrays. *Angewandte Chemie, 124*, 12904−12907.

Zhang, Z., Shao, C., Li, X., Wang, C., Zhang, M., & and Liu, Y. (2010b). Electrospun nanofibers of p-type NiO/n-type ZnO heterojunctions with enhanced photocatalytic activity. *ACS Applied Materials and Interfaces*, *2*, 2915−2923.

Zhu, K., Vinzant, T. B., Neale, N. R., & Frank, A. J. (2007). Removing structural disorder from oriented TiO_2 nanotube arrays: reducing the dimensionality of transport and recombination in dye-sensitized solar cells. *Nano Letters, 7,* 3739−3746.

Zielińska-Jurek, A., Kowalska, E., Sobczak, J. W., Lisowski, W., Ohtani, B., & Zaleska, A. (2011). Preparation and characterization of monometallic (Au) and bimetallic (Ag/Au) modified-titania photocatalysts activated by visible light. *Applied Catalysis B: Environmental*, *101*, 504−514.

Zwilling, V., Aucouturier, M., & Darque-Ceretti, E. (1999). Anodic oxidation of titanium and TA6V alloy in chromic media. An electrochemical approach. *Electrochimica Acta*, *45*, 921−929.

LIST OF PUBLICATIONS AND PAPERS PRESENTED

Papers Published

1. Sim, L. C., Leong, K. H., Ibrahim, S., & Saravanan, P. (2014). Graphene oxide and Ag engulfed TiO_2 nanotube arrays for enhanced electrons mobility and visible-light driven photocatalytic performance. *Journal of Materials Chemistry A, 2*, 5315−5322.
2. Sim, L. C., Ng, K. W., Ibrahim, S., & Saravanan, P. (2014). Synthesis features and solar-light-driven photocatalytic activity of TiO_2 nanotube arrays loaded with SnO_2. *Journal of Nanoscience and Nanotechnology, 14*, 7001−7009.
3. Sim, L. C., Ng, K. W., Ibrahim, S., & Saravanan, P. (2013). Preparation of improved p-n junction NiO/TiO_2 nanotubes for solar-energy-driven light photocatalysis. *International Journal of Photoenergy, 2013*, 1−10.

Paper in Consideration

1. Sim, L. C., Ibrahim, S., & Saravanan, P. (2014). Rapid thermal reduced graphene oxide-Pt/TiO_2 nanotube arrays for enhanced visible-light-driven photocatalytic performance. *Carbon*, under review.

Conference Presentations

1. Sim, L. C., Ng, K. W., Saravanan, P., & Ibrahim, S. "NiO/TiO_2 nanotube arrays photocatalyst for enhanced visible light harvesting." International Conference on X Rays & Related Techniques on Research & Industry 2012 (ICXRI 2012). 3−5 July (2012) Penang, Malaysia.
2. Sim, L. C., Ng, K. W., Saravanan, P., & Ibrahim, S. "Synthesis features and solar light-driven photocatalytic activity of TiO_2 nanotube arrays loaded with SnO_2." The 3rd ISESCO International Workshop and Conference on Nanotechnology 2012 (IWCN 2012). 5−7 December (2012) Universiti Kebangsaan Malaysia, Malaysia.

3. Sim, L. C., Leong, K. H., Ibrahim, S., & Saravanan, P. “Graphene oxide-Ag doped TiO_2 nanotube arrays for enhanced photocatalytic activity.” IWA Symposium on Environmental Nanotechnology (IWASEN 2013). 24−27 April (2013) Nanjing, China.
4. Sim, L. C., Leong, K. H., Ibrahim, S., & Saravanan, P. “Graphene oxide-Ag doped TiO_2 nanotube arrays with enhanced photocatalytic activity.” 1st International Conference on Energy Environment and Human Engineering (ICEEHE 2013). 21−23 Dec (2013) Yangon, Myanmar.
5. Sim, L. C., Ibrahim, S., & Saravanan, P. “Rapid thermal reduced graphene oxide-Pt doped TiO_2 nanotube arrays.” 8th European Meeting on Solar Chemistry and Photocatalysis: Environmental Applications. 25−28 June (2014) Thessaloniki, Greece.